Design of Homogeneous / Heterogeneous Interfacial Electrocatalytic Systems for Value-Added Products

A Dissertation Submitted to the

Indian Institute of Technology Guwahati

in Partial Fulfilment for the Degree of

DOCTOR of PHILOSOPHY

By

Nitul Kalita

Roll No:206122110

DEPARTMENT OF CHEMISTRY

INDIAN INSTITUTE OF TECHNOLOGY GUWAHATI

GUWAHATI, ASSAM, INDIA

JANUARY 2026

STATEMENT

I hereby declare that the scientific findings included in this thesis entitled, "**Design of Homogeneous / Heterogeneous Interfacial Electrocatalytic Systems for Value-Added Products**" is the outcome of research work carried out by me under the supervision of Prof. Mohammad Qureshi, at the Department of Chemistry, Indian Institute of Technology Guwahati, Assam, India, for the award of the degree of Doctor of Philosophy.

The work embodied in this thesis is the result of original research done by me except where otherwise stated in this thesis with proper citations. I confirm that the investigations were conducted in accord with the ethics policies and integrity standards of the Indian Institute of Technology Guwahati and that the research data are presented honestly and without prejudice. The thesis work has not been submitted for a degree or professional qualification to any other university or institution.

IIT-Guwahati
January 2026

Nitul Kalita
Candidate
Department of Chemistry
IIT-Guwahati
Guwahati-781039, Assam
India

Dr. Mohammad Qureshi
Professor
Department of Chemistry
Indian Institute of Technology, Guwahati
Assam – 781039
Email: mq@iitg.ac.in

CERTIFICATE

Certified that the work described in this thesis entitled "**Design of Homogeneous / Heterogeneous Interfacial Electrocatalytic Systems for Value-Added Products**" by Mr. Nitul Kalita, Department of Chemistry, Indian Institute of Technology Guwahati has been carried out his thesis work under my supervision and has not been submitted elsewhere for a degree.

Guwahati
January 2026

Mohammad Qureshi
Thesis supervisor
Department of Chemistry
Indian Institute of Technology Guwahati
Guwahati-781039

ACKNOWLEDGEMENT

This thesis represents not only the research work carried out by me at IIT Guwahati and in the Materials Science Laboratory (MSL, CHEL-109), but also the remarkable journey I have experienced throughout my tenure here. The past half-decade has been truly enriching and transformative. From my very first day at IITG, I have been surrounded by exceptional individuals who have continuously supported and guided me in achieving important milestones. I was fortunate to receive unique opportunities and even more fortunate to make the most of them.

Foremost, I would like to express my sincere gratitude to my thesis supervisor, Prof. Mohammad Qureshi, for providing me the opportunity to work under his expert supervision. I am deeply thankful to him for introducing me to the specialized research areas of *electrochemical water splitting and CO_2 reduction*. His constant encouragement, insightful suggestions, and unwavering faith in my abilities greatly motivated me throughout my research journey. His support in providing alternative research directions strengthened my scientific understanding, while the freedom and intellectual space he offered allowed me to explore ideas independently and grow as a researcher.

I am also grateful to my thesis committee members for their invaluable guidance over the years. I sincerely thank Prof. Chivukula Vasudeva Sastri (Chairperson), Dr. Akshai Kumar Alape Seetharam, and Dr. Selvaraju Narayanasamy for their continuous support, constructive feedback, and periodic evaluation of my research work. I would like to especially acknowledge Prof. C. V. Sastri for his direct involvement and significant contribution toward the completion of two chapters of this thesis.

I gratefully acknowledge the Prime Minister's Research Fellowship (PMRF) for providing financial support and essential resources that enabled me to carry out my research work effectively. I also extend my sincere thanks to all the faculty members and staff of the Department of Chemistry, IIT Guwahati, for their assistance in various academic and administrative aspects. My heartfelt thanks go to the staff of the Central Instruments Facility for their guidance and support in the utilization of advanced instrumental facilities.

Many individuals have contributed to my growth, from a novice learner to a professional researcher. I am deeply thankful to my lab seniors for their invaluable guidance and support. I sincerely thank Dr. Sourav Bhowmick, Dr. Ching Thian Moi, and Dr. Manoj Kumar Mohanta for being mentors as well as friends, making my time in the laboratory both productive and enjoyable. I am also grateful to my lab mates and juniors for their cooperation and helping hands throughout my research work.

I would like to extend special thanks to Dr. Jagnyesh Kumar Satpathy for his continuous assistance in my research, and to my friend Dr. Upasana Nath for her support during my thesis work. I would like to express my heartfelt gratitude to my dear Shibu (Barsha Rani Bora) for her unwavering love, constant encouragement, and steadfast emotional support throughout this journey. Her belief in me and her presence during challenging times have been a source of strength and motivation. I am also sincerely thankful to my friends Akash Dev Roshan and Nikumoni Das for their encouragement and support which have made this journey all the more meaningful.

Above all, this thesis is dedicated to my parents. My mother, Kalpana Kalita, whose unconditional love, faith, and emotional strength have been my greatest source of motivation, and my father, Keshab Kalita, whose sacrifices, wisdom, and support have shaped my confidence and determination to pursue my goals.

It is difficult to acknowledge everyone in a single piece of writing; therefore, any unintentional omission does not reflect a lack of gratitude.

Nitul

Dedicated to

My Family

TABLE OF CONTENTS

Thesis Title:	Design of Homogeneous / Heterogeneous Interfacial Electrocatalytic Systems for Value-Added Products
Name of the Candidate:	**Nitul Kalita**
Registration Number:	206122110
Thesis Supervisor:	Prof. Mohammad Qureshi
Department:	Chemistry
Institute:	Indian Institute of Technology Guwahati, Assam – 781039, India.

Thesis Overview

Chapter 1: Introduction

A comprehensive overview of electrocatalytic systems for sustainable value-added product formation via water electrolysis and CO_2 reduction is presented in this work. The study focuses on the design and development of efficient catalytic interfaces, functional membranes, and hybrid reaction environments to achieve improved charge separation, accelerated reaction kinetics, and enhanced product selectivity. Emphasis is placed on understanding the mechanistic aspects of hydrogen and oxygen evolution reactions, highlighting the significance of interfacial charge transfer and catalyst–electrolyte interactions. The role of bipolar membranes in promoting water dissociation and maintaining distinct pH conditions is explored as a strategy to achieve efficient ion transport and separation of HER and OER processes. Furthermore, the investigation extends toward CO_2 electroreduction, where synergistic homogeneous–heterogeneous interfaces enable selective conversion of CO_2 into value-added fuels. Overall, the study establishes a unified approach combining catalyst design, interfacial engineering, and membrane optimization to advance integrated electrochemical systems for sustainable energy generation and carbon utilization.

Chapter 2: Experimental

The instrumental methods and procedures employed for material characterization and device fabrication are outlined, along with a brief overview of key electrochemical analysis techniques such as cyclic voltammetry, galvanostatic charge-discharge, and electrochemical impedance spectroscopy, followed by distribution of relaxation time analysis.

Chapter 3: Redox Synchronization:

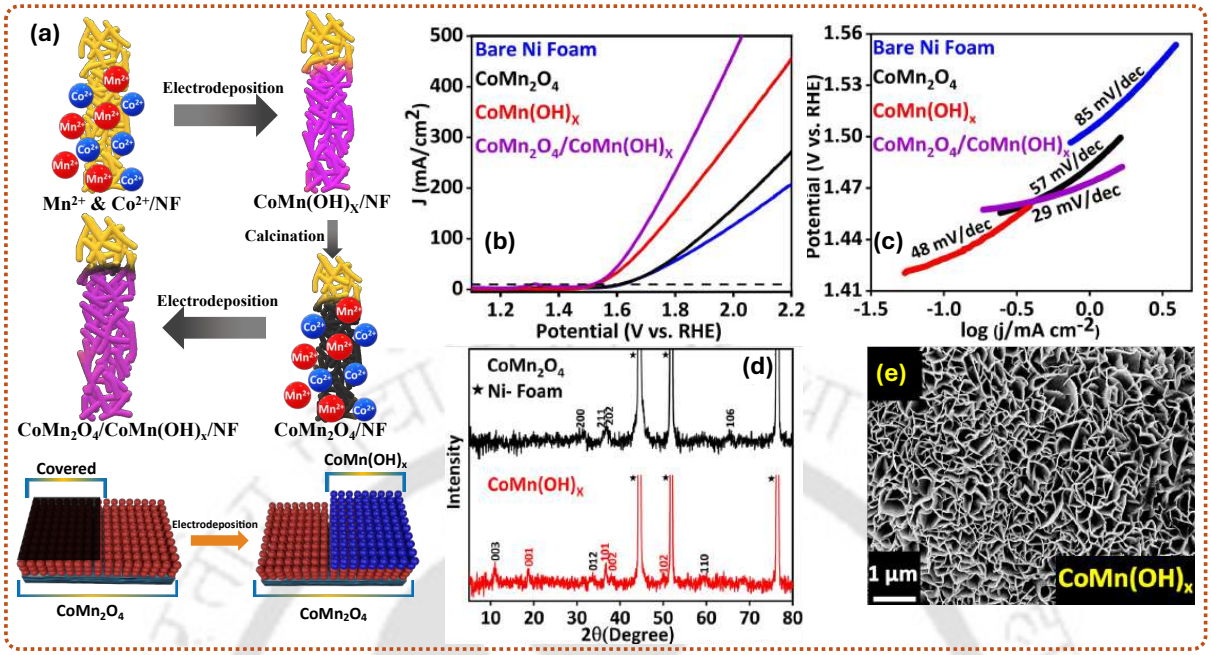

Figure 1. *(a) Stepwise fabrication of CMOH/CMO/Ni-foam working electrode; (b, c) electrochemical analysis (d, e) material characterizations* ***[Ref: N. Kalita, et. al. Chemical Communications, 2022, 58, 13747-13750]***

This work focuses on the rational design and development of cost-effective, high-performance electrocatalysts for the oxygen evolution reaction (OER) in alkaline water electrolysis. To address the high overpotential and sluggish kinetics associated with conventional transition metal oxides, a two-step electrodeposition strategy was employed to fabricate a composite catalyst comprising $CoMn_2O_4$ (CMO) and its hydroxide analogue, $CoMn(OH)_x$ (CMOH), directly on Ni foam. The $CoMn_2O_4$ spinel, featuring mixed-valence Co and Mn sites, provides abundant redox-active centers and robust structural stability, while the overlayer of $CoMn(OH)_x$ enhances interfacial charge transfer through synchronized redox coupling of Co^{2+}/Co^{3+} and Mn^{3+}/Mn^{4+} pairs. This integrated electrode exhibits superior catalytic activity, delivering overpotential of 260 mV a current density of 10 mA cm^{-2} with a remarkably low Tafel slope of 29 mV dec^{-1}, and demonstrates a four-fold enhancement in turnover frequency compared to pristine $CoMn_2O_4$. The improved electrocatalytic performance is attributed to enhanced carrier mobility, reduced charge-transfer resistance, and optimized electrode–electrolyte interactions. This study establishes an efficient and scalable electrochemical synthesis route for transition-metal-based OER catalysts, providing a

viable pathway toward developing stable, earth-abundant, and high-activity materials for sustainable hydrogen generation through water electrolysis.

Chapter 4: *Electronic Band Gap Modulation:*

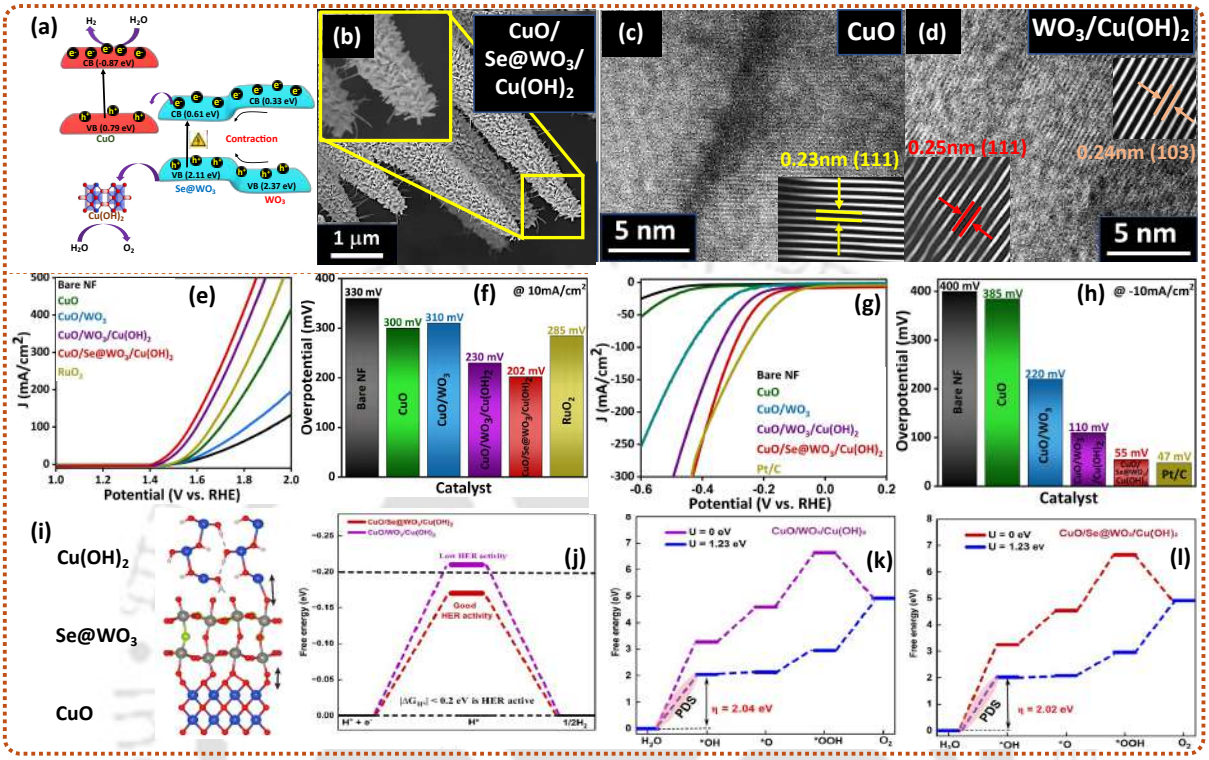

Figure 2. *(a) Schematic of electron transfer across heterojunction in water splitting; (b, c, d) material characterizations; (e and h) electrochemical analysis; (I, l) Free energy profile for HER and OER* ***[Ref: N. Kallita, et. al. Journal of Materials Chemistry A, 2025, 13, 10723-10735]***

This project focuses on the rational design and electronic structure modulation of a CuO/Se@WO_3/$Cu(OH)_2$ heterostructured catalyst to achieve efficient and stable overall water splitting. A dendritic CuO layer was first electrodeposited on Ni foam, followed by the formation of Se-doped WO_3 (Se@WO_3), creating a p–n heterojunction that enhances interfacial charge transfer. Selenium doping plays a pivotal role in reducing the WO_3 band gap by approximately 0.54 eV, increasing the electron density around W sites and enabling a Z-scheme electron transfer mechanism that minimizes charge recombination. To further accelerate the reaction kinetics, a $Cu(OH)_2$ layer was electrodeposited on the surface as a hole-extraction interface, synchronizing the Cu^{2+}/Cu^{+} redox couples between CuO and $Cu(OH)_2$, thereby reducing charge-transfer resistance. The synergistic architecture results in outstanding electrocatalytic activity, with overpotentials of 202 mV for OER and 55 mV for HER at 10 mA cm^{-2}, and Tafel slopes of 35 and 45 mV dec^{-1}, respectively exceeding the

performance of RuO_2 and comparable to Pt/C catalysts. DFT calculations confirm the enhanced electronic conductivity, charge redistribution, and favourable hydrogen adsorption energy (ΔG_{H^*} = −0.17 eV). Collectively, this work establishes a cost-effective and durable catalytic platform for sustainable hydrogen generation through alkaline water electrolysis.

Chapter 5: Bipolar Membrane for Water Dissociation:

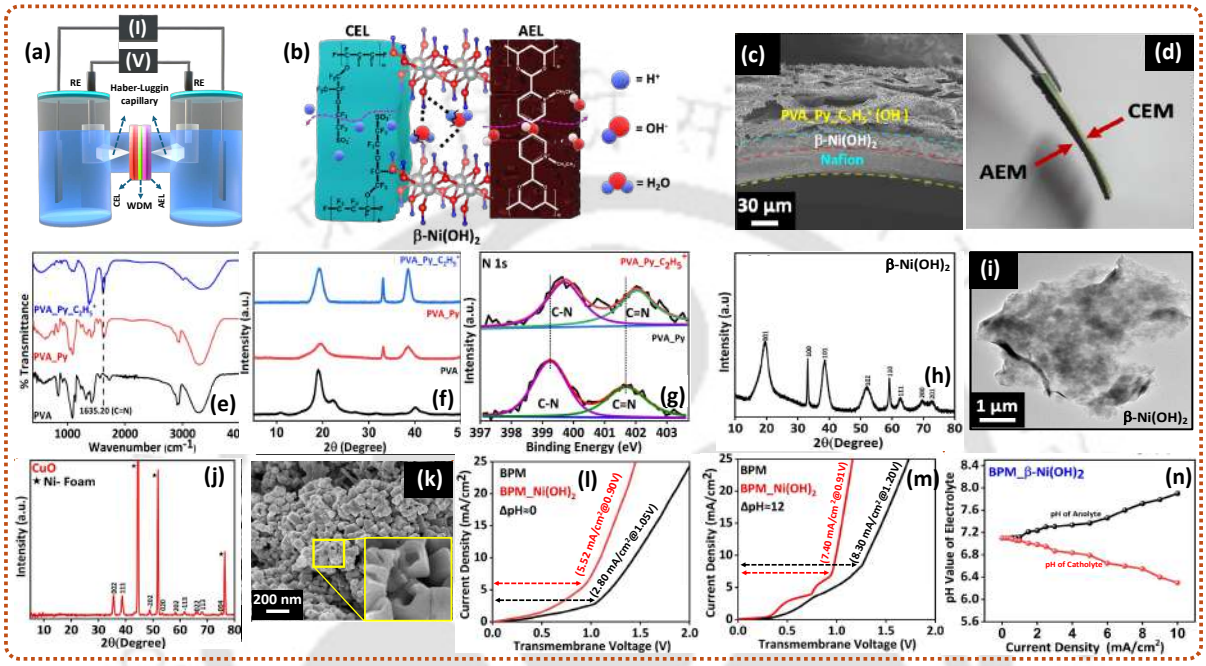

Figure 3. *(a, b) Schematic of electrochemical setup and proposed water dissociation mechanism; (c-k) material characterizations; (l-n) electrochemical analysis.* ***Ref: N. Kalita, et. al. The Journal of Physical Chemistry C, 2024, 7, 2776-2787]***

The present work delineates the rational design and optimization of a high-performance bipolar membrane (BPM) system engineered to enhance water dissociation (WD) kinetics and minimize transmembrane voltage during electrolysis. The BPM was constructed by integrating quaternized pyridine-functionalized poly(vinyl alcohol) (PVA) as the anion exchange membrane (AEM) and activated Nafion as the cation exchange membrane (CEM). The synthesized AEM exhibited an ion exchange capacity (IEC) of 2.3 mmol g^{-1}, comparable to the most efficient commercial counterparts. To further accelerate the interfacial WD process, two-dimensional β-$Ni(OH)_2$ nanosheets were incorporated at the interfacial layer (IL) between the AEM and CEM, where their abundant surface hydroxyl groups and strong water adsorption capabilities catalysed effective H^+/OH^- generation under reverse bias conditions. The resulting hybrid BPM exhibited a 55.7% enhancement in water uptake capacity and significantly

improved WD efficiency, achieving 0.90 V at ΔpH ≈ 0 and 0.91 V at ΔpH ≈ 12, corresponding to current densities of 5.52 and 7.40 mA cm^{-2}, respectively. Moreover, the adoption of an asymmetric electrode configuration, employing hollow cuboidal CuO (hC-CuO@NF) as the OER anode and Pt as the HER cathode, further amplified catalytic activity by optimizing local pH environments. Collectively, this integrated BPM–electrode architecture provides a robust, durable, and energy-efficient platform for sustainable and high-performance water electrolysis.

Chapter 6a: Integrating Homogeneous–Heterogeneous Catalytic Interfaces for Efficient Water Electrolysis:

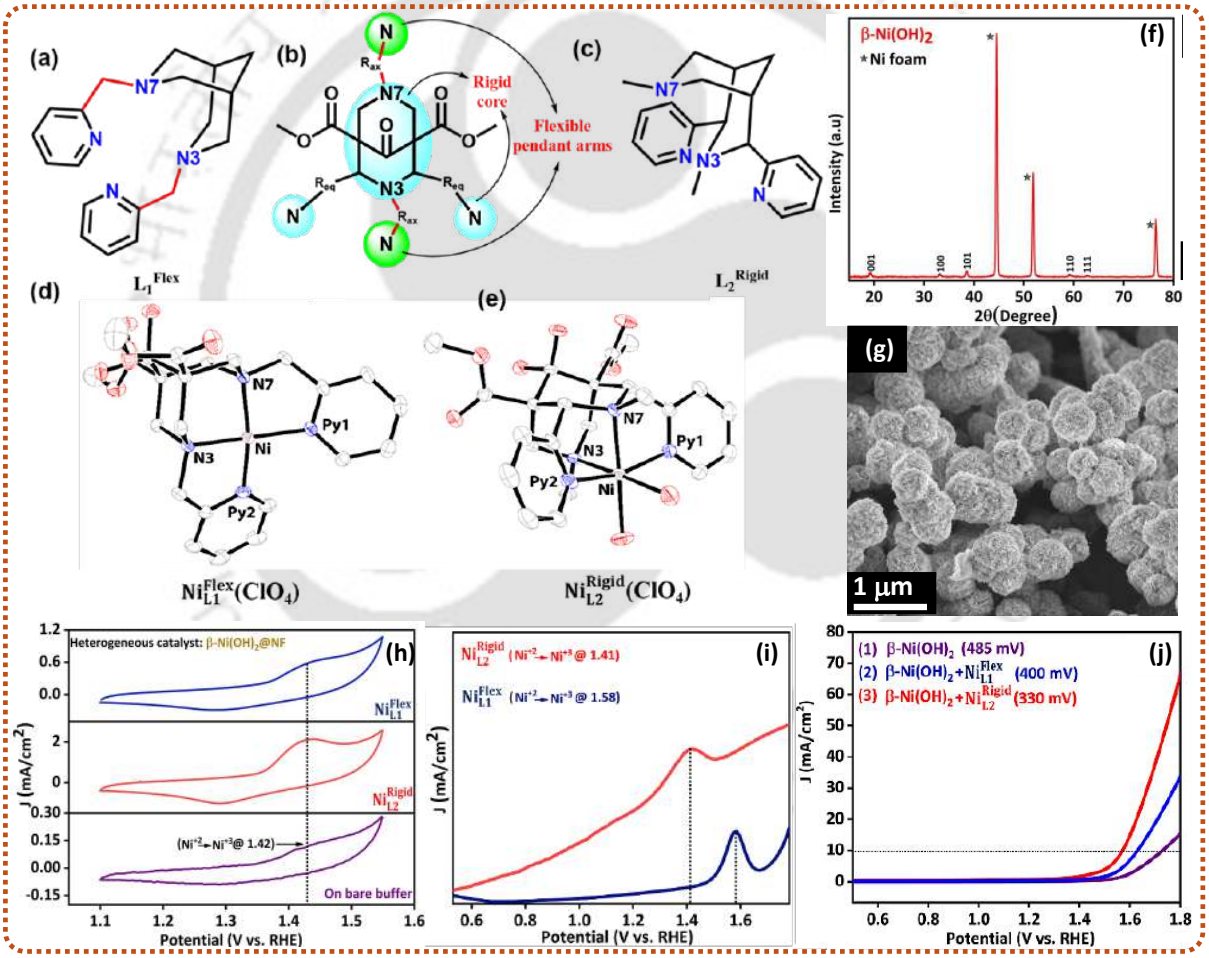

Figure 4. *(a-e) Ligand structures and corresponding complexes; (f, g) material characterizations; (h-j) electrochemical analysis* ***[Ref: N. Kalita, et. al. Chemistry of Materials, 2025, 5, 2026–2037]***

This project explores the integration of homogeneous and heterogeneous catalytic systems to achieve efficient and sustainable water oxidation under neutral conditions. Two geometrically distinct bispidine-based Ni(II) complexes—a flexible Ni_{L1}^{Flex} and a rigid Ni_{L2}^{Rigid}—

were employed as homogeneous catalysts, while β-$Ni(OH)_2$ nanoflowers grown on Ni foam served as the heterogeneous counterpart. The study investigates how molecular geometry and electronic structure influence the catalytic synergy at the homogeneous–heterogeneous interface. The octahedral Ni_{L2}^{Rigid} complex, featuring cis-labile aqua ligands, exhibited a significantly lower overpotential (330 mV at 10 mA cm^{-2}) and a smaller Tafel slope (97 mV dec^{-1}) compared to the distorted tetrahedral Ni_{L1}^{Flex} complex. Single-crystal XRD confirmed that the rigid framework of Ni_{L2}^{Rigid} facilitates O–O bond formation, while Mulliken spin density analysis revealed a higher spin localization (~80%) on the Ni center, promoting efficient Ni^{2+}/Ni^{3+} redox transitions. The integration of these homogeneous Ni complexes with the β-$Ni(OH)_2$ electrode enhances charge transfer kinetics across the solid–liquid interface through redox synchronization of identical Ni sites in both phases. This combined system leverages the molecular tunability of homogeneous catalysis and the durability of heterogeneous catalysis, providing a model framework for hybrid catalytic water oxidation using earth-abundant, non-noble metal systems.

Chapter 6b: Influence of Homogeneous Catalysts on CO_2 Reduction Selectivity at Heterogeneous Interfaces:

The present work explores a hybrid homogeneous–heterogeneous catalytic strategy for the selective electrocatalytic reduction of CO_2 to ethanol under neutral aqueous conditions. The system integrates $Cu_{1.5}Mn_{1.5}O_4$ (CMO) as a heterogeneous electrode with bispidine-based Cu(II) complexes as molecular co-catalysts to overcome the intrinsic kinetic barriers associated with CO_2 activation and C–C coupling. Two structurally distinct Cu(II) complexes—$[Cu^{L1}{}_{Flex}]$ with a flexible backbone and $[Cu^{L2}{}_{Rigid}]$ with a rigid tetradentate ligand—were investigated to understand the role of ligand rigidity on interfacial electron transfer and intermediate stabilization. The rigid complex, $[Cu^{L2}{}_{Rigid}]$, exhibits a Cu^{2+}/Cu^{+} redox potential closely aligned with the Cu^{+}/Cu^{0} transition of CMO, facilitating rapid electron exchange and efficient relay of *CO intermediates from the molecular to the solid-state interface. This redox synchronization enables a tandem catalytic pathway wherein *CO generated by the homogeneous complex undergoes C–C coupling on the CMO surface, yielding ethanol as the primary product. The hybrid catalyst achieved a Faradaic efficiency of ~68% for ethanol at –0.5 V vs RHE, with a 1.5-fold enhancement in turnover frequency relative to the flexible analogue. Electrochemical impedance and distribution of relaxation time (DRT) analyses confirmed minimized charge-

transfer resistance, while in situ ATR–IRAS spectroscopy revealed the stabilization of $*CO_{bridge}$ and $*OC_2H_5$ intermediates, highlighting a cooperative electron-transfer mechanism that underpins the system's exceptional C_2 selectivity.

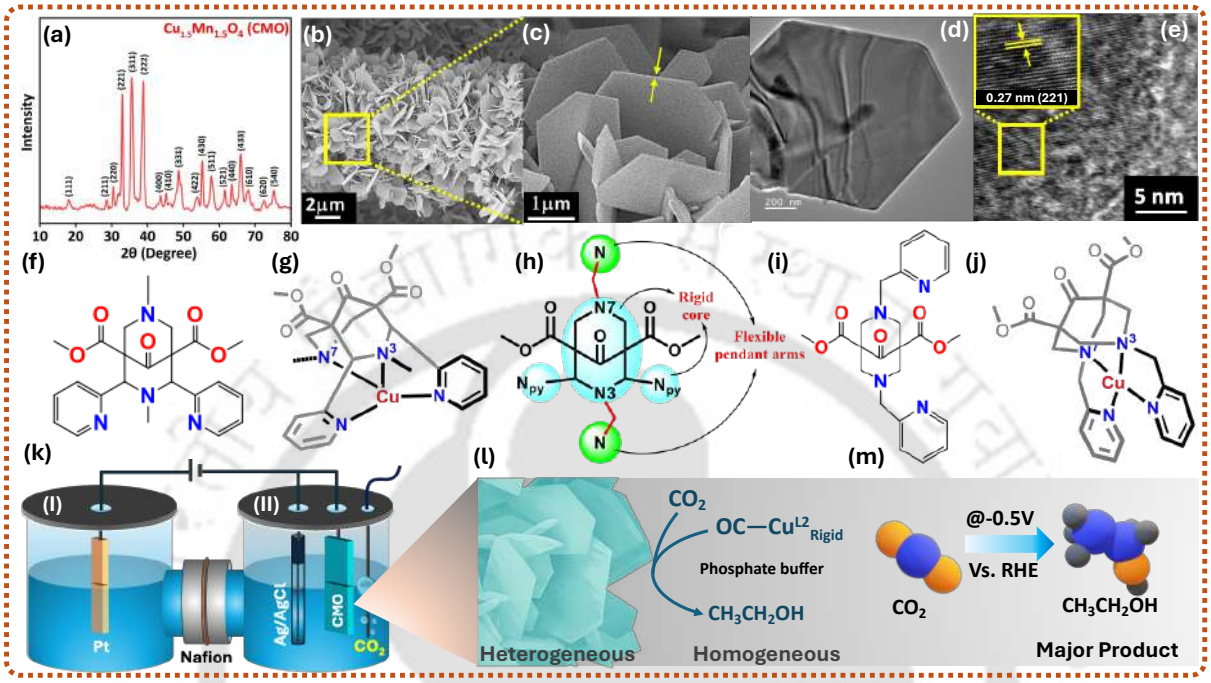

Figure 5. *(a-e) Material characterizations for heterogenous catalysts; (f, i) Ligand structures and corresponding complexes of homogeneous catalysts; (k-m) Schematic of H-cell setup and CO_2 reduction via heterogeneous and homogeneous catalysts.* ***[Ref: N. Kalita, et. al. Journal of Materials Chemistry A, 2026, DOI: 10.1039/D6TA02689C]***

CHAPTER 1

Introduction and Literature Survey

This chapter presents a comprehensive discussion on electrochemical water splitting and CO_2 reduction as promising pathways for sustainable fuel generation and carbon-neutral energy conversion. It begins with an overview of the global energy landscape, emphasizing the limitations of current non-renewable energy sources and the urgent need to transition toward renewable alternatives. The section also highlights recent advancements in the design and optimization of electrode materials that govern the efficiency of electrochemical processes. Particular attention is given to the catalytic mechanisms and surface reaction kinetics of transition metal oxide & hydroxide–based electrodes, which play a pivotal role in both water splitting and CO_2 electroreduction. Furthermore, key challenges associated with the development of efficient, durable, and cost-effective electrode systems are outlined, along with strategies adopted to modulate surface activity and promote favorable adsorption–desorption behavior of intermediate species.

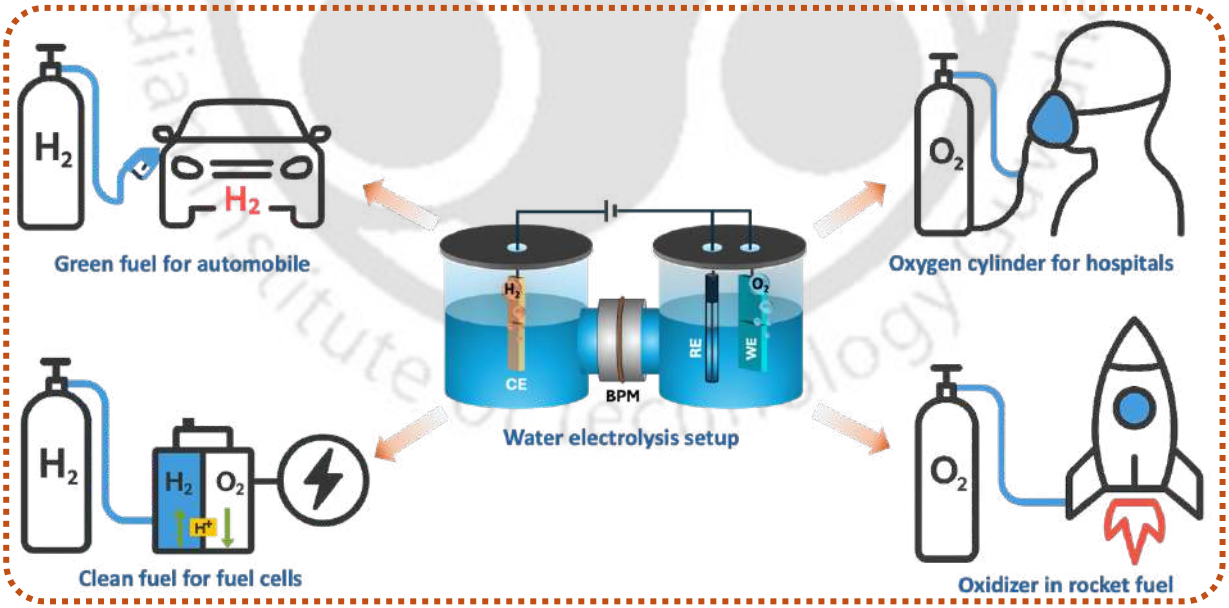

1.1 Emerging Carbon-Neutral Energy Platforms:

The ever-growing global energy demand, coupled with escalating environmental concerns, has prompted the scientific community to pursue sustainable alternatives capable of replacing fossil fuels. The transition toward carbon-neutral and renewable energy systems is essential to mitigate CO_2 emissions and restore ecological equilibrium.[1] Unlike conventional non-renewable sources that are geographically constrained, renewable energy resources such as solar, wind, and biomass are more uniformly distributed and inexhaustible in nature.[2] Among these, solar energy possesses the greatest potential, with the sun delivering approximately 1.73×10^5 TW of energy to earth's surface annually — far exceeding current global energy requirements.[3] However, despite its immense potential, the lack of efficient and economically viable technologies for large-scale solar energy conversion remains a major limitation.[4]

To address these challenges, significant attention has been directed toward alternative, zero-carbon energy carriers, with molecular hydrogen (H_2) emerging as one of the most promising candidates due to its high energy density (~141.7 MJ kg^{-1}) and environmentally benign combustion by-products.[5] Traditionally, H_2 production has relied on energy-intensive processes such as methane steam reforming and coal gasification, which unfortunately contribute to greenhouse gas accumulation. In contrast, water electrolysis offers a cleaner and more sustainable route for hydrogen generation, as it allows direct conversion of renewable electricity into chemical energy stored in H_2, achieving high purity and efficiency.[6]

In parallel, electrocatalytic CO_2 reduction (CO_2RR) has gained increasing attention as a complementary approach to water splitting, offering a dual advantage of carbon mitigation and renewable fuel production.[7] Through rational design of catalytic interfaces - particularly using transition metal oxides and hydroxides systems - CO_2 can be selectively converted into value-added products such as CO, formate, ethanol, and other hydrocarbons under mild conditions. Together, electrochemical water splitting and CO_2 reduction represent a unified platform for clean energy conversion and storage, contributing significantly toward achieving a sustainable, circular carbon economy.[8]

1.2. Water Electrolysis:

Water electrolysis (electrochemical water splitting) is a fundamental process in which electrical energy is used to dissociate water into hydrogen and oxygen. Owing to the abundance of water and the possibility of sourcing electricity from renewable technologies

such as solar cells, this reaction is considered one of the most promising pathways for sustainable hydrogen production.[9] In a conventional electrolyzer, two electrodes - an anode and a cathode - are placed in separate compartments and immersed in an electrolyte to maintain ionic conductivity and complete the electrical circuit (Figure 1.1). At the cathode, hydrogen is generated, while oxygen evolution occurs at the anode. Although the cell configuration may vary, the underlying electrochemical reactions are straightforward. Under neutral conditions, the overall water-splitting process can be summarized by the following equation:

$$H_2O \longrightarrow H_2 + \frac{1}{2}O_2 \; (\Delta G \sim 237.4 \text{ kJ/mol}, 1.23 \text{ V vs NHE})$$

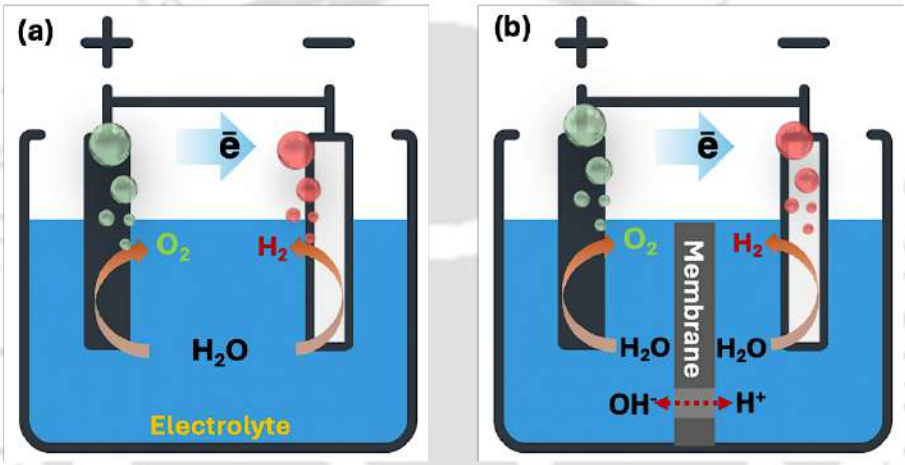

Figure 1.1. *Schematic representation of water electrolysis under two different configurations: (a) single-cell electrolysis without a membrane, and (b) dual-compartment electrolysis with a membrane separator. In both systems, water is reduced at the cathode to generate H_2 and oxidized at the anode to produce O_2, while in (b) the separator allows ionic transport between compartments while preventing gas crossover.*

To reduce the energetic losses associated with water electrolysis, the process is typically carried out under strongly acidic or alkaline conditions. In acidic media, the hydrogen evolution reaction (HER) proceeds efficiently because protons are readily available for discharge, enabling rapid H_2 generation.[10] However, achieving high activity in such environments requires catalysts based on noble metals - most notably **Ir** or **Ru** based oxides and alloys - which significantly increases cost. Consequently, state-of-the-art water-splitting systems still rely heavily on precious and scarce metals,[11] such as **Pt** for HER[12] and Ir[13] or Ru[13]

for the oxygen evolution reaction (OER), despite ongoing efforts to develop more economical alternatives.

Outlined below are the reactions expected to proceed in acidic and alkaline media during electrochemical water splitting.

In acidic:

$$2H_2O\ (l) \rightarrow 4H^+\ (aq.) + 4e^- + O_2\ (g)\ (at\ anode)$$

$$4e^- + 4H^+\ (aq.) \rightarrow 2H_2\ (g)\ (at\ cathode)$$

In alkaline:

$$4OH^-\ (aq.) \rightarrow 2H_2O\ (l) + 4e^- + 2O_2\ (g)\ (at\ anode)$$

$$4e^- + 4H_2O\ (l) \rightarrow 4OH^-\ (aq.) + 2H_2\ (g)\ (at\ cathode)$$

The reaction pathway associated with HER suggests that hydrogen evolution proceeds most efficiently in an acidic electrolyte. The Tafel mechanism for HER is described below, where *S* refers to the catalytic electroactive site.

$$H^+\ (aq.) + S + e^- \rightarrow S{-}H\ (adsorption\ and\ discharge\ of\ proton)$$

$$2S{-}H \rightarrow H_2\ (g) + 2S\ (chemical\ desorption\ of\ H_2)$$

Distinct from the HER pathway, the OER operates via an electrochemical oxide route, as described below.[14,15]

In acidic:

$$S + H_2O \rightarrow S{-}OH + H^+\ (aq.) + e^-$$

$$S{-}OH \rightarrow S{-}O + H^+\ (aq.) + e^-$$

$$2S{-}O \rightarrow 2S + O_2\ (g)$$

In alkaline:

$$S + OH^-\ (aq.) \rightarrow S{-}OH + e^-$$

$$S{-}OH + OH^-\ (aq.) \rightarrow S{-}O + H_2O + e^-$$

$$2S{-}O \rightarrow 2S + O_2\ (g)$$

Water splitting is an energetically demanding process, requiring an input of energy because it is thermodynamically uphill (ΔG = +237.4 kJ mol^{-1}, corresponding to 1.23 V vs NHE).[16] Although 1.23 V represents the theoretical minimum, practical systems must operate at significantly higher potentials to overcome kinetic barriers and achieve appreciable hydrogen production, leading to substantial electrical energy consumption. Consequently, a central goal in electrocatalytic water splitting research is the development of materials that can lower the required overpotential and thereby enhance hydrogen generation efficiency.[17,18] Numerous strategies have been explored to address the limitations of existing catalysts and to improve their overall electrochemical performance.

1.3. Electrocatalytic CO_2 reduction:

Electrocatalytic reduction of carbon dioxide (CO_2RR) is a promising route to store renewable electricity in chemical bonds while reducing anthropogenic CO_2 emissions. This approach converts CO_2, typically using water as the proton source, into value-added fuels and chemicals under ambient conditions, offering a potential pathway toward carbon neutrality and a circular carbon economy.[19,20]

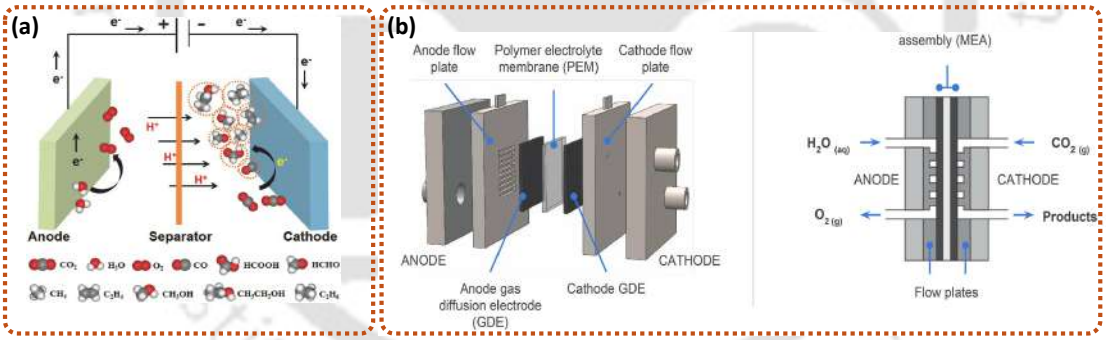

Figure 1.2. *(a) Schematic illustration of electrocatalytic CO_2 reduction pathways showing the conversion of CO_2 to various carbon-containing products (C_1 and C_2^+ products); (b) Schematic of a membrane-based reactor with a membrane–electrode assembly consisting of anode and cathode gas-diffusion electrodes on either side of a polymer electrolyte membrane, placed between current collectors and flow-field plates to separate the oxygen evolution reaction and carbon dioxide reduction reaction. (Ref. 19,20)*

In aqueous media, CO_2RR competes directly with the hydrogen evolution reaction (HER), which often limits faradaic efficiency toward carbonaceous products. Depending on catalyst identity, surface structure, and applied potential, CO_2 can be transformed via multielectron, multiproton pathways into C1 products such as CO,[21] formate,[22] methane,[23] and methanol,[24]

or C_2^+ products including ethylene,[25] ethanol,[26] and propanol.[27] For CO formation, the key step is typically the generation and stabilization of an adsorbed *COOH intermediate, followed by its further reduction and desorption of *CO, whereas deeper reduction requires additional proton–electron transfers, C–C coupling, and control over intermediate binding energies.[28]

Catalyst design is central to steering CO_2RR selectivity. Noble metals such as Au, Ag, and Pd show high selectivity to CO in the two-electron pathway, but their scarcity motivates development of earth-abundant alternatives.[29,30] Transition-metal–nitrogen–carbon (M–N–C) single-atom systems based on **Fe**, **Co**, **Ni**, **Cu**, or **Zn** can display well-defined active sites with tuned binding to *COOH and *CO, enabling high CO faradaic efficiencies while using non-precious metals.[31] In contrast, metallic **Cu** uniquely binds *CO with intermediate strength, enabling both C_1 (CH_4, CH_3OH) and C_2^+ (C_2H_4, C_2H_5OH, C_3H_7OH) formation through *CO dimerization and subsequent hydrogenation of C–C–containing intermediates.[32]

Rational catalyst engineering spans several dimensions: composition, nanostructure, defect chemistry, and coordination environment.[33] For **Cu**-based materials, approaches such as creating grain boundaries and twin defects,[34] alloying with oxophilic or CO-philic elements (e.g., **La**, **Ag**, **Ga**),[35,36] and heteroatom doping (**B**, **N**, **F**, **S**, **P**, **Cl**, **Sm**) modulate the local electronic structure and adsorption energetics of *CO, *CHO, and other key intermediates, thereby favouring specific pathways toward CH_4, C_2H_4, ethanol, or n-propanol.[37] Single-atom and diatomic catalysts further maximize metal utilization and introduce well-controlled coordination motifs;[38] for example, appropriately coordinated **Cu**, **Fe**, **Co**, **Ni**, **Zn**, or **Pb** centers on N-doped carbon can optimize *COOH stabilization and *CO release in CO_2→CO, or tune deeper reduction for CH_4 and alcohols.[39] Carbon-based materials doped with pyridinic, pyrrolic, or graphitic N can themselves function as CO-selective electrocatalysts by providing basic sites for CO_2 adsorption and tailored barriers for *COOH formation.[40,]

Tandem architectures decouple the CO_2→CO step from downstream C–C coupling or further hydrogenation, using one component as a CO generator and Cu (or another C–C–active phase) as a sink for CO dimerization to C_2H_4, ethanol, or C_3 products.[42] Such systems often combine CO-selective phases (Au, Ag, Zn, Ni–N–C, Co–N–C, Fe porphyrins) with Cu surfaces optimized for *CO coverage and C–C coupling, thereby overcoming the intrinsic limitation of Cu in the initial CO_2→CO step. More complex coupled electrocatalytic schemes introduce nitrogen sources (e.g., NO_3^-, NO_2^-, N_2, NO) to enable concurrent C–N bond formation, producing urea, amines, and other organonitrogen products via co-reduction of CO_2-derived

and N-derived intermediates at appropriately designed single-atom, diatomic, or vacancy-rich oxide catalysts.[43]

Table 1.1. Possible Half-Reactions for Electrochemical CO_2 Reduction. *(Adapted from Ref. 41)*

Half-Reaction	Electrode Potential
$CO_2(g) + 2H^+ + 2e^- \rightarrow CO(g) + H_2O(l)$	−0.53 V vs NHE
$CO_2(g) + 2H^+ + 2e^- \rightarrow HCOOH(l)$	−0.61 V vs NHE
$CO_2(g) + 8H^+ + 8e^- \rightarrow CH_4(g) + 2H_2O(l)$	−0.24 V vs NHE
$2CO_2(g) + 12H^+ + 12e^- \rightarrow C_2H_4(g) + 4H_2O(l)$	−0.349 V vs NHE
$2CO_2(g) + 14H^+ + 14e^- \rightarrow C_2H_6(g) + 4H_2O(l)$	−0.270 V vs NHE
$3CO_2(g) + 12H_2O(l) + 18e^- \rightarrow C_3H_6(g) + 18OH^-$	0.13 V vs RHE
$CO_2(g) + 6H^+ + 6e^- \rightarrow CH_3OH(l) + H_2O(l)$	−0.380 V vs NHE
$2CO_2(g) + 12H^+ + 12e^- \rightarrow CH_3CH_2OH(l) + 3H_2O(l)$	−0.329 V vs NHE
$3CO_2(g) + 18H^+ + 18e^- \rightarrow CH_3CH_2CH_2OH(l) + 5H_2O(l)$	−0.310 V vs NHE

Electrolyte composition, pH, and cation identity strongly affect CO_2RR by controlling CO_2 solubility, local pH, double-layer structure, and surface coverage of reaction intermediates and H*. High-concentration electrolytes, ionic liquids, and tailored organic cations can suppress HER, stabilize key intermediates, and enhance CO_2 affinity, improving both selectivity and current density.[39] From a device perspective, flow cells and gas-diffusion electrodes are essential to achieve industrially relevant current densities (>100–200 mA cm^{-2}) for CO and formate, yet scaling multicarbon and organonitrogen products will require further optimization of catalyst stability, tandem configurations, and reactor engineering, as well as careful consideration of renewable electricity cost and integration with solar-driven processes.[44]

1.4 Strategic approaches for enhancing electrochemical water electrolysis and CO_2 Reduction:

Electrochemical water splitting and CO_2 reduction are governed by a complex interplay of intrinsic catalytic activity and extrinsic physicochemical factors associated with the catalyst–electrolyte interface. Although the thermodynamic potentials for hydrogen evolution (0 V vs RHE) and oxygen evolution (1.23 V vs RHE) suggest low-voltage operation, practical systems

require substantially higher cell voltages due to kinetic barriers, sluggish interfacial charge transfer, and mass-transport limitations. In aqueous environments, the reactions occur at a triphasic boundary involving the solid catalyst, liquid electrolyte, and evolving gaseous species. For instance, during the oxygen evolution reaction in alkaline media, OH^- species migrate toward catalytically active sites, engage in sequential adsorption and surface-bond rearrangements, and ultimately release O_2 into the electrolyte.[45] These elementary steps—mass transport, electron transfer, and surface reaction dynamics—collectively dictate the overall reaction rate. Optimizing electrocatalytic performance therefore requires not only increasing the number and accessibility of active sites but also enhancing intrinsic reactivity, accelerating interfacial charge transport, facilitating efficient diffusion pathways, and ensuring structural/chemical robustness under operating conditions. To achieve these objectives, several advanced design strategies have been developed.[44]

For water electrolysis, approaches such as heterojunction design,[46] doping-induced electronic modulation,[47] redox-state synchronization,[48] interfacial engineering via bipolar membranes,[49] surface reconstruction, and morphology/defect tailoring[50] have shown significant promise in improving OER and HER kinetics. These strategies help align energy levels, improve conductivity, stabilize key intermediates, and maintain favorable ion-transport environments.

Many of these concepts are also directly applicable to electrocatalytic CO_2 reduction. In CO_2RR, heterojunction construction,[51] controlled doping,[52] redox synchronization, surface/interface regulation, and integration of homogeneous[53] and heterogeneous[54] catalytic domains are widely employed to steer reaction pathways toward specific products, stabilize CO_2-derived intermediates, promote C–C coupling, and suppress competing hydrogen evolution. While bipolar membrane integration is uniquely relevant to water-splitting configurations for managing pH gradients, the other strategies offer parallel advantages in tailoring both electronic and structural characteristics for selective CO_2 conversion.

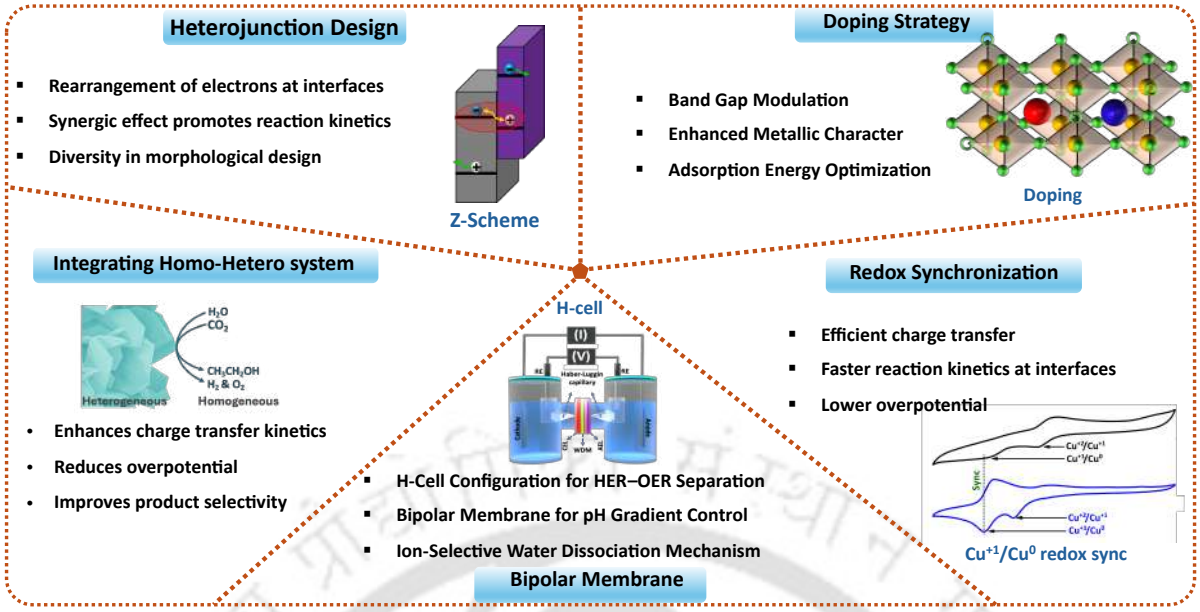

Figure 1.3. Schematic representation of major design strategies to enhance overall electrocatalytic performance.

1.4.1. Heterojunction design:

Heterojunction engineering has emerged as one of the most powerful approaches for advancing electrocatalytic water splitting, owing to its ability to tailor active electronic states and generate highly reactive interfacial sites. In heterogeneous catalysts, the junction between two distinct phases induces redistribution of charge carriers, modifies the local coordination environment, and facilitates the formation of electronically complementary active motifs. These interfacial effects accelerate the fundamental steps of water electrolysis—including reactant adsorption, intermediate formation, and product desorption—thereby enabling superior performance compared to single-phase catalysts.[55] The advantages of heterojunction formation arise from multiple synergistic factors. First, lattice mismatch at the interface often produces compressive or tensile strain, which increases the density of coordinatively unsaturated atoms and exposes a greater number of high-energy active sites. Second, the integration of components with diverse structural motifs allows fine-tuning of the surface area and porosity, enhancing electrolyte penetration and mass transport. Third, electronic coupling across the heterointerface promotes rapid charge redistribution, leading to optimized adsorption energies for key intermediates (e.g., H*, OH*, OOH*) and reduced activation barriers for both HER and OER. As a result, heterojunctions typically offer

higher intrinsic activity, superior conductivity pathways, and improved operational stability relative to their parent materials.[56]

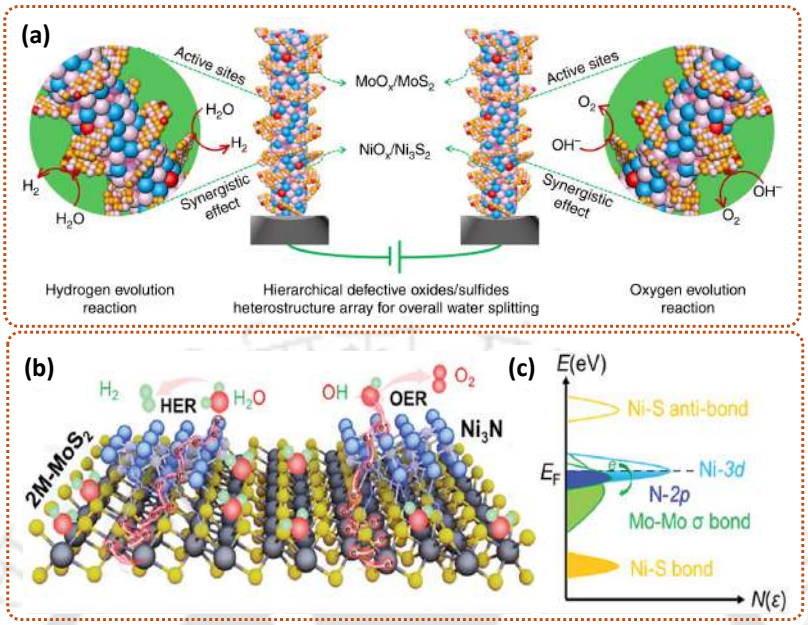

Figure 1.4. *(a) Schematic of the synthesis process and overall water-splitting operation using a $NiMoO_x$/NiMoS array in a two-electrode configuration. Element colors: Mo (blue), S (pink), O (red), Ni (yellow); (b) Schematic of the overall water-splitting mechanism on Ni_3N@2M–MoS_2 (elements: H-green, O-red, Mo-black, S-yellow, N-silver, Ni-blue); (c) Illustration of charge-modulation at the Ni_3N@2M–MoS_2 interface regulating the active electronic states. (Ref. 57,58)*

Recent advances clearly demonstrate the advantages of such interfacial design. Zhai *et al.* constructed hierarchical MoO_x/MoS_2–NiO_x/Ni_3S_2 heterostructure arrays through surface reconfiguration,(Figure 1.4. (a)) producing highly active interfacial centers with optimized intermediate adsorption energies.[57] The resulting $NiMoO_x$/NiMoS catalyst achieved overpotentials as low as 38 mV (HER) and 186 mV (OER) at 10 mA cm^{-2}, while maintaining stability at current densities up to 500 mA cm^{-2}. Assembled in a full electrolyzer, it delivered 500–1000 mA cm^{-2} at record low cell voltages (1.60–1.66 V), underscoring the impact of engineered interfacial sites on large-scale hydrogen production. Similarly, Wu *et al.* designed a metallic Ni_3N@2M–MoS_2 heterostructure capable of decoupling water and hydroxyl adsorption, (Figure 1.4. (b)) overcoming limitations typically seen in alkaline media at industrial current densities.[58] The strong charge interaction between Ni_3N and monoclinic MoS_2 tuned the electronic states around the Fermi level, enabling rapid kinetics and high conductivity. This catalyst drove alkaline water electrolysis at 1000 mA cm^{-2} with an ultralow

cell voltage of 1.644 V and exceptional 300-hour durability, far surpassing noble-metal references.

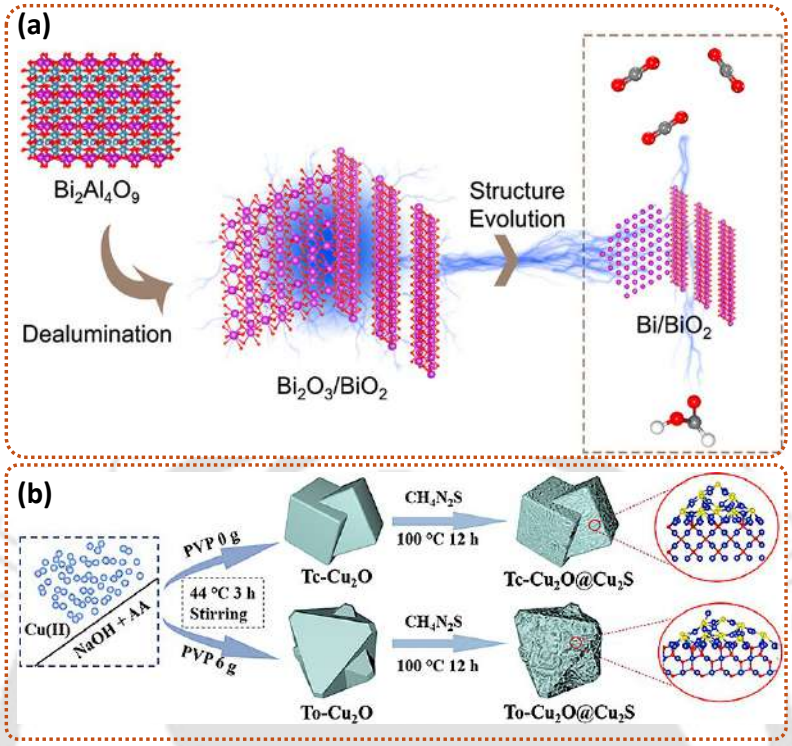

Figure 1.5. *(a) Bi_2O_3/BiO_2 heterostructure enabling selective formate production. (b) Cu_2O@Cu_2S twin junctions stabilizing Cu^+ and promoting ethanol formation. (Ref. 22, 59)*

Further heterojunction engineering also enhances CO_2 electroreduction by creating interfaces with redistributed charge density, optimized band alignment, and strengthened binding of key intermediates. These interfacial effects improve *CO generation, lower C–C coupling barriers and facilitate multi-electron transfer pathways. Overall, the synergistic electronic modulation at heterointerfaces accelerates elementary steps and markedly boosts CO_2RR activity, selectivity, and product specificity. Recently Feng et al. demonstrate that a molten-alkali–derived Bi_2O_3/BiO_2 heterostructure undergoes in situ transformation into a Bi/BiO_2 Mott–Schottky interface (Figure 1.5 (a)), which strengthens CO_2 and *OCHO adsorption, enabling >95% formate selectivity with a partial current density of −111.42 mA cm^{-2}.[22] Li et al. show that Cu_2O@Cu_2S twin heterojunctions (Figure 1.5(b)—particularly nanocubes—stabilize Cu^+, enrich interfacial *CO, and promote *CHOH–*CO coupling, delivering ethanol at −0.45 V and achieving Faradaic efficiencies of 34% (H-cell) and 43.9% (flow cell). Both studies highlight interface-engineered heterostructures as precision platforms for boosting CO_2RR selectivity and multi-electron reaction pathways.[59]

1.4.2. Doping Strategy:

Elemental heteroatom doping is a powerful materials-engineering strategy that enhances electrocatalytic water splitting by modulating the physicochemical characteristics of transition-metal-based catalysts at the atomic scale. Incorporation of aliovalent or isovalent dopants into the host lattice tailors the d-band center, redistributes charge density, and alters local coordination environments, thereby optimizing the adsorption free energies (ΔG^*_H, ΔG^*_{OH}, ΔG^*_O, ΔG^*_{OOH}) of key HER and OER intermediates. Such electronic perturbations promote faster proton–electron transfer and lower activation barriers for surface elementary steps.[60] Moreover, dopant-induced lattice distortion generates oxygen vacancies, cation deficiencies, and other defect sites, which increase the density of catalytically active centers and facilitate improved electron/ion transport pathways. Heteroatom incorporation can also enhance intrinsic conductivity by narrowing band gaps or creating mid-gap states, strengthening catalytic turnover under high-current operation. In multicomponent systems, synergistic interactions between dopant and host metal centers modulate metal–ligand covalency and stabilize high-valence states crucial for OER catalysis. Collectively, these atomic-level modifications improve catalytic kinetics, durability, and energy efficiency, positioning controlled heteroatom doping as a key design principle for next-generation, high-performance water-splitting electrocatalysts.[61]

Recent reports demonstrate the strong performance benefits of such doping strategies. Liu *et al.* synthesized heteroatom-doped M-$ZnRuO_x$ (M = **Co**, **Ni**, **Fe**) amorphous/crystalline nanocages, where dopant-induced electronic regulation and heterophase coupling markedly improved both HER and OER kinetics (Figure 1.6. (a)).[62] Among them, Co-$ZnRuO_x$ delivered an ultralow HER overpotential of 17 mV at 10 mA cm^{-2} and a Tafel slope of 21.61 mV dec^{-1}, surpassing Pt/C, while all M-doped variants exhibited enhanced OER stability due to suppression of Ru over-oxidation. Niu *et al.* similarly showed that non-metallic Se doping transforms FeOOH into an efficient OER catalyst (Figure 1.6. (b)), achieving 500 mA cm^{-2} at only 348 mV and enabling a solar-to-hydrogen efficiency of 18.55% in a practical solar-driven system.[63] Collectively, these results confirm that heteroatom doping significantly elevates activity, durability, and scalability in advanced water-splitting electrocatalysts.

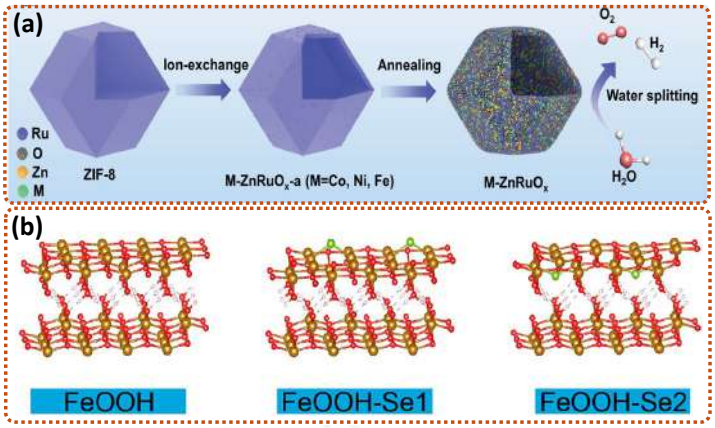

Figure 1.6. *(a) Schematic illustration of the fabrication process of amorphous/crystalline M-ZnRuO$_x$ nanocages; (b) Structures of FeOOH and various Se-doped FeOOH models. Fe atom (orange), O atom (red), Se atom (green). (Ref. 62,63)*

Heteroatom doping has also emerged as a powerful strategy to enhance electrocatalytic CO_2 reduction as well by precisely tuning the electronic structure and surface chemistry of Cu-based catalysts. Introducing foreign atoms modulates the *d*-band center, alters charge distribution, and reshapes local coordination environments, thereby optimizing the adsorption and stabilization of key intermediates such as *CO and *CO–CO, which are crucial for C–C coupling toward C_2^+ products. Dopant-induced lattice distortion and defect formation increase active-site density and improve reactant activation, while enhanced conductivity facilitates faster charge transfer and lowers the overpotential. Furthermore, doping can suppress the competing HER by modifying surface proton affinity, enabling higher selectivity toward multi-carbon species. The tunability, simplicity, and scalability of doping strategies make them particularly attractive for designing next-generation CO_2RR catalysts with improved activity, stability, and C_2^+ product yield, thus supporting sustainable carbon-neutral energy pathways.[52]

Among the different doping strategies explored for enhancing CO_2RR, Pd doping markedly enhances Cu-based CO_2RR catalysts by strengthening *CO adsorption, stabilizing $Cu^{\delta+}$ sites, and lowering the energy barrier for C–C coupling. The Cu/Pd-1% system exemplifies this effect, delivering high C_2^+ selectivity and elevated current density through increased *CO surface coverage. Complementarily, Zhang *et al.* demonstrated that charge-separated Pd–Cu_3N pairs further promote *CO binding and coupling, boosting C_2^+ Faradaic efficiency by over an order of magnitude.[64] Similarly Ag incorporation into Cu frameworks has proven highly effective in boosting *CO generation and lowering C–C coupling barriers. Hoang *et al.* reported that Ag–

Cu interfaces significantly enrich *CO coverage and enable efficient C–C coupling, achieving C_2H_4 Faradaic efficiencies near 60% and ~25% for ethanol at ~300 mA cm^{-2}. Such Ag–Cu synergistic architectures provide optimized active sites and markedly enhance overall C_{2}^{+} production.[65]

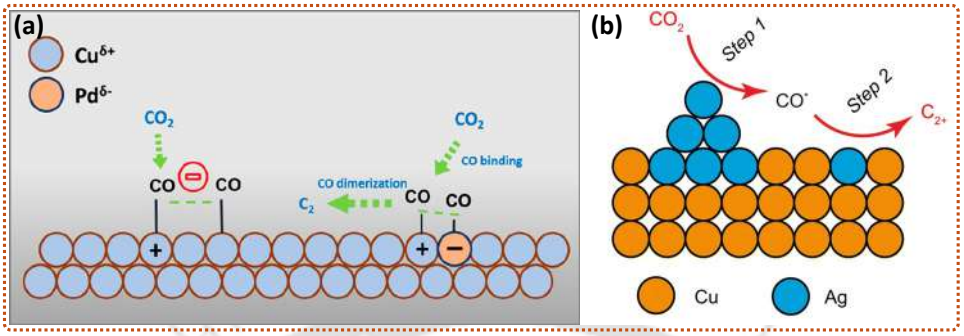

Figure 1.7. *(a) Cu–Pd and (b) Cu–Ag tandem catalyst scheme. (Ref. 64,65)*

1.4.3. Bipolar Membrane–Driven Water Dissociation Process:

The electrochemical splitting of water into H_2 and O_2 is well established, but large-scale implementation remains challenging because the product gases must be kept separate. Ion-exchange membranes (IEMs) are commonly used to isolate the anode and cathode compartments, yet their inclusion increases solution resistance and can limit catalytic efficiency.[66] Bipolar membranes (BPMs) offer an effective alternative, as their internal junction promotes water dissociation into H^+ and OH^-, which are subsequently converted to H_2 and O_2 at the respective electrodes.[67-69]

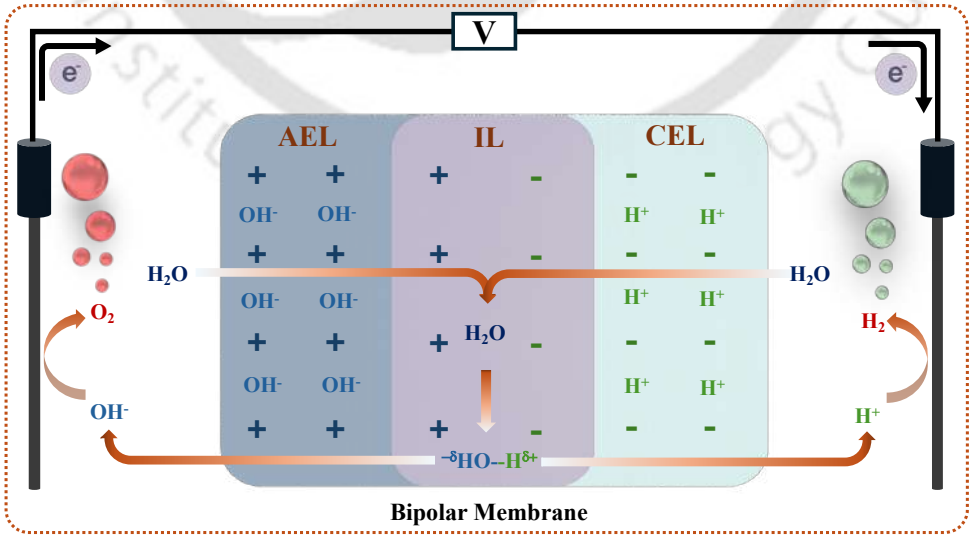

Figure 1.8. *Schematic representation for the dissociation of water into H^+ and OH^- ions at the junctions of a bipolar membrane under reverse bias. (Adapted from Ref. 67)*

HER catalysts typically perform best in acidic media, whereas OER catalysts show superior activity in alkaline conditions. BPMs enable these reactions to operate simultaneously at their optimal pH by maintaining a stable pH gradient across the membrane. In water electrolysis, this configuration lowers the overall cell overpotential and enhances system efficiency. A BPM consists of a cation-exchange layer (CEL) and an anion-exchange layer (AEL), whose junction—known as the interfacial layer—facilitates water dissociation into H^+ and OH^- without gas formation. Upon application of current across a BPM, the ions in the bulk solution cannot sustain the ionic current through the membrane as either ions are unable to pass both the layers of a BPM. Hence, the generated H^+ and OH^- ions at the membrane interface carriers the ionic current. With respect to the electrodes, the alignment of BPM is critical to ensure the flux of H^+ and OH^- ions along the electric field, thus the CEL should be towards the cathode while the AEL towards anode (reverse bias condition). This intrinsic ion-generation mechanism justify the effectiveness of BPMs in pH-asymmetric electrolysis systems.[70-72]

A BPM operates analogously to a reverse-biased p–n junction, where charge carriers are withdrawn from the interface, creating a depletion region with an intrinsic potential.[73,74] When immersed in electrolyte, the junction between the AEL and CEL develops a built-in voltage that depends on the pH gradient across the membrane and follows the Nernst relation.

$$\Delta V_{BPM} = 2.3\frac{RT}{F}(pH_{Anolyte} - pH_{Catholyte}) \quad (1.1)$$

Under a full pH difference (ΔpH = 14), this potential approaches ~0.83 V, which corresponds to the onset of water dissociation. In reverse bias, ion depletion at the interfacial layer produces a space-charge region and a limiting current, after which the current rises sharply due to field-induced generation of H^+ and OH^-.[75] Under reverse bias condition, a space charge region at the IL is generated resulting initially in high resistance (determined by a limiting current), thereby a region where current quickly increases with the voltage (Figure 1.9).[76,77] The rapid increase in the current is due to the generation of H^+ and OH^- ions at the junction depending upon the electric field at the bipolar junction.[78]

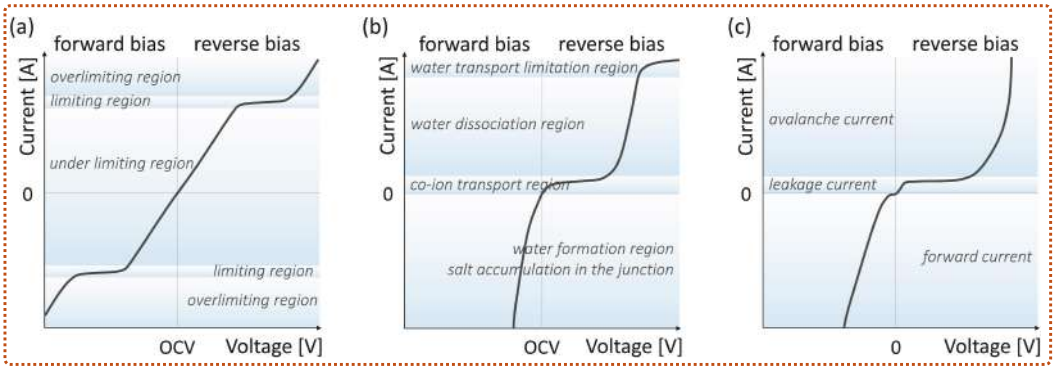

Figure 1.9. *Representative qualitative I–V characteristics of (a) an ion-exchange membrane, (b) a bipolar membrane, and (c) a p–n junction diode, illustrating their distinct electrochemical and charge-transport behaviours. (Ref. 69)*

Water dissociation in BPMs is commonly explained by two complementary mechanisms.[79,80] The second Wien effect attributes dissociation to the strong electric field at the bipolar junction, which explains that there is an increase in the dissociation degree and ion mobility of electrolytes at high electric fields.[81] In parallel, the protonation–deprotonation mechanism describes catalytic proton-transfer interactions between water and fixed charged groups within the junction, forming H^+ and OH^- via acid–base reactions.[82,83] Incorporating catalytic sites at the interface enhances this pathway. In case of a weak base (B), the protonation-deprotonation reaction can be written as.[84-86]

$$B + H_2O \xrightarrow{k_1} BH^+ + OH^-$$

$$BH^+ + H_2O \xrightarrow{k_2} B + H_3O^+$$

where BH^+ is the catalytic centre (i.e., fixed charged groups of membrane), k_1, k_2 the forward rate constants.

In case of weak acid (AH), the reactions at the bipolar junction can be written as.

$$AH + H_2O \xrightarrow{k_1} A^- + H_3O^+$$

$$A^- + H_2O \xrightarrow{k_2} AH + OH^-$$

where A^- is the catalytic centre in the membrane.

The reactions can be summarized as.

$$2H_2O \rightarrow H_3O^+ + OH^-$$

A unified model proposed by Strathmann combines both effects: at low electric fields, salt ions dominate transport; increasing the electric field causes ion depletion and a limiting current; beyond this point, water splitting supplies the necessary charge carriers, and diffusive water replenishes the junction. Overall, catalytic proton-transfer reactions initiate water dissociation, while the electric field accelerates the process, jointly enabling efficient ion generation within the BPM.

1.4.4. Redox Synchronisation and Hybrid Homogeneous–Heterogeneous Electrocatalysis:

1.4.4.1. Redox Synchronisation in between Heterojunctions (Solid-Solid Interfaces):

The concept of redox synchronization - where distinct catalytic domains undergo oxidation–reduction transitions within overlapping potential windows - has emerged as a powerful strategy for accelerating multi-electron electrochemical reactions. In heterojunction catalysts, we demonstrated that: closely aligned redox couples across adjacent layers facilitate rapid interfacial charge movement, minimize kinetic barriers, and increase the density of active states participating in catalysis. In our oxide–hydroxide system, $CoMn_2O_4$ and $CoMn(OH)_x$ exhibit redox transitions for Mn^{3+}/Mn^{4+} and Co^{2+}/Co^{3+} within nearly the same potential range.[48] This synchronized behaviour enables more efficient electron shuttling during OER, lowers the interfacial charge-transfer resistance, and enhances catalytic turnover. Building upon this concept, we extend redox synchronization beyond solid–solid interfaces and introduce it for the first time between a heterogeneous electrode surface and a homogeneous molecular catalyst dissolved in the electrolyte.

1.4.4.2. Redox Synchronisation beyond Solid-Solid Interfaces:

Heterogeneous OER catalysts such as transition-metal oxides, phosphides, and sulfides are robust and cost-effective, their performance in neutral electrolytes is inherently limited by low conductivity and slow proton/hydroxide transport. Homogeneous catalysts, on the other hand, offer tunable coordination environments, well-defined redox cycles, and mechanistic clarity but often suffer from instability, insufficient turnover, and poor interaction with electrode surfaces. Importantly, each catalytic platform alone lacks the ability to efficiently accumulate and relay oxidative equivalents under neutral conditions.[87]

To overcome these limitations, we integrate a heterogeneous Ni-based hydroxide electrode with water-soluble Ni(II) bispidine complexes functioning as homogeneous redox mediators.[88] This hybrid approach leverages the mechanical stability and electron-delivery capability of a solid catalyst together with the fast molecular redox cycling offered by homogeneous species. Crucially, both components share the same transition-metal center (**Ni**), ensuring intrinsic redox compatibility. Their Ni^{2+}/Ni^{3+} and higher-valent transitions occur within a common potential window, thus enabling synchronized charge accumulation and rapid electron exchange between phases.

1.4.4.3. Extending the Hybrid Redox-Synchronized Strategy to Selective CO_2 Reduction:

The same design rationale can be translated to another complex multi-electron transformation: the electrocatalytic reduction of CO_2. The conversion of CO_2 into energy-rich fuels is desirable but challenging due to the molecule's thermodynamic stability and the multistep proton-electron transfers involved. Heterogeneous catalysts, especially Cu-based materials, are capable of C–C coupling and C_2 product formation, yet they often struggle to efficiently activate CO_2 in neutral electrolytes. Conversely, homogeneous catalysts excel at the initial $CO_2 \rightarrow CO$ reduction step but rarely produce multicarbon products.[89]

To bridge these complementary capabilities, we developed a redox-synchronized hybrid system that integrates a heterogeneous $Cu_{1.5}Mn_{1.5}O_4$ (CMO) catalyst with water-soluble Cu(II) bispidine complexes. The CMO surface offers a Cu^{+}/Cu^{0} redox couple that drives *CO dimerization and C–C bond formation, while the homogeneous bispidine complexes rapidly convert CO_2 to CO in neutral electrolyte, ensuring a continuous supply of intermediates for downstream C_2-product generation.

1.5. Motivation and Objectives of The Present Work:

The global pursuit of sustainable and carbon-neutral energy technologies has intensified due to the escalating climate crisis and the imminent depletion of fossil resources. Among next-generation energy conversion platforms, water electrolysis and electrocatalytic CO_2 reduction (CO_2RR) have emerged as two complementary routes capable of storing renewable electricity in chemical bonds while producing clean fuels.[90] However, despite their conceptual simplicity, both processes suffer from inherent kinetic sluggishness, large overpotentials,

poor selectivity, and inadequate stability under industrially relevant conditions. These limitations primarily stem from inefficient charge transfer, suboptimal intermediate adsorption, and structural degradation of active sites during operation.

Recent advances reveal that interface-driven electronic modulation—achieved through heterojunction design, controlled doping, and redox synchronization—can effectively overcome these challenges by tuning local charge distribution, optimizing energy levels, and stabilizing reaction intermediates.[91] Yet, the precise interplay between these strategies in governing catalytic performance, especially under neutral or near-neutral conditions, remains poorly understood. A fundamental understanding of how heterostructure formation, dopant incorporation, and redox coupling collectively influence electrocatalytic kinetics could unlock the next generation of high-efficiency bifunctional catalysts for sustainable water splitting and CO_2 reduction.

To systematically address these overarching challenges, this thesis is structured to progress logically from fundamental half-cell reactions to complex, integrated energy conversion systems. The research initially focuses on water electrocatalysis, beginning with an isolated investigation of the oxygen evolution reaction (OER). Building upon these fundamental insights, the study advances to overall water electrocatalysis by developing bifunctional single electrodes capable of simultaneously driving both the hydrogen evolution reaction (HER) and OER in a shared alkaline environment. To further optimize the practical implementation of these systems and ensure high product purity, subsequent work explores the physical separation of the HER and OER processes. This is accomplished using an H-cell configuration integrated with a bipolar membrane, thereby preventing gas crossover and facilitating seamless product separation.

Recognizing the practical limitations and degradation issues associated with the harsh alkaline environments used in these earlier stages, the research subsequently transitions to water electrolysis under neutral conditions. This operational shift is successfully achieved by employing redox synchronization between homogeneous and heterogeneous catalysts to facilitate efficient charge transfer. Finally, leveraging the kinetic and mechanistic principles established during these progressive water electrolysis studies, the thesis culminates in the investigation of a more complex electrocatalytic system: CO_2 reduction. By once again

exploiting the synergistic synchronization of homogeneous and heterogeneous catalysts, this final phase focuses on the selective electrocatalytic reduction of CO_2 for the targeted production of ethanol.

The sequential progression of the research chapters is illustrated in the workflow below, highlighting the transition from fundamental water oxidation to complex CO_2 reduction.

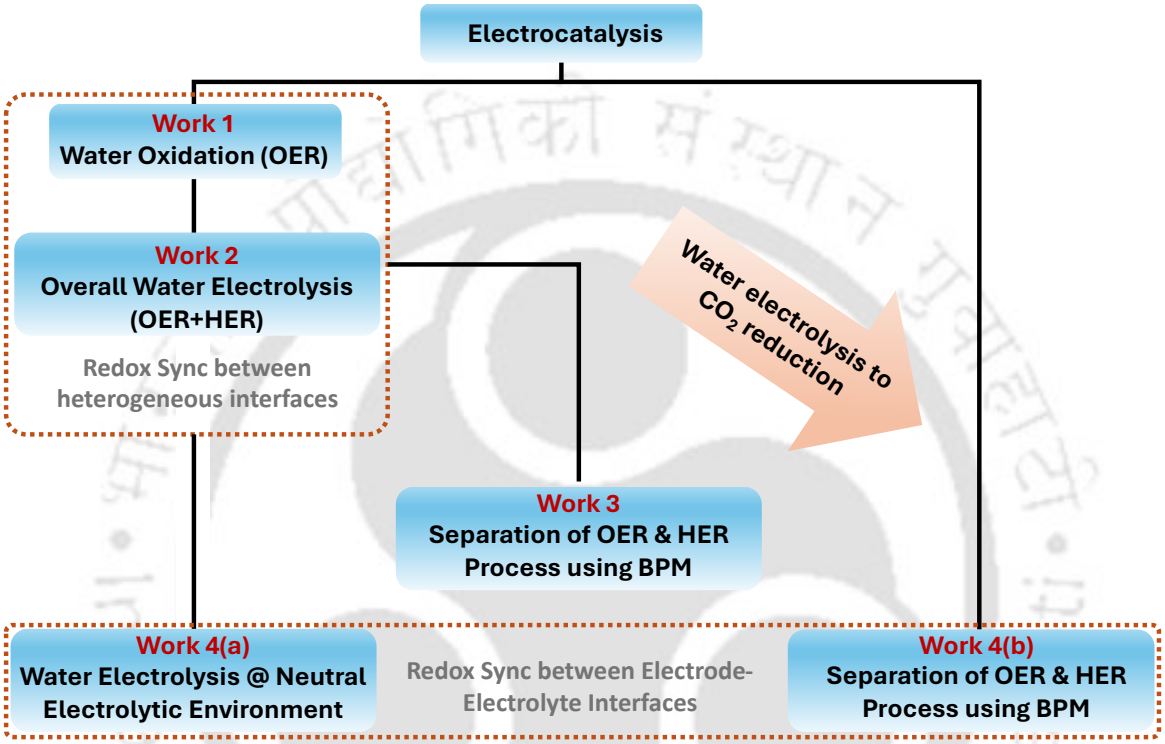

Figure 1.10. *Stepwise evolution of the thesis objectives. The schematic maps the transition from isolated water oxidation to advanced energy conversion, highlighting key methodological shifts such as bifunctional catalyst design, physical compartment separation, environmental optimization (neutral media), and the final implementation of tandem catalysis for CO_2-to-ethanol conversion.*

Motivation:

- To address the urgent demand for efficient carbon-neutral energy conversion through water splitting and CO_2 reduction.
- To develop cost-effective, earth-abundant catalysts capable of rivalling noble metal–based systems in terms of activity and durability.
- To unravel how interfacial charge redistribution, dopant–host interactions, and redox coupling synergistically enhance electrochemical reaction kinetics.

- To explore hybrid homogeneous–heterogeneous architectures that bridge molecular precision with solid-state robustness for dual catalytic functionality.

Objectives:

- Design and synthesize heterojunction-engineered transition-metal-based catalysts for efficient overall water splitting.
- Employ strategic elemental doping to modulate electronic structure, generate defect sites, and enrich active-site density for both HER and OER.
- Investigate the effect of redox synchronization between structurally distinct catalytic domains on interfacial charge transport and turnover frequency.
- Extend the redox-synchronized hybrid strategy to electrochemical CO_2 reduction by coupling heterogeneous catalysts with homogeneous molecular mediators for selective C_2^+ product generation.
- Correlate structure–property–activity relationships through advanced electrochemical and physicochemical characterization, establishing design principles for next-generation bifunctional electrocatalysts.

1.6. References:

1. J. Zhang, X. Fu, S. Kwon, K. Chen, X. Liu, J. Yang, H. Sun, Y. Wang, T. Uchiyama, Y. Uchimoto, S. Li, Y. Li, X. Fan, G. Chen, F. Xia, J. Wu, Y. Li, Q. Yue, L. Qiao, D. Su, H. Zhou, W. A. Goddard and Y. Kang, *Science*, 2025, **387**, 48.
2. Y.H. Wang, C.C. Hsu, S.H. Hong, J.F. Ding, U.S. Jeng, D.Y. Kang, S.C. Luo, S.H. Tung, C.L. Liu, *ACS Sustainable Chemistry & Engineering*, 2025, **13**, 4231.
3. D. J. C. MacKay, *Phil. Trans. R. Soc. A.* 2013, **371**, 20110431.
4. H. Tüysüz, *Acc. Chem. Res.*, 2024, **57**, 558.
5. S. S. Lam, V. Nguyen, M. T. N. Dinh, D. Q. Khieu, D. D. La, H. T. Nguyen, D. V. N. Vo, R. S. Varma, M. Shokouhimehr, C. C. Nguyen, Q. V. Le and W. Peng. *J. Mater. Chem. A*, 2020, **8**, 10571.

6. X. Zhang, C. Cao, T. Ling, C. Ye, J. Lu and J. Shan, Adv. Energy Mater., 2024, **14**, 2402633.
7. S. Su, Y. Zhou, L. Xiong, S. Jin, Y. Du and M. Zhu, *Angew. Chem., Int. Ed.*, 2024, **63**, e202404629.
8. Q. Chen, X. Wang, Y. Zhou, Y. Tan, H. Li, J. Fu and M. Liu, *Adv. Mater.*, 2024, **36**, e2303902.
9. J. K. Lee, F. Babbe, G. Wang, A. W. Tricker, R. Mukundan, A. Z. Weber and X. Peng, *Joule*, 2024, **8**, 2357.
10. Z. Huang, T. Cheng, A. H. Shah, G. Zhong, C. Wan, P. Wang, M. Ding, J. Huang, Z. Wan, S. Wang, J. Cai, B. Peng, H. Liu, Y. Huang, W. A. Goddard and X. Duan, *Nat. Catal.*, 2024, **7**, 678.
11. L. Quan, H. Jiang, G. Mei, Y. Sun and B. You, *Chem. Rev.*, 2024, **124**, 3694.
12. T. Yu, G. Liu, T. Nie, Z. Wu, Z. Song, X. Sun and Y.-F. Song, *ACS Catal.*, 2024, **14**, 14937.
13. Y. Zi, C. Zhang, J. Zhao, Y. Cheng, J. Yuan and J. Hu, *Small*, 2024,**20**, 2406657.
14. X. Zhou, H. Dong and A.-M. Ren, *Int. J. Hydrogen Energy*, 2016, **41**, 5670.
15. J. O. Bockris and T. Otagawa, *J. Phys. Chem.*, 1983, **87**, 2960.
16. M. He, C. Feng, T. Liao, S. Hu, H. Wu and Z. Sun, *ACS Appl. Mater. Interfaces*, 2019, **12**, 2225.
17. A. Kundu, S. Gautam and B. Chakraborty, *J. Mater. Chem. A*, 2024, **13**, 2920.
18. R. Q. Li, S. Guo, X. Wang, X. Wan, S. Xie, Y. Liu, C. Wang, G. Zhang, J. Cao, J. Dai, M. Ge and W. Zhang, *Chem. Sci.*, 2024, **15**, 10084.
19. S. A. Farooqi, A. S. Farooqi, S. Sajjad, C. Yan and A. B. Victor, *Environ. Chem. Lett.*, 2023, **21**, 1515.
20. D. M. Weekes, D. A. Salvatore, A. Reyes, A. Huang and C. P. Berlinguette, *Acc. Chem. Res.*, 2018, **51**, 910.
21. Z.-H. Gao, K. Wei, T. Wu, J. Dong, D.-E. Jiang, S. Sun and L.-S. Wang, *J. Am. Chem. Soc.*, 2022, **144**, 5258.
22. X. Feng, H. Zou, R. Zheng, W. Wei, R. Wang, W. Zou, G. Lim, J. Hong, L. Duan and H. Chen, *Nano Lett.*, 2022, **22**, 1656.
23. Z. Wang, Q. Yuan, J. Shan, Z. Jiang, P. Xu, Y. Hu, J. Zhou, L. Wu, Z. Niu, J. Sun, T. Cheng and W. A. Goddard, *J. Phys. Chem. Lett.*, 2020, **11**, 7261.

24. C. L. Rooney, M. Lyons, Y. Wu, G. Hu, M. Wang, C. Choi, Y. Gao, C.-W. Chang, G. W. Brudvig, Z. Feng and H. Wang, *Angew. Chem., Int. Ed.*, 2024, **63**, e202310623.
25. X. She, L. Zhai, Y. Wang, P. Xiong, M. M.-J. Li, T.-S. Wu, M. C. Wong, X. Guo, Z. Xu, H. Li, H. Xu, Y. Zhu, S. C. E. Tsang and S. P. Lau, *Nat. Energy*, 2024, **9**, 154.
26. F. Xu, B. Feng, Z. Shen, Y. Chen, L. Jiao, Y. Zhang, J. Tian, J. Zhang, X. Wang and L. Yang, *J. Am. Chem. Soc.*, 2024, **146**, 9365.
27. Z. Gu, H. Shen, Z. Chen, Y. Yang, C. Yang, Y. Ji, Y. Wang, C. Zhu, J. Liu, J. Li, T.-K. Sham, X. Xu and G. Zheng, *Joule*, 2021, **5**, 429.
28. P. Wang, H. Yang, C. Tang, Y. Wu, Y. Zheng, T. Cheng, K. Davey, X. Huang and S. Qiao, *Nat. Commun.*, 2022, **13**, 3754.
29. H. Wang, S. Liu, H. Zhang, S. Yin, Y. Xu, X. Li, Z. Wang and L. Wang, *Nanoscale*, 2020, **12**, 13507.
30. Q. Deng, X. Duan, D. H. Ng, H. Tang, Y. Yang, M. Kong, Z. Wu, W. Cai and G. Wang, ACS Appl. Mater. Interfaces, 2012, **4**, 6030.
31. F. Franco, C. Rettenmaier, H. S. Jeon and B. Roldan Cuenya, *Chem. Soc. Rev.*, 2020, **49**, 6884.
32. S. Nitopi, E. Bertheussen, S. B. Scott, X. Liu, A. K. Engstfeld, S. Horch, B. Seger, I. E. L. Stephens, K. Chan, C. Hahn, J. K. Norskov, T. F. Jaramillo and I. Chorkendorff, *Chem. Rev.*, 2019, **119**, 7610.
33. C. Xiao and J. Zhang, *ACS Nano*, 2021, **15**, 7975.
34. C. Tang, J. Shi, X. Bai, A. Hu, N. Xuan, Y. Yue, T. Ye, B. Liu, P. Li, P. Zhuang, J. Shen, Y. Liu and Z. Sun, *ACS Catal.*, 2020, **10**, 2026.
35. P. Chen, B. Lei, X. Dong, H. Wang, J. Sheng, W. Cui, J. Li, Y. Sun, Z. Wang and F. Dong, *ACS Nano*, 2020, **14**, 15841.
36. D. Bagchi, J. Raj, A. K. Singh, A. Cherevotan, S. Roy, K. S. Manoj, C. P. Vinod and S. C. Peter, *Adv. Mater.*, 2022, **34**, 2109426.
37. H. Cui, Y. Guo, L. Guo, L. Wang, Z. Zhou and Z. Peng, *J. Mater. Chem. A*, 2018, **6**, 18782.
38. A. Hassan, M. Dar, and M. A. Dar, *ACS Appl. Mater. & Interfaces,* 2025, **17**, 53056.
39. K. A. Gandionco, J. Kim, L. Bekaert, A. Hubin and J. Lim, *Carbon Energy*, 2024, **6**, e410.
40. Z. Mao, Y. Fu, X. Long, C. Li, M. Li, F. Zhu, W. Ye, Z. Fan and X. Yao, *Chem. Synth.*, 2025, **5**, 67.

41. X. Li, Y. Chen, X. Zhan, Y. Xu, L. Hao, L. Xu, X. Li, M. Umer, X. Tan, B. Han, A. W. Robertson and Z. Sun, *Innov. Mater.*, 2023, **1**, 100014.
42. T. Zhang, Z. Li, A. K. Ummireddi and J. Wu, *Trends Chem.*, 2023, **5**, 252.
43. Z. Tao, C. L. Rooney, Y. Liang and H. Wang, *J. Am. Chem. Soc.,* 2021, **143**, 19630.
44. G. O. Larrazábal, A. J. Martín and J. Pérez-Ramírez, *J. Phys. Chem. Lett.*, 2017, **8**, 3933.
45. J. Li, *Nano-Micro Lett.,* 2022, **14**, 112.
46. G. Y. Jang, S. Kim, J. Choi, J. Park, S. An, J. Baek, Y. Z. Li, T. K. Liu, E. Kim, J. H. Lee, H. T. Wang, M. Kim, H. S. Cho, X. L. Zheng, J. S. Yoo, K. Seo and J. H. Park, *Adv. Energy Mater.*, 2024, **14**, 2303924.
47. A. De, R. Madhu, K. Bera, H. N. Dhandapani, S. Nagappan, S. Singha Roy and S. Kundu, *J. Mater. Chem. A*, 2023, **11**, 25055.
48. N. Kalita, A. Sahu, S. Bhowmick and M. Qureshi, *Chem. Commun.*, 2022, **58**, 13747.
49. L. Chen, Q. Xu, S. Z. Oener, K. Fabrizio and S. W. Boettcher, *Nat. Commun.*, 2022, **13**, 3846.
50. J. Joo, T. Kim, J. Lee, S.-I. Choi and K. Lee, *Adv. Mater.*, 2019, **31**, 1806682.
51. Y. Liu and X. Peng, *et al.* , *ACS Catal.*, 2024, **14**, 138.
52. S. You, J. Xiao, S. Liang, W. Xie, T. Zhang, M. Li, Z. Zhong, Q. Wang and H. He, *Energy Environ. Sci.*, 2024, **17**, 5795.
53. H. Takeda, C. Cometto, O. Ishitani and M. Robert, *ACS Catal.*, 2017, **7**, 70.
54. K. Zhong, P. P. Sun and H. Xu, *Small*, 2024, 2310677.
55. J. Liu, X. Yang, F. Si, B. Zhao, X. Xi, L. Wang, J. Zhang, X.-Z. Fu and J.-L. Luo, *Nano Energy*, 2022, **103**, 107753.
56. Q. Xu, J. Zhang, H. Zhang, L. Zhang, L. Chen, Y. Hu, H. Jiang and C. Li, *Energy Environ. Sci.*, 2021, **14**, 5228.
57. P. Zhai, Y. Zhang, Y. Wu, J. Gao, B. Zhang, S. Cao, Y. Zhang, Z. Li, L. Sun and J. Hou, *Nat. Commun.*, 2020, **11**, 5462.
58. T. Wu, E. Song, S. Zhang, M. Luo, C. Zhao, W. Zhao, J. Liu and F. Huang, *Adv. Mater.*, 2022, **34**, e2108505.
59. J. Li, R. Cai, H. Mu, J. Guo, X. Zhong, J. Wang, X. Du, J. Zhang and F. Li, *ACS Catal.*, 2024, **14**, 3266.
60. J. Wang, T. Liao, Z. Wei, J. Sun, J. Guo and Z. Sun, *Small Methods*, 2021, **5**, 2000988.
61. H. Sun, X. Xu, Y. Song, W. Zhou and Z. Shao, *Adv. Funct. Mater.*, 2021, **31**, 2009779.

62. D. Liu, Z. Wu, J. Liu, H. Gu, Y. Li, X. Li, S. Liu, S. Liu and J. Zhang, Small, 2023, **19** , e2207235.
63. S. Niu, W.-J. Jiang, Z. Wei, T. Tang, J. Ma, J.-S. Hu and L.-J. Wan, *J. Am. Chem. Soc.*, 2019, **141**, 7005.
64. Z. Zhang, S. Chen, J. Zhu, C. Ye, Y. Mao, B. Wang, G. Zhou, L. Mai, Z. Wang, X. Liu and D. Wang, *Nano Lett.*, 2023, **23**, 2312.
65. T. T. H. Hoang, S. Verma, S. Ma, T. T. Fister, J. Timoshenko, A. I. Frenkel, P. J. A. Kenis and A. A. Gewirth, *J. Am. Chem. Soc.*, 2018, **140**, 5791.
66. J. Lee, J. Yun, S. -R. Kwon, W. J. Chang, K. T. Nam and T. D. Chung, *Sci. Rep.*, 2017, **7**, 12281.
67. L. Chen, Q. Xu, S. Z. Oener, K. Fabrizio and S. W. Boettcher, *Nat. Commun.*, 2022, **13**, 3846.
68. R. A. Tufa, M. A. Blommaert, D. Chanda, Q. Li, D. A. Vermaas and D. Aili, *ACS Appl. Energy Mater.*, 2021, **4**, 7419.
69. R. Pärnamäe, S. Mareev, V. Nikonenko, S. Melnikov, N. Sheldeshov, V. Zabolotskii, H. Hamelers and M. Tedesco, *J. Membr. Sci.*, 2021, **617**, 118538.
70. S. Z. Oener, M. J. Foster and S. W. Boettcher, *Science*, 2020, **369**, 1099.
71. Z. Yan, R. J. Wycisk, A. S. Metlay, L. Xiao, Y. Yoon, P. N. Pintauro and T. E.Mallouk, *ACS Cent. Sci.*, 2021, **7** (6), 1028.
72. F. Alvarez, R. Alvarez, J. Coca, J. Sandeaux, R. Sandeaux and C. Gavach, *J. Membr. Sci.*, 1997, **123**, 61.
73. I. C. Bassignana and H. Reiss, *J. Membr. Sci.*, 1983, **15**, 27.
74. H. G. L. Coster, *Biophys. J.*, 1965, **5**, 669.
75. R. A. Tufa, M. A. Blommaert, D. Chanda, Q. Li, D. A. Vermaas and D. Aili, *ACS Appl. Energy Mater.*, 2021, **4** (8), 7419.
76. B. Lovrecek, A. Despic and J. O. M. Bockris, *J. Phys. Chem.*, 1959, **63**, 750.
77. V. J. Frilette, *J. Phys. Chem.*, 1956, **60**, 435.
78. P. Ramirez, H. Rapp, S. Mafe and B. Bauer, *J. Electroanal. Chem.*, 1994, **375**, 101.
79. L. Onsager, *J. Chem. Phys.*, 1934, **2**, 599.
80. H. C. Eckstrom and C. Schmeltzer, *Chem. Rev*., 1939, **24**, 367.
81. H. Strathmann, H. J. Rapp, B. Bauer and C. M. Bell, *Desalination*, 1993, **90**(1–3), 303.
82. V. Zabolotskii, N. Sheldeshov and S. Melnikov, *Desalination*, 2014, **342**, 183.

83. V.I. Zabolotskii, N. V Shel, N.P. Gnusin, *Russ. Chem. Rev.*, 1988, **57**, 801.

84. Z. Yan, L. Zhu, Y. C. Li, R. J. Wycisk, P. N. Pintauro, M. A. Hickner and T. E. Mallouk, *Energy Environ. Sci.*, 2018, **11**, 2235.

85. M. B. McDonald and M. S. Freund, *ACS Appl. Mater. Interfaces*, 2014, **6**, 13790.

86. M. S. Kang, Y. J. Choi, H. J. Lee and S. H. Moon, *J. Colloid Interface Sci.*, 2004, **273**, 523.

87. J. Li, C. A. Triana, W. Wan, D. P. Adiyeri Saseendran, Y. Zhao, S. E. Balaghi, S. Heidari and G. R. Patzke, *Chem. Soc. Rev.*, 2021, **50**, 2444.

88. N. Kalita, J. K. Satpathy , R. Yadav, C. V. Sastri and M. Qureshi, *Chem. Mater.*, 2025, **37**, 2026.

89. B. Chang, H. Pang, F. Raziq, S. B. Wang, K. W. Huang, J. H. Ye and H. B. Zhang, *Energy Environ. Sci.*, 2023, **16**, 4714.

90. A. J. Martín, G. O. Larrazábal and J. Pérez-Ramírez, *Green Chem.*, 2015, **17**, 5114.

91. P. Zeng, X. Q. Li, B. Zhao, J. C. Gao, W. Feng, Q. Y. Wang, Y. Z. Song, *Adv. Energy Mater.* 2025, **15**, 2501603.

CHAPTER 2

Experimental Section

This chapter details the synthesis strategies adopted for preparing the electrocatalysts and their corresponding support materials. It further outlines the sequential procedure used for fabricating the working electrodes. In addition, a comprehensive description of the analytical and electrochemical techniques employed for catalyst characterization and performance evaluation is provided.

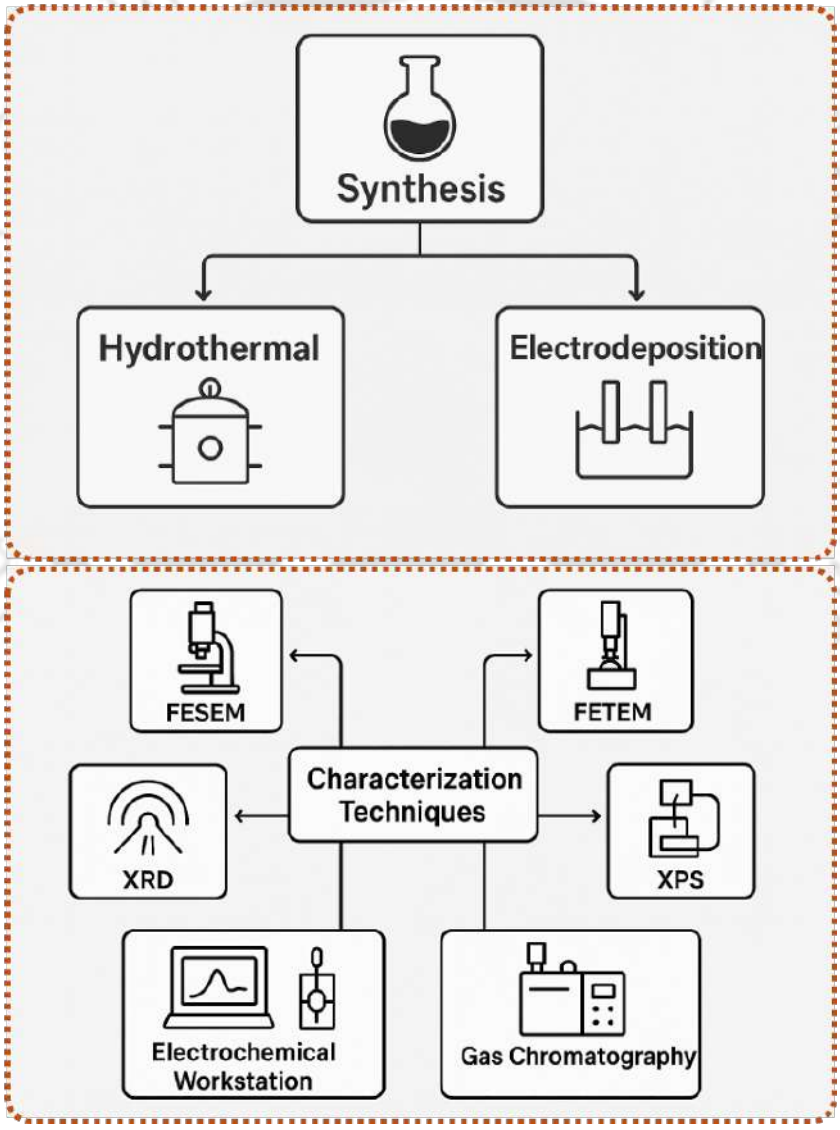

2.1 Introduction:

This chapter outlines the synthesis routes adopted for preparing various electrocatalysts, along with the methodologies employed in fabricating the working electrodes used for electrochemical water splitting. It further provides an overview of the key analytical techniques utilized for characterizing the synthesized materials. Additionally, the reagents and substrates involved in both the synthesis and electrode preparation processes are itemized. The electrochemical performance metrics applied to evaluate the catalytic activity are also discussed comprehensively.

2.2. Reagents and Chemicals Used:

All chemicals and materials used throughout my work were of analytical grade and procured from reputed suppliers to ensure high reproducibility and reliability of the synthesis and electrochemical measurements.

For my first work i.e. Chapter 3 of this thesis, concentrated hydrochloric acid (36 wt%) used for Ni-foam cleaning was obtained from *Finar, India*. The electrodeposition bath comprised potassium chloride (KCl, *Merck*), cobalt(II) chloride hexahydrate ($CoCl_2 \cdot 6H_2O$, *Sigma-Aldrich*), and manganese(II) chloride tetrahydrate ($MnCl_2 \cdot 4H_2O$, *Sigma-Aldrich*). The Ni-foam substrate was purchased from *HI-TECH Scientific Equipment*, while Pt wire and Ag/AgCl (saturated KCl) electrodes were standard electrochemical-grade components.

In Chapter 4, Ni-foam substrates (*Hi-TECH Scientific Equipment*) were used for catalyst growth. Copper(II) sulfate and H_2WO_4 (99%) were purchased from *Sigma-Aldrich* for the synthesis of CuO and WO_3, respectively. Oxalic acid and urea were also sourced from *Sigma-Aldrich*. Hydrochloric acid (36%) and sulfuric acid (98%) were purchased from *Finar, India*, whereas acetonitrile was obtained from *Finar*. Cu foil for $Cu(OH)_2$ preparation was procured from *Sigma-Aldrich*. Potassium hydroxide (KOH) used for electroanalysis was supplied by *Merck*.

In Chapter 5, the synthesis of the catalyst and membrane assemblies utilized poly(vinyl alcohol) (PVA), 2-pyridinecarbaldehyde (99%), bromoethane (98%), copper(II) sulfate, nickel(II) acetate, poly(4-styrenesulfonic acid) solution (18 wt% in H_2O), Nafion® membranes,

Nafion® resin solutions, and PTFE membranes (100 nm pore size), all sourced from *Sigma-Aldrich*. Potassium hydroxide (KOH), sodium chloride (NaCl), and hydrogen peroxide (50%) were supplied by *Merck*. Hydrochloric acid (36%), sulfuric acid (98%), aqueous ammonia (25%), DMF, and acetone were purchased from *Finar, India*. Ethyl alcohol was procured from *TMEDA*. Milli-Q water (18.2 MΩ·cm) was used in all preparative and electrochemical procedures.

The Ni-foam substrates used for the synthesis of heterogeneous catalyst in for Chapter 6a has been purchased from *Hi-TECH Scientific Equipment India.* nickel nitrate hexahydrate ($Ni(NO_3)_2 \cdot 6H_2O$) and urea were purchased from *Sigma-Aldrich*. Hydrochloric acid (36%) and ethyl alcohol were obtained from *Finar, India*, while potassium hydroxide (KOH) used as the electrolyte was sourced from *Merck*.

For Chapter 6b, heterogeneous catalyst synthesis employed commercial carbon paper (*ThermoFisher Scientific*), manganese(II) acetate (*Sigma-Aldrich*), copper(II) acetate (*Sigma-Aldrich*), urea (*Finar*, India), ethanol (*Finar*, India), and deionized laboratory water.

The ligand synthesis for the homogeneous catalysts described in Chapters 6a and 6b utilized dimethyl acetonedicarboxylate (*Sigma-Aldrich*), methanol (*Merck*), aqueous formaldehyde (37%, *Merck*), 2-picolylamine (*Sigma-Aldrich*), cold ethanol (*Finar*), and acetonitrile (*Merck*). Additional ligand precursors included pyridine-2-carboxaldehyde (*Sigma-Aldrich*), methylamine (*Sigma-Aldrich*), dimethyl acetonedicarboxylate (*Sigma-Aldrich*), methanol (*Merck*), and aqueous formaldehyde (37%, *Merck*).

2.3. Analytical Characterization of Materials and Fabricated Electrochemical Devices:

A comprehensive suite of analytical and electrochemical techniques was employed to investigate the structural, morphological, compositional, and functional properties of the synthesized materials and fabricated devices.

1. Powder X-ray Diffraction (PXRD): The crystalline structure and phase purity of all samples were examined using a Rigaku SmartLab diffractometer equipped with a Cu K_α radiation source (λ = 1.54 Å, 9 kW).

2. Micro-Raman Spectroscopy: Vibrational features and molecular fingerprints were recorded using a Horiba Jobin Yvon LabRAM HR Raman system with 488 nm and 514 nm excitation lasers.

3. Fourier-Transform Infrared Spectroscopy (FT-IR): FT-IR spectra were obtained using a PerkinElmer Spectrum-II spectrometer with KBr pellets to identify functional groups and bonding characteristics.

4. UV–Visible Absorption Spectroscopy: UV–Vis spectra were recorded using an Agilent 8453 spectrophotometer equipped with either a temperature-controlled circulating water bath or a liquid nitrogen cryostat (Unisoku) for precise temperature regulation.

5. Field-Emission Scanning Electron Microscopy (FESEM): Surface morphology and microstructural features were analyzed using Zeiss Gemini and Zeiss Sigma FESEM instruments operating at 3–10 kV.

6. Field-Emission Transmission Electron Microscopy (FETEM): High-resolution imaging, elemental mapping, d-spacing measurements, and SAED patterns were recorded on a JEOL JEM-2100F microscope operated at 200 kV.

7. X-ray Photoelectron Spectroscopy (XPS): Elemental composition, oxidation states, and electronic environments were probed using a Thermo Fisher ESCALAB Xi+ spectrometer with a monochromatic Al K_α source (hv = 1486.6 eV). Additional measurements were performed using a Thermo Scientific NEXA system (micro-focused Al K_α, 72 W, 12 kV). Charge correction was applied using the C 1s reference peak at 284.77 eV, and spectral deconvolution was conducted with XPSPEAK 4.1.

8. Nuclear Magnetic Resonance (NMR) Spectroscopy: Functional group incorporation and ligand structures were confirmed using a 500 MHz NMR spectrometer.

9. Electrospray Ionization Mass Spectrometry (ESI-MS): High-resolution ESI-MS spectra of Ni(II) and Cu(II) complexes were obtained on an Agilent G6546A UHPLC-QTOF-HRMS mass spectrometer (spray voltage: 2 kV; capillary temperature: 80 °C; temperature: 298 K).

10. Single-Crystal X-ray Diffraction (SCXRD): Single-crystal structures were determined at room temperature using a SuperNova CCD diffractometer from Agilent Technologies equipped with a fine-focus 1.75 kW sealed Mo-Kα (λ = 0.71073 Å) X-ray source.

11. Contact Angle Measurements: Wettability and surface properties were evaluated using a KRÜSS Drop Shape Analyzer (DSA-25), where advancing and receding contact angles were recorded at four different locations using deionized water droplets.

12. Mechanical Testing: The mechanical strength of polymer-based materials (2 cm × 1 cm × 1 cm) was assessed using an Instron 5944 universal testing machine (Norwood, MA, USA).

13. Electrochemical Workstations (General Measurements): Linear sweep voltammetry (LSV), cyclic voltammetry (CV), and chronoamperometry were performed using a Gamry Interface 1010E instrument.

14. Electrochemical Impedance Spectroscopy (EIS): Impedance measurements for device characterization were carried out using a Gamry Interface 1010E instrument.

15. Comprehensive Electrochemical Analysis: Additional electrochemical parameters—including LSV, CV, chronoamperometry, EIS, Mott–Schottky (MS) analysis, current–voltage characteristics (CVC), and chronopotentiometry—were recorded using a Gamry Interface 1010E system.

16. Gas Chromatography (GC): Quantification of product gases and Faradaic efficiency calculations were performed using an Agilent 7820A gas chromatograph.

2.4. Steps Involved for the Fabrication of Heterogeneous (Working Electrode) and Homogenous Catalysts:

In our study, heterogeneous catalyst electrodes were fabricated through two primary routes: a hydrothermal synthesis process and an electrodeposition method. After synthesis, all electrodes were subjected to high-temperature calcination to convert the as-prepared materials into more stable oxide phases appropriate for electrocatalytic evaluations. The general steps followed for preparing catalyst-coated conducting substrates are outlined below. Notably, all electrode materials in this study were prepared in situ.

1. In my first work (Chapter 3), a two-step electrochemical deposition strategy was employed, involving initial metal-oxide deposition followed by re-electrodeposition of a mixed metal hydroxide layer over Ni-foam substrate to enhance interfacial charge-transfer characteristics during alkaline OER.

2. In the fourth chapter of my work, a hierarchical electrode was fabricated through a sequential multi-step strategy involving electrodeposition, hydrothermal growth in an autoclave, electrochemical doping, high-temperature calcination for oxide formation, and a final anodization step to introduce a surface-modifying hydroxide layer in situ.

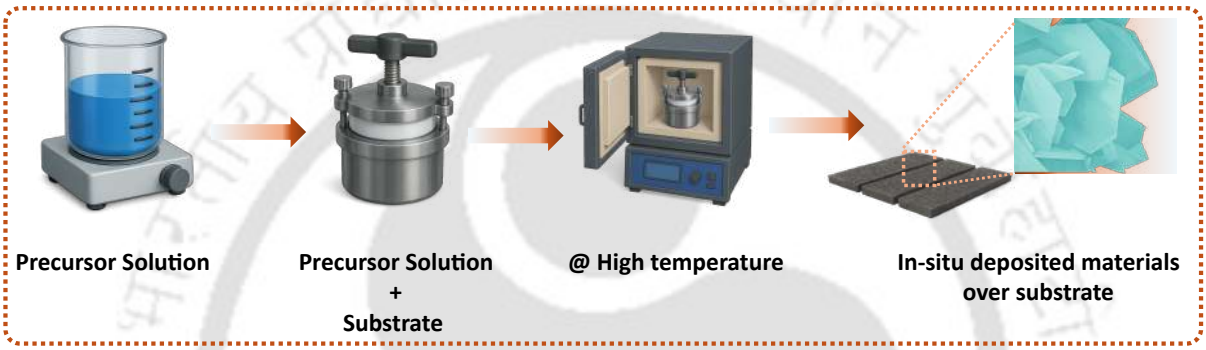

Figure 2.1. Schematic illustration of the hydrothermal in situ synthesis process used for direct material growth on the substrate.

3. In chapter 5, the bipolar membrane was prepared through a sequence of polymer functionalization, membrane casting, interlayer fabrication, and lamination steps. The polymer was first modified via an acetalization reaction under controlled acidity and temperature, purified by precipitation, and further quaternized through alkylation under reflux, followed by ion exchange in alkaline medium to obtain the functionalized anion-exchange layer. The commercial cation-exchange membrane was activated through thermal treatments in oxidizing, aqueous, and acidic environments. The inorganic interlayer was produced by precipitating an aqueous precursor under basic conditions, isolating and drying the solid, redispersing it with a binder, and forming a uniform film through vacuum-assisted filtration. Final BPM assembly was achieved by laminating the anion-exchange layer, inorganic interlayer, and activated cation-exchange membrane with a thin binder layer under cold pressing. Additionally, a metallic foam substrate used for device integration was modified through electrodeposition followed by calcination to obtain a stable surface layer.

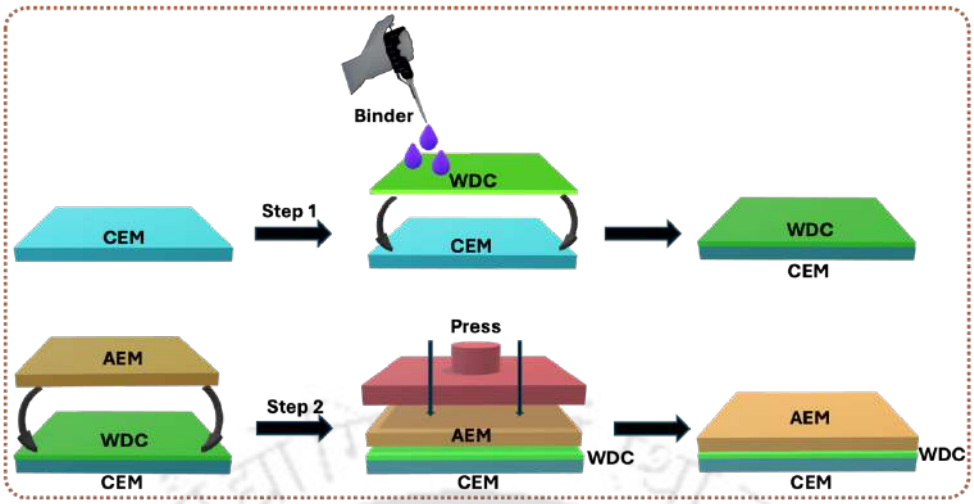

Figure 2.2. *Schematic Representation of the Fabrication of BPM*

4. In the next chapter (Chapter 6a), the heterogeneous catalyst was fabricated through a hydrothermal method in which pre-cleaned Ni-foam substrate was immersed in an aqueous precursor solution containing metal salts and a precipitating agent. The assembly was then subjected to sealed autoclave treatment at elevated temperature, enabling the controlled growth of the desired phase directly on the substrate.

The ligands were synthesized through multistep condensation reactions involving ester, aldehyde, and amine precursors under low-temperature conditions. This was followed by reflux-assisted cyclization and subsequent recrystallization, allowing the isolation of purified organic scaffolds suitable for coordination studies.

Metal–ligand complexes were obtained by reacting the organic frameworks with metal salts in an appropriate organic solvent under ambient conditions. The resulting coordination compounds were isolated by filtration, purified using vapor-diffusion techniques, and, when required, modified through counter-anion exchange to obtain well-defined crystalline products.

5. In my last project (Chapter 6b) The heterogeneous catalyst was prepared by first cleaning a carbon-based substrate and immersing it in an aqueous precursor solution. The mixture was subjected to hydrothermal treatment to induce the in situ growth of an intermediate layer.

The resulting film was washed, vacuum-dried, and finally crystallized through calcination in air using a controlled heating profile.

For the homogeneous catalyst precursors, flexible and rigid ligands were obtained through sequential condensation reactions performed in alcoholic media under controlled temperature conditions. Each step involved dropwise addition of reagents, prolonged stirring or reflux to complete the condensations, followed by isolation of intermediates through filtration, washing with cold solvents, and vacuum drying. Crystallization was achieved either by slow cooling or by storing concentrated solutions at low temperatures, with recrystallization used when necessary to improve purity.

For complex formation, the prepared ligands were reacted with a metal precursor in an organic solvent under ambient conditions with continuous stirring. The reaction mixtures were purified by filtration and subsequently subjected to vapor-diffusion–assisted crystallization at low temperatures, yielding well-defined crystals suitable for structural analysis.

2.5. Electrochemical Measurements:

Electrochemical characterization of the prepared electrodes was conducted using a Gamry Interface 1010E electrochemical workstation across Chapters 3–6b, employing a standard three-electrode configuration. Alkaline measurements were performed in 1 M NaOH (pH ≈ 12.6) using a polypropylene cell (Chapters 3 and 4), whereas neutral studies utilized a phosphate buffer (pH ≈ 7.3) in Chapters 6a and 6b. In Chapter 5, which involves bipolar membrane–based investigations, measurements were additionally carried out in acidic (1 M H_2SO_4), alkaline (1 M KOH), and neutral (1 M NaCl) media. The catalyst-coated substrates served as the working electrodes throughout (Chapters 3–6b). Depending on the study, Ag/AgCl (saturated KCl) was used as the reference electrode in Chapters 6a and 6b, while Hg/HgO was employed in Chapters 3 and 4. The counter electrode consisted of Pt wire for Chapters 6a and 6b, and a graphite rod for Chapters 3 and 4. Before each measurement, the electrolyte was purged with N_2 to eliminate dissolved oxygen. Figure 2.3 presents a schematic diagram of the electrochemical setup used for water-splitting experiments.

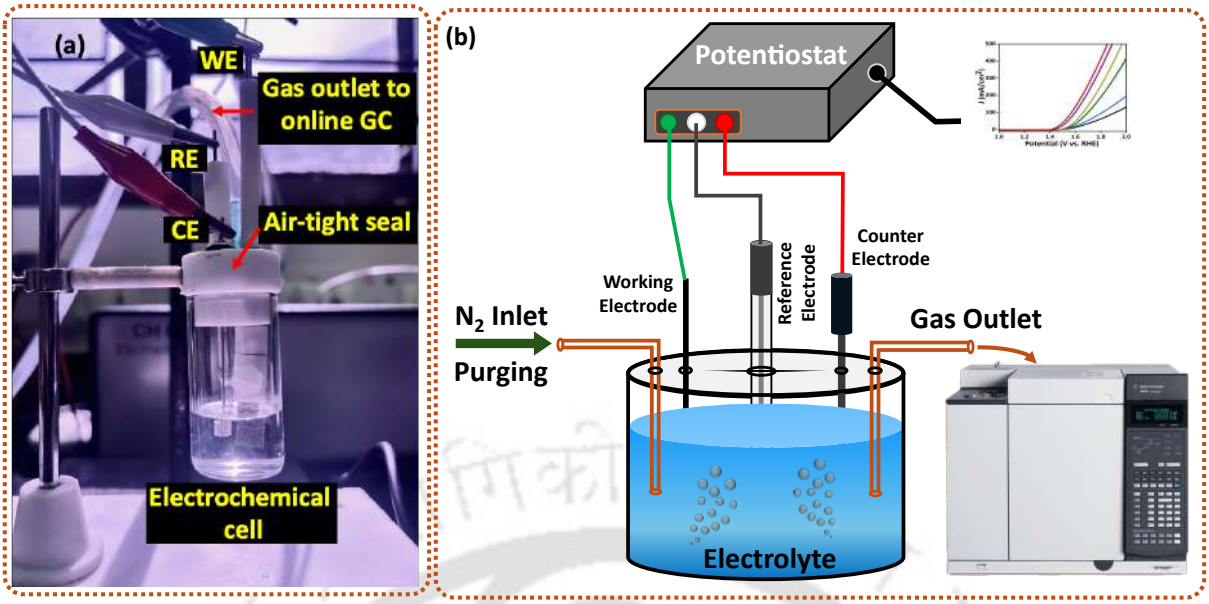

Figure 2.3. *Schematic illustration of the electrochemical water-splitting setup, depicting the three-electrode configuration operated under an applied potential controlled by the potentiostat.*

All applied potentials were converted to the reversible hydrogen electrode (RHE) scale using Equation 2.1 for measurements with the Ag/AgCl reference electrode and Equation 2.2 for those using the Hg/HgO reference electrode,

$$E_{RHE} = E_{Ag/AgCl} + 0.059pH + E^{0}_{Ag/AgCl} \quad (2.1)$$

Here, E_{RHE} denotes the potential referenced to the reversible hydrogen electrode, $E^{0}_{Ag/AgCl}$ = 0.1976 V at 25 °C represents the standard potential of the Ag/AgCl (saturated KCl) reference electrode, $E_{Ag/AgCl}$ corresponds to the experimentally measured potential versus this reference, and pH reflects the hydrogen ion activity of the electrolyte.

$$E_{RHE} = E_{Hg/HgO} + 0.059pH + E^{0}_{Hg/HgO} \quad (2.2)$$

In this relation, E_{RHE} represents the reversible hydrogen electrode potential, $E^{0}_{Hg/HgO}$ = 0.098 V at 25 °C denotes the standard potential of the Hg/HgO (saturated KOH) reference electrode, $E_{Hg/HgO}$ is the experimentally recorded potential versus this reference, and pH corresponds to the acidity of the electrolyte.

For the electrochemical study the linear sweep voltammetry was carried out within potential windows and scan rates optimized for each study: 1.1–2.2 V at 5 mV s^{-1} vs RHE (Chapter 3), 0.2–1.2 V at 5 mV s^{-1} vs. Hg/HgO (Chapter 4), -0.1–2.0 V at 5 mV s^{-1} vs Ag/AgCl

(Chapter 5), 0.5–1.8 V at 5 mV s^{-1} vs. RHE (Chapter 6a) and 1.2– -0.5 V at 5 mV s^{-1} vs RHE (Chapter 6b),. Electrochemical active surface area (ECSA) was estimated from double-layer capacitance values obtained by CV in the non-Faradaic region using chapter-specific potential windows and scan rate difference of 1mV/sec. Electrochemical impedance spectroscopy was performed from 0.1 Hz to 10^5 Hz at fixed potentials relevant to each study, while Mott–Schottky analyses were recorded at 1 kHz over chapter-specific potential ranges.

For bipolar membrane (BPM) evaluation (Chapter 5), galvanostatic and potentiostatic analyses were conducted in a four-probe H-cell (Figure 2.4) using platinum as both electrodes and calomel electrodes positioned in Haber–Luggin capillaries for precise potential measurement. The anodic and cathodic chambers, separated by the fabricated BPM (1 cm × 1 cm), contained 1 M NaCl electrolyte. Potentiodynamic scans quantified the voltage drop across the BPM with increasing current, and chronopotentiometry was performed at the limiting current to assess steady-state water dissociation behaviour.

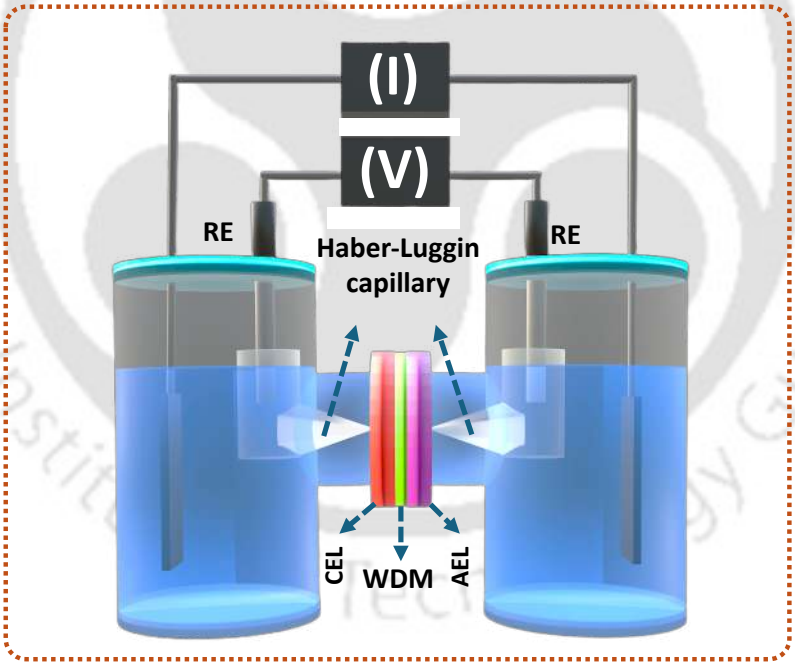

Figure 2.4. *Schematic representation of the setup used during the electrochemical measurements.*

2.6. Electrochemical Performance Parameters:

The performance of the fabricated electrochemical devices was evaluated using the parameters outlined in the following sections.

2.6.1. Overpotential (η) at a defined current density:

Overpotential in an electrochemical process refers to the excess potential that must be applied beyond the thermodynamic (reversible) potential to drive a reaction at a sustained rate. For reference, the reversible potentials for the hydrogen evolution reaction (HER) and oxygen evolution reaction (OER) are 0 V and 1.23 V vs. the Reversible Hydrogen Electrode (RHE), respectively. Accordingly, the governing expressions are given as follows.[1-3]

$$\eta_{OER} = E_{RHE} - 1.23V, \text{ and} \quad (2.3)$$

$$\eta_{HER} = E_{RHE} - 0V \quad (2.4)$$

was used for OER and HER, respectively, to calculate their overpotentials at a desired current density

A current density of 10 mA cm^{-2} is widely adopted as a standard benchmark for determining overpotential (using eqs. 2.3 and 2.4), enabling consistent comparison and characterization of electrocatalysts for both HER and OER across different electrolyte environments.

2.6.2. Tafel Slope:

Tafel analysis is a fundamental approach for assessing the intrinsic electrocatalytic activity toward water-splitting reactions. By examining the HER and OER Tafel behaviour, insights into the reaction kinetics and mechanistic pathways of the catalyst can be obtained.[4,5] The correlation between current density and overpotential at an electrode–electrolyte interface is described by the Butler–Volmer equation, expressed as follows:

$$I = I_0 [\exp(\alpha_A \eta F / RT \times \eta) - \exp(-\alpha_C \eta F / RT \times \eta)] \quad (2.5)$$

In this expression, 'I' represents the measured current, 'I_o' is the exchange current density corresponding to the equilibrium condition, α_A and α_C denote the anodic and cathodic charge-transfer coefficients, n is the number of electrons involved in the reaction, F is the Faraday constant (96,485 C mol^{-1}), *R* is the universal gas constant, T is the absolute temperature, and *η* is the applied overpotential. At equilibrium, the anodic and cathodic contributions become identical, resulting in an observed current equal to I_o. Under conditions of sufficiently large

overpotentials, the Butler–Volmer expression simplifies to the anodic and cathodic Tafel forms, which are given below:

$$\ln I = \ln I_0 + (-\alpha_C \eta F / RT)\, \eta \quad (2.6)$$

$$\ln I = \ln I_0 + (\alpha_A \eta F / RT)\, \eta \quad (2.7)$$

Equations 2.6 and 2.7 follow the linear form $y = b + mx$, producing a straight line when $\log I$ is plotted against η, commonly referred to as the Tafel plot. The slope of this linear region - characteristic of the cathodic or anodic branch - can be expressed for each polarization as follows:

$$\text{Slope } (d \log j / d\eta) \text{ for cathodic reaction} = (2.303RT / -\alpha_C \eta F) \quad (2.8)$$

$$\text{Slope } (d \log j / d\eta) \text{ for anodic reaction} = (2.303RT / \alpha_A \eta F) \quad (2.9)$$

The Tafel slope serves as a semi-quantitative indicator of the intrinsic reaction rate at an electrocatalytic interface. As shown in equations 2.8 and 2.9, the slope is inversely proportional to the charge-transfer coefficient (α), implying that a smaller Tafel slope corresponds to more efficient charge transfer and faster interfacial kinetics. In water-splitting electrocatalysis, this parameter is widely used to benchmark and compare catalyst activities under identical experimental conditions.

2.6.3. Electrochemically active surface area (ECSA):

ECSA is commonly employed to assess activity trends among structurally related electrocatalysts and to rationalize variations in their performance under identical conditions.[6,7] In this study, ECSA was estimated from the double-layer capacitance (C_{dl}), determined using cyclic voltammetry in the non-Faradaic region. Because ECSA scales proportionally with C_{dl}, it can be expressed as:

$$ECSA = C_{dl} / C_S \quad (2.10)$$

Here, C_S represents the specific capacitance of the material, while C_{dl} is extracted from cyclic voltammograms recorded in the non-Faradaic region. The C_{dl} value is determined as half of the slope obtained by plotting the difference in current density between the anodic and cathodic scans ($J_{anodic} - J_{cathodic}$) at a fixed potential against the corresponding scan rate.

2.6.4. Turnover frequency (TOF):

The turnover frequency (TOF) serves as a kinetic descriptor for evaluating the intrinsic rate of the HER and/or OER on a given catalyst surface. Used alongside Tafel analysis, it provides deeper insight into the fundamental reaction kinetics governing gas evolution processes.[8,9] Since both HER and OER typically proceed through pseudo–first-order pathways, TOF is expressed on a per-second basis (s^{-1}). The TOF values for the electrochemical reactions were calculated using equation 2.11.

$$\text{TOF} = \frac{J \times A}{n \times m \times N_S} \tag{2.11}$$

Here, *J* denotes the current density at the selected potential, *A* represents the geometric area of the working electrode (1 cm^2), *n* is the number of electrons involved in the reaction pathway (n = 4 for OER and n = 2 for HER), *m* corresponds to the total moles of catalytically active metal sites, and *F* is Faraday's constant (96,485 C mol^{-1}). For CO_2 reduction reactions (Chapter 6b), *n* was assigned based on the electron requirement for the formation of the specific product - for example, 12 electrons for the generation of ethanol.

2.6.5. Faradaic Yield (FE):

Faradaic efficiency represents the selectivity of a catalyst toward a specific electrochemical reaction, indicating how effectively the supplied charge is directed toward the formation of the desired product.[10,11] Alongside activity and stability, selectivity forms one of the three core performance criteria for electrocatalysts. The Faradaic yield is determined as the ratio between the experimentally measured amounts of evolved gases (H_2 or O_2) and their theoretically expected quantities, as described by equation 2.12.

$$\text{Faradaic Yield} = \frac{\text{Amount of experimentaly evolved gasses}}{\text{Amount of theoretically calculated gasses}} \tag{2.12}$$

The theoretical calculation for the amount of gas evolved was done by using equation 2.13,

$$\text{Amount of gas evolved} = \frac{\text{J} \times \text{t}}{\text{n} \times \text{F}} \tag{2.13}$$

Here, *J* denotes the current density (mA cm^{-2}), *t* is the electrolysis time (s), *n* represents the number of electrons required to generate one mole of product (n = 2 for H_2 and n = 4 for

O_2), and *F* is the Faraday constant (96,485 C mol^{-1}). The experimentally evolved gases during water splitting were quantified using an online gas chromatograph (GC).

2.6.6. Electrochemical impedance spectroscopy (EIS) analysis:

Electrochemical impedance spectroscopy (EIS) is a powerful tool for probing charge-transfer kinetics at semiconductor–electrolyte interfaces. This alternating-current (AC) method distinguishes resistive and capacitive contributions by monitoring the system's frequency-dependent response. In a typical EIS experiment, a small sinusoidal perturbation is superimposed on a fixed DC bias, and the resulting current response is recorded over a broad frequency range (commonly 0.1 Hz to 10^6 Hz). The impedance data are commonly represented as Nyquist plots, which map the imaginary component of impedance against the real component.[12-14]

A Nyquist plot generally exhibits two characteristic regions. The high-frequency domain reflects charge-transfer dynamics and often presents a semicircular arc arising from the parallel behaviour of interfacial resistance and capacitance. The low-frequency region, by contrast, is dominated by mass-transport limitations and displays a more diffusive character. The overall shape of the spectrum is influenced by the intrinsic properties of the electrode and electrolyte, as well as experimental conditions. To interpret these features, the impedance spectra are commonly fitted using equivalent circuit models, such as the Randles circuit. In this model, the solution resistance (Rs) is placed in series with a parallel combination of the charge-transfer resistance (R_{ct}) and interfacial capacitance (C_{int}), representing the simultaneous contribution of Faradaic and non-Faradaic processes. More complex systems may require additional R||C elements connected in series to account for multiple interfacial processes or additional semicircle arcs.

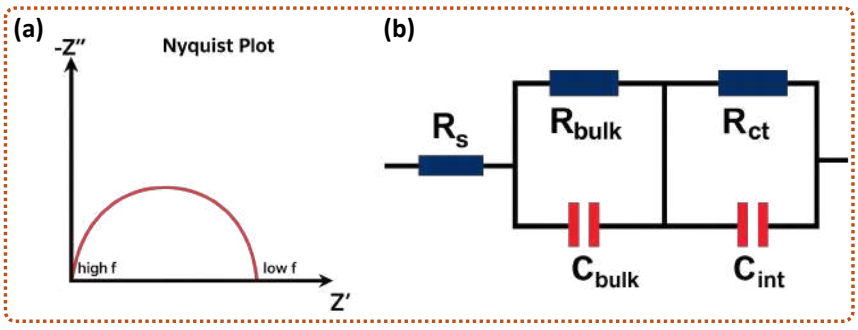

Figure 2.5. *(a) A typical Nyquist plot, and (b) equivalent circuit used to interpret the EIS data.*

2.6.7.1. Distribution of relaxation time (DRT) analysis:

To resolve the time constants and resistance values associated with interfacial relaxation processes, Distribution of Relaxation Times (DRT) analysis was performed using MATLAB on the AC impedance spectra (Figure 2.5a).[15,16] This method deconvolutes the impedance response into distinct processes, each defined by a characteristic relaxation time, enabling separation of overlapping electrochemical phenomena across different timescales. In the context of water electrolysis and electrocatalytic CO_2 electroreduction, timescale-resolved analysis can also provide critical insights into ionic transport, charge transfer, diffusion constraints and interfacial dynamics, along with contributions from less resolved processes. The mathematical relationship between the impedance response and the DRT function is expressed in equation (2.14).

$$Z(\omega) = R_{\infty} + R_{pol} \int_{-\infty}^{\infty} \frac{\Gamma(\log(\tau))}{1 + i\omega\tau} d(\log(\tau)) \qquad (2.14)$$

In this context, $Z(\omega)$ denotes the overall impedance, where R_{∞} corresponds to the series (ohmic) resistance, and R_{pol} represents the total polarization resistance associated with the electrochemical processes. Γ is the distribution function of relaxation times, τ signifies the characteristic relaxation time, and ω denotes the angular frequency of the applied perturbation.

After transformation, the DRT converts impedance data, originally collected as a function of frequency, into a spectrum of time constants (or relaxation times) associated with different electrochemical processes. Each peak in the DRT plot corresponds to a distinct process occurring at a specific timescale, and the area under each peak represents the polarization resistance of that particular process, presented in Figure 2.6b.

- **Explanation of Each Region:**

  I. **High Frequency region:** interfacial contact/conductivity of composite. Typically assigned to *ohmic resistance* or fast interface phenomena, such as the electrolyte resistance in supercapacitors

  II. **Mid-frequency region:** associated with charge-transfer resistance, adsorption/desorption processes, or other electrode reaction kinetics.

III. **Low-frequency region:** diffusion processes of the electrolyte, and reveal how efficiently ions can fill all available spaces in the electrodes over longer timescales

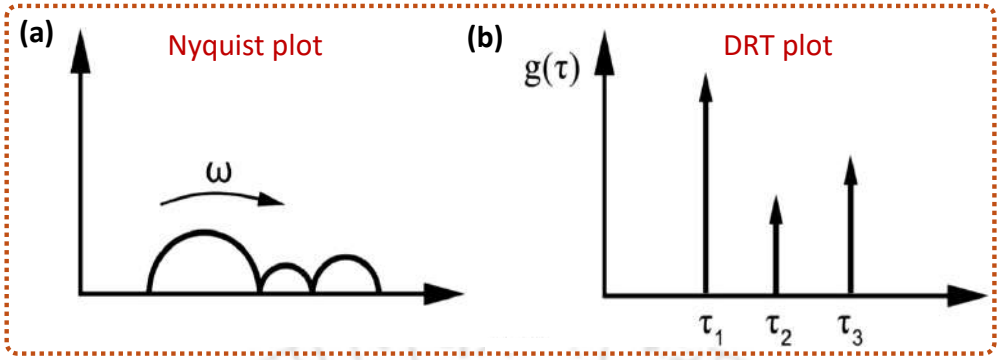

Figure 2.6. *Distribution of relaxation time curve showing conversion of frequency domain EIS data (a) to time domain data (b).*

2.6.7.2. DRT Analysis Methodology and Data Interpretation:

Open-source MATLAB script-based software (DRT Tools) was used to calculate DRT from the impedance data and the Gaussian method was used for data discretization. The DRT plots was obtained from the EIS data using Gaussian basis function and 0.01 regularization parameter. Each peak is defined by its central position, its total area (which corresponds to its effective resistance) and its width.[15]

The related time constant can be calculated by t= $\frac{1}{2\pi f}$. Here, f represents the frequency, and it is independent of the surface area and represents the intrinsic properties of each process. Regarding parameter selection, the series resistance across the electrolyte and electrode interface possesses very small time constant, with its peak observed around 10^{-4} to 10^{-3} s.

The charge transfer at the electrode/electrolyte interface is more rapid than that of cathode materials delivering the time constant of 10^{-2} to 10^{-1} s. The diffusion in electrodes or materials is the most sluggish process because the diffusion is only driven by the concentration gradient. The time constant for diffusion reaches more than 10 s to 100 s.[17]

To calculate the contribution from each peak we have to follow the steps given below:

1. We have to find out the total area by summing up all the area of peak, where peak area represents the impedance of the corresponding process.

2. Next step is to find out the total resistance (uncompensated and charge transfer resistances are denoted as R_u and R_{CT}, respectively) from the fitted EIS Nyquist plot.

2.6.8. Mott-Schottky analysis:

Mott–Schottky (M–S) analysis was employed to determine essential semiconductor parameters, particularly the flat-band potential (EF) and the semiconductor type (n- or p-type). The flat-band potential corresponds to the applied potential at which no band bending occurs, meaning the potential drop between the electrode surface and the bulk is zero.[18,19] This value provides critical insight into the alignment of the semiconductor energy bands relative to the redox levels of the electrolyte. M–S measurements were carried out using a standard three-electrode potentiostat setup, analogous to that used for electrochemical current analysis.[20,21] From the resulting M–S plots, EF was extracted using the M–S relationship, with the flat-band potential determined according to Equation 2.15.

$$\frac{1}{C^2} = \frac{2}{A^2 N_D e \varepsilon \varepsilon^0}\left[E - E_{FB} - \frac{kT}{e}\right] \qquad (2.15)$$

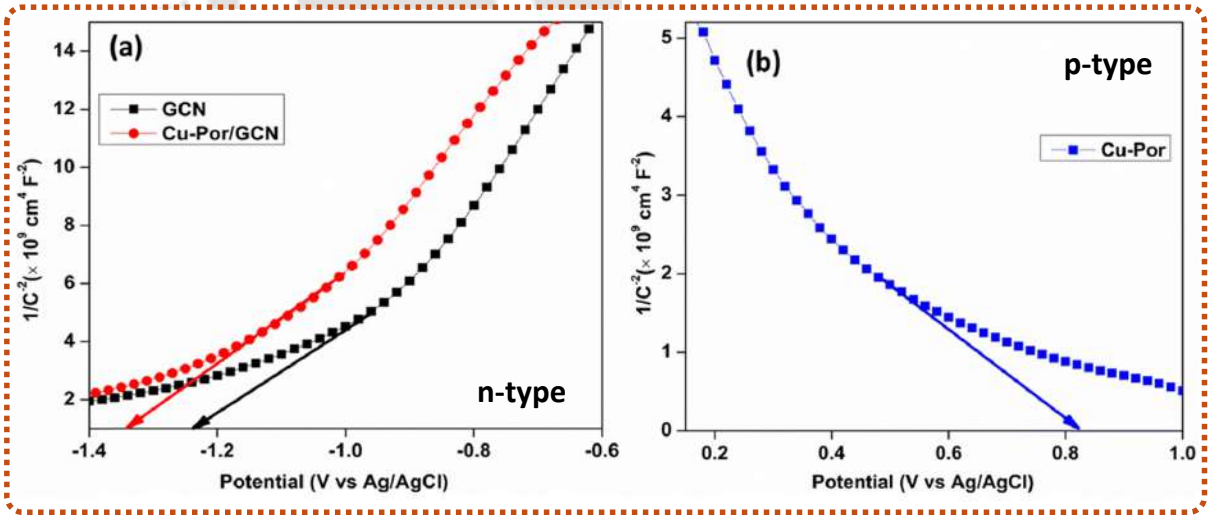

Figure 2.7. *Typical Mott-Schottky plot for semiconductor photoanode, showing the nature of conductivity, (a) positive (n-type), (b) negative (p-type). (Ref. 22)*

In this relationship, C represents the semiconductor capacitance, $A$is the photoelectrode surface area, $N_D$denotes the charge-carrier density, $e$is the elementary charge, $\varepsilon_0$is the

vacuum permittivity, $\varepsilon$is the semiconductor dielectric constant, $E$is the applied potential, $k$is the Boltzmann constant, and T is the absolute temperature. The slope of the Mott–Schottky plot ($1/C^2$ vs. E) provides insight into the semiconductor conductivity type, where a positive slope indicates n-type behavior and a negative slope signals p-type characteristics, as illustrated in Figure 2.7.[22]

2.6.9. Water Dissociation Performance Parameters:

range of analytical techniques can be employed to investigate water dissociation and ion-transport phenomena in membrane systems. Many of these approaches were originally established for electrochemical electrode studies and later adapted for membrane characterization. The principal methods are outlined below.

2.6.9.1. Current-Voltage characteristics:

The electrochemical behaviour of bipolar membranes (BPMs) is typically characterized through voltametric techniques. Among these, the current–voltage curve (CVC) provides a straightforward means to evaluate the overall potential drop across the membrane assembly without resolving individual contributions.[23-26] Under reverse-bias operation, the BPM facilitates water dissociation at the junction interface, enabling analysis of interfacial catalytic activity and ion-transport phenomena.

Under reverse-bias operation, the current–voltage curve of a BPM can be segmented into four characteristic regions (Figure 2.8(a))[23,27]. The initial linear region reflects the ohmic resistance of the membrane assembly (R_{Ohm}). The subsequent plateau corresponds to the first limiting current (I_{lim1}), which arises from co-ion transport; membranes with higher permselectivity exhibit a lower I_{lim1}. The third region, defined by the slope beyond this plateau, represents the water-dissociation resistance (R_{diss}), indicating the membrane's efficiency in promoting interfacial water splitting—lower R_{diss} denotes enhanced catalytic activity.[23,28] The final plateau is associated with the second limiting current (I_{lim2}), where the supply of water to the interfacial layer becomes insufficient to sustain the dissociation reaction, leading to mass-transport limitations and partial depletion of water within the junction region.

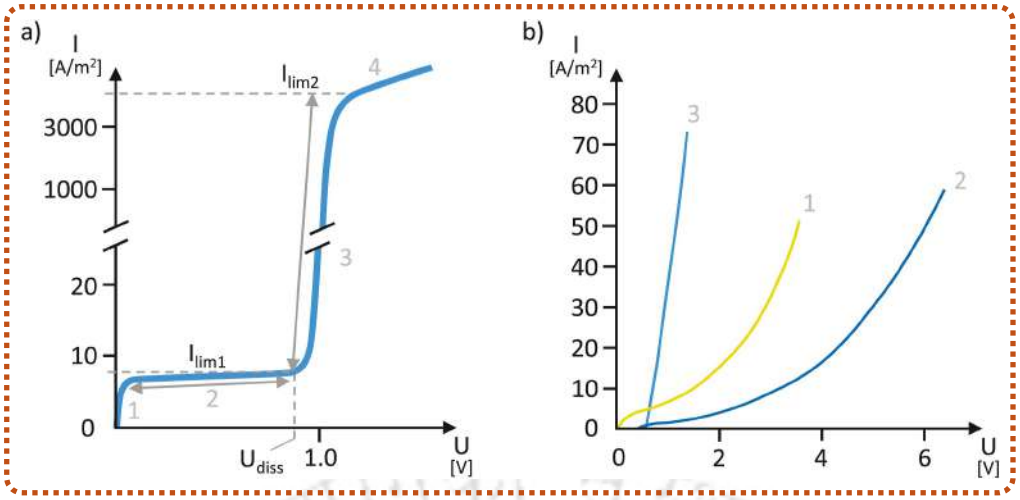

Figure 2.8. *(a) Schematic current-voltage curve of a BPM in a salt solution, and (b) Current-voltage characteristic of asymmetric bipolar membranes (ABPM) 1) in a 0.01 M NaCl solution, 2) in a 0.01 M NaOH | ABPM | 0.01 M HCl system, and 3) CVC of an ABPM with a water dissociation catalyst measured in the same acid-alkali system. (Ref. 23)*

The current–voltage behaviour of a bipolar membrane varies markedly when measured in a neutral salt electrolyte versus an acid–alkali configuration, where the cation-exchange layer faces an acidic solution and the anion-exchange layer contacts an alkaline solution (Figure 2.8b). In the acid–alkali arrangement, the CVC exhibits a pronounced deviation from zero potential even at low polarization currents (Figure 2.8b, curves 2 and 3). This shift originates from the Donnan potential established at the bipolar junction, typically around 0.83 V. A Donnan potential closer to its equilibrium value indicates enhanced interfacial catalytic activity, whereas larger deviations suggest diminished performance.

2.6.10. Chronopotentiometry:

Chronoamperometry (CA) is the preferred method for evaluating the long-term stability of electrodes in water electrolysis and CO_2 reduction. By maintaining a constant potential, CA allows researchers to monitor current density over time; a stable response indicates a durable electrocatalyst, whereas a decline suggests degradation or poisoning. In CO_2reduction, CA is vital for tracking Faradaic efficiency and ensuring consistent product selectivity over extended periods. This technique distinguishes between high-performing, robust materials and those that succumb to surface restructuring or activity loss in harsh electrochemical environments.[29,30]

Chronopotentiometry is also a powerful tool for probing the time-dependent behaviour of ion transport and coupled chemical processes within ion-exchange membranes (IEMs) and their adjacent diffusion layers. In this technique, the potential drop across the membrane assembly is monitored as a function of time while a constant current density is applied. When the applied current exceeds the limiting value, a distinct rise in the potential is observed at the transition time (τ). At this stage, the concentration of co-ions near the membrane becomes depleted, leading to a sharp increase in the membrane resistance and a corresponding jump in voltage. Simultaneously, the electric field at the bipolar junction intensifies, significantly accelerating water dissociation. As the dissociation rate grows to a level capable of sustaining the imposed current, the system gradually stabilizes and attains a steady-state potential profile.[23-27]

2.7. References:

1. S. Niu, S. Li, Y. Du, X. Han and P. Xu, *ACS Energy Lett.*, 2020, **5**, 1083.
2. A. M. Appel and M. L. Helm, *ACS Catal.*, 2014, **4**(2), 630.
3. Z. P. Ifkovits, J. M. Evans, M. C. Meier, K. M. Papadantonakis and N. S. Lewis, *Energy Environ. Sci.*, 2021, **14**, 4740.
4. O. van der Heijden, S. Park, R. E. Vos, J. J. J. Eggebeen and M. T. M. Koper, *ACS Energy Lett.*, 2024, **9**, 1871.
5. N. Kalita, U. Nath, A. Singha, M. Sarma and M. Qureshi, *J. Mater. Chem. A*, 2025, **13**, 10723.
6. S. S. Jeon, P. W. Kang, M. Klingenhof, H. Lee, F. Dionigi and P. Strasser, *ACS Catal.*, 2023, **13**, 1186.
7. N. Kalita, A. Sahu, S. Bhowmick and M. Qureshi, *Chem. Commun.*, 2022, **58**, 13747.
8. S. Anantharaj, P. E. Karthik and S. Noda, *Angew. Chem., Int. Ed.*, 2021, **60**, 23051.
9. D. Voiry, M. Chhowalla, Y. Gogotsi, N. A. Kotov, Y. Li, R. M. Penner, R. E. Schaak and P. S. Weiss, *ACS Nano*, 2018, **12**, 9635.
10. N. Dutta, D. Bagchi, G. Chawla and S. C. Peter, *ACS Energy Lett.*, 2024, **9**, 323.
11. P. A. Kempler and A. C. Nielander, *Nat. Commun.*, 2023, **14**, 1158.
12. A. C. Lazanas and M. I. Prodromidis, *ACS Meas. Sci. Au*, 2023, **3**(3), 162.
13. S. Anantharaj and S. Noda, *ChemElectroChem*, 2020, **7**, 2297.

14. A. Sanginario and S. Hernández, *Curr. Opin. Green Sustainable Chem.*, 2023, **39**, 100727.
15. Y. Lu, C. Zhao, J. Huang and Q. Zhang, *Joule* 2022, **6**, 1172.
16. C. Sheng, F. Yu, C. Li, H. Zhang, J. Huang, Y. Wu, M. Armand and Y. Chen, *J. Phys. Chem. Lett.* 2021, **12**, 2064.
17. S. Shit, W. Jang, S. Bolar, N. C. Murmu, H. Koo and T. Kuila, *ACS Appl. Mater. Interfaces*, 2019, **11**, 21634.
18. K. Gelderman, L. Lee and S. W. Donne, *J. Chem. Educ.*, 2007, **84**, 685.
19. H.S. Gugtapeh, A.H. Aghaii, and A. Simchi, *J. Chem. Educ.*, 2025, 102, 3567.
20. M. Krishnamachari, S. Lenus, K. Pradeeswari, R. Arun Pandian, M. Kumar and J.-H. Chang, *ACS Appl. Nano Mater.*, 2023, **6**, 16106.
21. Y. Tong, W. Liu, C. Li, X. Liu, J. Liu and X. Zhang, *Sustain. Energy Fuels*, 2023, **7**, 12.
22. B. Das, L. P. R. Pala, M. K. Mohanta, M. Devi, D. Chakraborty, N. R. Peela, M. Qureshi and S. S. Dhar, *J. Mater. Chem. A*, 2022, **10**, 23691.
23. R. Pärnamäe, S. Mareev, V. Nikonenko, S. Melnikov, N. Sheldeshov, V. Zabolotskii, H. Hamelers and M. Tedesco, *J. Membr. Sci.*, 2021, **617**, 118538.
24. V. I. Zabolotskii, N. V. Shel'deshov and N. P. Gnusin, *Russ. Chem. Rev.*, 1988, **57**, 801.
25. F. G. Wilhelm, N. F. A. Van Der Vegt, H. Strathmann and M. Wessling, *J. Appl. Electrochem*., 2022, **32**, 455.
26. R. Simons and G. Khanarian, *J. Membr. Biol.*, 1978, **38**, 11.
27. F. G. Wilhelm, I. Pünt, N. F. A. van der Vegt, H. Strathmann and M. Wessling, *Ind. Eng. Chem. Res.*, 2022, **41**, 579.
28. J. Balster, S. Srinkantharajah, R. Sumbharaju, I. Pünt, R. G. H. Lammertink, D. F. Stamatialis and M. Wessling, *J. Membr. Sci.*, 2010, **365**, 389.
29. P. J. Lingane, *Anal. Chem.*, 1964, **36**, 1723.
30. S. Anantharaj and S. Noda, *Energy Adv.*, 2022, **1**, 511.

CHAPTER 3

Synchronized Redox Pairs for Water Oxidation: Enhanced Electrocatalytic Activity Enabled by Identical Metal Centers across $CoMn_2O_4/CoMn(OH)_x$ Heterojunction Interfaces

This chapter focuses on the effect of two-step electrodeposition on the performance of the oxygen evolution reaction (OER). Here, $CoMn_2O_4$ and its chemical analogue $CoMn(OH)_x$ have been synthesized via a two-step electrodeposition method directly over Ni-foam. The resulting $CoMn_2O_4$ / $CoMn(OH)_x$ composite catalyst exhibits an excellent water oxidation overpotential of 260 mV at a current density of 10 mA/cm2 with a Tafel slope of 29 mV/dec along with a four-fold increase in turnover frequency. The enhanced efficacy of the composite catalyst is realized through the mechanism of synchronized redox pairs and superior carrier transport.

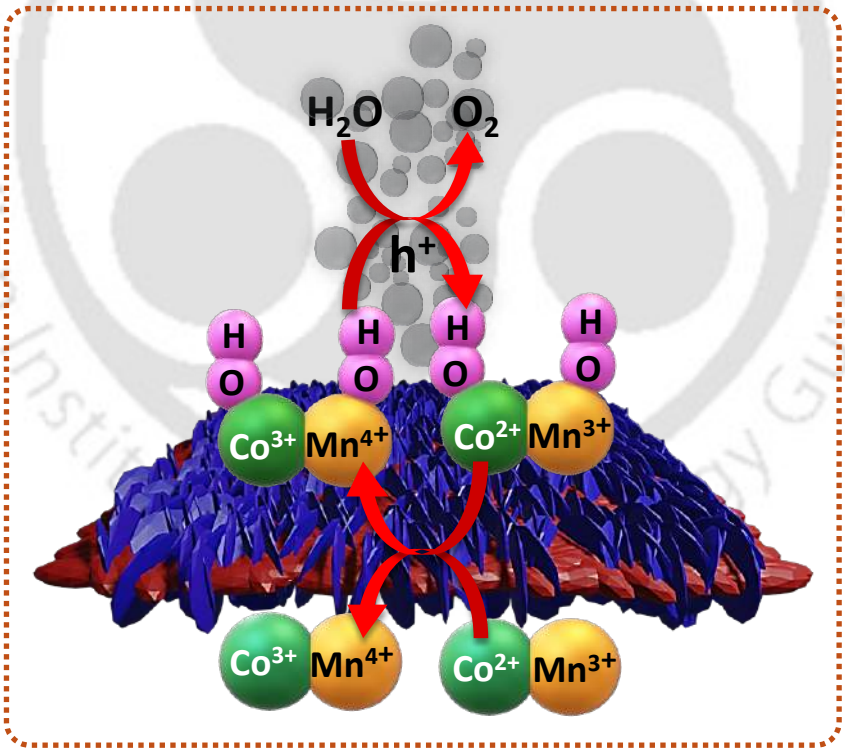

N. Kalita, et. al. *Chemical Communications*, 2022, 58, 13747-13750

3.1 Introduction:

The rising dependence on fossil fuels has intensified concerns over environmental pollution, thereby necessitating renewable, earth-abundant, and high-calorific alternatives.[1] Hydrogen, with its high energy density and clean combustion characteristics, is an attractive substitute for conventional fuels.[2] Among various H_2-generation pathways, electrocatalytic water splitting powered by renewable energy has emerged as a highly promising approach.[3,4] Its major limitation, however, lies in the substantial energy input required to overcome the high potential barrier of electrolysis.[5] Consequently, the development of efficient oxygen evolution reaction (OER) catalysts with high conductivity, long-term stability, and cost-effectiveness is essential.6 Although RuO_2 and IrO_2 exhibit exceptional OER activity in acidic media, their high cost and limited durability in alkaline conditions hinder large-scale application.[3,7] This has shifted attention toward affordable, non-noble transition-metal-based materials such as oxides,[6] phosphides,[8] sulfides,[9] nitrides,[10] carbides,[11] and hydroxides.[12] Their intrinsic performance, however, still requires improvement, prompting strategies such as elemental doping,[13–15] heterojunction engineering,[6,16] morphological control,[17–19] and the exploration of new catalytic systems.

Transition metals including **Ni**, **Co**, **Fe**, **Mn**, **W**, **Mo**, and **Cu** have attracted significant interest due to their favorable redox properties.[20–23] In particular, first-row transition metal oxides have been widely explored as OER electrocatalysts.[24–27] Spinel mixed-valence oxides—such as $FeCo_2O_4$, $NiCo_2O_4$, and $CoMn_2O_4$—exhibit promising activity because their multivalent states facilitate redox cycling, increase the electrochemically active surface area, and enhance structural robustness.[28–32] For example, Zu et al. achieved an overpotential of 337 mV at 10 mA cm^{-2} for $CoMn_2O_4$ grown on carbon hybrid nanofibers,[33] while Du et al. reduced this value to 310 mV using $CoMn_2O_4$/graphene nanodots.[34] Bahadur et al. further improved performance by sulfurizing $CoMn_2O_4$ micro-spikes, achieving an overpotential of 300 mV at 10 mA cm^{-2}.[19] Notably, no modification of $CoMn_2O_4$ has yet achieved overpotentials below 300 mV at 10 mA cm^{-2}. While cobalt exhibits benchmark catalytic activity for the oxygen evolution reaction, its commercial deployment is heavily restricted by elemental scarcity and supply chain vulnerabilities. To overcome these limitations, this study explores the development of bimetallic Co-based electrocatalysts utilizing cost-effective, earth-abundant

transition metals. This strategic integration serves to drastically reduce absolute cobalt loading without sacrificing the exceptional efficiency necessary for sustainable water electrolysis.

In this work, we introduce a simple two-step electrochemical deposition strategy to realize enhanced alkaline OER performance. A binary oxide, $CoMn_2O_4$ (CMO), is first synthesized and then coated with a mixed metal hydroxide layer, $CoMn(OH)_x$, to construct a Ni/CMO/CMOH composite electrode with improved charge-transfer characteristics. The rationale for incorporating $CoMn(OH)_x$ stems from its ability to promote faster electron transport during OER, where Mn and Co undergo the redox transitions $Mn^{3+} \leftrightarrow Mn^{4+}$ and $Co^{2+} \leftrightarrow Co^{3+}$, respectively. Because identical metal ions are present in both the oxide and hydroxide layers, these redox events occur within similar potential ranges, thereby lowering charge-transfer resistance and enabling more efficient electrocatalysis.

3.2. Experimental Section

3.2.1. Synthesis of $CoMn_2O_4$/$CoMn(OH)_2$ (CMO/CMOH):

Before electrodeposition, Ni foam was ultrasonically cleaned in concentrated HCl (36 wt%) for 5 min to remove surface NiO, followed by rinsing with deionized water and ethanol. For electrodeposition, 0.01 M $CoCl_2 \cdot 6H_2O$, 0.02 M $MnCl_2 \cdot 4H_2O$, and 0.1 M KCl (supporting electrolyte) were dissolved in 50 mL deionized water and stirred for 15 min at room temperature. The deposition was performed in a three-electrode configuration using pre-cleaned Ni foam (1 × 0.3 cm^2) as the working electrode, a Pt wire counter electrode, and an Ag/AgCl (saturated KCl) reference electrode. Potentiostatic electrodeposition was carried out at −1.1 V (vs. Ag/AgCl) for 10 s at 92 °C to obtain the initial $CoMn(OH)_x$ layer.

The as-deposited $CoMn(OH)_x$ was washed with deionized water and ethanol to remove residual impurities and dried at room temperature under vacuum. Calcination was then performed at 350 °C for 6 h with a ramp rate of 1 °C min^{-1}, yielding black, interconnected, thin-walled flake-like $CoMn_2O_4$ (CMO). To fabricate the CMOH/CMO/Ni-foam working electrode, an additional $CoMn(OH)_x$ layer (CMOH) was electrodeposited onto the preformed CMO using the same deposition protocol. The final mass loading of the catalysts was 355 µg cm^{-2} for bare CMO and 500 µg cm^{-2} for the CMO/CMOH composite.

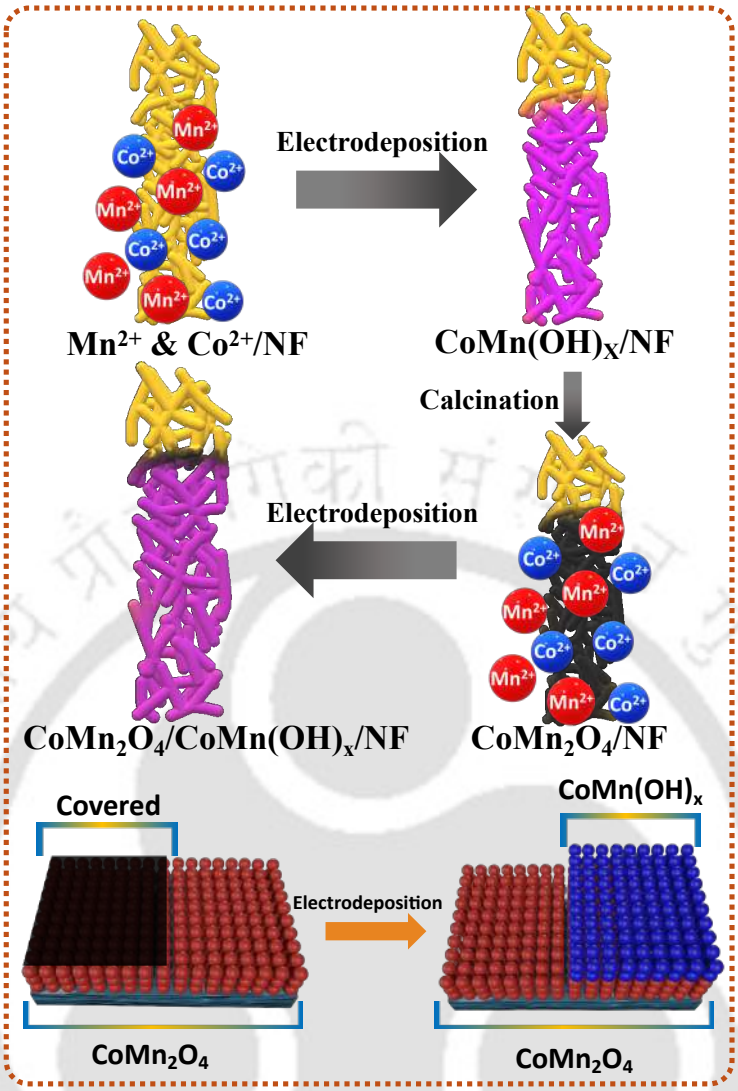

Figure 3.1. *Stepwise fabrication of the CMOH/CMO/Ni-foam working electrode via an electrodeposition protocol.*

3.3. Results and Discussions:

3.3.1. Phase and structure analysis:

Figure 3.2(a) shows the XRD patterns of the prepared catalyst over Ni-foam, *i.e.* both CMO and CMOH, where the peaks at (2θ) 31.94°, 36.04°, 36.90°, and 65.66° correspond to the (200), (211), (202), and (106) planes of CMO (ICSD no. 01-077-0471), respectively. For CMOH the observed peaks correspond to a mixed phase pattern, *i.e.*, the peaks at (2θ) 11.00°, 33.66°, and 59.00° correspond to the (003), (012), and (110) planes of α-$Co(OH)_2$ (ICSD no. 74-1057),

and the peaks at 18.80°, 36.65°, 38.11°, and 50.00° correspond to the (001), (101), (002), and (102) planes of $Mn(OH)_2$ (ICSD no. 00-008-0171).

The morphological characteristics of CMO, CMOH, and the CMO/CMOH composite on Ni-foam were examined using FESEM (Fig. 3.2 (d,e and f)). The SEM image of CMOH (Fig. 3.2 d) reveals a uniform, interconnected flake-like architecture, which is expected to enhance electrical conductivity and increase the density of accessible catalytic sites. Fig. 1e shows the surface morphology of CMO grown on Ni-foam. Structural verification of the CMO/CMOH composite was further supported by HRTEM (Fig. 3.2b). The lattice fringes displayed interplanar spacings of 0.25 nm for the (211) plane of CMO and 0.27 nm and 0.24 nm for the (012) and (002) planes of CMOH, respectively (Fig. 3.2c). Elemental mapping obtained from EDX (Fig. 3.2(f–i)) confirms a uniform distribution of all constituent elements within the composite.

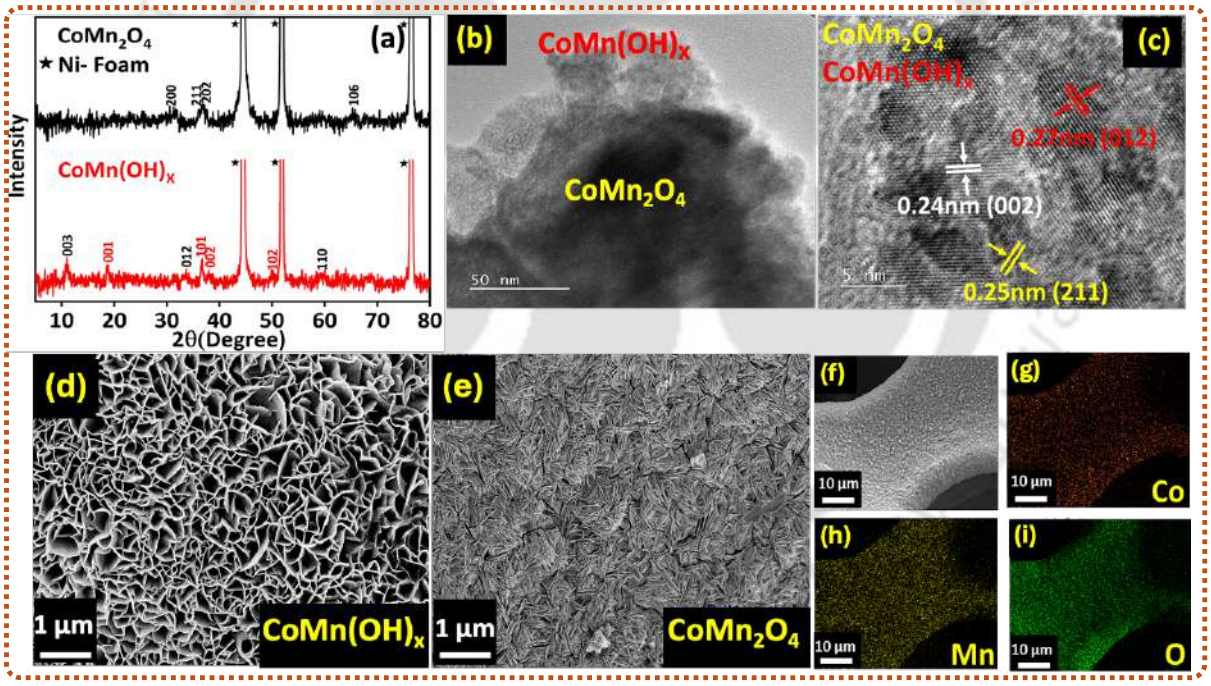

Figure 3.2. *(a) XRD patterns of $CoMn(OH)_x$ (CMOH) and $CoMn_2O_4$ (CMO) over Ni foam; (b) FESEM images of $CoMn(OH)_x$ (CMOH) and (c) $CoMn_2O_4$ (CMO) deposited over Ni-foam; (d) FETEM image of the composite CMO/CMOH; (e) HRTEM image of the composite CMO/CMOH ($CoMn_2O_4$ (yellow), $Co(OH)_2$ (red) and $Mn(OH)_2$ (white)); (f) FESEM image of CMO/CMOH; and (g–j) EDX elemental mapping of the CMO/CMOH composite, showing the homogeneous distribution of all elements.*

To confirm the formation of the overlayer in the composite, we have synthesized the bare CMO over Ni-foam as mentioned in the synthetic procedure, then intentionally covered half of the CMO with the CMOH overlayer so that we can observe the borderline between bare CMO and CMOH distinctively in the FESEM images. The images shown below (figure 3.3) show the two distinct layers of CMO and CMOH deposited over Ni-foam.

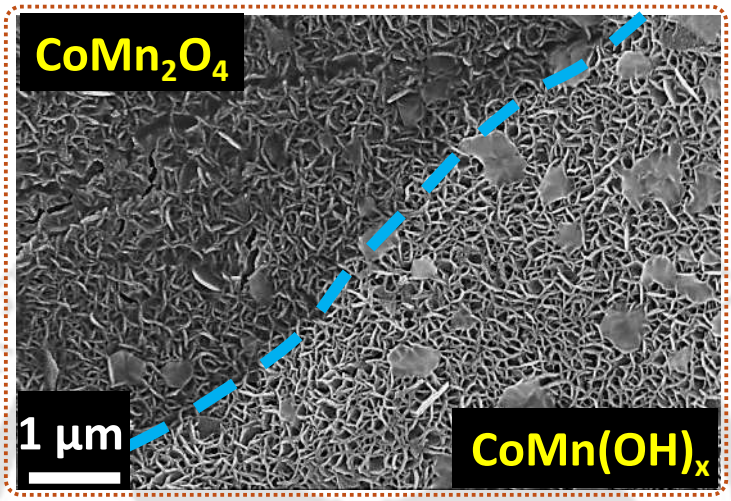

Figure 3.3. *FESEM images of the CMO/CMOH composite electrode illustrating the deliberate formation of a heterojunction. Bare CMO was first deposited on Ni foam, after which one half of the CMO surface was selectively coated with a CMOH overlayer. The micrographs clearly reveal a well-defined borderline between the uncovered CMO region and the CMOH-coated region, confirming the successful formation of two distinct layers (CMO and CMOH) on the Ni-foam substrate.*

Raman spectroscopy was performed to understand the electronic interactions among the components, as shown in the figure above instance peak at 620 cm-1 corresponds to E_g vibrational mode of $CoMn_2O_4$. After the formation of the composite, the shift toward higher frequency represents the successful formation of the heterostructure. Additional peaks at 175cm^{-1} and 305cm^{-1} were observed, which corresponds to the vibrational mode from $CoMn(OH)_x$ layer.

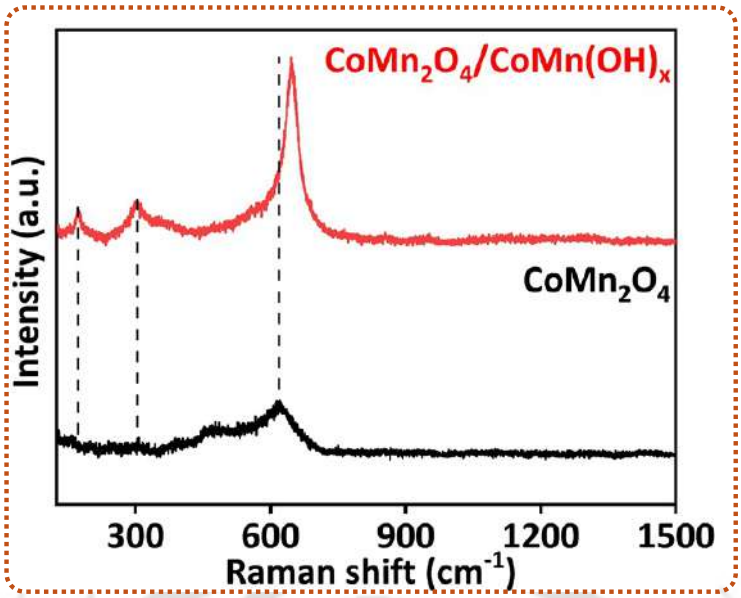

Figure 3.4. *Raman spectra of the $CoMn_2O_4$/$CoMn(OH)_x$ heterostructure. The blue shift of the $CoMn_2O_4$ E_g mode (620 cm^{-1}) confirms electronic coupling within the composite. Peaks at 175 and 305 cm^{-1} correspond to $CoMn(OH)_x$ vibrational modes, verifying successful heterostructure formation.*

FTIR spectra displayed absorption bands around 3700 -2690 and 1635 cm-1, attributed to the stretching vibrations of -OH and the bending vibrations of H-O-H from water molecules on the surface and this is consistent with the published data.1 Importantly, the characteristic peak above 551.49 cm^{-1} and at 1108.82 cm^{-1} confirm the spinel structure of the product.

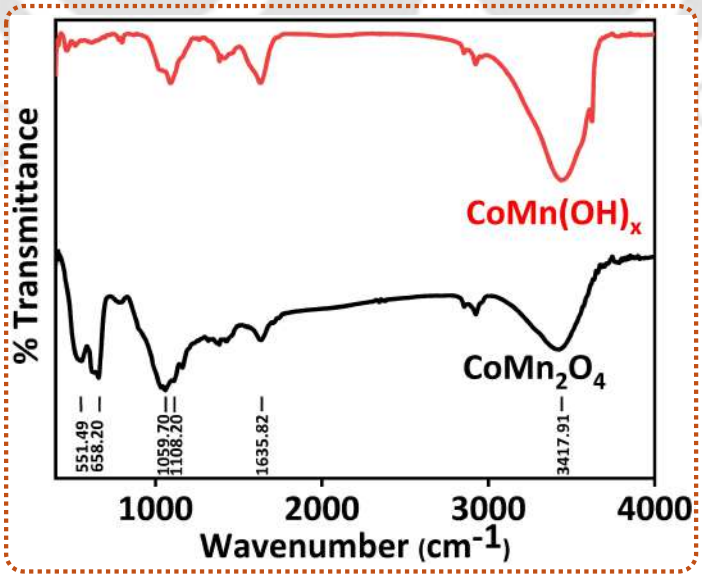

Figure 3.5. *FTIR spectra of synthesized $CoMn_2O_4$ and $CoMn(OH)_x$, displaying -OH/H-O-H bands at 3700–2690 and 1635 cm^{-1} (adsorbed water) and spinel $CoMn_2O_4$ peaks above 551 and at 1108 cm^{-1}.*

XPS analysis was conducted to examine the surface composition and electronic structure of CMO, CMOH, and the CMO/CMOH composite. The survey spectrum (Fig. 3.6d) confirms the presence of all constituent elements in the composite. Mn 2p and Co 2p spectra (Fig. 3.6a,b) show that bare CMO exhibits Mn $2p_{3}/_{2}$ peaks at 641.57/643.02 eV and Mn $2p_{1}/_{2}$ at 653.38/654.11 eV, while Co $2p_{3}/_{2}$ appears at 780.19/781.81 eV and Co $2p_{1}/_{2}$ at 795.20/796.77 eV, along with satellite features at 645.20, 786.40, and 803.08 eV.

In the CMO/CMOH composite, Mn $2p_{3}/_{2}$ shifts to 642.33/643.53 eV and Mn $2p_{1}/_{2}$ to 654.18/654.46 eV; Co $2p_{3}/_{2}$ shifts to 780.89/782.68 eV and Co $2p_{1}/_{2}$ to 795.89/797.55 eV, with satellites at 646.88, 786.25, and 802.98 eV. These systematic shifts toward higher binding energies indicate strong electronic interaction between CMO and CMOH and reduced surface electron density, consistent with improved OER activity. The O 1s spectra (Fig. 3.6c) show lattice oxygen, hydroxyl species, and adsorbed oxygen at 530.70, 531.01, and 531.82 eV in the composite. Bare CMO exhibits O_L, M–O–H, and O_V at 529.79, 530.71, and 531.62 eV, while CMOH shows O_L, M–O–H, and O_{ads} at 529.92, 531.22, and 532.01 eV, respectively.

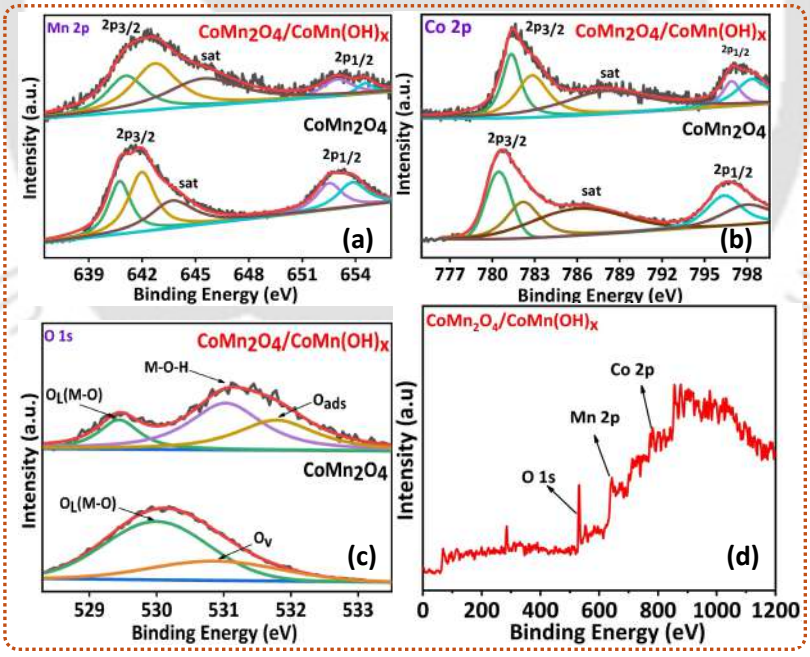

Figure 3.6. *XPS core level spectra, (a) Mn 2p and (b) Co 2p of bare CMOH, CMO, and CMO/CMOH composite (c) O 1s of CMOH, CMO, and CMO/CMOH (d) XPS survey spectra of CMO/CMOH*

3.3.2. Electrochemical analysis:

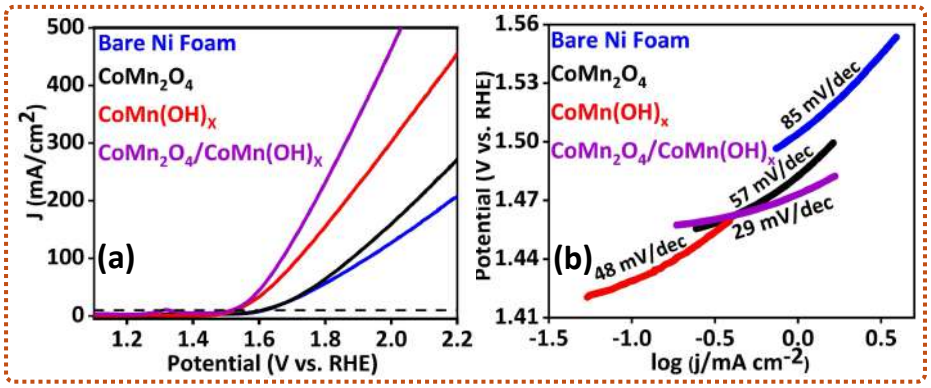

Figure 3.7. *(a) LSV curves of bare Ni-foam, CMO, CMOH, and CMO/CMOH recorded in 1 M KOH at 5 mV s^{-1}, showing the lowest overpotential for the CMO/CMOH composite at 10 mA cm^{-2}. (b) Corresponding Tafel plots, highlighting the reduced Tafel slope of the composite, indicative of faster OER kinetics.*

Linear sweep voltammetry (LSV) was performed in 1 M KOH at a scan rate of 5 mV s^{-1} using a three-electrode configuration with a graphite counter electrode and Hg/HgO reference. The CMO/CMOH composite exhibits the lowest overpotential, requiring only 260 mV to reach 10 mA cm^{-2} (Fig. 3.7a), outperforming bare CMO (360 mV) and CMOH (290 mV). Tafel analysis (figure 3.7b) further confirms improved kinetics: the composite shows a Tafel slope of 29 mV dec^{-1}, significantly lower than those of CMO (57 mV dec^{-1}) and CMOH (48 mV dec^{-1}), indicating faster OER reaction kinetics and enhanced catalytic efficiency.

The improved activity of the CMO/CMOH composite is further clarified by evaluating its electrochemical surface area (ECSA), which reflects the number of accessible catalytic sites. ECSA was estimated from the double-layer capacitance (C_{dl}), obtained through cyclic voltammetry performed in the non-Faradaic potential window (−0.08 to 0.04 V vs. Hg/HgO) at scan rates of 1–10 mV s^{-1} (Figure 3.5). C_{dl} was determined from the slope of the plot of Δj ($j_{anodic} - j_{cathodic}$ at 0.95 V vs. RHE) versus scan rate, where C_{dl} equals half the slope. ECSA was then calculated using:

$$ECSA = C_{dl} / C_s \quad (3.1)$$

where C_s is the specific capacitance of the material. Although C_s cannot be precisely determined without an atomically smooth planar surface, its value in alkaline media typically lies between 0.022 and 0.130 mF cm^{-2}, with an average of 0.040 mF cm^{-2} commonly used.

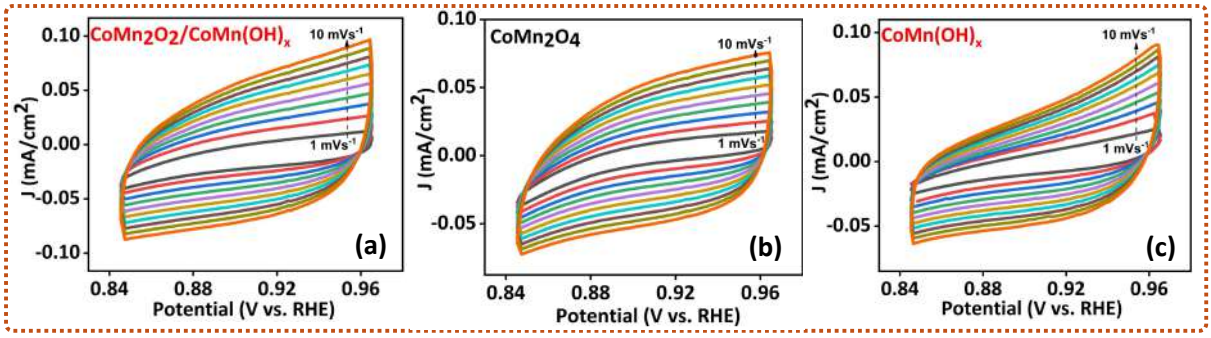

Figure 3.8. *Cyclic voltammetry plots at different scan rates under alkaline conditions in a three-electrode electrochemical cell in a non-faradaic region of the respective catalysts (a) Bare CMO, (b) MCO/CMOH composite.*

From these measurements (Fig. 3.9(a), the composite shows a C_{dl} of 13 mF cm^{-2} (ECSA ≈ 325 cm^2), exceeding that of CMO (7 mF cm^{-2}; ECSA ≈ 175 cm^2) and CMOH (9 mF cm^{-2}; ECSA ≈ 225 cm^2), confirming significantly greater exposure of active sites.[35] Electrochemical impedance spectroscopy further reveals enhanced charge-transfer characteristics for the composite.[36,37] The Nyquist plot (Fig. 3.9(b)) shows the lowest R_{ct} (7.15 Ω) for CMO/CMOH, compared with bare CMO (37.71 Ω) and CMOH (15.45 Ω), demonstrating faster electron transfer and superior OER kinetics.

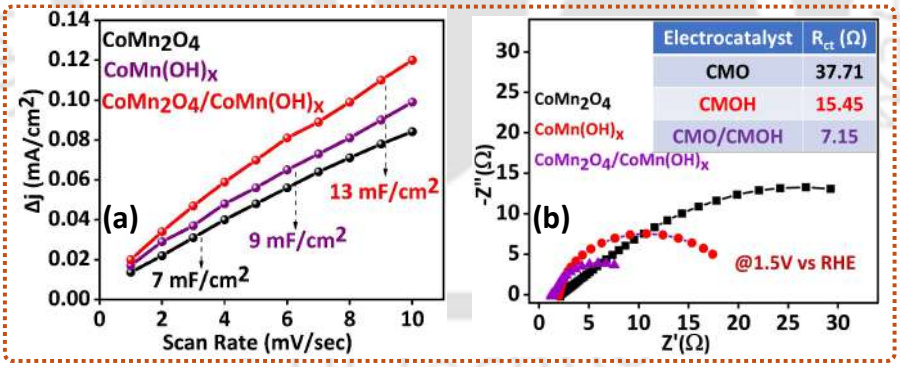

Figure 3.9. *(a) Double-layer capacitance (C_{dl}) plots derived from CV measurements, comparing bare CMO, CMOH, and the CMO/CMOH composite, where the composite exhibits a higher C_{dl}, indicating a larger electrochemically active surface area. (b) Nyquist plots obtained from EIS measurements, showing a significantly reduced charge-transfer resistance (R_{ct}) for the CMO/CMOH composite relative to bare CMO and CMOH, reflecting improved charge transport and OER kinetics.*

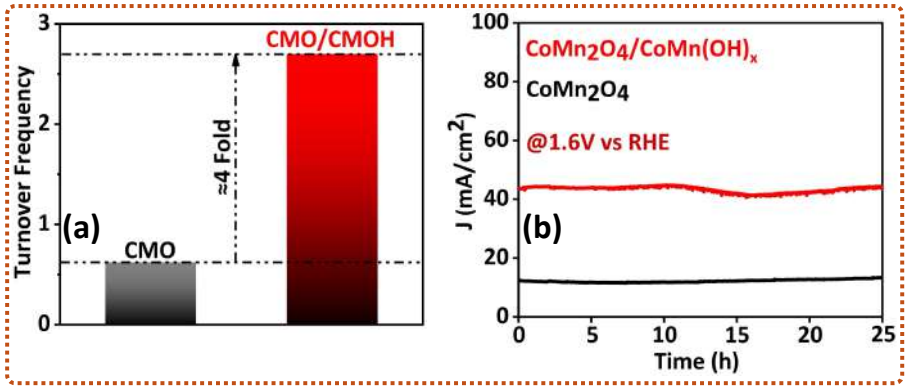

Figure 3.10. *(a) Turnover frequency (TOF) of bare CMO and the CMO/CMOH composite calculated at 0.95 V vs. RHE, highlighting the significantly enhanced intrinsic catalytic activity of the composite. (b) Chronoamperometric stability test of CMO and CMO/CMOH recorded at a constant potential of 1.6 V vs. RHE, demonstrating the higher and sustained current density of the composite during prolonged OER operation.*

The intrinsic catalytic activity was further quantified by calculating the turnover frequency (TOF) at 0.95 V vs. RHE. The CMO/CMOH composite exhibits a TOF of 2.7 s^{-1}, markedly higher than that of bare CMO (0.65 s^{-1}) (Fig. 3.10a), corresponding to an approximately fourfold enhancement.[38] This improvement reflects accelerated surface reaction kinetics, consistent with the increased ECSA and reduced charge-transfer resistance observed for the composite.

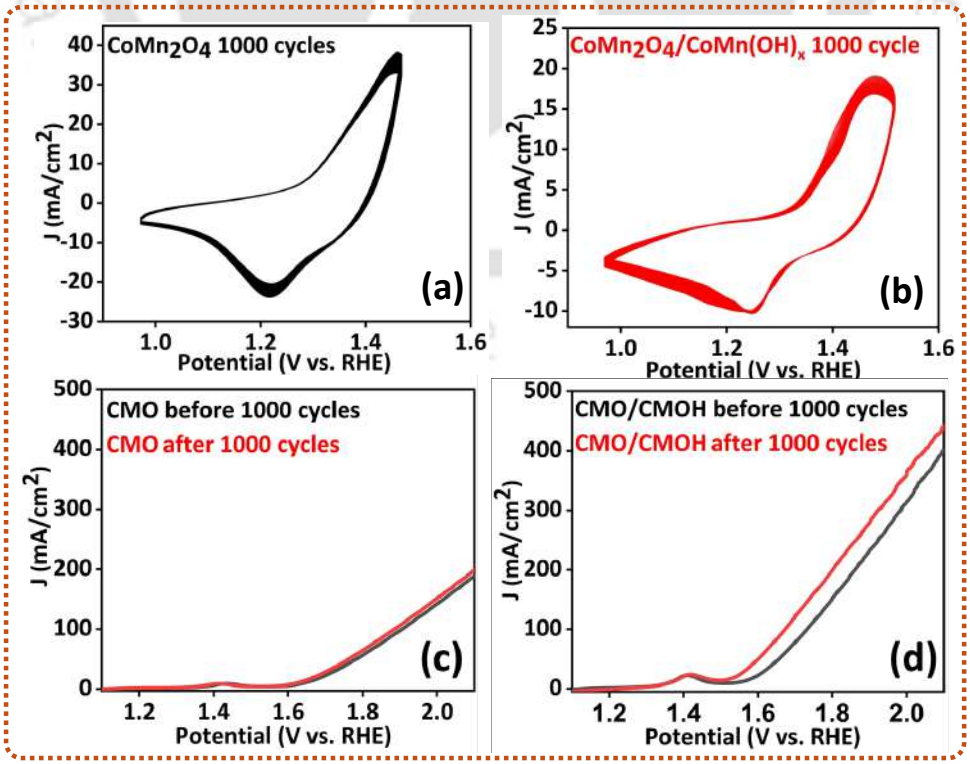

Figure 3.11: *To check the stability of the $CoMn_2O_4/CoMn(OH)_x$ catalyst and its bare counterpart. (a, b) 1000 cycles of cyclic voltammetry of $CoMn_2O_4$ and $CoMn_2O_4/CoMn(OH)_x$ respectively at the scene rate of 10 mV/sec in the region 0.90V to 1.50V vs RHE, (c, d) Current density of the S11 bare $CoMn_2O_4$ and $CoMn_2O_4/CoMn(OH)_x$ composite measured before and after the long term stability test that shows no such decrease in current density confirming the stability of both the electrodes.*

The operational stability of the catalysts was evaluated by chronoamperometric measurements at a constant potential of 1.6 V vs. RHE. Under these conditions, bare CMO delivered a steady current density of ~10 mA cm^{-2}, whereas the CMO/CMOH composite sustained a significantly higher current density of ~40 mA cm^{-2} (Fig. 3.10b). Notably, the composite maintained stable performance over 25 h of continuous operation, demonstrating excellent long-term durability for OER.

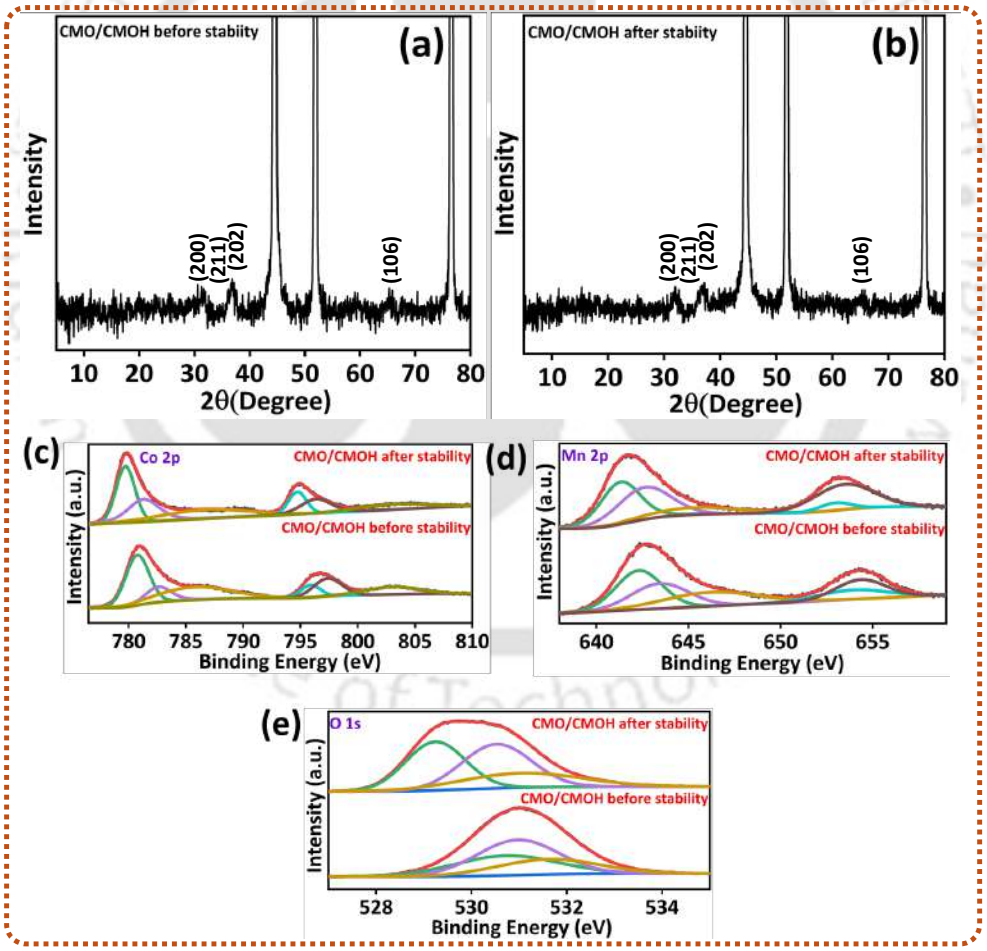

Figure 3.12: *(a,b) XRD pattern for CMO/CMOH before and after stability; (c,d,e) X-ray photoelectron spectroscopy data for Co 2p, Mn 2p and O1s before and after the stability test*

Further cyclic voltammogram in figure 3.11 (a, b) shows stability test till 1000 cycles of CV measurement for CMO and CMO/CMOH respectively, at the scan rate of 10 mV/sec in the region (0.90 – 1.50 V vs RHE). Figure 3.11 (c, d) shows the current density of the CMO/CMOH composite, and the bare CMO measured before and after 1000 cycles of CV displays an insignificant change in current density, confirming the stability of both electrodes. To evaluate the structural and chemical robustness of the electrocatalyst, we performed comprehensive post-electrocatalytic characterization using both X-ray diffraction (XRD) and X-ray photoelectron spectroscopy (XPS). The XRD patterns of the composite material remained unchanged following the stability tests, with no evidence of secondary phases or crystallinity loss, confirming that the bulk phase purity remained intact. Complementing this, XPS analysis revealed that the oxidation states and surface elemental composition were preserved, showing no significant binding energy shifts or surface leaching after prolonged operation. Together, these results provide definitive evidence of the catalyst's exceptional structural and chemical stability under rigorous electrochemical conditions.

3.3.3. Mechanism:

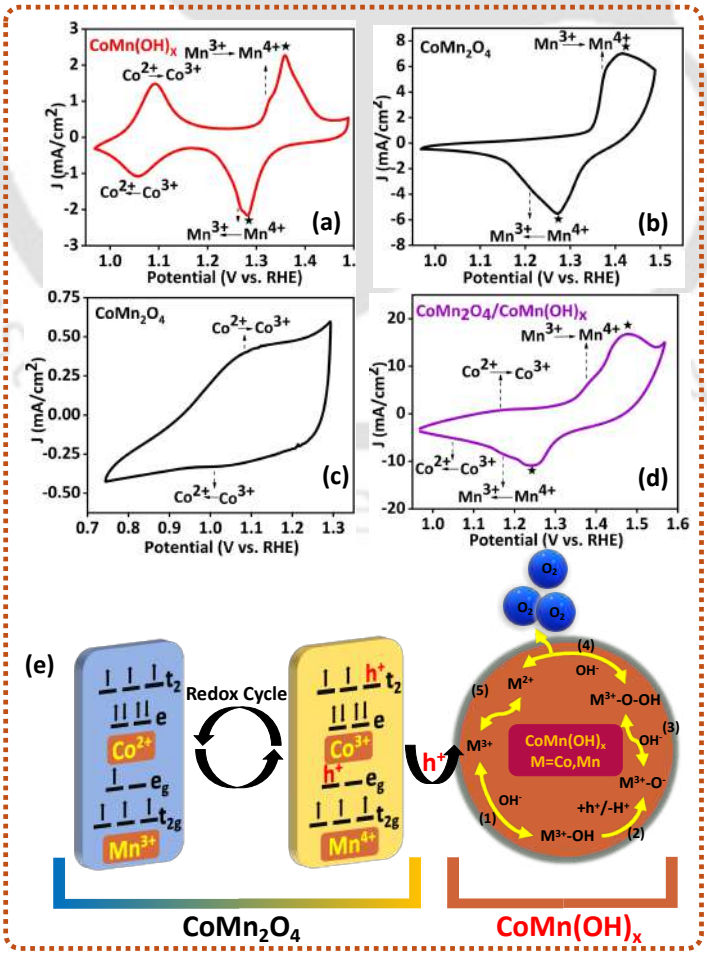

Figure 3.13. *Cyclic voltammograms showing the ($Co^{2+}/Mn^{3+} \leftrightarrow Co^{3+}/Mn^{4+}$) redox cycle in (a) bare CMOH, (b and c) bare CMO, and (d) the CMO/CMOH composite (* for the NF substrate); and (e) the mechanistic pathway of the CMO/CMOH composite through different redox cycles for an efficient oxygen evolution reaction.*

Table 3.1. *OER activity comparison with previously reported $CoMn_2O_4$-based electrocatalysts.*

Electrocatalyst	Synthesis route	Electrolyte concentration (KOH)	Potential (mV @ 10 mA cm^{-2} vs RHE)	Tafel slope (mV dec^{-1})	Ref.
$CoMn_2O_4$/$CoMn(OH)_x$	Electrodeposition	1 M	260	29	This work
10S-$CoMn_2O_4$/FTO	Electrodeposition	0.1 M	300	26.28	19
$CoMn_2O_4$ nanodots/rGO	Hot injection & heating-up method	0.1 M	310	56	34
Mn_3O_4@$CoMn_2O_4$–Co_xO_y	One-pot two-step method	0.1 M	310	81	40
$Mn_xCo_{3-x}O_4$ spinel oxides	Sol–gel method	1 M	327	79	41
$CoMn_2O_4$/N-doped porous carbon	Solvothermal	0.1 M	570	Not mentioned	42

The cyclic voltammetry (CV) responses shown in Fig. 3.13(a–d) reveal the presence of multiple redox-active centers, corresponding to the reversible Mn^{3+}/Mn^{4+} and Co^{2+}/Co^{3+} couples. Based on the electrochemical analysis and XPS data a plausible reaction mechanism is illustrated in Fig. 3.13(e), highlighting the synergistic role of $CoMn_2O_4$ (CMO) and its hydroxide analogue, $CoMn(OH)_x$ (CMOH). Upon application of an external potential, charge carriers are generated, wherein electrons are transported to the Ni-foam current collector, while holes participate in the oxidation of Co^{2+} to Co^{3+} and Mn^{3+} to Mn^{4+} within the CMO lattice.[39] The surface CMOH overlayer functions as an efficient co-catalyst by enabling a synchronized redox interplay between CMO and CMOH. Specifically, CMOH facilitates water oxidation by rapidly scavenging the electrogenerated holes accumulated at the electrode

surface through concurrent oxidation of low-valent Co and Mn species to higher valence states (M^{3+}/M^{4+}). These high-valent metal centers serve as the active sites for oxygen evolution and are subsequently reduced back to lower oxidation states upon completion of the catalytic cycle. Such a dynamic redox synchronization accelerates interfacial hole extraction, suppresses surface charge recombination, and thereby enhances oxygen evolution reaction kinetics. Consistent with this mechanistic interpretation, electrochemical impedance spectroscopy (EIS) measurements confirm that the CMO/CMOH composite exhibits the lowest charge-transfer resistance (R_{ct}), indicative of improved interfacial charge-transport properties.

3.4. Conclusions:

In summary, the work demonstrates a synchronized metal oxide/hydroxide composite for enhanced OER performance. The significant improvement in the composite performance can be attributed to the efficient hole extraction behavior of the $CoMn(OH)_x$ overlayer from the $CoMn_2O_4$ surface that has accumulated over time, which proceeds the oxygen evolution process with better kinetics. High stability, low cost, easy synthetic procedure, and environmentally friendly nature due to the use of a minimal number of metal atoms make this composite a model system for future catalytic systems to be used in industrial applications.

While the development of this synchronized composite successfully addresses the kinetic bottlenecks associated with the anodic oxygen evolution reaction, practical water electrolysis also necessitates a highly efficient cathodic hydrogen evolution reaction (HER). Typically, employing disparate catalysts for these two half-reactions increases system complexity, integration challenges, and overall cost. Therefore, building upon the interfacial engineering strategies and mechanistic insights established in this study, the subsequent chapter explores the design of a singular, bifunctional electrocatalyst. By optimizing a single electrode system to simultaneously drive both OER and HER within a shared environment

3.5 References:

1. D. Li, H. Baydoun, C. Verani, S. Brock, *J. Am. Chem. Soc.,* 2016, **138**, 4006-4009.
2. X. Zhang, Y. Zhau, Y. Zhau, R. Shi, G. Waterhouse, T. Zhang, Adv. Energy Mater, 2019, **9**, 1900881.
3. J. Yu, Q. He, G. Yang, W. Jhou, Z. Shao, M. Ni, *ACS Catal.,* 2019, **9**, 9973-10011.
4. B. You and Y. Sun, *Acc. Chem. Res.*, 2018, **51**, 1571–1580.
5. X. Xiao, D. Huang, Y. Fu, M. Wen, X. Jiang, X. Lv, M. Li, L. Gao, S. Liu, M. Wang, C. Zhao and Y. Shen, *ACS Appl. Mater. Interfaces*, 2018, **10**, 4689–4696.
6. C. Zhu, A. L. Wang, W. Xiao, D. Chao, X. Zhang, N. H. Tiep, S. Chen, J. Kang, X. Wang, J. Ding, J. Wang, H. Zhang and H. J. Fan, *Adv. Mate.*, 2018, **30**, 1705516.
7. X. Gao, J. Chen, X. Sun, B. Wu, B. Li, Z. Ning, J. Li and N. Wang, *ACS Appl. Nano Mater.*, 2020, **3**, 12269–12277.
8. Y. Shi and B. Zhang, *Chem. Soc. Rev.*, 2016, **45**, 1529–1541.
9. Q. Lu, Y. Yu, Q. Ma, B. Chen and H. Zhang, *Adv. Mate.*, 2016, **28**, 1917–1933.
10. S. Dong, X. Chen, X. Zhang and G. Cui, *Coord. Chem. Rev.*, 2013, **257**, 1946–1956.
11. Y. Zhong, X. H. Xia, F. Shi, J. Y. Zhan, J. P. Tu and H. J. Fan, *Adv. Sci.*, 2016, **3**, 1500286.
12. T. Tang, W. Jiang, S. Niu, N. Liu, H. Luo, Q. Zhang, W. Wen, Y. Chen, L. Huang, F. Gao, J. Hu. Adv. *Funct. Mater.*, 2018, **28**, 1704594.
13. P. Zhou, X. Lv, D. Xing, F. Ma, Y. Liu, Z. Wang, P. Wang, Z. Zheng, Y. Dai and B. Huang, *Appl. Catal. B*, 2020, **263**, 118330.
14. H. Su, S. Song, S. Li, Y. Gao, L. Ge, W. Song, T. Ma and J. Liu, *Appl. Catal. B*, 2021, **293**, 120225.
15. Y. Yan, J. Lin, J. Cao, S. Guo, X. Zheng, J. Feng and J. Qi, *J. Mater. Chem. A*, 2019, **7**, 24486–24492.
16. Z. Li, M. Hu, P. Wang, J. Liu, J. Yao and C. Li, *Coord. Chem. Rev.*, 2021, **439**, 213953.
17. J. Joo, T. Kim, J. Lee, S. Choi, K. Lee, *Adv. Mater.*, 2019, **31**, 1806682.
18. C. Hu, Y. Hu, A. Zhu, M. Li, J. Wei, Y. Zhang and W. Xie, *Chemistry - A European Journal*, 2022, **28**, e202200138.
19. A. Bahadur, W. Hussain, S. Iqbal, F. Ullah, M. Shoaib, G. Liu and K. Feng, *J. Mater. Chem. A*, 2021, **9**, 12255–12264.
20. Y. Ding, H. Li and Y. Hou, *Int. J. Hydrogen Energy*, 2018, **43**, 19002–19009.

21. C. Qiang, L. Zhang, H. He, Y. Liu, Y. Zhao, T. Sheng, S. Liu, X. Wu and Z. Fang, *J. Colloid Interface Sci.*, 2021, **604**, 650–659.
22. G. Ou, P. Fan, H. Zhang, K. Huang, C. Yang, W. Yu, H. Wei, M. Zhong, H. Wu and Y. Li, *Nano Energy*, 2017, **35**, 207–214.
23. M. Wang, L. Zhang, M. Huang, Q. Zhang, X. Zhao, Y. He, S. Lin, J. Pan and H. Zhu, *J. Mater. Chem. A*, 2019, **7**, 22405–22411.
24. J. Wang, W. Cui, Q. Liu, Z. Xing, A. M. Asiri and X. Sun, *Adv. Mater.*, 2016, **28**, 215–230.
25. D. Wang and D. Astruc, *Chem. Soc. Rev*, 2017, **46**, 816–854.
26. T. N. Huan, G. Rousse, S. Zanna, I. T. Lucas, X. Xu, N. Menguy, V. Mougel and M. Fontecave, *Angew. Chem.*, 2017, **129**, 4870–4874.
27. R. Elakkiya, R. Ramkumar and G. Maduraiveeran, *Mater. Res. Bull.*, 2019, **116**, 98–105.
28. P. Moni, S. Hyun, A. Vignesh and S. Shanmugam, *Chem. Commun.*, 2017, **53**, 7836–7839.
29. B. Zhu, S. Tang, S. Vongehr, H. Xie, J. Zhu and X. Meng, *Chem. Commun.*, 2016, **52**, 2624–2627.
30. W. Sun, Y. Wang, H. Wu, Z. Wang, D. Rooney and K. Sun, *Chem. Commun.*, 2017, **53**, 8711–8714.
31. G. Janani. S. Subramani, H. Choi, M. Han, U. Sim, *Small*, 2021, **17**, 2103613.
32. J. Lee, N. Son, N. K. Park, H. J. Ryu, J. I. Baek, Y. Sohn, J. Y. Do and M. Kang, *Electrochim. Acta*, 2021, **379**, 138168.
33. H. Zhu, D. Yu, S. Zhang, J. Chen, W. Wu, M. Wan, L. Wang, M. Zhang and M. Du, *Small*, 2017, **13**, 1700468.
34. J. Du, C. Chen, F. Cheng and J. Chen, *Inorg. Chem.*, 2015, **54**, 5467–5474.
35. S. Hao, L. Chen, C. Yu, B. Yang, Z. Li, Y. Hou, L. Lei and X. Zhang, *ACS Energy Lett*, 2019, **4**, 952–959.
36. Y. Li, L. Zhang, X. Xiang, D. Yan and F. Li, *J. Mater. Chem. A*, 2014, **2**, 13250–13258.
37. J. Li, Y. Wang, T. Zhou, H. Zhang, X. Sun, J. Tang, L. Zhang, A. Al-Enizi, Z. Yang, G. Zheng, *J. Am. Chem. Soc.*, 2015, **137**, 14305-14312.
38. A. K. Shah, S. Bhowmick, D. Gogoi, N. R. Peela and M. Qureshi, *Chem. Commun.*, 2021, **57**, 8027–8030.

39. S. Bai, H. Chu, X. Xiang, R. Luo, J. He and A. Chen, *Chemical Engineering Journal*, 2018, **350**, 148–156.
40. Z. Luo, E. Irtem, M. Ibánez, R. Nafria, S. MartÍ-Sánchez, A. Genç, M. de La Mata, Y. Liu, D. Cadavid, J. Llorca, J. Arbiol, T. Andreu, J. R. Morante and A. Cabot, *ACS Appl. Mater. Interfaces*, 2016, **8**, 17435.
41. K. Lankauf, K. Cysewska, J. Karczewski, A. Mielewczyk-Gryń, K. Górnicka, G. Cempura, M. Chen, P. Jasiński and S. Molin, *Int. J. Hydrogen Energy*, 2020, **45**, 14867.
42. J. L. Digol, M. F. M. Labata, M. F. Divinagracia and J. D. Ocon, *ECS Trans*, 2017, **77**, 525.

CHAPTER 4

p–n Heterojunction Engineering for Overall Water Electrolysis: Band Gap Modulation via Selenium Doping to Enhance Charge Separation and Catalytic Efficiency at the CuO/Se@WO_3 heterojunction

This chapter focuses on electronic structure tuning and interfacial engineering of a CuO/Se@WO_3/$Cu(OH)_2$ catalyst fabricated on Ni foam via sequential electrodeposition for efficient overall water splitting. Se-doped WO_3 coupled with dendritic CuO forms a p–n heterojunction with optimized band alignment, enabling a Z-scheme charge-transfer pathway and suppressed electron–hole recombination, while the $Cu(OH)_2$ layer acts as an effective hole extractor. Consequently, the catalyst achieves overpotentials of 202 mV (OER) and 55 mV (HER) at 10 mA cm^{-2} with Tafel slopes of 35 and 45 mV dec^{-1}, outperforming RuO_2 and comparable to Pt/C. DFT and DRT analyses confirm increased electron density at W sites, reduced band gap, favorable hydrogen adsorption (ΔG_{H^*} = −0.17 eV), and accelerated interfacial charge-transfer and diffusion kinetics, establishing this system as a low-cost, high-performance catalyst for sustainable water splitting.

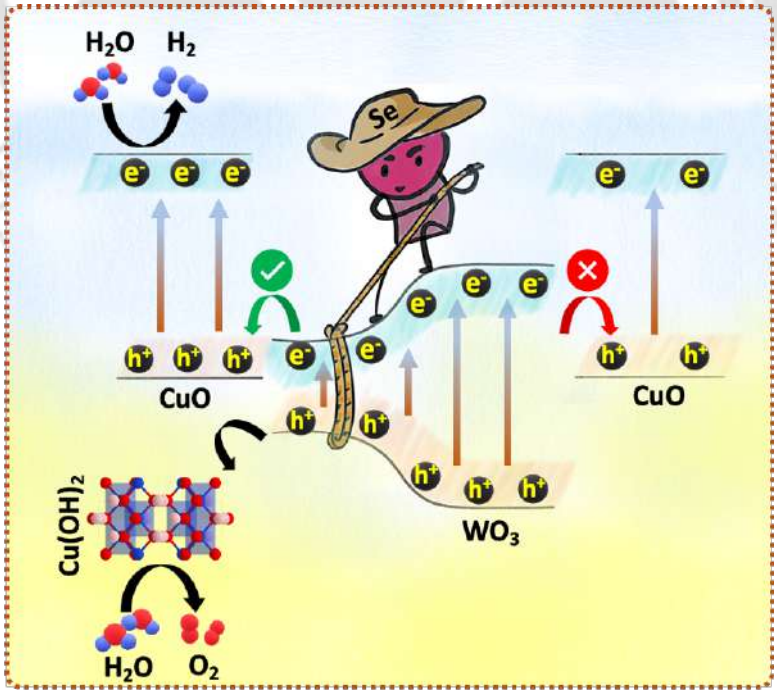

N. Kallita, et. al. *Journal of Materials Chemistry A*, 2025, 13, 10723-10735

4.1. Introduction:

Electrocatalytic water splitting is widely recognized as an efficient strategy for converting renewable energy into clean hydrogen fuel, where hydrogen evolution (HER) occurs at the cathode and oxygen evolution (OER) at the anode of a water electrolyzer[1]. However, the fundamentally different reaction mechanisms of HER and OER make it challenging to employ a single catalyst for both processes, as materials optimized for one reaction typically perform poorly for the other. State-of-the-art systems rely on Pt-based catalysts for HER and IrO_2/RuO_2 for OER[2], but the scarcity, high cost, and the need for separate cathodic and anodic materials increase fabrication complexity, cost, and the risk of cross-contamination. Consequently, the development of earth-abundant, bifunctional electrocatalysts capable of driving overall water splitting is highly desirable. In this context, first-row transition metals such as **Ni**[3], **Fe**[4], and **Co**[5]- mainly in the form of hydroxides[6], oxides[7], sulfides[8], chalcogenides[9], and phosphides[10]—have attracted significant attention, with performance enhancement achieved through doping, heterojunction formation, surface engineering, and nanostructuring[1].

Incorporation of electronegative chalcogens or pnictogens (X = **N**, **P**, **S**, **Se**) into transition-metal frameworks induces localized negative charge density within M–X surface motifs, enhancing H^+ adsorption in acidic media or H_2O activation in alkaline conditions[11]. Simultaneously, electronic structure modulation weakens the M–H bond, reducing HER energy barriers. However, OER in such materials typically proceeds via high-valence metal species formed under anodic polarization, which often leads to oxidative corrosion and structural instability[12,13]. Similarly, HER activity degrades due to corrosion-induced compositional and structural changes. These challenges are exacerbated under intermittent renewable energy operation, where frequent power interruptions induce depolarization and reverse currents, accelerating electrode degradation[2].

Thus, the development of low-cost, durable bifunctional catalysts with intrinsic active sites remains critical, particularly for stable operation under fluctuating power inputs. Although extensive efforts have focused on compositional and structural tuning, electronic band-gap and band-position engineering at electrocatalytic heterojunctions remains relatively unexplored[14,15]. In contrast, band-gap engineering is well established in photocatalysis,

though many classical photoactive oxides and sulfides—such as TiO_2[16], WO_3[17], ZnO[18], SnO_2[19], CeO_2[20], $BiVO_4$[21], CdS[22], ZnS[23], and MoS_2[24]- exhibit limited electrocatalytic activity.

Only a few studies have demonstrated the benefits of band-position tuning in electrocatalysis. Zeng et al.[14] reported enhanced OER activity via band alignment in a MnCo–CH@NiFe–OH p–n junction, achieving up to 10-fold and 500-fold improvements over NiFe–OH and MnCo–CH, respectively, and surpassing Pt/C||RuO_2 performance. Guo et al.[25] constructed a nitrogen-vacancy-rich Co_2N/CoP@CC p–n junction, delivering excellent HER and OER activities with overpotentials of 44 mV and 227 mV, respectively, and a low overall water-splitting voltage of 1.5 V at 10 mA cm^{-2}. DFT analysis attributed the performance to nitrogen vacancies and the built-in electric field facilitating charge transfer and intermediate adsorption. More recently, Adhikari et al.[26] demonstrated a p–n junction in $MnCo_2O_{4.5}$@Ni_3S_2 on Ni foam for urea-assisted water splitting, where optimized band alignment, enhanced conductivity, and in situ NiOOH formation significantly improved OER and UOR kinetics.

In this work, we introduce a photoactive cocatalyst strategy for electrocatalytic overall water splitting, achieved by precise band-gap and band-position tuning through doping. A dendritic CuO layer was electrodeposited onto Ni foam, followed by deposition of selenium-doped WO_3 (Se@WO_3), forming a CuO/Se@WO_3 p–n heterojunction. The interfacial built-in electric field arises from differences in work function and Fermi energy levels (E_f), driving charge redistribution until equilibrium is reached[14,27,28]. This enhances the adsorption/desorption kinetics of hydrogen and oxygen intermediates in alkaline media, thereby improving HER and OER activities.

A key modification involves ~6% Se substitution at O sites in WO_3, which introduces partial metallic character and reduces the band gap by ~0.54 eV. This shifts the conduction band of Se@WO_3 closer to the valence band of CuO, enabling a Z-scheme charge-transfer pathway that promotes electron flow from n-type Se@WO_3 to p-type CuO while suppressing electron–hole recombination. To further reduce interfacial charge-transfer resistance, a needle-like $Cu(OH)_2$ layer was electrodeposited atop the heterojunction, serving as an efficient hole extractor, as confirmed by FESEM analysis. The effectiveness of this design stems from synchronized redox activity between CuO and $Cu(OH)_2$, where identical Cu redox couples (Cu/Cu^{2+}) operate at similar potentials, lowering overpotential requirements[29].

As a result, the CuO/Se@WO_3/$Cu(OH)_2$ catalyst exhibited low overpotentials of 202 mV for OER and 55 mV for HER at 10 mA cm^{-2}, with corresponding Tafel slopes of 35 mV dec^{-1} (OER) and 45 mV dec^{-1} (HER), indicating favorable reaction kinetics. The catalyst outperformed RuO_2 for OER and showed near-Pt/C-level HER activity. DFT calculations corroborated these findings, revealing band-gap narrowing in Se@WO_3 and enhanced W_d orbital contribution near E_f, which increases electron density at W sites and facilitates energetically favorable d–d electron transfer from W_d to Cu_d orbitals, strengthening the Z-scheme pathway. Furthermore, the ΔG_{H^*} value of −0.17 eV ($|\Delta G_{H^*}| < 0.20$ eV) confirms optimal HER thermodynamics compared to CuO/WO_3/$Cu(OH)_2$ (ΔG_{H^*} = 0.21 eV)[30]. The reduced OER overpotential is attributed to multifunctional interfacial active sites and efficient hole extraction by $Cu(OH)_2$.

4.2. Experimental Section:

4.2.1. Material Synthesis:

4.2.1.1. Synthesis of Dendritic CuO on Ni Foam:

Dendritic copper hydroxide oxide was grown on the nickel foam substrate through an electrodeposition method. The stock solution was prepared by dissolving 0.05 M $CuSO_4 \cdot 5H_2O$, 1 M H_2SO_4, and 2 M HCl in 50 mL of deionized water, followed by vigorous stirring at ambient temperature for 15 minutes to ensure complete mixing. The electrodeposition was carried out in a two-electrode setup, where cleaned Ni foam (1 cm^2) was used as the anode and a platinum (Pt) electrode served as the cathode. A direct current (DC) power supply was employed to apply a current density of 1 A cm^{-2} for 10 seconds. Post-deposition, the film was thoroughly rinsed with deionized water and ethanol to remove any residual contaminants, and subsequently dried under vacuum at room temperature.

4.2.1.2. Formation of the CuO/Se@WO_3 p–n Junction:

In the subsequent step for synthesizing selenium-doped WO_3, a layer of tungsten hydroxide was deposited onto the pre-fabricated dendritic copper hydroxide using a hydrothermal process. A precursor solution was prepared by mixing 3 mL of H_2WO_4 (0.05 M) and 0.02 g of urea in 12.5 mL of acetonitrile, followed by stirring for 30 minutes to ensure complete dissolution. Subsequently, 0.5 mL of concentrated HCl (6 M) was added to the

mixture, and the solution was stirred for an additional 15 minutes. The resulting solution was then transferred into a 25 mL stainless steel autoclave, where the dendritic copper hydroxide deposited on Ni-foam was immersed. The hydrothermal treatment was carried out at 180 °C for 2 hours. After the reaction, the obtained films were thoroughly rinsed with deionized water and ethanol to remove any residual impurities.

Prior to converting the hydroxide to the oxide form *via* calcination, selenium doping was performed using an electrochemical approach. A solution was prepared by dissolving 1 mM SeO_2 and 100 mM NaCl as the supporting electrolyte in 100 mL of deionized water, followed by stirring at 60 °C for 30 minutes to ensure complete dissolution. This solution served as the electrolyte for the electrochemical doping. The working electrode consists of the above prepared material, with platinum and Ag/AgCl functioning as the counter and reference electrodes, respectively. Selenium deposition was carried out using cyclic voltammetry for 10 cycles from 0 to −0.8 V at a sweep rate of 10 mV s^{-1}. The next step involved calcining the synthesized electrode at 400 °C with a ramp rate of 2 °C min^{-1} for two hours, converting the metal hydroxides to their respective oxides, thereby forming the CuO/Se@WO_3 composite on the Ni foam substrate.

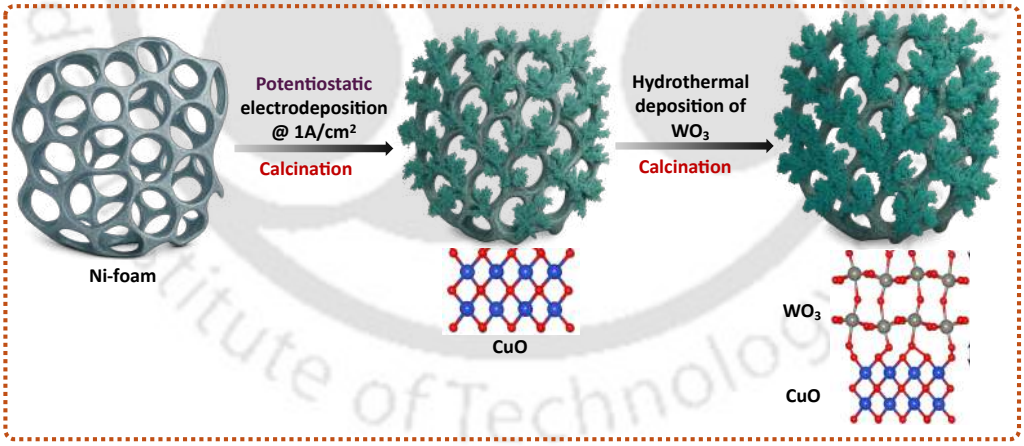

Figure 4.1. *Schematic representation for the synthesis of p-n heterojunction in between WO_3 and CuO.*

4.2.1.3. Electrodeposition of $Cu(OH)_2$ as a Charge-Extraction Layer over CuO/Se@WO_3 p–n Junction:

In the final step, a needle-like $Cu(OH)_2$ hole-extracting layer was deposited onto the CuO/Se@WO_3 structure using an anodization method. A three-electrode system was employed, consisting of as-synthesized CuO/Se@WO_3 as the working electrode, Cu-foil as the

counter electrode, and an Hg/HgO reference electrode, all immersed in a 1 M KOH solution. Electrodeposition was carried out by applying a constant potential of −0.1 V for 100 seconds, achieving the desired morphology, as confirmed by FESEM imaging. The resulting CuO/Se@WO_3/$Cu(OH)_2$ electrode was thoroughly rinsed with deionized water and ethanol, then stored under vacuum for subsequent electroanalysis.

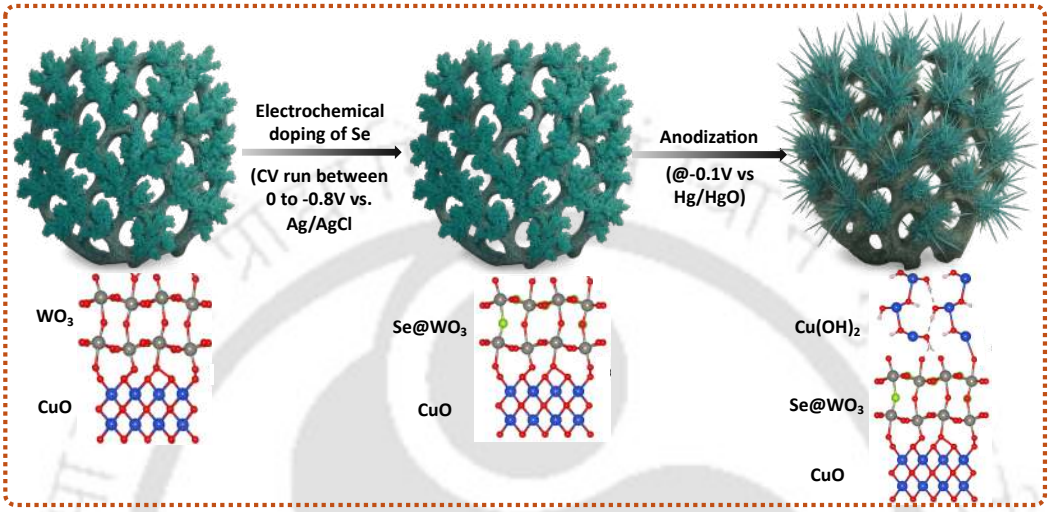

Figure 4.2. *Schematic representation of Se doping onto WO_3 and electrochemical deposition of top $Cu(OH)_2$ hole extracting layer.*

4.3. Computational methodology:

Density functional theory (DFT) calculations were carried out using generalized gradient approximation with Perdew-Burke-Ernzerhof (PBE) functional via Vienna ab initio simulation package (VASP).[32–34] The projector-augmented wave describes the interaction behavior of the ion and electron.[35] A plane wave basis was obtained for all calculations through a kinetic energy cutoff of 600 eV and a Monkhorest-Pack grid of 2×2×1.[36] To reduce the lattice mismatch 2×2, 2×2 and 3×1 supercells of CuO, WO_3, and $Cu(OH)_2$ are used with the cell dimension of a=10.61 Å and b = 10.41 Å. The detail description (cell dimension and the interlayer distances) of the construction of the heterostructure were represented in section 1 of the supporting information. A 40 Å vacuum was added along the c-axis to prevent image interactions generated by periodic boundary conditions. Grimme's proposed empirical vdW correction approach (DFT-D3) was applied to explain the interlayer long-range interactions.[37] The final structure of CuO/WO_3/$Cu(OH)_2$ and CuO/Se@WO_3/$Cu(OH)_2$ are shown in Figure 4.3. Gibbs

free energy (ΔG) was calculated to understand the HER and OER activity of the systems according to the equation (1).[38]

$$\boldsymbol{\Delta G = \Delta E + \Delta ZPE - T\Delta S} \qquad (\mathbf{4.1})$$

Here, ΔE, ΔZPE, and TΔS represent the adsorption energy of all the reaction intermediates, zero-point energy, and entropy change of the intermediates at 298.15 K, respectively, resulting from DFT calculations. Nørskov et al. developed the computational hydrogen electrode (CHE) model to measure the free energy (ΔG) of the formation of all intermediates in electrocatalytic processes.[39]

For HER,[40]

$$* + \boldsymbol{H_2O} + \boldsymbol{e^-} = \boldsymbol{H^*} + \boldsymbol{OH^-}$$

For OER,[41,42]

$$\boldsymbol{\Delta G_1 = * + OH^- = HO^* + e^-}$$

$$\boldsymbol{\Delta G_2 = HO^* + OH^- = O^* + H_2O + e^-}$$

$$\boldsymbol{\Delta G_3 = O^* + OH^- = HOO^* + e^-}$$

$$\boldsymbol{\Delta G_4 = HOO^* + OH^- = * + O_2 + H_2O + e^-}$$

The overpotential (η) of OER can be evaluated by the following formula:

$$\eta = \frac{\mathbf{max}\{\Delta G_1, \Delta G_2, \Delta G_3, \Delta G_4\}}{e} - \mathbf{1.23\ V}$$

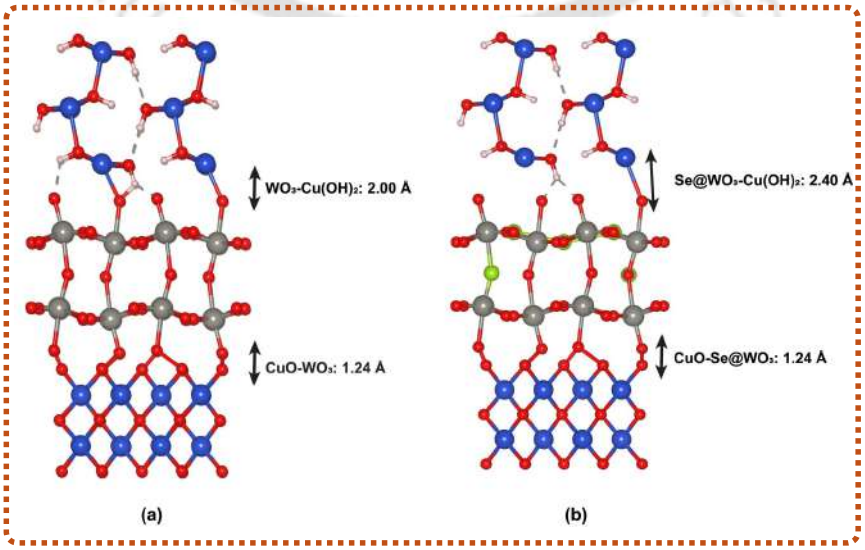

Figure 4.3. : *Structure of composite material used for the theoretical analysis (a) $CuO/WO_3/Cu(OH)_2$ and (b) $CuO/Se@WO_3/Cu(OH)_2$.*

4.4. Results and discussion:

In this work the electrochemical activity and performance were enhanced by increasing the electrochemically active surface area through morphological tuning and creating a heterojunction that supports Z-scheme charge separation for efficient HER and OER. FESEM analysis presents the morphological characteristics of the synthesized materials. Figures 4.2(a), (b), and (c) illustrate the structural features of CuO, WO_3, and $Cu(OH)_2$, respectively. The FESEM images reveal that the dendritic structure of CuO, serving as the base layer, provides an extensive electrocatalytic active surface area of 0.52 cm^2/mg that has been derived from ECSA calculation. Figures 4.4(d) and (e) show WO_3 and Se-doped WO_3 deposited on CuO, where a nano-block morphology is observed on the CuO surface, indicating that Se doping does not significantly alter the morphology. Figure 4.4(f) presents the final heterostructure, showing needle-like morphology of $Cu(OH)_2$, grown via anodization, extending from the p-n heterojunction.

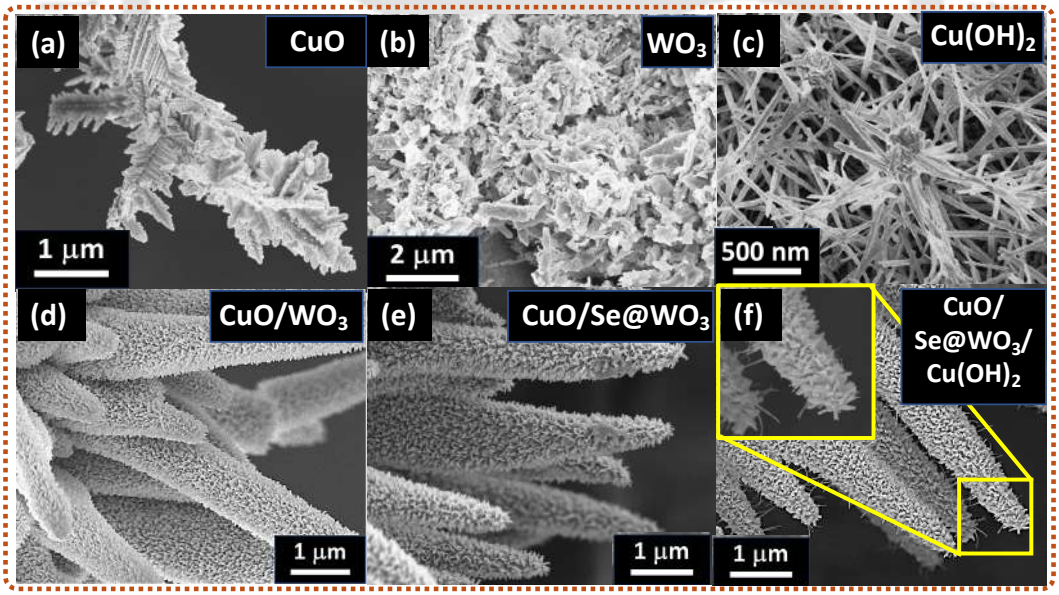

Figure 4.4. *(a,b,c) FESEM image of dendritic CuO, WO_3 nano blocks and $Cu(OH)_2$ needle individually deposited over Ni-foam; (d,e) FESEM image of CuO/WO_3 with and without Se doping onto WO_3; (f) FESEM image of $CuO/Se@WO_3/Cu(OH)_2$ composite.*

The morphological characteristics were further verified using FETEM, as shown in Figure 4.5(a). Figure 4.5(b) and (c) represent the high-resolution TEM images obtained from the dendritic CuO and $WO_3/Cu(OH)_2$ structures, with d-spacing values determined through

inverse fast Fourier transform (IFFT) corresponding to specific crystal planes. Elemental mapping of the CuO/Se@WO_3/$Cu(OH)_2$ composite was performed using FESEM-EDX (Figures 4.5(e), (f), (g), and (h)), confirming the uniform distribution of all constituent elements.

The synthesized compounds phase formation was confirmed using powder X-ray diffraction (Figure 4.5(d)). The XRD analysis verified the pure formation of CuO on the Ni foam substrate, as indicated by its characteristic peaks at 2θ values 35.5°, 38.7°, 48.8°, 58.2°, 61.8°, 66.1°, 67.9°, and 75.2° corresponding to the (002), (111), (-202), (202), (-113), (022), (113), and (-222) planes of CuO (ICSD No. 00-002-1040).

Following the deposition of the next layer, XRD measurements were conducted for both CuO/WO_3 and CuO/Se@WO_3 composites. The XRD pattern for CuO/WO_3 exhibited peaks at 2θ values 37.2°, 43.3°, and 62.8°, corresponding to the (103), (032), and (150) planes of the monoclinic phase of WO_3 (ICSD No. 00-043-1035) and another peak was observed at 75.2°, corresponds to the (-222) plane from CuO. For the Se@WO_3, peaks were observed at 2θ values 29.7°, 37.2°, 43.3°, and 62.8°, which corresponded to the (211), (103), (032), and (150) planes of WO_3, in agreement with ICSD No. 01-072-0677.

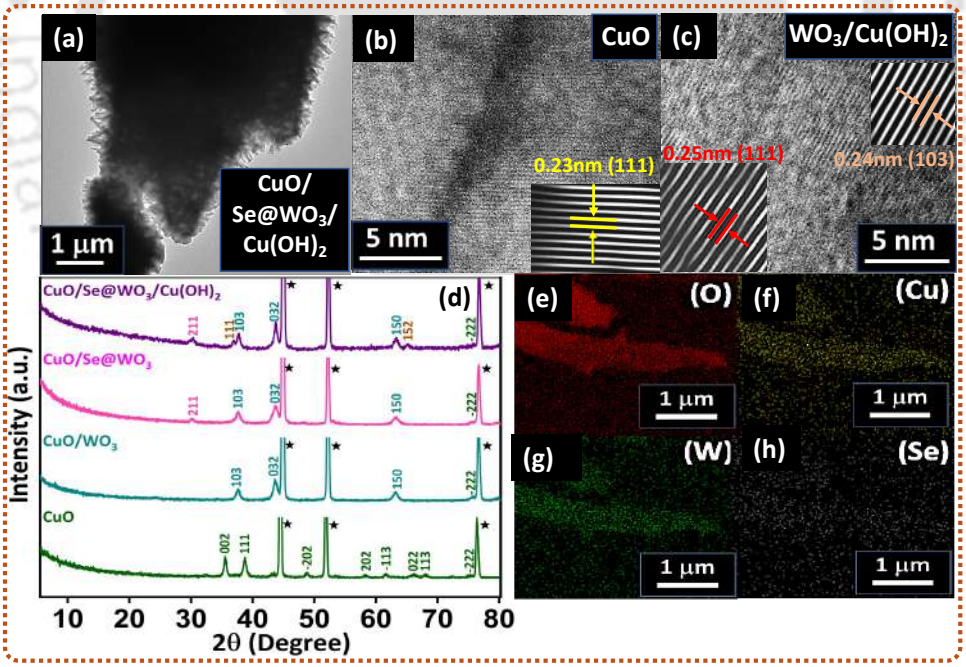

Figure 4.5. *(a) FETEM image of CuO/Se@WO_3/$Cu(OH)_2$; (b) HRTEM image of CuO representing (111) crystal plane; (c) HRTEM image of WO_3/$Cu(OH)_2$ showcasing the (103) crystal plane from WO_3 and (111) from $Cu(OH)_2$ with the inset displaying the corresponding IFFT pattern; (d) XRD plot representing CuO (green), CuO/WO_3 (cyan), Se@WO_3 (pink) and CuO/Se@WO_3/$Cu(OH)_2$ (violate). (e-h) FESEM-EDX mapping showing the homogeneous distribution of O, Cu, W and Se.*

Electrochemical measurements reveal that the formation of a p-n heterojunction between p-type CuO and n-type Se@WO_3, along with a $Cu(OH)_2$ hole-extracting layer, significantly improves overall water splitting performance. The semiconductor nature was confirmed through Mott-Schottky analysis (Figure 4.6), the negative slope of CuO identified it as p-type and the positive slope of WO_3 and Se@WO_3 represent it as n-type semiconductor.

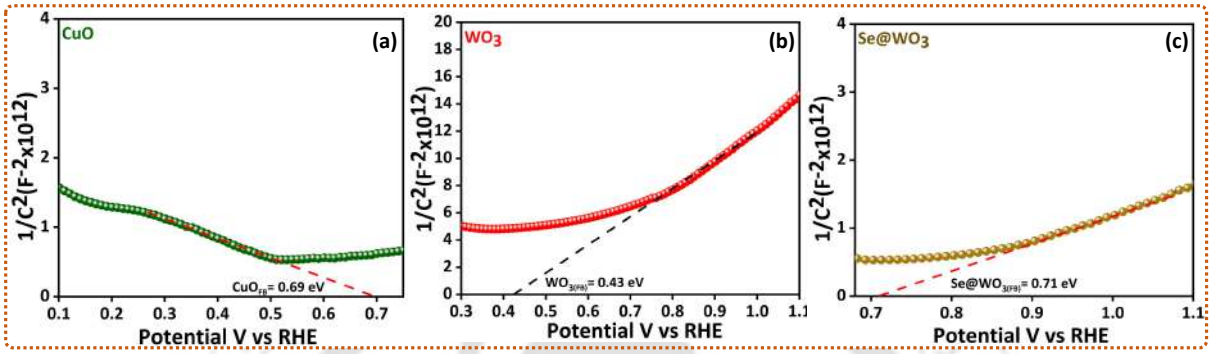

Figure 4.6. Mott–Schottky plots for (a) CuO, (b) WO_3, and (c) Se@WO_3. *The negative slope of the CuO plot indicates p-type semiconducting behaviour, while the positive slopes observed for WO_3 and Se@WO_3 confirm their n-type nature.*

Linear sweep voltammetry (LSV) data (Figure 4.7(a and d)) indicate that the CuO/Se@WO_3/$Cu(OH)_2$ composite exhibits an overpotential of 202 mV for the oxygen evolution reaction (OER) and 55 mV for the hydrogen evolution reaction (HER). The OER performance surpasses that of the benchmark catalyst RuO_2, while the HER activity approaches the benchmark value achieved by Pt/C. The bar diagram in Figure 4.7(b and e) illustrates the overpotential values for the oxygen evolution reaction (OER) and hydrogen evolution reaction (HER). After doping selenium (Se) into n-type WO_3, a reduction in overpotential was observed, with a reduction of 28 mV for OER and 55 mV for HER with respect to the undoped counterpart i.e. CuO/WO_3/$Cu(OH)_2$. This improvement can be attributed to two main factors: first Se doping imparts a metallic character to WO_3 by increasing the density of states at the E_f, as revealed by theoretical projected density of state (PDOS) analysis. Experimental results also confirm a significant band gap reduction, aligning with theoretical predictions. Second, the reduced band gap facilitates a Z-scheme mechanism, enabling effective separation of electron-hole pairs, thereby enhancing the efficiency of HER and OER within their respective potential ranges. When comparing the electrochemical performance of the composite without the $Cu(OH)_2$ hole-extracting layer, higher overpotential values were observed for both OER (Figure 4.7(b)) and HER (Figure 4.7(e)). This can be attributed to the intrinsic property of $Cu(OH)_2$ layer, where it continuously extracts holes

generated at the p-n junction and transfers them into the electrolyte, facilitating a faster water oxidation process. Consequently, the counter electrons generated are directed through the external circuit to the cathode, where they contribute to the water reduction process. The significance of a third metal hydroxide layer in OER is evident from the overpotential values in Figure 4.7(b). Although CuO/WO_3 has a p-n heterojunction that could enhance charge separation and accumulation, CuO alone shows a slight lower overpotential (300 mV) compared to CuO/WO_3 (310 mV). This suggests that an electroactive layer above the p-n junction is necessary to effectively extract charges generated at the heterojunction.

The water oxidation kinetics of the electrocatalyst were assessed through Tafel slope analysis, which provide insights into the charge transfer efficiency. As shown in Figure 4.7(c and f), the addition of a $Cu(OH)_2$ layer significantly decreases the Tafel slope for OER from 102 mV/dec (CuO/WO_3) to 40 mV/dec ($CuO/WO_3/Cu(OH)_2$), indicating an enhanced charge transfer kinetics due to the metal hydroxide layer acting as a hole extractor. A similar improvement was observed in HER, with the Tafel slope dropping from 140 mV/dec to 72 mV/dec, confirming an increased charge transfer rate with the $Cu(OH)_2$ addition. The Tafel slope decreases further from 40 mV/dec to 35 mV/dec for OER and from 72 mV/dec to 45 mV/dec for HER between $CuO/WO_3/Cu(OH)_2$ and $CuO/Se@WO_3/Cu(OH)_2$, highlighting the role of Se doping in enhancing water electrolysis performance by improving charge the separation process.

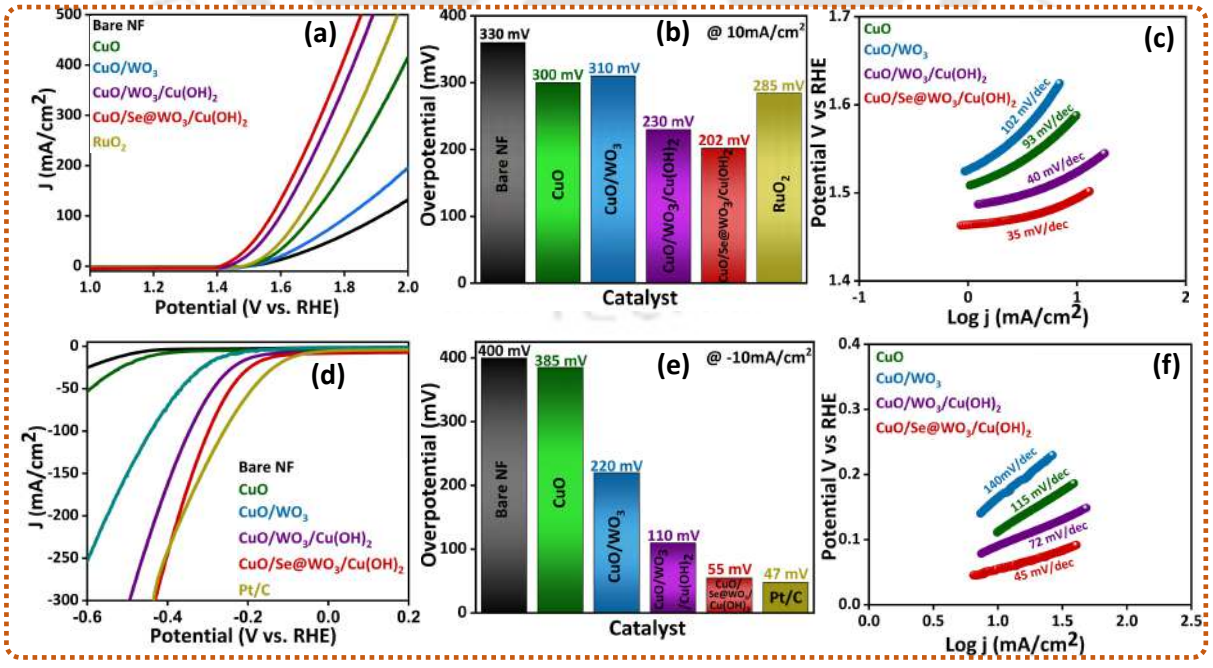

Figure 4.7. *(a,d) LSV polarisation curves for OER and HER representing bare Ni-foam, CuO, CuO/WO_3, CuO/WO_3/Cu(OH)$_2$ and CuO/Se@WO_3/Cu(OH)$_2$ compared with the benchmark catalyst RuO for OER and Pt/C for HER; (b,e) bar diagram for OER and HER representing overpotentials @10 mA/cm^2 derived from figure (a) and (d); (c,f) corresponding Tafel slope of CuO, Cu/WO_3, CuO/WO_3/Cu(OH)$_2$ and CuO/Se@WO_3/Cu(OH)$_2$ derived from LSV curve taken at a sweep rate of 5 mV/sec in 1M KOH.*

To optimize the doping percentage of selenium (Se) on tungsten trioxide (WO_3) for enhanced electrocatalytic activity, we performed doping using cyclic voltammetry (CV) with varying cycle numbers ranging from 5 to 20. The number of CV cycles was used as a controlled parameter to modulate the amount of Se incorporated into the WO_3 matrix. The resulting selenium-doped WO_3 (Se@WO_3) were used in the composites were then fabricated into electrodes, and their electrocatalytic performance was evaluated through linear sweep voltammetry (LSV). Notably, the electrocatalyst synthesized using 10 CV cycles demonstrated the most favorable performance. All electrodeposition processes were conducted using a 1 mM SeO_2 solution, as described in detail in the materials synthesis section.

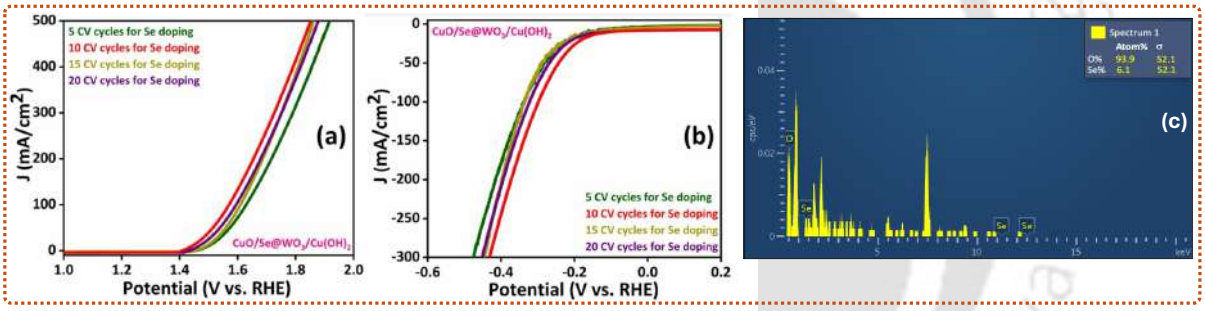

Figure 4.8. *Optimization of Se doping to determine the ideal doping percentage for enhanced performance in (a) OER and (b) HER; (c) STEM-EDS analysis done on Se@WO_3 to show the doping percentage of Se, replacing oxygen from WO_3.*

The transmission electron microscopy energy-dispersive spectrometry (STEM-EDS) analysis was performed on the optimized Se-doped WO_3 sample (deposited through 10 CV cycle), which demonstrated the highest electrocatalytic OER and HER, the analysis show that approximately 6% of the total oxygen in the lattice was substituted with selenium, corresponding to a total substitution of about 4.7% relative to the complete WO_3 lattice. This doping percentage was used in subsequent theoretical calculations to gain a deeper understanding of the composite material's properties. To obtain more accurate measurements, we have performed ICP-MS (Inductively Coupled Plasma Mass Spectrometry) analysis for Se-doped WO_3 to quantify the atomic concentration of Se doping. The ICP-MS measurements were conducted on Se doped WO_3, and the W and Se concentration was found

to be 756.5 ppb and 58 ppb respectively. Thus, the final composition of Se-doped WO_3 is determined to be $WO_{2.82}Se_{0.18}$.

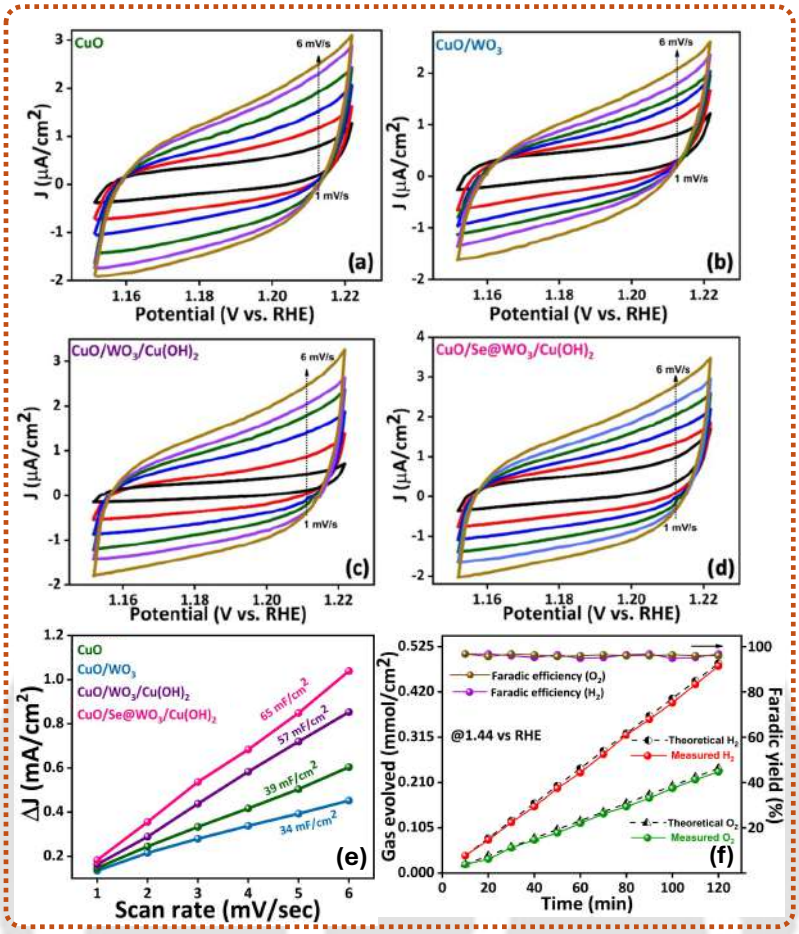

Figure 4.9. *Cyclic voltammetry plots at scan rates ranging from 1 mV/s to 6 mV/s under alkaline conditions in a three-electrode electrochemical cell taken at the non-faradaic region for the catalyst (a) CuO, (b) CuO/WO_3, (c) $CuO/WO_3/Cu(OH)_2$ and (d) $CuO/Se@WO_3/Cu(OH)_2$ composited over glassy carbon electrode; (e) C_{dl} plot of CuO, Cu/WO_3, $CuO/WO_3/Cu(OH)_2$ and $CuO/Se@WO_3/Cu(OH)_2$; (f) Faradic yield plot for $CuO/Se@WO_3/Cu(OH)_2$ for O_2 and H_2 at 1M KOH.*

The improvement in electrochemical performance is often attributed to an increased number of electroactive sites within the catalyst. To quantify this, the electrochemically active surface area (ECSA) was estimated via the double-layer capacitance (C_{dl}) obtained from cyclic voltammetry measurements. CVs of CuO, CuO/WO_3, $CuO/WO_3/Cu(OH)_2$, and $CuO/Se@WO_3/Cu(OH)_2$ electrodes were recorded in the non-Faradaic potential window of 1.15–1.22 V vs. RHE at scan rates ranging from 1 to 6 mV s^{-1}. (figure 4.9a-d) Prior to measurement, the catalyst was sonicated from the Ni foam substrate, centrifuged, and 1 mg of the isolated powder was drop-cast onto a glassy carbon electrode. The C_{dl} values, which directly reflect the ECSA, were extracted from the linear fit of the current density difference

($j_{anodic} - j_{cathodic}$) at 1.21 V vs. RHE as a function of scan rate, where the C_{dl} corresponds to half of the slope (Figure 4.9e)).Performing CVs at low scan rates allows for optimal adsorption of charged species on the electrode surface, providing deeper insight into double-layer formation. As shown in Figure 4.9(e), C_{dl} increases significantly from 19 μF/cm² for CuO/WO_3 to 27 μF/cm² for $CuO/WO_3/Cu(OH)_2$, attributed to the additional electroactive and morphologically beneficial $Cu(OH)_2$ layer and trending with the values associated with the overpotentials. Following Se doping, $CuO/Se@WO_3/Cu(OH)_2$ exhibits an even higher C_{dl} of 31 μF/cm² implying the increase in electroactive sites on WO_3 due to doping process, which imparts additional metallic character to WO_3

A good electrocatalyst should have high stability to be used in harsh conditions. To test the durability of the synthesized electrocatalyst, chronoamperometry measurements were performed at a fixed potential of 1.43 V vs the RHE for OER and -0.60 V vs RHE for HER. Figure 4.10 shows the stability for $CuO/Se@WO_3/Cu(OH)_2$ with negligible decrease in the current density even after 60 h of continuous operation. The inset shows the constancy in the LSV curve of the composite material toward the OER and HER measured before and after the stability test. After the analysis it can be confirmed that the electrocatalyst is highly stable as there is negligible change in the current density values.

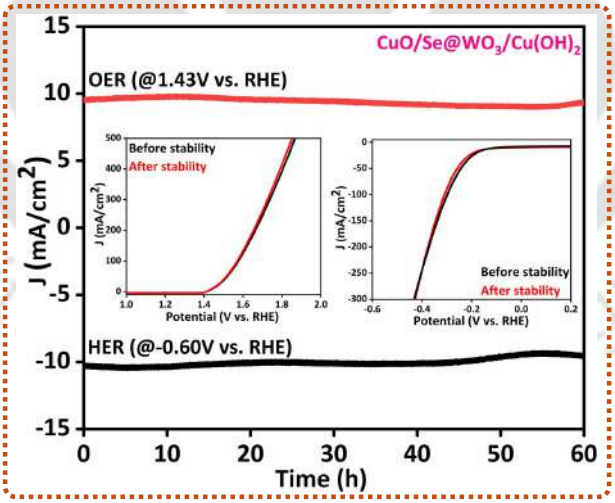

Figure 4.10. *stability curve showing the stability of $CuO/Se@WO_3/Cu(OH)_2$ at 1K KOH at an applied potential of 1.43V vs RHE for OER and -0.60V vs RHE for HER for 60 hours.*

Enhancement in electrochemical performance is often linked to efficient charge transfer kinetics at the electrolyte - electrode interface. Electrochemical impedance spectroscopy (EIS) was used to assess charge mobility at the electrode–electrolyte interface by measuring charge transfer resistance (R_{ct}). As shown in Figure 4.11a, EIS conducted at 1.43 V vs RHE provides

Nyquist plots for the individual catalysts, and the resulting R_{ct} values align with the Tafel slope trends, illustrating improvements in reaction kinetics. According to equation 2.8 & 2.9, the Tafel slope is inversely proportional to the material's charge transfer coefficient (i.e., Tafel slope $\propto 1/\alpha$). The Nyquist plot reveals that the CuO/Se@WO_3/$Cu(OH)_2$ composite exhibits the lowest R_{ct} value, at 4.2 Ω, this superior charge transfer in p-n heterojunction electrocatalysts is driven by the built-in electric field enhancing charge separation and transport, while the metal hydroxide top layer ensures a high charge transfer coefficient. CuO/WO_3/$Cu(OH)_2$ shows a slightly higher R_{ct} value of 5.3 Ω, due to less effective charge separation via the Z-scheme mechanism. In comparison, CuO/WO_3 without the $Cu(OH)_2$ hole extracting layer has a higher R_{ct} value of 7.1 Ω, indicating reduced charge transfer efficiency at the electrolyte interface.

To understand the time constants associated with different relaxation processes across the interfaces, we have analyzed the distribution of relaxation time (DRT) constants using DRT tool in MATLAB based on the data of AC impedance spectra (Figure 4.11a).[43,44] This analysis enables the identification of distinct kinetic processes, each exhibiting characteristic relaxation behaviors that are observable across multiple timescales. Analyzing timescale information in water splitting offers insights into key kinetic challenges, including ionic conduction, charge transfer, diffusion control, interfacial evolution, and other previously unexplored kinetic processes. The Distribution of Relaxation Times (DRT) method enables direct identification of the time constants associated with major electrochemical processes, simplifying impedance analysis and greatly enhancing the accuracy of kinetics interpretation within these timescales. The relationship between the distribution function and impedance is defined by Equation 4.2.

$$Z(\omega) = R_{\infty} + R_{pol}\int_{-\infty}^{\infty}\frac{\Gamma(\log(\tau))}{1+i\omega\tau}d(\log(\tau)) \qquad (4.2)$$

In this context, Z(ω) represents the total impedance, R_∞ is the series resistance, R_{pol} denotes the total polarization resistance of the processes, Γ is the distribution function of relaxation times, τ is the relaxation time, and ω is the frequency of the applied input.

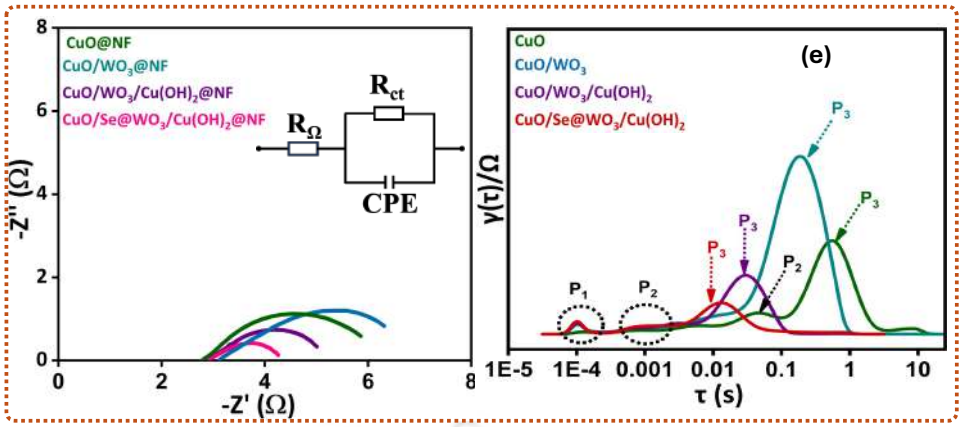

Figure 4.11 *(a) Nyquist plots obtained from electrochemical impedance spectroscopy (EIS) measurements of all electrocatalysts recorded at an applied potential of 1.43 V vs the reversible hydrogen electrode (RHE), illustrating differences in charge transfer resistance at the electrode–electrolyte interface. (b) Distribution of relaxation times (DRT) analysis derived from the EIS data, resolving the total polarization resistance into distinct contributions associated with series resistance (P1), interfacial charge transfer processes (P2), and mass transport/diffusion phenomena (P3), thereby providing deeper insight into the enhanced charge transfer and diffusion kinetics of the CuO/Se@WO_3/$Cu(OH)_2$ composite catalyst.*

Following the application of DRT analysis to the EIS data, the resulting DRT plot (Figure 4.11(b)) reveals three distinct peaks, each corresponding to the resistance contribution of an individual electrochemical process to the electrode's total polarization resistance. The time constant (**τ**) is unique to each polarization process, with the area under each peak indicating the extend of polarization resistance (R_P) contribution of a specific electrochemical process to the overall cell polarization. Thus, changes in the DRT profile can directly reflect alterations in the nature and magnitude of the electrode reactions. Three peaks represented as **P_1, P_2, and P_3** in the DRT plot, each correspond to characteristic time constants, where **P_1** represents the high-frequency semicircle, attributed to series resistance across the electrolyte and electrode interface. **P_2** corresponds to the mid-frequency semicircle, associated with charge transfer reactions at the interface and **P_3**, in the low-frequency region, is linked to diffusion processes. Our comparative study reveals that the peaks **P_3** and **P_2**, associated with the diffusion and charge transfer processes both has shifted to a higher frequency with reduced peak intensities in the final modified catalyst i.e. CuO/Se@WO_3/$Cu(OH)_2$. These findings indicate that ion diffusion and charge transfer kinetics are highest when CuO/Se@WO_3/$Cu(OH)_2$ electrode is used as the electrocatalyst. This improvement is further reflected in the calculated effective resistance values as shown in Table 4.1. It is observed that resistance values are significantly

reduced for the diffusion resistance **P_3** (4.2 Ω) and charge transfer resistance **P_2** (0.01 Ω) along with faster relaxation times for charge transfer processes (**P_2**, **P_3**) observed in the $CuO/Se@WO_3/Cu(OH)_2$ composite, compared to other electrode modifications highlighting its enhanced electrochemical kinetics.

Table 4.1. *Effective resistance values calculated for various electrochemical processes across different catalytic systems.*

System	P_1 (Ω)	P_2 (Ω)	P_3 (Ω)
CuO@NF	1.5×10^{-5}	0.076	5.47
CuO/WO_3@NF	1.4×10^{-4}	0.014	10.55
$CuO/WO_3/Cu(OH)_2$@NF	1.2×10^{-5}	0.023	5.33
$CuO/Se@WO_3/Cu(OH)_2$@NF	1.1×10^{-5}	0.01	4.2

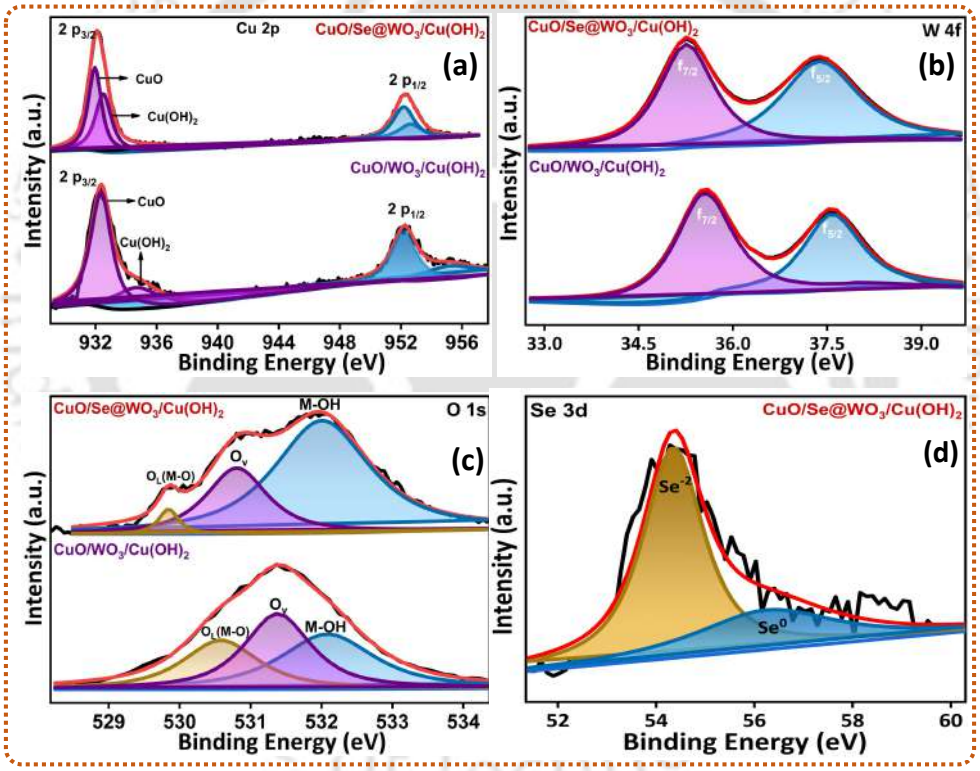

Figure 4.12. *High-resolution XPS spectra of (a) Cu 2p (b) W 4f and (c) O1s for $CuO/WO_3/Cu(OH)_2$ (bottom) and $CuO/Se@WO_3/Cu(OH)_2$ (top); (d) XPS core level spectra for Se 3d for $CuO/Se@WO_3/Cu(OH)_2$.*

X-ray photoelectron spectroscopy (XPS) was conducted to analyse the changes in electronic structure of $CuO/WO_3/Cu(OH)_2$ before and after Se doping. As shown in Figures 4.12(a) and (b), both the Cu 2p and W 4f core-level spectra exhibit shift towards the lower binding energies after Se doping. Specifically, in the Cu 2p spectrum (Figure 4.12(a)), a significant shift of approximately 1.2 eV is observed for both the $2p_{3/2}$ and $2p_{1/2}$ peaks in the $Cu(OH)_2$ layer. For

W 4f, a similar shift is evident, where both the peaks $4f_{5/2}$ and $4f_{7/2}$ has moved around 0.3 eV towards lower binding energy.

The observed shift to lower binding energies supports the successful incorporation of Se into the WO_3 layer. Due to its lower electronegativity and greater metallic character compared to oxygen, Se can donate local electron density to neighboring metal atoms, increasing electron density around these atoms. This increased electron density reduces the energy required to remove electrons from the core levels, resulting in the observed shifts toward lower binding energies. Figure 4.12(c) shows the O 1s core-level spectra, which display three distinct peaks from lower to higher binding energies. These peaks correspond to lattice oxygen (O_L), oxygen vacancies (O_v), and for the metal hydroxides or adsorbed water molecules, respectively. Following Se doping, a prominent shift towards the lower binding energy is observed in the lattice oxygen peak. This shift is likely to occur due to oxygen atoms bonding to the metal that are replaced by less electronegative Se atoms, which partially donate electron density to the adjacent metal and oxygen atoms, resulting in a lower binding energy for the lattice oxygen. Figure 4.12(d) shows the Se 3d core-level spectra, where peaks corresponding to both Se^0 and Se^{-2} states are observed. The intensity ratio of Se^0 to Se^{-2} indicates a higher proportion of Se in the -2-oxidation state. This predominance of Se^{-2} suggests successful incorporation of Se into the crystal lattice by the substitution of O^{-2}, while the Se^0 represents undoped elemental Se.

To gain a deeper understanding of the electrocatalytic mechanism, we have conducted both experimental and theoretical analyses of the materials. Experimentally, Mott-Schottky analysis was performed on both CuO and WO_3 to identify the p-n junction. Additionally, to examine how Se doping affects the flat band potential of WO_3, we have performed Mott-Schottky analysis for Se@WO_3 as well. As shown in Figure 4.6(a), CuO exhibits a negative slope, confirming its p-type semiconductor nature, while WO_3 shows a positive slope (Figure 4.6(b)), characteristic of an n-type semiconductor. The Mott-Schottky analysis of Se@WO_3 also reveals a shift in flat band potential towards higher value compared to undoped WO_3, indicating that Se doping alters the band positions for WO_3. The exact band positions and band gaps of the individual materials were determined using a combination of XPS valence band spectra (Figure 4.13 (d-f)) and Tauc plots (Figure 4.13 (a-c)) derived from ultraviolet-visible diffuse reflectance spectroscopy (UV-Vis DRS) data.

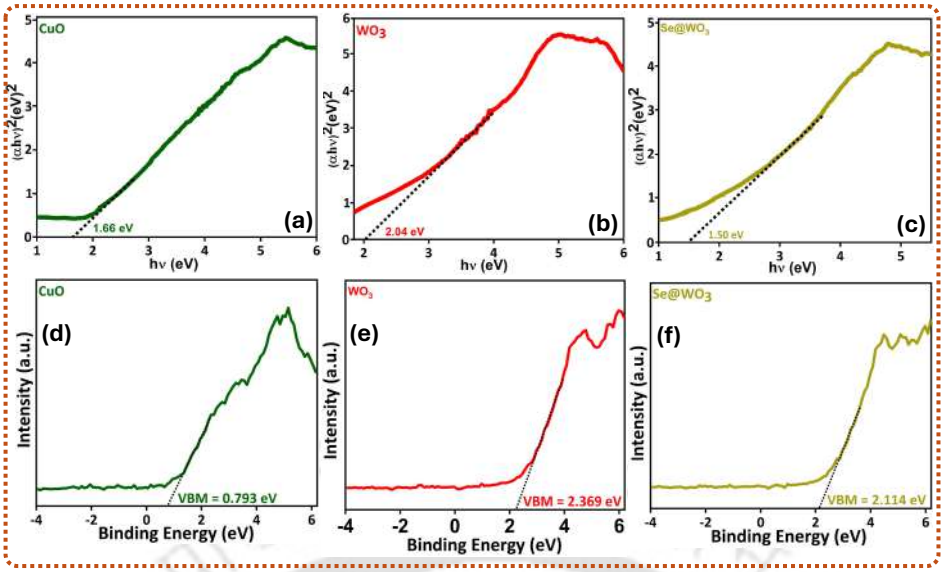

Figure 4.13. *Tauc plots derived from UV–Vis DRS data for (a) CuO, (b) WO_3, and (c) Se@WO_3, used to determine the optical band gaps by extrapolation of the linear region. Corresponding XPS valence band spectra for (d) CuO, (e) WO_3, and (f) Se@WO_3, showing the valence band maximum (VBM) positions. The combined analysis highlights the band gap narrowing and VBM shift induced by Se doping in WO_3, providing insight into band alignment and charge-transfer behaviour in the heterojunction.*

Table 4.2. *Summary of the band positions of the materials determined from the Tauc plot and XPS valence band spectra.*

Material	Band Gap (eV)	Valence Band (eV)	Conduction Band (eV)
CuO	1.66	0.79	-0.87
WO_3	2.04	2.37	0.33
Se@WO_3	1.50	2.11	0.61

For our study all the UV-Vis DRS measurements were performed over the 200–800 nm range. The band gap values were obtained by extrapolating the linear portion of each Tauc plot to the x-axis, where the intercept on the *hv* axis gives E_g. Results indicate a band gap of 1.66 eV for p-type CuO, 2.04 eV for n-type WO_3, and a reduced band gap of 1.50 eV for Se-doped WO_3. This reduction in WO_3's band gap after Se doping has been previously discussed. After determining the band gap, our next objective was to identify the precise band positions of the materials to better understand the underlying mechanism. Although Mott-Schottky measurements can estimate band positions, they often lack accuracy due to assumptions about carrier density and ideal semiconductor behavior, which may not apply to real

materials. Surface states and experimental conditions can also affect the flat-band potential, leading to inconsistencies. Therefore, XPS valence band spectra offer a more reliable method for determining valence band positions. From the XPS valence band spectra, the valence band maximum (VBM) of CuO and WO_3 were found to be 0.793 eV and 2.369 eV, respectively, determined by extrapolating the leading edge of the valence band spectrum to the baseline, representing the highest occupied energy state below the Fermi level. After Se doping, the VBM of WO_3 shifted to 2.114 eV (Figure 4.13(f)), indicating a band gap change due to the doping process. Combining this VBM data with band gap information from the above experimental approaches provides a clearer understanding of the band positions of each material in the heterojunction and their roles in the charge transfer mechanism during water splitting. For better understanding and visualization, we have added a table (Table 4.2) representing the summary of the band positions of the materials determined from the Tauc plot and XPS valence band spectra.

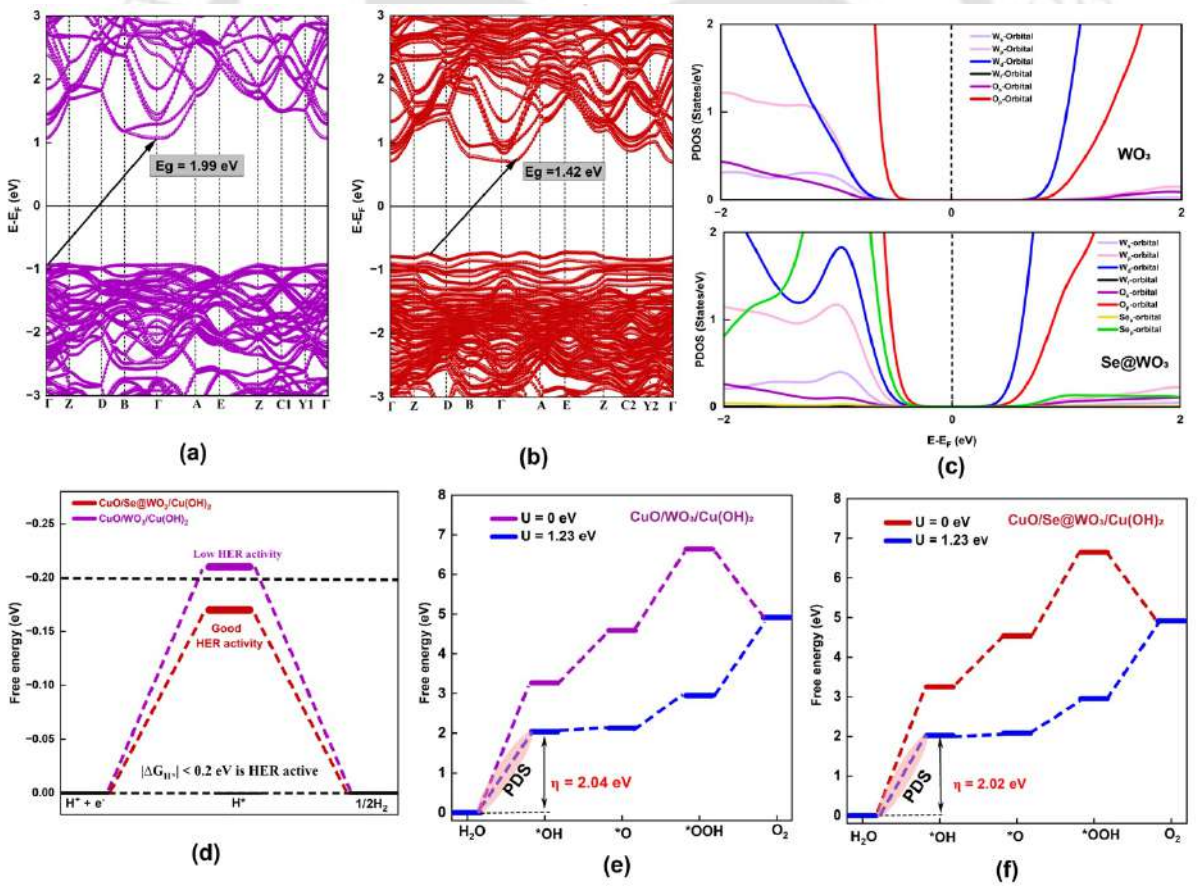

Figure 4.14. *Electronic band structures of (a) WO_3, (b) Se@WO_3, and (c) Projected density of states (PDOS) plots of WO_3 and Se@WO_3. Free energy profile for (d) HER and (e-f) OER in CuO/WO_3/$Cu(OH)_2$ and CuO/Se@WO_3/$Cu(OH)_2$.*

This plausible mechanism proposed is further supported by theoretical studies, where Figure 4.14 (a-c) shows the electronic band structure and projected partial density of states (PDOS) plots of WO_3 and Se@WO_3. The electronic band structure analysis revealed that WO_3 exhibits semiconductor properties having a band gap of 1.99 eV.[45] Additionally, it has been shown that incorporating Se atoms significantly decreases the band gap of the system to 1.42 eV. As shown in the PDOS of bulk WO_3 in Figure 4.14c, the valence and conduction bands mainly consist of O 2p and W 4d states. However, the PDOS plot of Se@WO_3 shows the p-orbital of the Se-atom overlaps with the W_p and W_d orbitals at the valance band region closer to the E_f. Additionally, the valence band state of Se@WO_3 approaches the E_f mainly because the doping, increases the electron density at the W-atom, promoting electron transport.

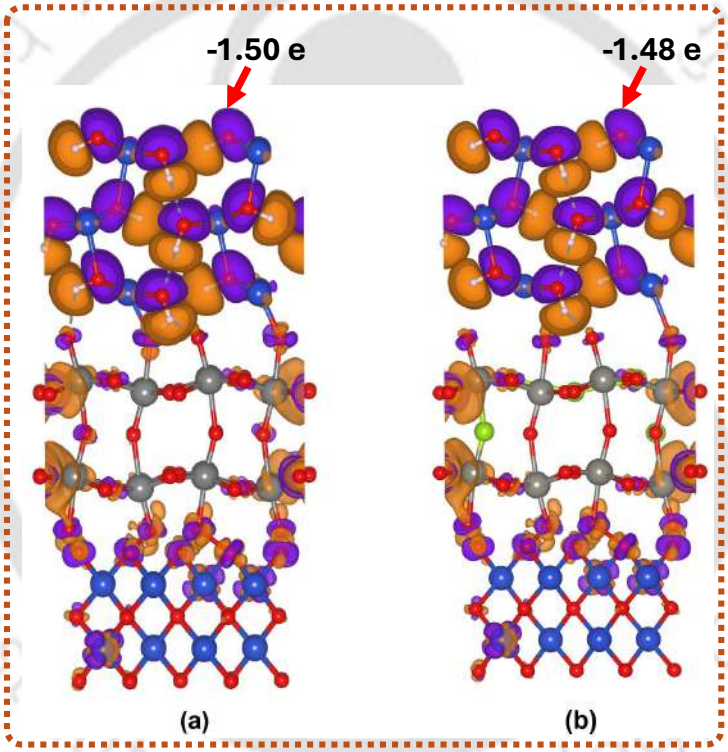

Figure 4.15. *Charge density difference (CDD) plot of (a) CuO/WO_3/$Cu(OH)_2$ and (b) CuO/Se@WO_3/$Cu(OH)_2$. Purple and orange colors represent the charge accumulation and depletion region, respectively.*

The hydrogen adsorption energy (*H) serves as a significant descriptor for evaluating the efficiency of various catalysts in the HER process.[46,47] The active site of the catalyst was investigated through a charge density difference (CDD) plot, where the O-site of $Cu(OH)_2$ acts as an active site with the charge accumulation region (Figure 4.15). From the CDD, it was also observed that the electron density at the O-atom of the Se-doped system is lower than that of the pristine one. The hydrogen atom is bounded with the O-atom with calculated free

energy -0.21 and -0.17 eV for $CuO/WO_3/Cu(OH)_2$ and $CuO/Se@WO_3/Cu(OH)_2$, respectively, as shown in Figure 4.14(d). Our results indicate that $CuO/Se@WO_3/Cu(OH)_2$ show improved HER efficiency as $|G_H|$.[30] The calculated H adsorption-free energy of Pt(111) was reported to be -0.09 eV,[48] -0.15 eV,[49] or -0.17[50] eV, which subsequently followed the Volmer-tafel mechanism.[47] Since the calculated free energy for $CuO/Se@WO_3/Cu(OH)_2$ in our system is -0.17 eV, it is predicted to follow the Volmer-tafel mechanism.

To evaluate the electrocatalytic activities of the oxygen evolution reaction (OER), we have calculated the free energy changes of the intermediates such as ΔG_{*OH} (ΔG_1), ΔG_{*O} (ΔG_2), and ΔG_{*OOH} (ΔG_3). Ideal OER electrocatalysts are defined by energy barriers of 1.23 eV for two adjacent elementary steps and an η-OER value of zero.[42] For instance, ΔG_1, ΔG_2, and ΔG_3 of the $CuO/WO_3/Cu(OH)_2$ in the OER are 3.27, 1.32, and 2.0 respectively, while it is 3.25, 1.29, and 2.11 eV for the $CuO/Se@WO_3/Cu(OH)_2$ as displays in Figure 4.15(e-f). Thus, the first step (H_2O-OH*) is the most energy-consuming, and it is the potential determining step (PDS) with the overpotential (η) 2.04 and 2.02 eV, $CuO/WO_3/Cu(OH)_2$ and $CuO/Se@WO_3/Cu(OH)_2$, respectively. The results clearly showed that Se-doping had minimal effect on the OER activity of the catalyst; however, the overpotential (η) of the systems in this work is found to be lower than many previously reported electrocatalysts.[51,52]

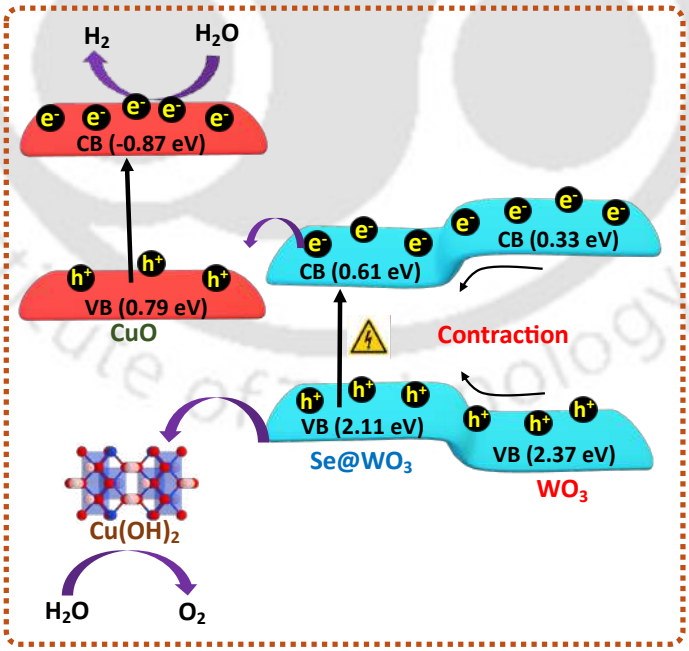

Figure 4.16. *Schematic representing the electron transfer process across the heterojunction for overall water splitting.*

4.5. Conclusions

In summary, the CuO/Se@WO_3/$Cu(OH)_2$ catalyst system on Ni foam demonstrates a significant advancement in electrocatalytic water splitting through strategic structural and electronic modifications. The dendritic CuO base layer, combined with Se-doped WO_3, forms a stable p-n junction that enhances electron mobility and reduces recombination, facilitated by a Z-scheme-like charge transfer mechanism. Selenium doping in WO_3 narrows the band gap by 0.54 eV, effectively increasing electron density at W_d orbitals and aligning the conduction band with CuO's valence band for efficient HER and OER. The addition of a $Cu(OH)_2$ layer further reduces charge transfer resistance by acting as a hole extractor, as evidenced by Tafel slopes of 35 mV/dec (OER) and 45 mV/dec (HER) and achieving overpotentials of 202 mV and 55 mV for OER and HER, respectively, at 10 mA/cm^2. DFT calculations reinforce the experimental observations, showing that Se doping improves electronic conductivity and reduces the HER overpotential with $\Delta G_H^* = -0.17$ eV, enhancing the catalyst's performance compared to conventional RuO_2 for OER and nearly matching Pt/C for HER. The catalyst's robust performance under intermittent renewable energy conditions, attributed to its structural and electronic stability, highlights its promise as a scalable, cost-effective solution for sustainable hydrogen production in water electrolysis systems. This study underscores the value of band gap tuning and interfacial engineering in electrocatalysis, paving the way for next-generation bifunctional catalysts.

While the developed CuO/Se@WO_3/$Cu(OH)_2$ bifunctional catalyst demonstrates exceptional intrinsic activity, its deployment in an undivided single-cell configuration presents critical challenges for practical application. The simultaneous evolution of hydrogen and oxygen in a shared environment leads to inevitable gas mixing, which not only severely compromises product purity but also introduces significant safety hazards associated with explosive gas mixtures. To overcome these operational bottlenecks, the subsequent chapter shifts focus from catalyst design to practical device engineering. Specifically, the next phase of this research investigates the physical separation of the HER and OER processes by utilizing a compartmentalized H-cell setup integrated with a bipolar membrane. This strategic configuration is designed to prevent gas crossover, ensure the safe collection of high-purity hydrogen, and bridge the gap between high-performance nanomaterial design and scalable electrolyzer architecture.

4.6. References:

(1) B. You, Y. Sun, *Acc. Chem. Res.* **2018**, *51*, 1571.

(2) B. Suryanto, R. H, Y. Wang, R. K. Hocking, W. Adamson, C. Zhao, *Nat. Commun.* **2019**, *10*, 5599.

(3) C. Lv, X. Wang, L. Gao, A. Wang, S. Wang, R. Wang, X. Ning, Y. Li, D. W. Boukhvalov, Z. Huang, C. Zhang, *ACS Catal.* **2020**, *10*, 13323.

(4) A. Kundu, S. Gautam, B. Chakraborty, *J. Mater. Chem. A* **2024,** 13, 2920.

(5) J. Jiao, W. Yang, Y. Pan, C. Zhang, S. Liu, C. Chen, D. Wang, *Small* **2020**, *16*, 2002124.

(6) T. Tang, W. J. Jiang, S. Niu, N. Liu, H. Luo, Q. Zhang, W. Wen, Y. Y. Chen, L. B. Huang, F. Gao, J. S. Hu, *Adv. Funct. Mater.* **2018**, *28*, 1704594.

(7) F. Wang, L. Xiao, Y. Jiang, X. Liu, X. Zhao, Q. Kong, A. Abdukayum, G. Hu, *Mater. Horiz.* **2025**.

(8) P. Zhai, Y. Zhang, Y. Wu, J. Gao, B. Zhang, S. Cao, Y. Zhang, Z. Li, L. Sun, J. Hou, *Nat. Commun.* **2020**, *11*, 5462.

(9) K. Fan, H. Zou, Y. Lu, H. Chen, F. Li, J. Liu, L. Sun, L. Tong, M. F. Toney, M. Sui, J. Yu, *ACS Nano* **2018**, *12*, 12369.

(10) R. Q. Li, S. Guo, X. Wang, X. Wan, S. Xie, Y. Liu, C. Wang, G. Zhang, J. Cao, J. Dai, M. Ge, W. Zhang, *Chem. Sci.* **2024**, *15*, 10084.

(11) S. Anantharaj, S. R. Ede, K. Sakthikumar, K. Karthick, S. Mishra, S. Kundu, *ACS Catal.* **2016**, *6*, 8069.

(12) V. Vij, S. Sultan, A. M. Harzandi, A. Meena, J. N. Tiwari, W. G. Lee, T. Yoon, K. S. Kim, *ACS Catal.* **2017**, *7*, 7196.

(13) B. Yan, D. Krishnamurthy, C. H. Hendon, S. Deshpande, Y. Surendranath, V. Viswanathan, *Joule* **2017**, *1*, 600.

(14) Y. Zeng, Z. Cao, J. Liao, H. Liang, B. Wei, X. Xu, H. Xu, J. Zheng, W. Zhu, L. Cavallo, Z. Wang, *Appl. Catal. B* **2021**, *292*, 120160.

(15) S. Bhowmick, A. Sarangi, C. T. Moi, S. Chakraborty, M. Qureshi, *ACS Appl. Mater. Interfaces* **2022**, *14*, 52204.

(16) S. M. Wu, L. Wu, N. Denisov, Z. Badura, G. Zoppellaro, X. Y. Yang, P. Schmuki, *J. Am. Chem. Soc.* **2024**, *146*, 16363.

(17) Z. Y. Liu, S. Jia, Y. Hu, Y. Fang, Y. Feng, D. Li, S. Bai, R. Luo, A. Chen, *Dalton Trans.* **2024**, *53*, 17059.

(18) I. P. Seetoh, A. K. Ramesh, W. X. Tan, C. Q. Lai, *Nanoscale* **2024**, *16*, 8401.

(19) M. Dhillon, A. Naskar, N. Kaushal, S. Bhansali, A. Saha, A. K. Basu, *Nanoscale* **2024**, *16*, 12445.

(20) D. Ghosh, D. K. Bora, A. B. Panda, *J. Mater. Chem. A* **2024**, *12*, 30783.

(21) S. Zhao, C. Jia, X. Shen, R. Li, L. Oldham, B. Moss, B. Tam, S. D. Pike, N. Harrison, E. A. Ahmad, A. Kafizas, *J. Mater. Chem. A* **2024**, *12*, 26645.

(22) M. Yang, Z. Fan, J. Du, C. Feng, R. Li, B. Zhang, N. Pastukhova, M. Valant, M. Finšgar, A. Mavrič, Y. Li, *Small* **2024**, *20*, 2311644.

(23) L. A. Ramos-Huerta, O. Aguilar-Martínez, V. Santes, F. J. Tzompantzi Morales, C. E. Santolalla-Vargas, *Chem. Eng. Sci.* **2024**, *294*, 120067.

(24) M. Kumar, T. C. Nagaiah, *J. Mater. Chem. A* **2023**, *11*, 18336.

(25) C. Guo, H. Xue, J. Sun, N. Guo, T. Song, J. Sun, Y. R. Hao, Q. Wang, *Chem. Eng. J.* **2023**, *470*, 144242.

(26) S. Adhikari, S. N. Steinmann, M. Arunachalam, S. H. Kang, D. H. Kim, *Small* **2024**, *20*, 2311548.

(27) Y. C. Wang, C. Y. Chang, T. F. Yeh, Y. L. Lee, H. Teng, *J. Mater. Chem. A* **2014**, *2*, 20570.

(28) Z. Feng, F. Lu, Q. Hu, J. Qiu, X. Lei, B. Wang, R. Guo, Y. Tian, X. Liu, J. You, *J. Mater. Chem. A* **2024**, *12*, 18047.

(29) N. Kalita, A. Sahu, S. Bhowmick, M. Qureshi, *Chem. Commun.* **2022**, *58*, 13747.

(30) J. Zhang, D. Li, L. Ju, G. Yang, D. Yuan, Z. Feng, W. Wang, *Phys. Chem. Chem. Phys.* **2023**, *25*, 10956.

(31) S. Niu, S. Li, Y. Du, X. Han, P. Xu, *ACS Energy Lett.* **2020**, *5*, 1083.

(32) G. Kresse, J. Furthmiiller, *Comput. Mater. Sci.* **1996**, *6*, 15.

(33) G. Kresse, J. Furthmü, *Phys. Rev. B* **1996**, *54*, 17953.

(34) J. P. Perdew, K. Burke, M. Ernzerhof, *Phys. Rev. Lett.* **1996**, *77*, 3865.

(35) P. E. Blochl, *Phys. Rev. Lett.* **1994**, *50*, 17953.

(36) H. J. Monkhorst, J. D. Pack, *Phys. Rev. B* **1976**, *13*, 5188.

(37) S. Grimme, J. Antony, S. Ehrlich, H. Krieg, *J. Chem. Phys.* **2010**, *132*, 154104.

(38) X. Zhou, H. Dong, A. M. Ren, *Int. J. Hydrogen Energy* **2016**, *41*, 5670.

(39) J. K. Nørskov, J. Rossmeisl, A. Logadottir, L. Lindqvist, J. R. Kitchin, T. Bligaard, H. Jónsson, *J. Phys. Chem. B* **2004**, *108*, 17886.

(40) L. Cao, Q. Luo, W. Liu, Y. Lin, X. Liu, Y. Cao, W. Zhang, Y. Wu, J. Yang, T. Yao, S. Wei, *Nat. Catal.* **2019**, *2*, 134.

(41) N. H. Kwon, M. Kim, X. Jin, J. Lim, I. Y. Kim, N. S. Lee, H. Kim, S. J. Hwang, *NPG Asia Mater.* **2018**, *10*, 659.

(42) G. Li, J. Yu, W. Yu, L. Yang, X. Zhang, X. Liu, H. Liu, W. Zhou, *Small* **2020**, *16*, 2001980.

(43) Y. Lu, C. Z. Zhao, J. Q. Huang, Q. Zhang, *Joule* **2022**, *6*, 1172.

(44) C. Sheng, F. Yu, C. Li, H. Zhang, J. Huang, Y. Wu, M. Armand, Y. Chen, *J. Phys. Chem. Lett.* **2021**, *12*, 2064.

(45) Y. Ma, B. Feng, J. Lang, F. Wang, Y. H. Hu, *J. Phys. Chem. C* **2019**, *123*, 25833.

(46) P. Ramirez-Vidal, R. L. S. Canevesi, G. Sdanghi, S. Schaefer, G. Maranzana, A. Celzard, V. Fierro, *ACS Appl. Mater. Interfaces* **2021**, *13*, 12562.

(47) E. Skúlason, V. Tripkovic, M. E. Björketun, S. Gudmundsdóttir, G. Karlberg, J. Rossmeisl, T. Bligaard, H. Jónsson, J. K. Nørskov, *J. Phys. Chem. C* **2010**, *114*, 18182.

(48) Y. Zheng, Y. Jiao, Y. Zhu, L. H. Li, Y. Han, Y. Chen, A. Du, M. Jaroniec, S. Z. Qiao, *Nat. Commun.* **2014**, *5*, 3783.

(49) N. Dubouis, A. Grimaud, *Chem. Sci.* **2019**, *10*, 9165.

(50) C. Tsounis, B. Subhash, P. V. Kumar, N. M. Bedford, Y. Zhao, J. Shenoy, Z. Ma, D. Zhang, C. Y. Toe, S. Cheong, R. D. Tilley, X. Lu, L. Dai, Z. Han, R. Amal, *Adv. Funct. Mater.* **2022**, *32*, 2203067.

(51) A. Ostadhossein, J. Guo, F. Simeski, M. Ihme, *Commun. Chem.* **2019**, *2*, 95.

(52) N. Yao, H. Jia, J. Zhu, Z. Shi, H. Cong, J. Ge, W. Luo, *Chem* **2023**, *9*, 1882.

CHAPTER 5

Bipolar Membrane for Water Dissociation: Electrolysis Enabled by Quaternized Pyridine-Functionalized PVA/β-Ni(OH)$_2$/Nafion BPM with Separation of HER and OER Compartments, Integrated with Asymmetric CuO Electrodes

This thesis presents a rationally engineered bipolar membrane (BPM) enabled by targeted functionalization, interfacial catalysis, and an asymmetric electrode configuration. A quaternized pyridine–functionalized PVA anion exchange membrane (AEM) with a high IEC of 2.3 mmol g^{-1} was coupled with activated Nafion (CEM). β-Ni(OH)$_2$ nanosheets introduced at the AEM/CEM interface markedly accelerated water dissociation (WD) and enhanced water uptake by 55.7%. An asymmetric electrode setup employing hollow cuboidal CuO further improved BPM-assisted water dissociation, delivering 0.90 V at ΔpH ≈ 0 (5.52 mA cm^{-2}) and 0.91 V at ΔpH ≈ 12 (7.40 mA cm^{-2}), demonstrating reduced voltage demand and high WD efficiency.

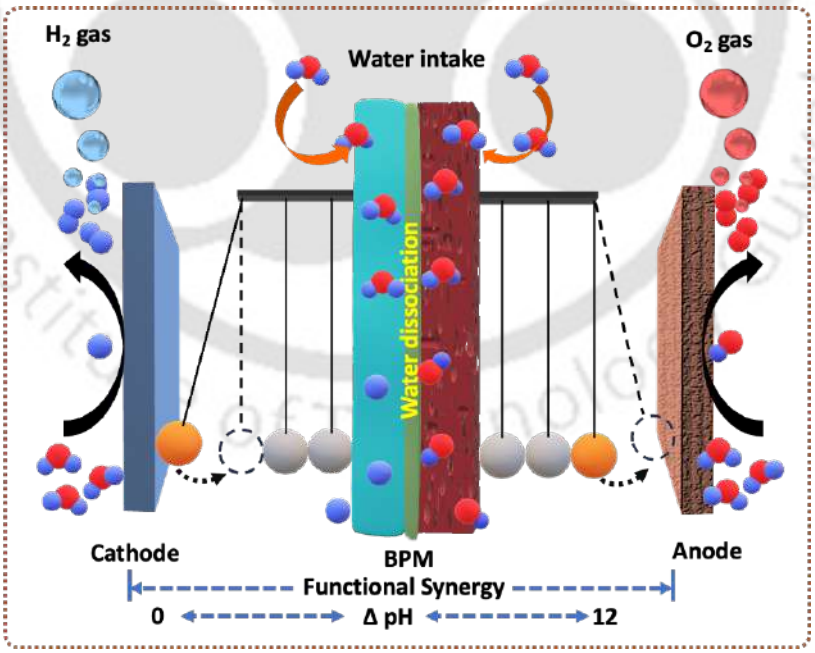

N. Kalita, et. al. *The Journal of Physical Chemistry C,* 2024, 7, 2776-2787

5.1. Introduction:

Significant endeavors have been directed towards the advancement of efficient and cost-effective catalysts aimed at mitigating the overpotential during the electrocatalytic processes of hydrogen evolution reaction (**HER**)[1] and oxygen evolution reaction (**OER**)[2] in water splitting. Little focus has been placed on the management of the transfer of reactants, ions, and products, which are also crucial occurrences for a reliable and stable electrolysis system[3,4]. In order to allow for the selective passage of electrolyte ions and the separation of the cathodic and anodic products, ion exchange membranes (IEMs) are primarily incorporated into an electrolysis system[5–7]. Bipolar membranes (**BPMs**) have been popular as alternatives to traditional anion- and cation-exchange membrane (**AEM** & **CEM**) separators due to their advantage in overcoming the difficulties associated with electrolytic cell[8–10]. In contrast to the oxygen evolution reaction, which is known to be most active in alkaline conditions, the hydrogen evolution reaction is found to be more active in acidic conditions. **BPMs**, therefore, offer the chance for the anode and cathode electrocatalyst to operate at various pH levels[8,11–13]. Consequently, using **BPM** in water electrolysis has demonstrated encouraging results, obtained by decreasing the system's overall overpotential through redox processes simultaneously under different pH conditions and by generating a pH gradient across the membrane[14,15]. Bipolar membranes comprise an anion-exchange layer (**AEL**) and a cation-exchange layer (**CEL**) attached together, which can be visualised as a p-n junction semiconductor[10,16,17]. Due to the formation of a depletion region when the BPMs are submerged in liquid electrolytes, the junction produced at the BPM interfacial layer (**IL**) has a built-in potential[10,13]. The Nernst equation provides the potential value across the **BPM**, which is dependent on the pH difference across it (Equation 5.1).

$$\Delta V_{BPM} = 2.303 \frac{RT}{F}(pH_{anolyte} - pH_{catholyte}) \quad (5.1)$$

By comparing **BPM** with a semiconductor (p-n junction), researchers were able to determine that the membrane has low resistance under forward bias conditions due to the ions that have accumulated at the junction. However, under the reverse bias, **BPM** initially exhibits high resistance (characterised by a low limiting current), then moves into a region where a small change in the voltage results in a sharp increase in the current values. The abrupt increase in current is caused by the production of H^+ and OH^- ions at the junction[10,18–20]. The fact that water dissociation only happens above a specific voltage suggests that the

electric field in the bipolar junction affects the dissociation rate[21,22]. Depending on the layer permselectivity, the BPM in an electrochemical H-cell separating two electrolytic solutions inhibits the transverse movement of co-ions (ions with the same charge as the fixed on the membrane polymer) through the membrane under the reverse bias condition[10,23]. By creating a strong electric field in the IL at a higher potential across the BPM, the resident water molecules are allowed to dissociate as a result of electrostatic polarization. The generated H^+ and OH^- upon water dissociation are the primary ionic current carriers that are going towards the cathode and anode through the **CEL** and **AEL**[24].

IEMs generally consist of extended polymeric chains containing functional groups that facilitate efficient ion migration within the membrane structure. Polymers are chosen as the foundation for IEMs due to their versatility in undergoing modifications that introduce specific charged groups. This process of functionalization enables the customization of membranes as anion **AEMs** and/or (**CEMs**), leading to improved ion exchange membrane (**IEM**) performance [25–28]. Among the available commercial options for cation exchange membranes, notable examples include Nafion, Aciplex K-101, and SFPAE-S-70[29]. Nafion, in particular, has been widely employed as a **CEM** due to its remarkable thermal, mechanical, and chemical stability[30]. However, in the case of **AEMs**, the choices are notably limited both in the literature and commercial market. In our present study, we have successfully synthesized a bipolar membrane utilizing pyridine-functionalized polyvinyl alcohol (**PVA**), which was further quaternized with bromoethane to create an efficient **AEM**, in combination with the commercial Nafion **CEM**. Meanwhile, bare **PVA** is partially water-soluble, the functionalization process with 2-pyridinecarbaldehyde effectively blocks the hydroxyl groups of **PVA**, rendering it water-insoluble and enabling its application in aqueous environments[31–33].

The optimization of the water dissociation reaction can be further advanced at the junction of the **BPM** through the introduction of a supplementary catalyst within the **IL** region. Catalysts are recognized for their ability to mitigate substantial activation energy associated with **WD** by facilitating the creation of reactive activated complexes, thereby offering alternate pathways for the reaction[34–36]. In conjunction with the integration of water dissociation catalyst **(WDC)** catalysts, achieving robust contact between the **AEL** and **CEL** is also a crucial objective, as this minimizes the interfacial resistance during the **BPM** fabrication process. To achieve this, we have utilized a Nafion perfluorinated resin solution which is found to exhibit exceptional efficacy in binding the **AEM** and **CEM** layers along with the **WDC** at the

intermediary region, including robust adhesive properties, a high capacity to retain water, favourable thermal and mechanical stability, and affinity for chemical cross-linking [37–39]. By incorporating Nafion solution within the IL, it functions as a binder that fosters improved interactions among **AEL** and **CEL** layers, while simultaneously preventing the occurrence of bubbles within the **BPM** structure. From this work, it was found that β–$Ni(OH)_2$, a recognized transition-metal hydroxide renowned for its potent catalytic and water adsorption capabilities, has emerged as a primary candidate for **WDC**. The findings of both theoretical and experimental investigations indicate the presence of non-covalent interaction between water molecules and β–$Ni(OH)_2$[40]. This interaction is characterized by a binding energy that is comparable in magnitude to that of the hydrogen bond in a water dimer. Central to this interaction is the presence of surface-exposed -OH groups, which can readily engage in hydrogen bonding with water molecules[41]. Theoretical studies have revealed that while the dissociation of an isolated water molecule encounters kinetic hindrances, the dissociation of a water molecule forming an interaction with the lattice hydrogen or oxygen of another crystal lattice, particularly from hydroxide or oxide, occurs more readily[42–45]. This enhanced dissociation process promotes the **WD** mechanism. In comparison to bulk materials and alternative nanostructured counterparts, the superiority of two-dimensional (2D) β–$Ni(OH)_2$ nanosheets as a **WDC** is evident due to their elevated specific surface area and the availability of exposed active sites, which are conducive to enhance the water adsorption. Consequently, these 2D β–$Ni(OH)_2$ nanosheets exhibit superior electrochemical and catalytic properties[46].

The present study encompasses an extensive investigation, wherein, we not only assessed the water dissociation capabilities of integrated β-$Ni(OH)_2$ nanosheets within the **BPM** context but also conducted an exploration into the influence of pH variations on water dissociation efficiency. To achieve this, various distinct local pH conditions were created within a H-cell configuration. Furthermore, our research endeavor encompassed the refinement of the electrode system. In this pursuit, we introduced an asymmetric electrode arrangement involving the introduction of hollow cuboidal CuO deposited over nickel foam (h_C-CuO@NF), serving as the anode for **OER**, alongside the utilization of a Pt cathode to facilitate the **HER**. The pivotal rationale behind adopting this asymmetrical electrode configuration was to significantly amplify the catalytic performance of both the **HER** and **OER** processes[47,48]. Specifically, the hollow cuboidal CuO electrode, characterized by its distinctive hollow

morphology results in a higher surface-to-volume ratio, which results in its improved catalytic activity for oxygen evolution across both neutral and acidic environments. In contrast, the Pt electrode demonstrated superior performance in terms of driving the hydrogen evolution reaction[49,50]. After using this asymmetric electrode setup, the noticeable difference in the performance of both water dissociation and **OER** performance highlights that our chosen electrode setup is working well.

From the current vs. voltage measurement, it is observed that the inclusion of β-$Ni(OH)_2$ nanosheet in the IL region notably improved water dissociation (WD) efficiency. Transmembrane voltage (V_{diss}) for **WD** reduced from 1.05V to 0.90V at ΔpH≈0 and from 1.20V to 0.91V at ΔpH ≈12 between the two chambers of H-cell separated by BPM. Chronopotentiometric stability test for 25 hours at 25 mA/cm^2 showed negligible transmembrane voltage change, signifying **BPM** stability. This study demonstrates the successful synthesis of a high-performance **BPM** utilizing pyridine-functionalized PVA as an AEM and β-$Ni(OH)_2$ as an IL catalyst. β-$Ni(OH)_2$ enhances **WD** efficiency, while the asymmetrical electrode system improves current density and reduces transmembrane voltages.

5.2. Materials and methods:

5.2.1. Synthesis of anion exchange membrane:

The pyridine-functionalized **PVA** was synthesized through a process involving acetalization of the hydroxyl groups in **PVA** with the aldehyde group derived from 2-pyridinecarbaldehyde. Subsequently, the polymer matrix was rendered positively charged by introducing an ethyl functional group onto the nitrogen atom of the pyridine ring. This modification resulted in the formation of a functionalized **PVA** polymer with the ability to undergo anion exchange. Scheme 1 depicts a generalized view of the synthesis process for the pyridine-functionalized **PVA** anion exchange membrane (PVA_Py_$C_2H_5^+$). Initially, 95 ml of deionized water was used to dissolve 5 g of **PVA** at 90 °C while agitating the mixture until it became homogenous and translucent. A suitable amount of 2-pyridinecarbaldehyde was then added to the **PVA** solution after cooling it to 25 °C (molar ratio of PVA:Py = 1:0.5). The aforesaid mixture's pH was then raised to 3 by adding aqueous HCl drop by drop and carried out the acetalization reaction at 75 °C for 48 hours while being constantly stirred in an argon atmosphere. The prepared pyridine-functionalized **PVA** was then subjected to a series of purification steps. First, the

polymer was precipitated into acetone to facilitate separation from the reaction mixture. Subsequently, the precipitated material was filtered, followed by thorough washing with acetone to remove impurities. Finally, the purified pyridine-functionalized **PVA** was dried under controlled conditions at a temperature of 40 °C in a vacuum oven to ensure the complete removal of residual solvent.

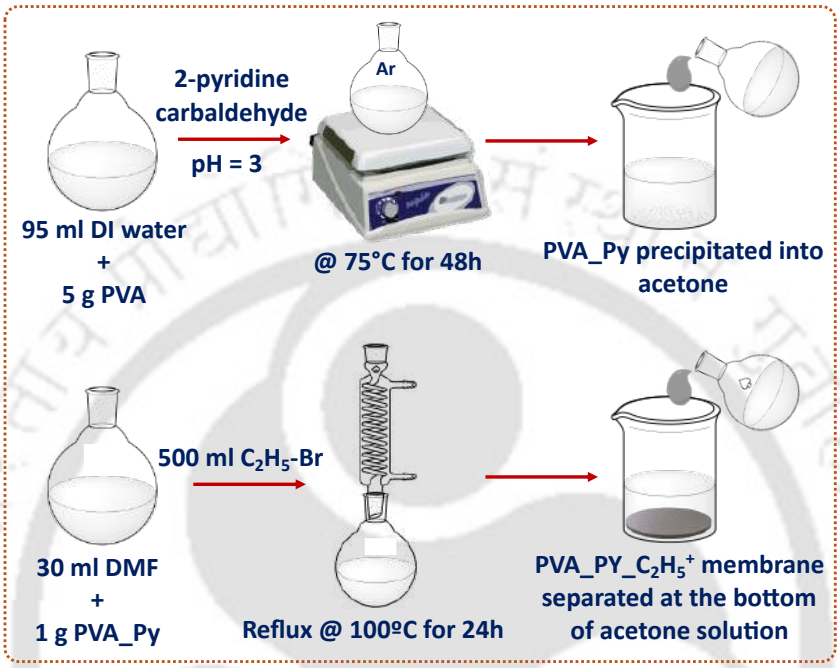

Scheme 5.1. *Schematic representation of synthesis procedure for anion exchange membrane ((PVA_Py_$C_2H_5^+$)).*

Direct quaternization of the pyridine group in the **PVA** chain by an alkyl halide was used to create the positively charged pyridine-functionalized **PVA** (PVA_Py_$C_2H_5^+$). In order to synthesize the PVA_Py quaternized with bromoethane, the as-prepared PVA_Py (1g) was first dissolved in DMF (30ml), then 500 µl of bromoethane was added while the mixture was under constant stirring. The above mixture was then allowed to keep under reflux conditions for 24 hours at 100 °C to get the final quaternized product. Thereafter the product was poured into a beaker filled with acetone and let to stand still for an hour in order to form the functionalized polymer membrane. Over the time, a thin membrane layer begins to accumulate at the beaker's bottom. By storing the obtained membrane in a 1 M KOH solution at room temperature for 24 hours, the free Br^- ions in the synthesized PVA_Py_$C_2H_5^+$ were ion-exchanged with OH^- to create PVA that has been functionalized with quaternized pyridine with free OH^- ions (Scheme 5.2).

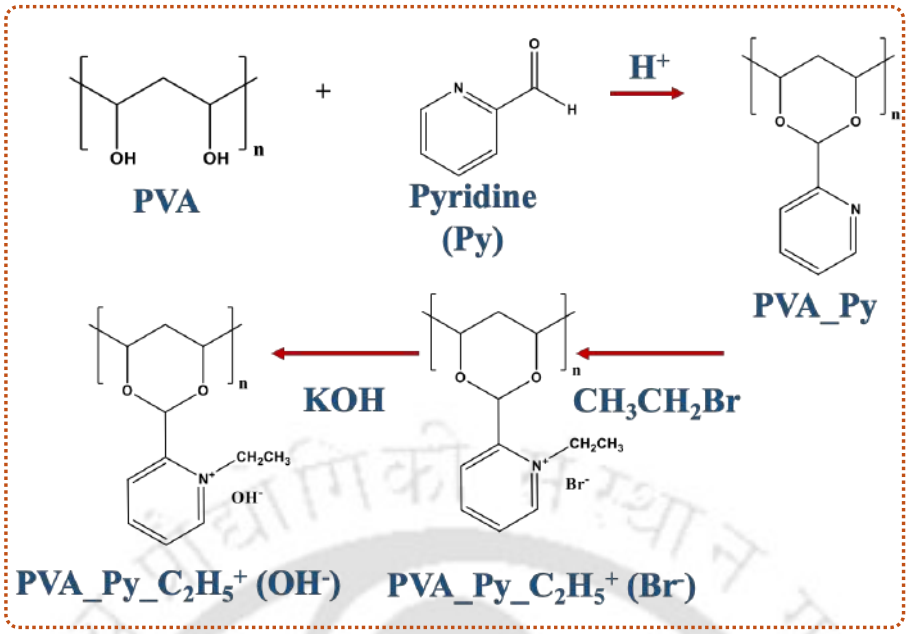

Scheme 5.2. *Overview of PVA_Py_$C_2H_5^+$ synthesis with Bromide ion exchange process.*

5.2.2. Activation of commercial Nafion membrane:

Initially, a 3% hydrogen peroxide (H_2O_2) solution was employed to immerse the Nafion membrane for a duration of one hour. Subsequently, the H_2O_2-treated membrane underwent an additional immersion step in deionized water for another hour. In both the aforementioned procedures, the temperature was maintained at 80°C. Finally, the membrane was carefully retrieved from the deionized water and stored in a 0.5 M sulfuric acid (H_2SO_4) solution at 80°C until its application for the fabrication of a bipolar membrane.

5.2.3. Synthesis of β-Ni(OH)$_2$ nanosheets membrane:

In order to synthesize β-Ni(OH)$_2$ powder, 0.35 g of Ni (II) acetate was added to 10 ml of DI water and stirred for 30 minutes to completely dissolve it. In the next step, 670 µl of 25% NH_3 was added to the mixture and stirred continuously for 24 hours in order to produce the green β-Ni(OH)$_2$ powder, which was then recovered from the solution via centrifugation process. The resulting powder was dried at 40 °C in a vacuum oven.

To fabricate the water dissociation catalyst's membrane, β-Ni(OH)$_2$ was dispersed at a concentration of 1 mg/mL in 40 ml of DI water. 2 mL of poly(4-styrene sulfonic acid) (**PSS**) solution was added during the dispersion's formation, and the mixture was allowed to be vacuum-filtered through a poly(tetrafluoroethylene) (**PTFE**) filtration membrane. Owing to β-Ni(OH)$_2$ nanosheets' high aspect ratio, they were assembled in a lamellar manner during the

vacuum-assisted filtration process evident from scanning electron microscopic studies. The resultant membrane was then carefully peeled off from the **PTFE** membrane after being dried in an oven at 80 °C.

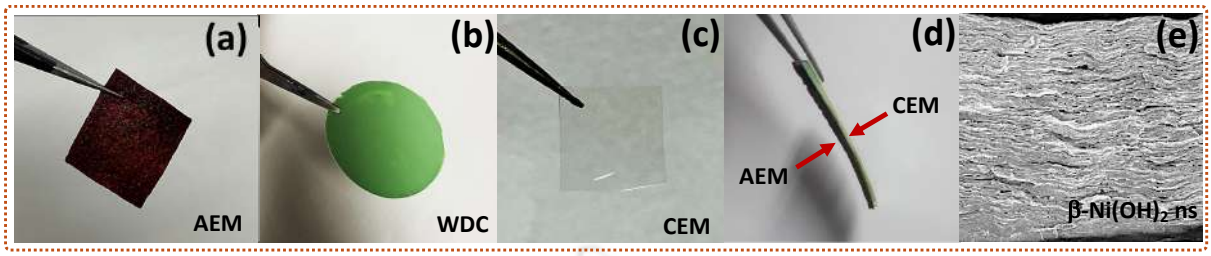

Figure 5.3. *Digital image of the individual membranes of (a) PVA_Py_$C_2H_5^+$ (AEM); (b) β-$Ni(OH)_2$ nanosheets membrane (WDC); (c) activated Nafion membrane; (d) β-$Ni(OH)_2$ nanosheets integrated bipolar membrane (BPM); (e) FESEM of the lamellar sheet's arrangement of β-$Ni(OH)_2$.*

5.2.4 Fabrication of the bipolar membrane:

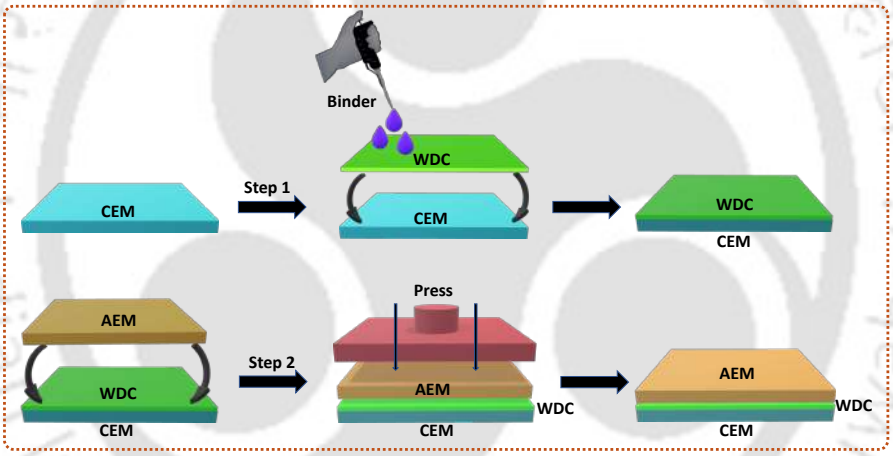

Scheme 5.1. *Schematic illustration of the stepwise fabrication of the bipolar membrane (BPM) by the lamination method. The Nafion cation-exchange membrane (CEM) is used as the bottom layer, followed by integration of the pre-synthesized β-$Ni(OH)_2$ nanosheet layer using Nafion resin as a binder, and subsequent lamination of the anion-exchange layer (AEM) under cold pressing to obtain the β-$Ni(OH)_2$-integrated BPM.*

The bipolar membrane (BPM) was fabricated by the lamination method with the addition of a binder to improve the adhesion between the layers[10]. The **AEL** and **WDC** membranes were fabricated independently using the above-mentioned process and commercial Nafion has been activated and utilized as a **CEM**. In the fabrication procedure, the Nafion membrane (2 x 2 cm^2) was used as the bottom layer and fixed to a solid surface. 50 µl of the Nafion resin solution was applied uniformly over the pre-synthesized β-$Ni(OH)_2$ membrane and placed above the Nafion membrane. The **AEM** was then placed over the

CEM_β-$Ni(OH)_2$ combination and left there for an hour under a cold press of 1 kg/cm^2 to get the final β-$Ni(OH)_2$ nanosheets integrated BPM (Scheme 5.1).

5.2.5. Synthesis of h_C-CuO@NF anode:

Hollow cuboidal copper oxide (h_C-CuO) structures were synthesized on Ni-foam substrate using an electrodeposition technique. A solution was prepared by combining 0.05 M $CuSO_4 \cdot 5H_2O$, 1.5 M sulfuric acid (H_2SO_4), and 2.5 M hydrochloric acid (HCl) in 100 mL of deionized water. The resulting solution was vigorously stirred at room temperature for 15 minutes to ensure homogeneity. For the electrodeposition process, a two-electrode cell was employed, with a pre-cleaned Ni-foam (1x0.3 cm^2) serving as the counter electrode and platinum (Pt) acting as the working electrode. A direct current (**DC**) power supply was utilized to carry out the electrodeposition, applying a current density of 1 A cm^{-2} for a duration of 1 minute. Following the electrodeposition step, the deposited film was carefully rinsed with deionized water and ethanol to eliminate any residual impurities. Subsequently, the film was dried under a vacuum at room temperature. To achieve the desired final hollow cuboidal CuO structure, the dried film underwent calcination at 350 °C for six hours, with a heating ramp rate of 1 °C per minute. This experimental process resulted in the successful fabrication of a hollow cuboidal CuO structure on the Ni-foam substrate.

5.3. Membrane characterization:

X-ray diffraction (**XRD**) patterns were recorded using a Rigaku Smartlab X-ray diffractometer equipped with a 9 kW rotating anode and copper K_α (λ = 1.54 Å) as the source. The scan rate for XRD analysis was set at 10°/min. For morphological analysis, field emission scanning electron microscopy (**FESEM**) was performed using a Zeiss Sigma 300 instrument operated at 5 kV. Field emission transmission electron microscopy (**FETEM**) was carried out using a JEOL JEM-2100F transmission electron microscope operating at 200 kV. Fourier-transform infrared (**FT-IR**) spectra were obtained using a PerkinElmer FT-IR spectrometer, (the Spectrum Two) model. Nuclear magnetic resonance (**NMR**) was acquired using a Bruker 500 MHz NMR spectrometer. Contact angles were measured using the Kruss Drop Shape Analyser-DSA-25 instrument under ambient conditions. Advancing and receding contact angles were determined by analyzing deionized water droplets at three different locations on each sample.

Mechanical properties of the polymeric membranes (2 cm × 1 cm) were analyzed using a universal testing machine (Instron 5944, Norwood, MA, U.S.A.).

The water uptake capacity percentage (**WU %**) of the membranes was determined by measuring the weight of the membranes under dry conditions (W_{dry}) and subsequently immersing them in deionized (**DI**) water for a period of 24 hours. After immersion, the membranes were carefully wiped to remove any excess water from the surfaces, and the weight was recorded as (W_{wet}). The **WU %** was calculated using the following formula:

$$WU\ \% = \frac{W_{wet} - W_{dry}}{W_{dry}} \times 100\ \% \quad (5.2)$$

Ion conductivity measurements were conducted using a Gamry interface 1010E, which allowed us to obtain Nyquist plots of the membranes. A two-probe cell configuration was employed, with the membrane placed between two copper plates. Electrochemical impedance spectroscopy (**EIS**) was performed over a frequency range spanning from 1 Hz to 10 MHz. By analysing the obtained data, the ionic conductivity of the membranes were determined using the following method

$$\sigma = \frac{l}{R \times A} \quad (5.3)$$

In the above equation, the parameter l (cm) represents the separation distance between the two electrodes. The resistance, denoted as R (Ω), is obtained from the Nyquist plot analysis. Additionally, A (cm^2) represents the geometric surface area of the prepared membrane.

The **IEC** of the pyridine-functionalized PVA anion exchange membrane was assessed through the titration method. Prior to the measurement, the **AEM** was thoroughly dried in a vacuum oven and weighed (W_{dry}). Subsequently, it was immersed in a 1 M HCl solution and allowed to remain undisturbed for 48 hours, thereby converting it to the Cl^- form. Excess Cl^- ions were eliminated by washing **DI**. The sample was then submerged in a 50 mL solution of 1 M aqueous KNO_3 for another 48 hours. The quantity of displaced Cl^- ions was determined by titrating the solution with $AgNO_3$ (0.05 M, aqueous) using K_2CrO_4 as an indicator. Finally, the IEC was calculated using the following formula:

$$IEC = \frac{C_{AgNO_3} \times V_{AgNO_3}}{W_{dry}} \quad (5.4)$$

Electrochemical measurements were conducted using a 4-probe H-cell, as depicted in section 2.5 (Figure 2.4), equipped with a Gamry interface 1010E. During the electrolysis

process, the platinum electrode was employed as the cathode for the **HER**, while h_C-CuO@NF served as the anode for the **OER** and calomel electrodes were utilized as the reference electrode. To make neutral, basic, and acidic electrolytes, 1 M aqueous solutions of NaCl, KOH, and H_2SO_4 were employed, respectively. Potentiodynamic analysis was performed to measure the voltage drop across the bipolar membrane (BPM) while increasing the applied current. The current density was swept from 0 to 25 mA/cm² at a scan rate of 0.001 mA/cm²/s, with a sampling period of 1 second. To assess the durability of the **BPM**, chronopotentiometry was conducted at a constant current density of 25 mA/cm². Before initiating the electrochemical measurements, the **BPMs** were precisely cut into uniform 1 cm × 1 cm dimensions using a doctor blade to ensure a consistent active geometric area. To monitor the pH variation during the water dissociation (WD) process, a pH meter (EUTECH pH 700) was employed.

5.4. Results and discussions:

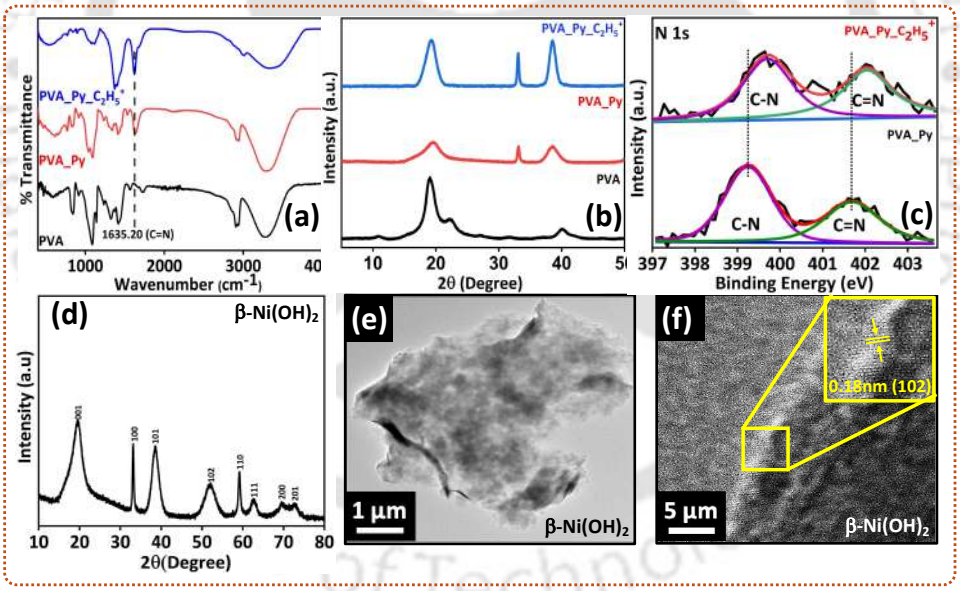

Figure 5.4. *(a) FT-IR spectra of pristine PVA, pyridine-functionalized PVA (PVA_Py), and quaternized PVA (PVA_Py_$C_2H_5^+$), confirming the successful incorporation of the pyridine ring and its subsequent quaternization through characteristic vibrational features. (b) X-ray diffraction (XRD) patterns of PVA, PVA_Py, and PVA_Py_$C_2H_5^+$, demonstrating the phase purity and structural integrity of the functionalized polymer matrices without the presence of secondary impurity phases. (c) High-resolution XPS N 1s core-level spectra of PVA_Py and PVA_Py_$C_2H_5^+$, showing a systematic shift toward higher binding energies after quaternization, indicative of the formation of positively charged pyridinium nitrogen species. (d) XRD pattern of the β-Ni(OH)₂ water dissociation catalyst (WDC),*

confirming the formation of a hexagonal β-phase with characteristic diffraction planes. (e) Field-emission transmission electron microscopy (FETEM) image of β-Ni(OH)₂ nanosheets, revealing their two-dimensional morphology. (f) High-resolution transmission electron microscopy (HRTEM) image of β-Ni(OH)₂, displaying clear lattice fringes with an interplanar spacing of ~0.18 nm corresponding to the (102) crystallographic plane.

The confirmation of the pyridine functionalization of polyvinyl alcohol (referred to as PVA_Py) and the quaternization of PVA_Py with CH_3CH_2Br (referred to as PVA_Py_$C_2H_5^+$) was conducted using the **FT-IR** spectroscopy technique. The FT-IR spectra displayed in Figure 5.4(a) clearly indicate the presence of the pyridine ring system in both PVA_Py and PVA_Py_$C_2H_5^+$, as evidenced by the prominent peak observed at 1635.20 cm^{-1}, which corresponds to the stretching frequency of the C=N bond characteristic of the pyridine ring. To verify the phase purity of the functionalized polyvinyl alcohol, the X-ray diffraction (XRD) technique was employed (Figure 5.4b). Analysis of the obtained spectra reveals the absence of potential impurity peaks in the Py_PVA and PVA_Py_$C_2H_5^+$ samples, indicating the high degree of purity and integrity of the functionalized polyvinyl alcohol. To investigate the changes in the electronic structure environment surrounding the nitrogen atom of the pyridine molecule after the quaternization process, **XPS** measurements were conducted. The N 1s core level spectra of PVA_Py and PVA_Py_$C_2H_5^+$ are presented in Figure 5.4(c). In the case of PVA_Py, the de-convoluted peaks at 399.3 eV and 402.5 eV correspond to the C-N and C=N bonds of the pyridine molecule. Upon analysis of the **XPS** spectra of PVA_Py_$C_2H_5^+$, it can be observed that both peaks from PVA_Py have shifted by ~0.45 eV towards the higher binding energies. This shift provides clear evidence of successful quaternization of the pyridine ring, resulting in the formation of a positive charge at the nitrogen atom. These observations further support the modification of the electronic environment around the nitrogen atom upon quaternization.

To elucidate the functionalization process of PVA using 2-pyridinecarbaldehyde, followed by the effective quaternization of the pyridine nitrogen with C_2H_5Br, comprehensive NMR spectroscopy was conducted on all the PVA modifications. In Figure 5.5(a), NMR data pertaining to unmodified PVA is presented. Upon closer examination within the chemical shift range of 7.40 ppm to 8.50 ppm (depicted in Figure 5.5(b)), it becomes apparent that no recognizable peaks are evident, indicating the absence of aromatic hydrogen moieties.

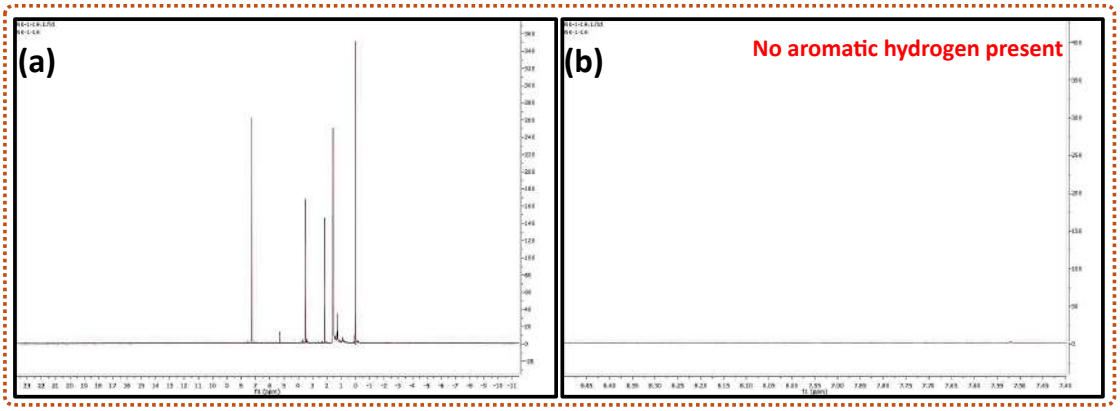

Figure 5.5. *(a) ^{1}H NMR spectrum of bare PVA, showing the characteristic signals of the polymer backbone. (b) Expanded aromatic region (7.40–8.50 ppm) of the same spectrum, confirming the absence of aromatic proton signals and thereby verifying that unmodified PVA contains no aromatic functionalities prior to chemical modification.*

Displayed in Figure 5.6(a) is the NMR data corresponding to pyridine-functionalized PVA (PVA_Py). Analysis of this data reveals the emergence of pronounced peaks within the chemical shift range of 7.40 ppm to 8.50 ppm (as depicted in Figure 5.6(b)). These peaks signify the presence of aromatic hydrogen moieties, providing clear evidence for the successful functionalization of PVA by pyridine molecules.

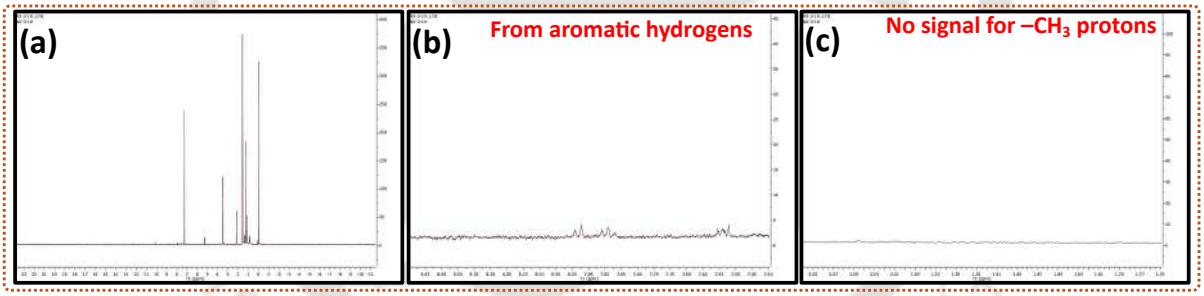

Figure 5.6. *(a) ^{1}H NMR spectrum of pyridine-functionalized PVA (PVA_Py), displaying the characteristic signals of the PVA backbone along with newly introduced resonances. (b) Expanded aromatic region (7.40–8.50 ppm), where distinct peaks assigned to pyridine protons confirm successful pyridine functionalization of PVA. (c) Enlarged aliphatic region around ~1.84 ppm, showing no significant resonance attributable to the $–CH_2$ group of a $–C_2H_5$ moiety, indicating that quaternization of the pyridine ring has not occurred at this stage.*

Figure 5.7(a) illustrates the NMR spectrum attributed to quaternized pyridine-functionalized PVA, denoted as PVA_Py_$C_2H_5^+$. Upon closer examination of the spectral region associated with aromatic hydrogen resonances, as depicted in Figure 5(b), a noticeable array of peaks originating from the pyridine ring becomes evident. Notably, following the process of quaternization, an additional triplet peak emerges around 1.84 ppm (as shown in Figure

5.7(c)). This new signal corresponds to the presence of the -CH_2 group stemming from the newly introduced -C_2H_5 moiety onto the pyridine ring structure. Significantly, this particular triplet is notably absent within the context of PVA_Py (as shown in Figure 5.7(c)).

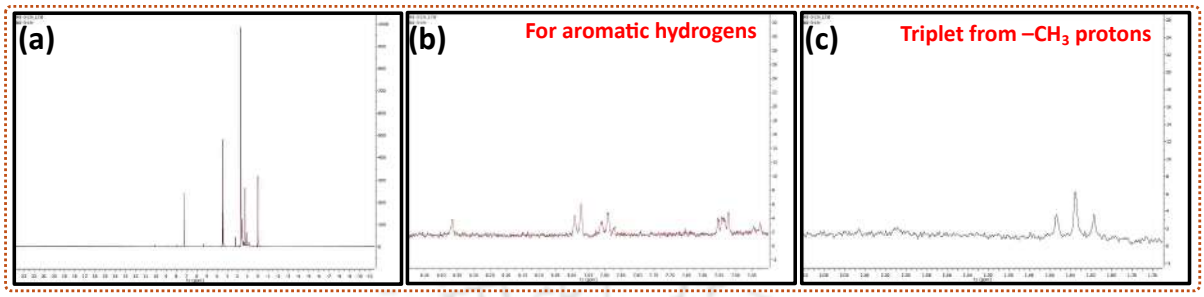

Figure 5.7. *(a) ^{1}H NMR spectrum of quaternized pyridine-functionalized PVA (PVA_Py_$C_2H_5^+$), showing additional resonances compared to PVA_Py. (b) Expanded aromatic region (7.40–8.50 ppm), where multiple peaks corresponding to pyridine protons are observed, confirming the retention of the pyridine ring after quaternization. (c) Enlarged aliphatic region highlighting the appearance of a new triplet at ~1.84 ppm, assigned to the –CH_2 group of the introduced –C_2H_5 moiety, providing clear evidence for successful quaternization of the pyridine nitrogen.*

We have undertaken the calculation of the grafting degree of the pyridine side chain into PVA and the quaternization degrees of pyridine groups by bromoethane from the NMR data. The assessment of the degree of grafting (DG %) pertaining to the pyridine side group onto the PVA molecule was carried out through the integral areal ratio of H_c to H_a peaks. Additionally, the determination of quaternization degrees of pyridine groups by bromoethane was performed by analysing the integral areal ratio of H_d to H_c. The application of the formula presented below facilitated these calculations, ensuring a precise and comprehensive analysis of the grafting and quaternization processes-

$$\text{DG \%} = \frac{A_{H_c}}{A_{H_a}/_2} \times 100\ \text{\%} \text{ (for pyridine side group at PVA)} \quad (5.5)$$

$$\text{DG \%} = \frac{A_{H_d}/_2}{A_{H_c}} \times 100\ \text{\%} \text{ (for quaternization degrees of pyridine groups by bromoethane)} \quad (5.6)$$

After calculation using the formula (5.5) and (5.6) we observed approximately 41% degree of grafting for pyridine side chain over PVA and 37% for quaternization degree of pyridine by bromoethane[51]. To benchmark our grafting percentage, we refer to relevant literature, specifically the study by Tong et al., who utilized 4-dimethylaminobenzaldehyde (DMABA) for PVA functionalization, yielding a grafting percentage of 35%. Additionally, Li et al. introduced a novel series of membranes featuring covalent self-crosslinking with a branch structure,

resulting in a observed cross-linking degree of 14%[52]. **XRD** spectra confirmed the pure formation of the β-$Ni(OH)_2$ **WDC**, displaying characteristic peaks associated with its hexagonal

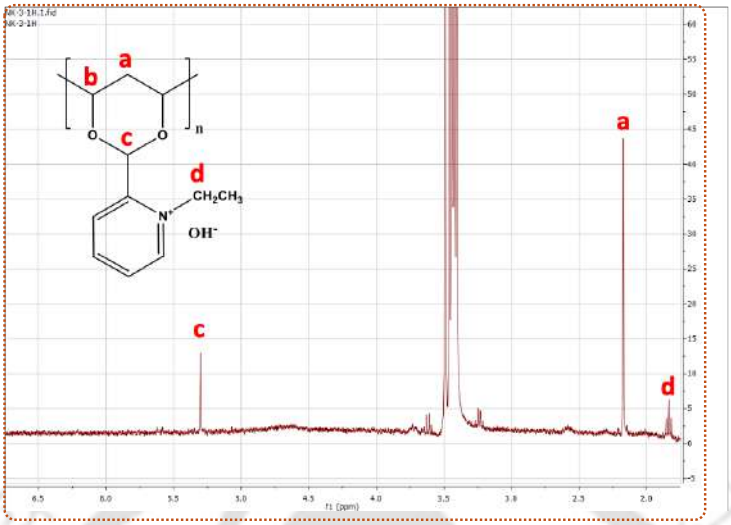

Figure 5.8. *The NMR spectra illustrate discernible peaks corresponding to protons located at positions a, c, and d, pivotal for the accurate determination of the degree of grafting.*

phase (ICSD no. 00-001-1047). Specifically, the observed peaks at (2θ) 19.1°, 33.1°, 38.6°, 52.2°, 59.1°, 62.8°, 69.5°, and 72.8° can be attributed to the (001), (100), (101), (102), (110), (111), (200), and (210) planes of β-$Ni(OH)_2$, respectively (Figure 5.4d). Figure 5.4(e) presents a transmission electron microscopy image of the β-$Ni(OH)_2$ nanosheets, illustrating its two-dimensional structural characteristics. From the high-resolution transmission electron microscopy (HRTEM) image (Figure 5.4(f)), the lattice spacing value of 0.18 nm corresponds to the (102) lattice plane of β-$Ni(OH)_2$. This finding provides further evidence of the specific crystal structure and lattice arrangement of the β-$Ni(OH)_2$ catalyst.

The individual membrane thickness and the laminated characteristics were evaluated by cross-sectional **FESEM** of each membrane separately (Figure 5.9a-c). The measurements indicate that the AEM exhibits a thickness of approximately 100 (±10) µm, whereas β-$Ni(OH)_2$ nanosheets (WDC) membrane has a thickness of 15 (±2) µm. Cross-sectional **FESEM** imaging also demonstrates the adhesion ability between the **AEM, WDC and CEM** layers in the fabricated bipolar membranes (BPMs). Figure 5.9(d) illustrates the structural features of the BPM composed of PVA_Py_$C_2H_5^+$ (**AEM**)/Nafion (**CEM**), however, a gap of approximately 10 µm at the IL region indicated lack of strong adhesion between the layers. To address this issue, the application of a Nafion resin binder has been implemented, which serves for strong adhesion between the ion-exchange layers. As illustrated in Figure 5.9(e), a cross-sectional depiction of the BPM with the binder reveals the effective cohesion achieved between these

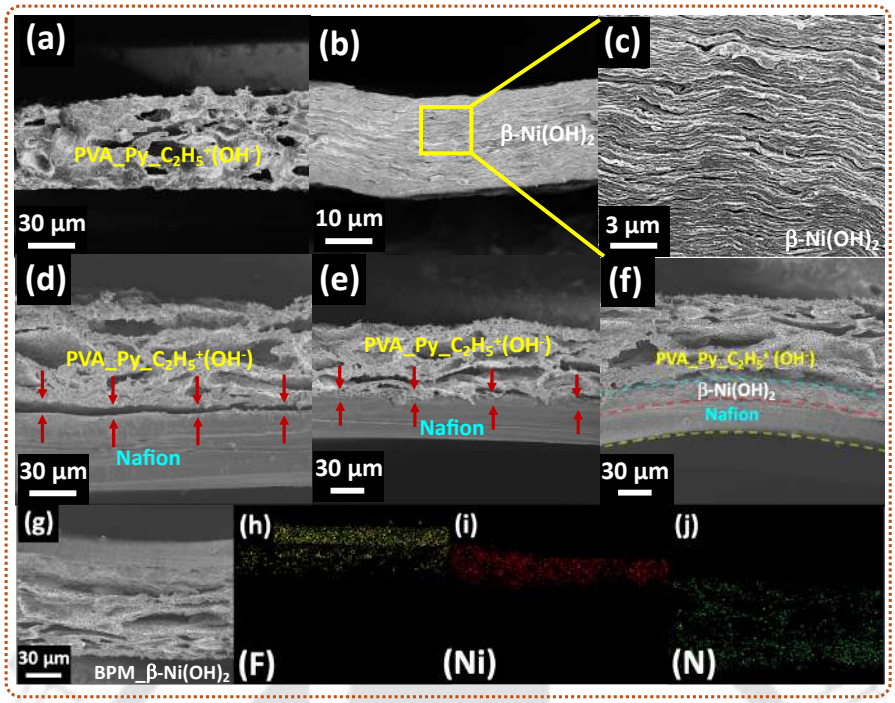

Figure 5.9. *Cross-sectional FESEM image of (a) AEM; (b) β-Ni(OH)₂ nanosheets (water dissociation catalyst); (c) high-resolution image of WDC; (d) BPM without Nafion binder; (e) BPM in the presence of Nafion binder; (f) β-Ni(OH)₂ integrated BPM; (h, i, j) FESEM-EDX mapping showing the presence of individual elements i.e fluorine from CEM (yellow) , nickel from WDC (red) and nitrogen (green) from AEM for the FESEM image (g).*

layers. Similarly, in Figure 5.9(f), the cross-sectional view of the β-Ni(OH)₂ (WDC)-integrated **BPM**, namely PVA_Py_$C_2H_5^+$(**AEM**)/ β-Ni(OH)₂ (**WDC**)/Nafion (**CEM**), displayed a layer of **WDC** with a thickness of approximately 15 (±2) µm between the **AEM** and the **CEM**. The presence of WDC in the IL region, combined with the use of the Nafion resin binder, achieved a robust adhesion between the **AEM** and **CEM** which can be clearly seen from mechanical strength measurements from the micro-**UTM** (Universal Testing Machine). From the **UTM** measurements, it can be observed that the β-Ni(OH)₂ (WDC)-integrated BPM has the highest tensile strength and Young's modulus value of 3.4 MPa and 2.5 MPa respectively compared to that of individual layers i.e. **AEM** (0.5 MPa & 1.1 MPa) and CEM (2.5 MPa & 2.3 MPa). To confirm the presence of β-Ni(OH)₂ as a **WDC** in the **IL** region, energy-dispersive X-ray spectroscopy (**EDS**) was performed. The **EDS** mapping represents the yellow colour corresponding to F atoms from Nafion (**AEM**), green indicating the N atoms from PVA_Py_$C_2H_5^+$(OH^-) (AEM), and red representing Ni atoms from β-Ni(OH)₂ within the **IL** region (Figure 5.9(h-j)).

To ensure uniformity, all membranes were cut into equal dimensions (2 cm × 1 cm), and their thickness was determined from cross-sectional **FESEM** images. The ultimate tensile strength (UTS) of the individual membranes was then determined from stress versus strain plots as shown in Figure 5.10a. UTS measurement represents the material's resistance to deformation or breakage when subjected to stretching or pulling forces. Analysis of the UTS curve reveals that the β-$Ni(OH)_2$-integrated **BPM** exhibits the highest tensile strength compared to the bare individual membranes. This result indicates the effective integration and proper bonding of the constituent membranes, i.e., the AEM, **WDC**, and **CEM**. The Young's modulus (E) values obtained from stress versus strain plots indicate that the β-$Ni(OH)_2$-integrated **BPM** has the higher E value (Figure 5.10b). The Young's modulus value, also known as the elastic modulus or modulus of elasticity, quantifies a material's stiffness or rigidity. It represents the ratio of stress to strain within the elastic deformation range.

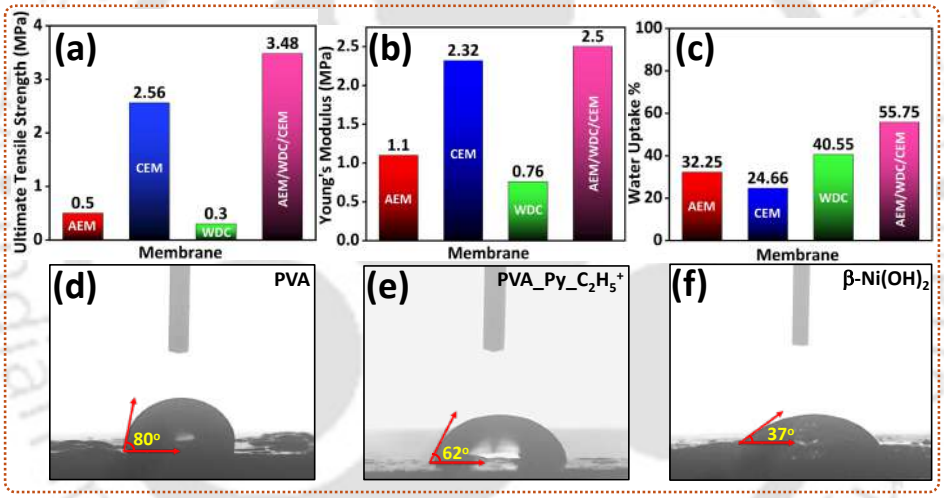

Figure 5.10 *(a) Ultimate tensile strength (UTS) of the individual membranes and the β-$Ni(OH)_2$-integrated bipolar membrane (BPM), representing the maximum stress the membrane can withstand before mechanical failure. (b) Young's modulus values derived from stress–strain curves, indicating the stiffness and elastic rigidity of the membranes within the elastic deformation region. (c) Water uptake (WU) capacities of the individual membranes, namely the anion exchange membrane (AEM), cation exchange membrane (CEM), β-$Ni(OH)_2$ layer, and β-$Ni(OH)_2$-integrated BPM, reflecting their ability to absorb and retain water, which is crucial for efficient water dissociation. (d–f) Static water contact angle measurements of (d) pristine PVA, (e) quaternized PVA_Py_$C_2H_5^+$, and (f) β-$Ni(OH)_2$, illustrating the surface wettability and hydrophilic nature of the membrane and catalyst layers.*

The increased Young's modulus in the β-$Ni(OH)_2$-integrated **BPM** can be attributed to the inherited stiffness from its constituent membranes and the presence of interfacial interactions

between them. The optimal wetting characteristics of each layer within a **BPM** system are crucial for the efficient **WD** process. Insufficient wetting capacity may result in the drying of the ion-conductive layer, leading to reduced efficiency. Conversely, excessive wetting can cause swelling of the ion-conductive layer, potentially leading to layer tearing or delamination. Figure 5.10c illustrates the **WU %** values of the individual membranes, revealing that the β-$Ni(OH)_2$-integrated **BPM** exhibits the highest water-holding capacity. This enhanced water uptake capacity can be attributed to the intrinsic property of water adsorption onto the surface of β-$Ni(OH)_2$ nanosheets and due to the presence of both **AEM** and **CEM** within the **BPM** system. The thermal stability of the membrane is also a critical parameter for high-performance **BPMs**. To assess the thermal stability, thermo gravimetric analysis (**TGA**) was employed. The **TGA** results, revealing that the synthesized anion exchange polymer membrane, PVA_Py_$C_2H_5^+$, remains stable up to 166 °C without any significant average mass loss. This suggests that quaternized PVA functionalized pyridine with C_2H_5-Br has the potential to serve as an ion exchange layer (**IEL**) for the fabrication of a stable and efficient BPM for use in the water dissociation process. At higher temperatures, pure PVA membrane demonstrated stability up to around 250 °C. Conversely, the functionalized **PVA** initiated degradation at an earlier stage, attributed to the introduction of quaternized pyridine functional groups that exhibit increased susceptibility to high-temperature-induced degradation.

For the synthesized AEM (PVA_Py_$C_2H_5^+$), the **IEC** values were determined through the titration method using equations 5.4. The obtained **IEC** values for the **AEM** were found to be within a similar range compared to state-of-the-art commercial **AEMs** listed in Table 5.1. In addition to IEC, the ionic conductivity of the individual layers is another important parameter for efficient water dissociation (WD) processes in a **BPM**. To evaluate the ionic conductivity, the resistance was measured using the Electrochemical Impedance Spectroscopy technique in a two-probe cell sandwiched between two copper plates. The ionic conductivity (σ) was then calculated from the obtained resistance values extracted from the Nyquist plots using equation 5.3. The obtained values for ionic conductivity and **WU %** of all individual membranes and layers have been compiled in Table 5.1. These measurements provide valuable insights into the performance and conductivity of each component within the BPM system, aiding in the assessment and optimization of its overall functionality.

Table 5.1. *IEC, Ionic-Conductivity, and water uptake capacity of the individual membranes and fabricated BPM.*

Membranes	IEC (mmol/g)	σ (μS/cm)	WU %
PVA_Py_$C_2H_5^+$ (AEM)	2.3	7142.8	32.2
Nafion (CEM)	1.1	253.6	24.6
β-$Ni(OH)_2$ integrated BPM		230.1	55.7

Table 5.2. *Comparison between the ion exchange capacity (IEC) values of the prepared anion exchange membrane (AEM) to those of the reported state-of-the-art AEMs.*

Membranes	IEC (mmol/g)	Ref.
PVA_Py_$C_2H_5^+$	2.3	This Work
Fumasep FAA-3-PP-75 (Commercial)	1.4-1.6	[53]
Fumasep FAA-3-50 (Commercial)	1.4-1.6	
Neosepta AFX (Commercial)	1.5-2.0	[54]
Neosepta AFM (Commercial)	2.0-3.5	

In this study, we have investigated the water-splitting process by maintaining different pH levels between the two chambers of the H-cell. Specifically, we maintained a pH difference of approximately zero (ΔpH ≈ 0), where neutral NaCl solution was present in both chambers and a pH difference of approximately twelve (ΔpH ≈ 12), achieved by using basic 1M KOH solution in one chamber and acidic 1M H_2SO_4 solution in the other chamber. For the electrolysis process, we employed a Pt electrode as the cathode for the **HER**, and a hollow cuboidal copper oxide deposited over a nickel foam (h_C-CuO@NF) as the anode for the **OER**. This choice of materials was based on the superior electrocatalytic properties of CuO, which exhibits excellent performance for water oxidation under basic conditions. By utilizing these electrode materials and creating distinct pH environments through β-$Ni(OH)_2$ integrated **BPM** consisting of novel quaternized pyridine functionalized **PVA** anion exchange layer, we aimed to investigate the water-dissociation process and evaluate the efficiency of electrochemical reactions involved in both **HER** and **OER**. This approach enables a comprehensive understanding of the fundamental processes and provides insights for the development of efficient water electrolysis systems in the presence of **BPM** separating the two chambers for HER and OER. Figure 5.11(a) shows the XRD patterns of the prepared catalyst over NF, i.e. h_C-CuO@NF, where the peaks at (2θ) 35.62°, 38.75°, 48.73°, 53.50°, 58.30°, 61.75°, 66.20°, 67.90°, and 75.30° correspond to the (002), (111), (-202), (020), (202), (-113), (022), (113), and (004) planes of CuO (ICSD no. 00-002-1040), respectively.

The morphological features of the as-prepared h_C-CuO@NF were analyzed using the Field Emission Scanning Electron Microscopy (FESEM) technique (Figure 5.11(b)). The analysis revealed a distinctive hollow cuboidal morphology of CuO, which exhibits a higher surface-to-volume ratio compared to normal cuboidal structures. This unique type of morphology is known to enhance electrocatalytic activity. Furthermore, the Transmission Electron Microscopy (TEM) image (Figure 5.11(c)) provided additional confirmation of the hollow structure of the prepared catalyst. The HRTEM analysis yielded an interplanar lattice spacing value of 0.24 nm, corresponding to the (111) lattice plane of CuO (Figure 5.11(d)).

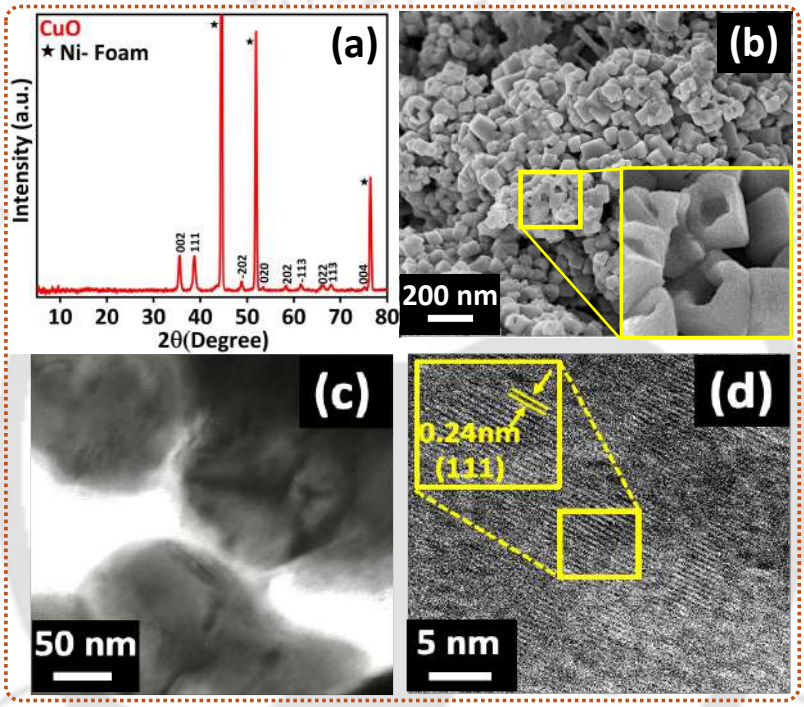

Figure 5.11. *(a) XRD pattern of hollow cubical CuO (h_C-CuO); (b,) FESEM images showing the hollow cubical structure of CuO; (c,d) FETEM and HRTEM image of h_C-CuO.*

The primary objective of fabricating **BPMs** is to facilitate the dissociation of water into its constituent ions, H^+ and OH^-. To evaluate the **WD** property of the fabricated **BPMs**, potentiodynamic analysis was conducted in a four-probe H-cell, as depicted in Figure 2.4. In this setup, an h_C-CuO@NF served as the anode, Pt electrode acted as the cathode, and calomel electrodes ($Hg/HgCl_2$) were used as the reference electrode, positioned within the Haber-Luggin capillaries. The two chambers of the H-cell were separated by the **BPM** of dimension 1 cm × 1 cm. To maintain a pH difference of ≈ 0 between the cathodic and anodic chambers of the H-cell, a 1 M NaCl electrolytic solution was utilized in both the compartment of the H-cell. To achieve a pH difference of ≈12, a 1 M KOH solution was employed in the

anodic compartment, as the **OER** process is more favorable under alkaline conditions and 1 M H_2SO_4 solution was utilized in the cathodic compartment, as the **HER** process exhibits greater feasibility under acidic conditions. Current-voltage curves (CVC) were acquired for the bipolar membranes (BPMs) under ΔpH≈0 and ΔpH≈12 conditions. At ΔpH≈0, the β-$Ni(OH)_2$-integrated BPM exhibited a transmembrane voltage (V_{trans}) of 1.09 V at a current density of 10 mA/cm^2, whereas the bare BPM required V_{trans} of 1.45 V. For ΔpH≈12, the β-$Ni(OH)_2$-integrated BPM achieved a V_{trans} of approximately 0.99 V at 10 mA/cm^2, while the bare BPM necessitated 1.31 V. These results indicate that the incorporation of β-$Ni(OH)_2$ enhances the catalytic properties of the BPM, resulting in an improved water dissociation within the interlayer (IL) region.

To gain a comprehensive understanding of the current-voltage curve (CVC) and evaluate the overall catalytic performance of the **BPMs**, the CVC can be divided into distinct regions[55]. The first region corresponds to the Ohmic resistance (R_{ohm}) of the membrane system. Following this, the second region represents the pseudo-limiting current ($I_{p\text{-}lim}$), which characterizes the current density resulting from the transportation of co-ions across the membranes. In this second region, the continuous flux of co-ions through the respective IEMs causes a depletion of salt ions at the IL region. Consequently, a higher resistance is formed, leading to an increase in the potential across the **BPM** with only a slight increment in current density. The inflection point at the end of the pseudo-limiting region corresponds to the minimum voltage required between the layers to initiate **WD** known as V_{diss}. The third region which signifies the **BPM's** ability to enhance the WD process is known as the **WD** resistance (R_{diss}). In this region, the membrane voltage surpasses the **WD** potential (V_{diss}), leading to a substantial WD occurring in the IL region generating H^+ and OH^- ions contributing to the total current during the process. As shown in Figure 5.12(a-b), the incorporation of β-$Ni(OH)_2$ into the bipolar membrane significantly lowers the voltage required to initiate the **WD** process (V_{diss}). Specifically, when the pH difference between the chambers is ≈ 0 and ≈ 12, water dissociation begins at 0.90V and 0.91V, respectively. Conversely, in the absence of β-$Ni(OH)_2$, water dissociation commences at 1.05V and 1.25V under the same pH difference conditions. The incorporation of β-$Ni(OH)_2$ into the bipolar membrane facilitates the interaction between water molecules and β-$Ni(OH)_2$ through non-covalent hydrogen bonding[55]. This interaction lowers the activation energy required for the water dissociation process, thereby enhancing its efficiency[40]. The contact angle measurements (Figure 5.10(f)) further confirmed the pronounced hydrophilicity of β-$Ni(OH)_2$, underscoring its favorable interaction with water. The

higher hydrophilicity of β-$Ni(OH)_2$ can be due to the presence of abundant surface hydroxyl groups facilitates the formation of hydrogen bonds with water molecules, promoting strong interactions and increased wettability. Upon comparing the contact angles of **PVA** (Figure 5.10d) and PVA_Py_$C_2H_5^+$ (AEM) (Figure 5.10e), notable differences emerge. The introduction of a positively charged functional group into the polymer matrix of **AEM** establishes an electrostatic attraction force between the polymer and water molecules, augmenting wettability. This augmentation results in stronger adsorption and a subsequent reduction in the contact angle for **AEM** as compared to bare **PVA**. Upon analyzing the current-voltage curve (CVC), it is evident that within the pseudo-limiting current region, the **WDC** integrated bipolar membrane (BPM) consistently exhibits higher current values compared to the bare **BPM** at any transmembrane potentials (V_{trans}). This higher current indicates that in addition to the crossover of co-ions, **WD** also occurs in this region to generate protons and hydroxide ions, even at activities below unity[54].

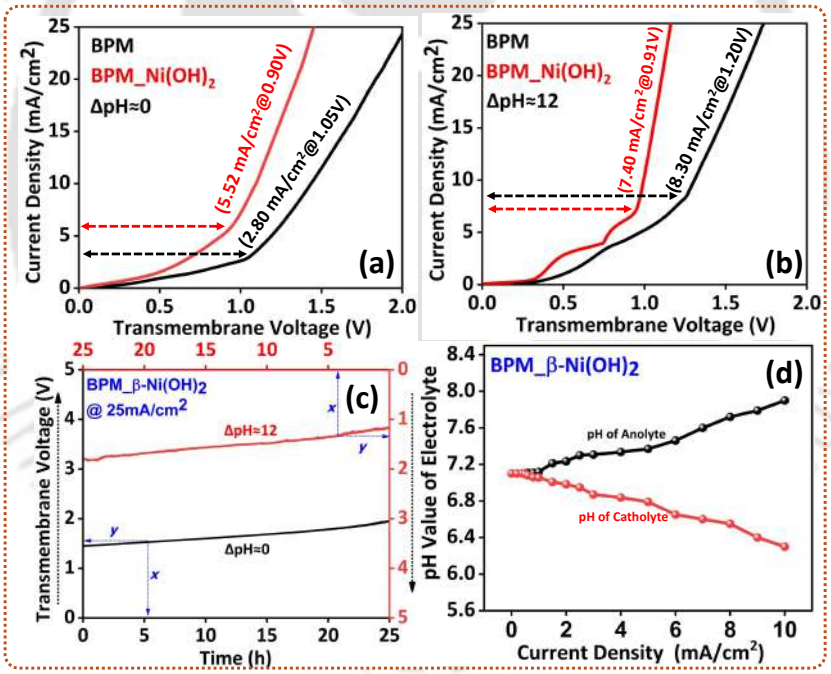

Figure 5.12. *CVC of BPM and β-$Ni(OH)_2$ integrated BPM at (a) @ ΔpH ≈ 0 (neutral medium on both the chambers of the H-cell); (b) @ ΔpH ≈ 12 (acidic in one chamber and basic on the other chamber of the H-cell); (c) Chronopotentiometry curve of β-$Ni(OH)_2$ integrated BPM at ΔpH≈0 (back) and ΔpH≈12 showing its stability for 25 hours operating at a current density of 25 mA/cm²; (d) plot of pH change of the anolyte and catholyte vs current density during the WD reaction for β-$Ni(OH)_2$ integrated BPM.*

To gain a deeper understanding of the crossover of co-ions in the pseudo-limiting region and the **WD** process, the pH variations of the electrolyte solution (1 M NaCl) in both

the cathodic (catholyte) and anodic (anolyte) chambers were measured as a function of current density for the β-$Ni(OH)_2$ integrated **BPM**, as depicted in Figure 5.12(d). Initially, at zero current density, the pH values of both the catholyte and anolyte were identical and were found to be 7.01. As the current density increased, the pH values of both chambers remained constant up to 0.60 mA/cm^2, indicating that the observed current was solely a result of the co-ion influx across the **BPM** layers. Beyond 0.60 mA/cm^2, a slight but noticeable change in the pH values of both the catholyte and anolyte was observed, indicating the occurrence of **WD** and the production of H^+ and OH^- ions at activities lower than unity alongside the co-ion transport. As the current density surpassed 5 mA/cm^2, the pH values exhibited wider variations with increasing current density, suggesting an intensified **WD** reaction and the extensive generation of H^+ and OH^- ions.

The water dissociation mechanism is depicted in Figure 5.15, illustrating the role of β-$Ni(OH)_2$ in enhancing the **WD** performance of the composite BPM. The optimization of the AEM thickness was carried out by systematically varying the membrane thickness and measuring the current-voltage curves (**CVC**) of the **BPM**. Figure S10(a) illustrates the **CVC** of **BPM** in the absence of β-$Ni(OH)_2$ in the **IL** region with different thicknesses. It was observed that a thickness of approximately 100 (±10) µm for the AEL resulted in improved **WD** performance. This enhancement can be attributed to the effective incorporation of water and reduced co-ion transport at higher current densities. The quantity of WDC present in the **IL** region plays a vital role in the performance of the **BPM**. An increase in the thickness of the layer with a higher **WDC** amount leads to elevated electrical resistance between the layers. On the other hand, a thinner layer has a reduced capacity to retain water for dissociation, potentially resulting in the drying up of the interfacial region[55]. To optimize the amount of **WDC** in the **BPM**, we fabricated a **WDC**-integrated **BPM** utilizing the **AEM** that exhibited the most promising results from the thickness optimization process. For the **WDC** amount optimization, we prepared **WDC** membranes by dispersing β-$Ni(OH)_2$ in water at concentrations ranging from 0.5 mg/ml to 1.5 mg/ml and subsequently forming membranes of diameter 3.5 cm using vacuum assisted filtration method. Through analysis of the **CVC**, we observed that the **WDC** membrane created using a 1 mg/ml dispersion of β-$Ni(OH)_2$ demonstrated the most favorable outcome in terms of water dissociation. This concentration yielded the highest performance among the tested dispersions, suggesting its effectiveness as an optimal **WDC** amount for the **BPM**.

In addition to achieving high **WD** performance, the long-term stability of **WDC** integrated bipolar membrane is also a crucial parameter to consider. To evaluate its durability, chronopotentiometry analysis was conducted at a current density of 25 mA/cm^2, corresponding to the **WD** potential (V_{diss}), under both ΔpH≈0 and ΔpH≈12 (Figure 5.12(d)) conditions. The analysis revealed that even after 25 hours of continuous testing, there was only a negligible decrease in the WD performance of the fabricated **BPM**, indicating its high stability. Prior to the analyses, the BPM underwent a drying process under a vacuum to eliminate any adsorbed water molecules.

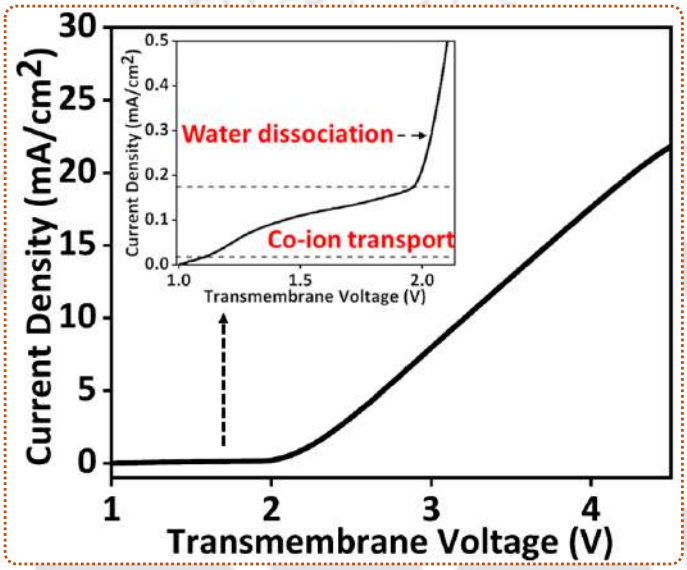

Figure 5.13. *The current vs. voltage curve under the symmetric electrode setup using β-Ni(OH)$_2$ integrated BPM as the separator between the two chambers of H-cell.*

To evaluate the impact of utilizing h_C-CuO@NF as the anodic material on the water dissociation process, we conducted a comprehensive analysis of the current-voltage curves (CVC). For this study, we employed Pt electrode in both the anodic (for **OER**) and the cathodic compartment (for **HER**) in the H-cell configuration, under ΔpH≈0 conditions. Remarkably, we observed a significantly higher V_{diss} (approximately 2V) in this system compared to the system where h_C-CuO@NF was employed in the anodic compartment and Pt electrode in the cathodic compartment (Figure 5.13). These findings strongly indicate that the incorporation of an asymmetric electrode setup in the H-cell configuration yields superior results compared to the symmetric configuration. This observation can potentially be attributed to the enhanced OER activity of h_C-CuO due to the increased surface-to-volume ratio resulting from the unique hollow cubical morphology. Consequently, these factors facilitate improved current flow between the electrode surface and the electrolyte solution. To assess the catalytic activity

enhancement resulting from the incorporation of the membrane in the H-cell configuration, we conducted a comparative analysis of the **OER** polarization curves (Figure 5.14).

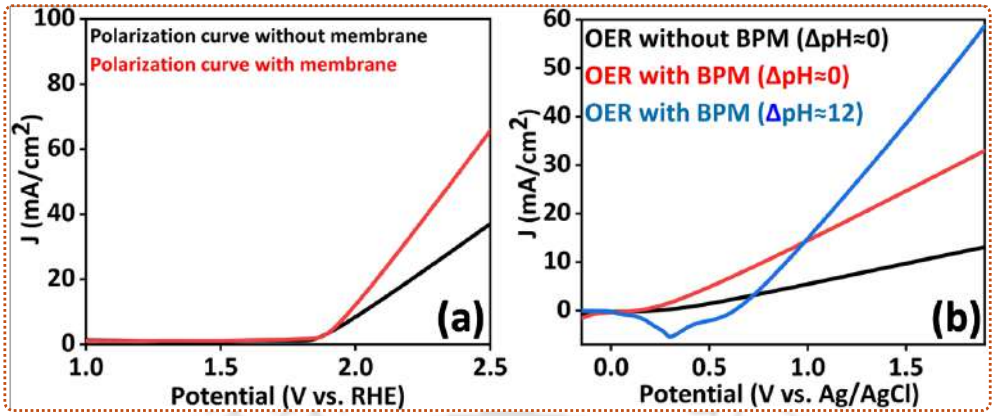

Figure 5.14. *(a) Polarization curve for water oxidation in the presence and absence of BPM; (b) polarisation curve for water oxidation at ΔpH≈0 (black; in the absence of membrane), ΔpH≈0 (red; in the presence of BPM) and ΔpH≈12 (blue; in presence of membrane).*

By maintaining a neutral NaCl solution on both sides of the electrolytic cell, we observed that the presence of the BPM yielded improved **OER** kinetics, as evidenced by the polarization curve. In contrast, the absence of the BPM in the system exhibited inferior **OER** performance. This observation highlights the beneficial impact of the **BPM** on the catalytic activity of the OER process.

5.5. Conclusions:

In this manuscript, we present a high-performance **BPM** fabricated using pyridine-functionalized **PVA** as the **AEM** and activated Nafion membrane as the cation exchange membrane (CEM), with β-$Ni(OH)_2$ incorporated between the two layers (interlayer, **IL**) of the BPM as the water dissociation catalyst. During the fabrication process of the **AEM**, we successfully functionalized **PVA** with pyridine and further quaternized the nitrogen atom from pyridine with an ethyl group. This functionalization process increased the hydrophilicity of the polymer membrane, as confirmed by contact angle measurements, resulting in improved water uptake capacity. Moreover, the functionalization of **PVA** rendered it water-insoluble by blocking the -OH groups through an acetalization reaction with 2-pyridinecarbaldehyde. Our analysis revealed that the incorporation of β-$Ni(OH)_2$ in the **IL** region significantly enhanced the efficiency of the **WD** reaction. The transmembrane voltage (V_{diss}) required for WD was reduced from 1.05V to 0.90V at ΔpH ≈ 0 between the two chambers of the H-cell and from 1.20V to 0.91V at a pH difference of ΔpH ≈ 12. Furthermore, we have investigated the effect

of an asymmetric electrode system by employing Pt electrode for the **HER** side and synthesized hollow cuboidal CuO deposited on a nickel foam (h_C-CuO@NF) for the **OER** side. We observed that this configuration resulted in higher current density and more efficient water dissociation at lower transmembrane voltages, which is more prominent at ΔpH≈12. To demonstrate the high performance and stability of the composite **BPM**, we conducted a 25-hour test run at a constant current density of 25 mA/cm^2. The results showed negligible changes in the transmembrane voltage, indicating the excellent stability of the **BPM** under these conditions. In summary, our findings highlight the successful fabrication of a high-performing **BPM** using pyridine-functionalized **PVA** as the **AEM** and β-Ni(OH)$_2$ as the **IL** water dissociation catalyst. The incorporation of β-Ni(OH)$_2$ enhances the efficiency of the **WD** reaction, while the asymmetric electrode system improves current density and reduces transmembrane voltages.

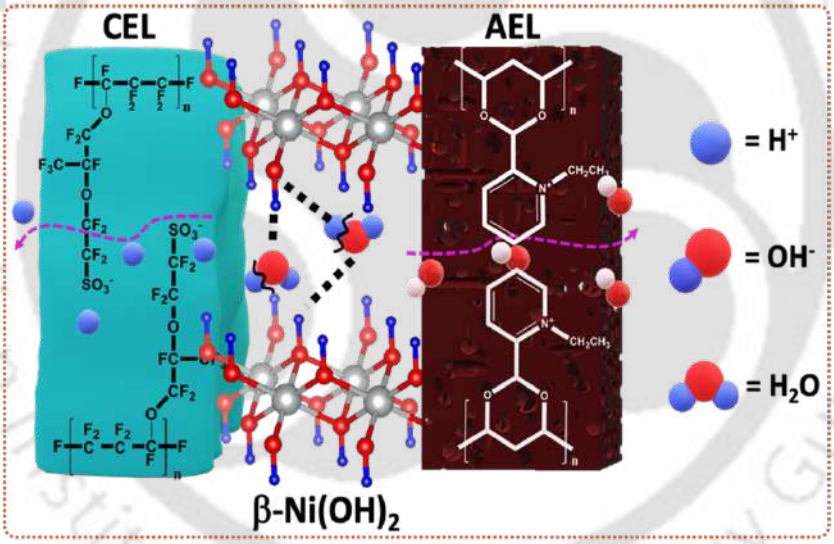

Figure 5.15. *Schematic mechanism of the plausible mechanism for water dissociation in 2D-Ni(OH)$_2$ integrated BPM, where β-Ni(OH)$_2$ acts as the water adsorption site and aids in the water cleavage process, generating H$^+$ and OH$^-$ ions.*

While the implementation of this composite BPM and asymmetric electrode configuration effectively resolves the challenges of product separation and demonstrates robust performance under significant pH gradients (e.g., ΔpH≈12), the reliance on extreme localized pH environments continues to pose long-term challenges for industrial scalability, including component corrosion and environmental safety concerns. To further advance the sustainability and practical deployment of these energy conversion systems, the subsequent

chapter investigates water electrolysis under entirely neutral conditions. Given the inherently sluggish kinetics associated with neutral water splitting, this next phase of research introduces a novel strategy employing redox synchronization between homogeneous and heterogeneous catalysts. By facilitating more efficient charge transfer pathways, this approach aims to overcome the kinetic barriers of neutral media

5.6. References:

1. X. Zheng, X. Shi, H. Ning, R. Yang, B. Lu, Q. Luo, S. Mao, L. Xi and Y. Wang, *Nat. Commun.*, **2023**, *14*, 4209.
2. C. Fang, J. Zhou, L. Zhang, W. Wan, Y. Ding and X. Sun, *Nat. Commun.*, **2023**, *14*, 4449.
3. S. Chabi, K. M. Papadantonakis, N. S. Lewis and M. S. Freund, *Energy Environ. Sci.*, **2017**, *10*, 1320–1338.
4. M. A. Modestino, S. M. H. Hashemi and S. Haussener, *Energy Environ. Sci.*, **2016**, *9*, 1533–1547.
5. J. Brauns, J. Schönebeck, M. R. Kraglund, D. Aili, J. Hnát, J. Žitka, W. Mues, J. O. Jensen, K. Bouzek and T. Turek, *J. Electrochem. Soc.*, **2021**, *168*, 014510.
6. S. Thiele, B. Mayerhöfer, D. McLaughlin, T. Böhm, M. Hegelheimer and D. Seeberger, *ACS Appl. Energy Mater.*, **2020**, *3*, 9635–9645.
7. H. A. Miller, K. Bouzek, J. Hnát, S. Loos, C. I. Bernäcker, T. Weißgärber, L. Röntzsch and J. Meier-Haack, *Sustain. Energy Fuels*, **2020**, *4*, 2114–2133.
8. D. Powers, A. N. Mondal, Z. Yang, R. Wycisk, E. Kreidler and P. N. Pintauro, *ACS Appl. Mater. Interfaces*, **2022**, *14*, 36092–36104.
9. J. Balster, R. Sumbharaju, S. Srikantharajah, I. Pünt, D. F. Stamatialis, V. Jordan and M. Wessling, *J. Membr. Sci.*, **2007**, *287*, 246–256.
10. R. Pärnamäe, S. Mareev, V. Nikonenko, S. Melnikov, N. Sheldeshov, V. Zabolotskii, H. V. M. Hamelers and M. Tedesco, *J. Membr. Sci.*, **2021**, *617*, 118538.
11. S. Z. Oener, M. J. Foster and S. W. Boettcher, *Science*, **2020**, *369*, 1099–1103.
12. S. Chabi, A. G. Wright, S. Holdcroft and M. S. Freund, *ACS Appl. Mater. Interfaces*, **2017**, *9*, 26749–26755.
13. Z. Yan, R. J. Wycisk, A. S. Metlay, L. Xiao, Y. Yoon, P. N. Pintauro and T. E. Mallouk, *ACS Cent. Sci.*, **2021**, *7*, 1028–1035.

14. S. Chabi, A. G. Wright, S. Holdcroft and M. S. Freund, *ACS Appl. Mater. Interfaces*, **2017**, *9*, 26749–26755.
15. D. A. Vermaas, M. Sassenburg and W. A. Smith, *J. Mater. Chem. A*, **2015**, *3*, 19556–19562.
16. F. Hanada, K. Hirayama and S. Tanaka, *US Pat.*, **1993**, 5221355.
17. H. Strathmann, *Desalination*, **2010**, *264*, 268–288.
18. B. Lovrecek, A. Despic and J. O. M. Bockris, *J. Phys. Chem.*, **1959**, *63*, 750–751.
19. V. J. Frilette, *J. Phys. Chem.*, **1956**, *60*, 435–439.
20. R. A. Tufa, M. A. Blommaert, D. Chanda, Q. Li, D. A. Vermaas and D. Aili, *ACS Appl. Energy Mater.*, **2021**, *4*, 7419–7430.
21. R. Simons, *Electrochim. Acta*, **1985**, *30*, 275–282.
22. P. Ramirez, H.-J. Rapp, S. Mafé and B. Bauer, *J. Electroanal. Chem.*, **1994**, *375*, 101–108.
23. D. A. Vermaas, S. Wiegman, T. Nagaki and W. A. Smith, *Sustain. Energy Fuels*, **2018**, *2*, 2006–2015.
24. P. K. Giesbrecht and M. S. Freund, *Chem. Mater.*, **2020**, *32*, 8060–8090.
25. Y. Liu and J. Wang, *J. Membr. Sci.*, **2020**, *596*, 117591.
26. N. M. Jalal, A. R. Jabur, M. S. Hamza and S. Allami, *Energy Procedia*, **2019**, *157*, 1494–1501.
27. P. T. Nonjola, M. K. Mathe and R. M. Modibedi, *Int. J. Hydrogen Energy*, **2013**, *38*, 5115–5124.
28. K. Venugopal and S. Dharmalingam, *Desalination*, **2012**, *296*, 37–45.
29. M. Pan, C. Pan, C. Li and J. Zhao, *Renew. Sustain. Energy Rev.*, **2021**, *141*, 110771.
30. V. Romero, M. V. Martínez de Yuso, A. Arango, E. Rodríguez-Castellón and J. Benavente, *Int. J. Electrochem.*, **2012**, *2012*, 349435.
31. X. J. Meng, Q. L. Liu, A. M. Zhu and Q. G. Zhang, *J. Membr. Sci.*, **2010**, *360*, 276–283.
32. C. Y. Wong, W. Y. Wong, K. S. Loh, W. R. W. Daud, K. L. Lim, M. Khalid and R. Walvekar, *Polym. Rev.*, **2020**, *60*, 171–202.
33. J. Qiao, T. Hamaya and T. Okada, *J. Mater. Chem.*, **2005**, *15*, 4414–4420.
34. Z. Ge, M. A. Shehzad, L. Ge, Y. Zhu, H. Wang, G. Li, J. Zhang, X. Ge, L. Wu and T. Xu, *ACS Appl. Energy Mater.*, **2020**, *3*, 5765–5773.
35. M. Manohar and D. Kim, *ACS Sustain. Chem. Eng.*, **2019**, *7*, 16493–16502.

36. S. Abdu, K. Sricharoen, J. E. Wong, E. S. Muljadi, T. Melin and M. Wessling, *ACS Appl. Mater. Interfaces*, **2013**, *5*, 10445–10455.
37. H. Y. Jung, J. Y. Kim and J. K. Park, *Solid State Ionics*, **2011**, *196*, 73–79.
38. M. B. Karimi, F. Mohammadi and K. Hooshyari, *Int. J. Hydrogen Energy*, **2019**, *44*, 28919–28938.
39. M. S. McGovern, E. C. Garnett, C. Rice, R. I. Masel and A. Wieckowski, *J. Power Sources*, **2003**, *115*, 35–39.
40. S. Jahangiri and N. J. Mosey, *Phys. Chem. Chem. Phys.*, **2018**, *20*, 11444–11455.
41. G. Wang, Y. Ling, X. Lu, T. Zhai, F. Qian, Y. Tong and Y. Li, *Nanoscale*, **2013**, *5*, 4129–4133.
42. C. Chen, K. Ruengkajorn, J. C. Buffet and D. O'Hare, *RSC Adv.*, **2018**, *8*, 34650–34660.
43. K. Jug, B. Heidberg and T. Bredow, *J. Phys. Chem. C*, **2007**, *111*, 6846–6851.
44. M. Zubair, M. Daud, G. McKay, F. Shehzad and M. A. Al-Harthi, *Appl. Clay Sci.*, **2017**, *143*, 279–292.
45. S. Bhowmick and M. Qureshi, *ACS Appl. Mater. Interfaces*, **2023**, *15*, 5466–5477.
46. M. Aghazadeh, A. N. Golikand and M. Ghaemi, *Int. J. Hydrogen Energy*, **2011**, *36*, 8674–8682.
47. X. R. Wang, J. Y. Liu, Z. W. Liu, W. C. Wang, J. Luo, X. P. Han, X. W. Du, S. Z. Qiao and J. Yang, *Adv. Mater.*, **2018**, *30*, 1800005.
48. T. J. Dai, J. Sun, X. S. Peng, J. N. Gong, Z. Y. Zhou and X. Q. Wang, *Energy Sci. Eng.*, **2022**, *10*, 4061–4071.
49. A. K. Shah, S. Bhowmick, D. Gogoi, N. R. Peela and M. Qureshi, *Chem. Commun.*, **2021**, *57*, 8027–8030.
50. S. Vijayapradeep, N. Logeshwaran, R. Shanmugam, R. K. Ae, S. Prabhakaran, H. K. Do and J. Y. Dong, *Chem. Eng. J.*, **2023**, *473*, 145348.
51. T. Mu, R. Liu, N. Shi, G. Wang and J. Yang, *ACS Appl. Polym. Mater.*, **2023**, *5*, 7110–7120.
52. J. Li, J. Liu, W. Xu, J. Long, W. Huang, Y. Zhang and L. Chu, *Chem. Eng. J.*, **2022**, *437*, 135414.
53. N. Du, C. Roy, R. Peach, M. Turnbull, S. Thiele and C. Bock, *Chem. Rev.*, **2022**, *122*, 11830–11874.
54. J. Luo, C. Wu, T. Xu and Y. Wu, *J. Membr. Sci.*, **2011**, *366*, 1–16.
55. S. Hu, Y. Li, D. Kim, M. Liu, L. Y. S. Lee and K. Y. Wong, *EcoMat*, **2022**, *4*, e12256.

CHAPTER 6

Hybrid Homogeneous–Heterogeneous Catalysis for Electrochemical Water Splitting and CO_2 Reduction

This chapter explores the integration of homogeneous molecular catalysts with heterogeneous electrode materials to enhance electrochemical catalytic transformation through synergistic hybrid interfaces. **Chapter 6a** focuses on water electrolysis, where bispidine-based Ni(II) complexes are coupled with β-$Ni(OH)_2$ electrodes to promote redox synchronization, efficient charge transfer, and enhanced oxygen evolution kinetics. **Chapter 6b** extends this strategy to electrocatalytic CO_2 reduction, demonstrating that bispidine-based Cu complexes interfaced with $Cu_{1.5}Mn_{1.5}O_4$ spinel electrodes enable efficient electron relay, improved C–C coupling, and highly selective CO_2-to-ethanol conversion. Overall, the chapter establishes hybrid homogeneous–heterogeneous catalysis as a powerful approach for advancing sustainable electrochemical water splitting and carbon conversion technologies.

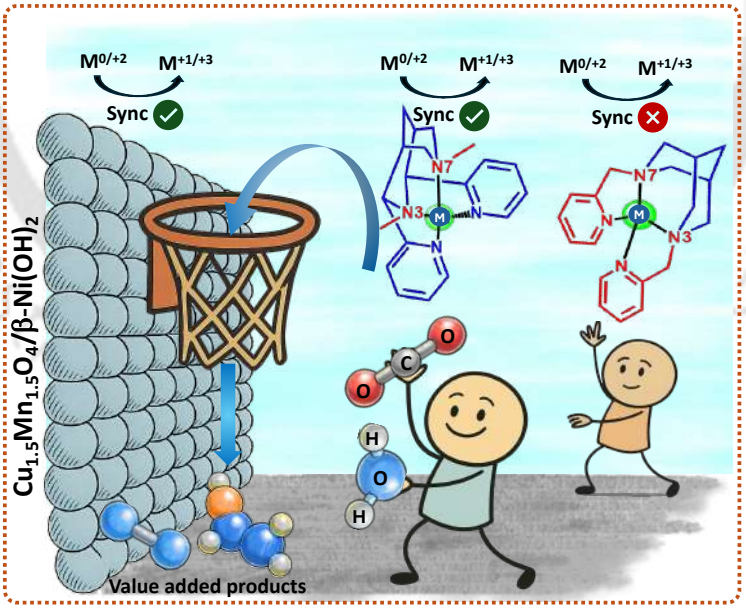

N. Kalita, et. al. *Chemistry of Materials*, 2025, 5, 2026–2037

N. Kalita, et. al. *J. Mater. Chem. A,* 2026, Just Accepted.

6a.1. Introduction:

Extensive research has been carried out towards substituting fossil fuels with sustainable energy alternatives like hydrogen produced via water splitting, mimicking artificial photosynthesis.[1–3] This process involves two half-reactions: oxygen and hydrogen evolutions respectively.[4] Identified as the primary challenge in water splitting, water oxidation involves a complex, energy-intensive and thermodynamically uphill four electron process. Consequently, substantial research endeavors have been focused on enhancing water oxidation catalysts, spanning molecular systems and materials.[1,5] Electrocatalytic water splitting, powered by renewable energy for clean H_2 production, is regarded as a viable approach among existing hydrogen generation methods. However, this technique is hindered by the significant energy requirements due to a high electrolysis potential barrier.[5] To overcome this, an effective oxygen evolution reaction (OER) catalyst must exhibit excellent catalytic activity, durability in electrochemical activity over the long term, and affordability. Currently, two primary catalytic strategies are employed in the water electrolysis process for water oxidation: heterogeneous[6–8] and homogeneous[9–11] catalysis. In heterogeneous catalysis, the focus is on engineering electrode materials tailored for enhanced electrolysis efficiency. This approach leverages the solid-state nature of catalysts to facilitate direct electron transfer processes at the electrolyte/electrode interface. On the other hand, homogeneous catalysis involves the development of soluble transition and non-transition metal complex molecules to enable electron transfer in a uniform reaction medium. Researchers in this domain aim to refine the electrolyte system by incorporating these synthesized catalysts and optimizing the reaction environment for improved efficiency.

When discussing homogeneous and heterogeneous catalytic systems, it is important to acknowledge that each method exhibits distinct advantages and limitations. Heterogeneous catalysis is highly regarded for its robustness and sustainability in long-term applications as well as its possibility of efficiently accelerating chemical reactions at a lower cost.[12] However, it often suffers from lower catalytic activity due to the electrocatalytically active surface area and active sites availability. On the contrary, homogenous water oxidation catalysis shows distinct advantages over heterogeneous catalysis through comprehensive mechanistic investigations and the ability to tailor chemical structures and properties.[13] However, it

encounters challenges in minimizing overpotential value, primarily due to the absence of an efficient catalyst in heterogeneous part (electrode materials), capable of functioning in synchronization with the homogeneous part under neutral pH conditions.

To date, catalysts based on scarce earth elements such as ruthenium (**Ru**)[14,15] and iridium (**Ir**)[16,17] have demonstrated higher efficiencies in both homogeneous and heterogeneous catalytic systems. For heterogeneous catalysis, high conductivity, durability, and cost-effectiveness are crucial factors. Currently the focus has shifted towards development of cost-efficient catalysts based on first-row transition metals.[18-30] Despite extensive studies that has already been done on material-based improvements for heterogeneous catalysts using strategies such as elemental doping,[31] morphological tuning,[32] and heterojunction[33] creation etc., but performance enhancements through the modification of electrolytic solutions in the presence of the homogenous catalyst remain scarce. Ruthenium (**Ru**) and iridium (**Ir**) water oxidation catalysts (WOC) have also demonstrated high efficiencies in homogeneous catalysis.[34-40] Consequently, recent research has extensively focused on WOC based on earth-abundant elements such as manganese (**Mn**), iron (**Fe**), cobalt (**Co**), nickel (**Ni**), and copper (**Cu**).[41] Notably, the Mn_4O_4Ca WOC in photosystem II is a rare example of a natural catalyst operating effectively at neutral pH.[42–44] Developing a first-row catalyst from more abundant elements that function at neutral pH and low overpotential remains a significant challenge in this field.

Recent pioneering research has highlighted the exceptional features of transition metal-based hydroxides as heterogeneous electrocatalysts for water oxidation.[45–47] Specifically monometallic transition metal hydroxides (MTMH) have been widely studied as cost-effective electrocatalysts for water oxidation in alkaline media, showing promising O_2 evolution capabilities. Despite their potential, these catalysts often show poor activity under neutral buffer conditions, limiting their broader applicability.[48] Yushan Yan and colleagues reported a simple method for α-$Ni(OH)_2$ nanocrystals, demonstrating their remarkable OER activity and stability in alkaline media.[49] Their study found that this highly nanostructured α-$Ni(OH)_2$ catalyst achieves a current density of 10 mA cm^{-2} at an overpotential of just 331 mV, with a Tafel slope of about 42 mV/dec in 0.1 M KOH. The superior OER performance is attributed to the in-situ formation of the γ-NiOOH phase, where the highly oxidized Ni (average oxidation state of 3.6) facilitates the formation of hydroperoxy (OOH) species, crucial intermediates in the OER, leading to efficient O_2 production. From the literature, it is observed that OER activity

in heterogeneous catalysis more effective under strong basic media due to high conductivity and OH^- availability, but in neutral media, its activity diminishes, and overpotential increases due to low conductivity. To address this, we combined homogeneous and heterogeneous catalysis to enhance charge transfer between the two phases, which in turn reduces the activation energy and improve reaction kinetics.[50]

Various homogenous based Ni(II) complexes are reported for electrochemical water oxidation reaction. For example, Ding's group reported mononuclear Ni(II) complexes with a series of tetradentate ligand frameworks, with the tetradentate N_4 based ligand act as a homogeneous molecular catalyst, whereas other complexes such as N_3O and N_2O_2 based Ni(II) complexes decompose into NiO_x nanoparticles, functioning as precatalysts.[53] Additionally, Najafpour and colleagues presented a tetranuclear Ni(II) complex with ligand HL, HL = bis-[(*E*)-*N*'-(1-(pyridin-2-yl)ethylidene)]carbohydrazide, which catalyzes water oxidation, with the active species being nickel oxide or free Ni(II) ions.[54] Additionally, the Sun group designed a Ni-Py5 complex, which functions as a homogeneous electrocatalyst for water oxidation in aqueous phosphate buffer solutions.[4] Junyu et al. prepared two water-soluble molecular nickel(II) homogenous catalysts,[43] where they have studied the effect of backbone flexibility of these N5-pentadentate ligands on the electrochemical water oxidation performance in neutral aqueous solutions. The second complex required an overpotential of 700 mV to reach a current density of 1 mA cm^{-2}, which is 40 mV less than that required by the first complex. The mentioned literature indicates that homogeneous catalysts based on Ni complexes exhibit a proper alignment of redox potentials with the electrochemical requirements of the OER process, demonstrating that their addition to the electrolyte positively impacts electrochemical performance. In terms of toxicity, nickel is also considered a` greener and more sustainable alternative to heavy metals like palladium, platinum, and gold, which pose environmental risks through leaching. Additionally, nickel is an essential trace nutrient crucial for biological processes in living organisms.[55] The limitation for 1st row transition elements as compared to the noble metal counterparts is the smaller atomic size of 1st row TM ions lowers its ability to accommodate the oxidative equivalents required in the $4e^-/4H^+$ water oxidation catalysis process, unlike noble metal catalysts that perform single site electrocatalysis at lower overpotentials (η).

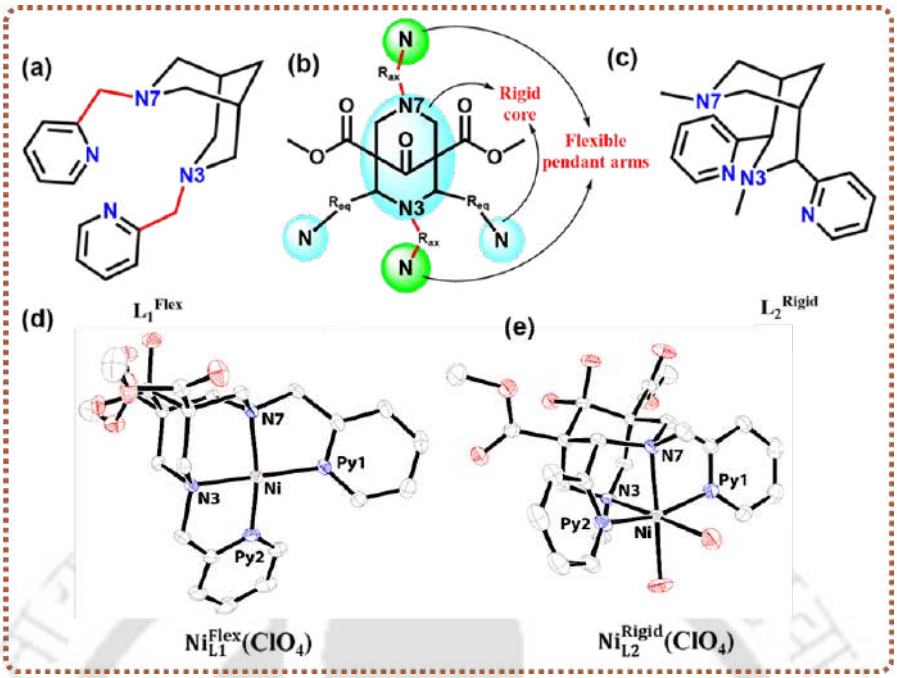

Figure 6a.1. *(a,b,c) ligand structurers (d,e) crystal structure (ORTEP images) of the corresponding metal complexes utilized in this study. (Hydrogens and counter ions are omitted for better clarity (Prob=30%).*

To the best of our knowledge, no detailed research has been conducted till now that combines both homogeneous and heterogeneous catalysis into a single system to study their behavior in the electrocatalytic water oxidation process. In this work, we aim to combine the fields of homogeneous and heterogeneous catalysis to leverage the benefits of both systems while addressing their individual limitations through charge transfers across the interfaces.[50] Here we have demonstrated how homogeneous catalysts enhance charge transfer kinetics at the phase interface by acting as redox mediator or forming transient species, reducing activation energy and charge transfer resistance. In this work, we have synthesized β-$Ni(OH)_2$ nanoflowers deposited on Ni foam as a heterogeneous counterpart and utilized two geometrically distinct Ni(II) tetradentate bispidine based complexes as homogeneous catalysts, dissolved in the electrolyte solution. The two ligands used have same molecular formula ($C_{23}H_{26}N_5O_5$) but distinct ligand architectures. The ligand L_1^{Flex} (dimethyl-3,7-bis(pyridine-2-ylmethyl)-9,9-hydroxo-3,7,-diazabicyclo[3.3.1]nonane]-1,5-dicarboxylate), contains two pendant pyridyl arms on to N3 and N7 nitrogens of the bispidine framework. These pendant arms will impart the flexibility to the metal center during the coordination. The ligand L_2^{Rigid} (dimethyl-2,4-bis(2-pyridyl)-3,7-dimethyl-9,9-hydroxo-3,7, -diazabicyclo[3.3.1]nonane]-1,5-dicarboxylate) has the two pyridine groups directly connected

to the adamantane backbone of the bispidine framework thus imparting an overall rigidity. This strategy has resulted in two different coordination environments around the Ni center. The use of nickel throughout the electrolysis system enhances the redox synchronization, thereby improving the catalytic activity.

6a.2. Experimental Section:

6a.2.1. Synthesis of Heterogeneous catalyst (β-Ni(OH)$_2$ @NF):

For the synthesis of β-Ni(OH)$_2$ over NF substrate we have taken a hydrothermal synthesis route. In this process at first Ni foam (NF) was cleaned by treating it sequentially in acetone, 1M HCl solution, deionized water, and absolute ethanol, each for 25 minutes. Subsequently, 3 mmol of nickel nitrate hexahydrate ($Ni(NO_3)_2 \cdot 6H_2O$) and 6 mmol of urea were dissolved in 60 mL of deionized water and ultrasonicated for 30 minutes. The resulting mixture, along with the pre-treated NF, was then transferred into a 50 mL Teflon-lined autoclave, which was filled to two-thirds of its volume with the solution. The autoclave was heated in an oven at 200°C for 12 hours to facilitate the growth of β-Ni(OH)$_2$ nanoflowers. After deposition, the β-Ni(OH)$_2$@NF electrodes were removed from the Teflon vessel and cleaned with deionized water and ethanol to eliminate any impurities.

6a.2.2. Synthesis of Homogeneous catalyst:

6a.2.2.1. Synthesis of L1$_{flexible}$ ligand:

Ligand L1$_{flex}$ was synthesized by modifying the previously reported procedures.[56,57] Dimethyl acetonedicarboxylate (1 eq.) was taken in 20 mL of CH_3OH and was cooled to 273 K. A solution of Formaldehyde (2 eq.) and 2-picolylamine (1 eq.) were added to it dropwise. After completion of addition, the solution was allowed to stir at 273 K overnight. The white precipitate thus obtained was faltered and washed with cold ethanol and dried in vacuum. The product obtained was of high purity (> 97%) and used as such for the next step.

To a suspension of the above obtained white solid (1 eq.) in 200 mL ethanol, aqueous formaldehyde (37%, 2.1 eq.) and 2-picolylamine (1 eq.) were added dropwise. The reaction was allowed to reflux for 4 h. The brown solution obtained after the end of the reaction was concentrated and kept at 258 K. White solid was obtained after several days. The white solid was recrystallized from acetonitrile.

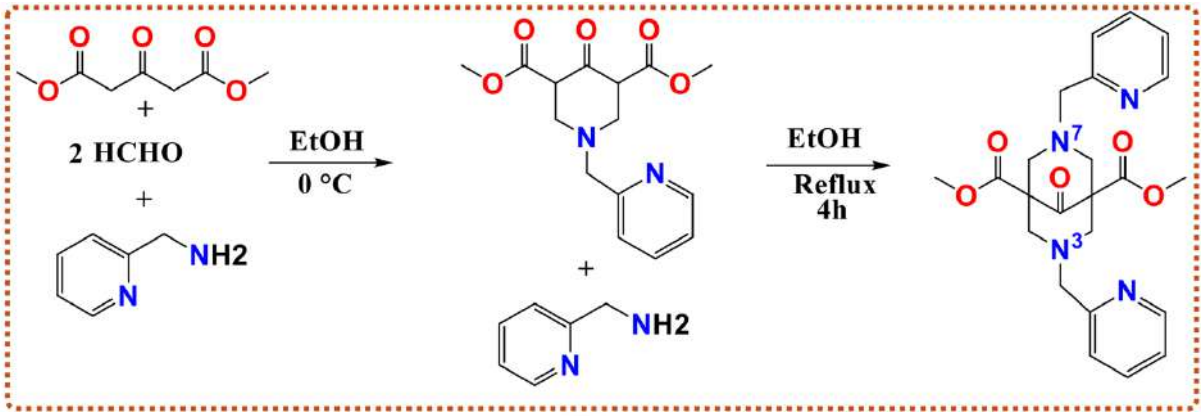

Figure 6a.2. *Synthetic rout for the preparation of L1 flexible ligand.*

6a.2.2.2. Synthesis of $L2_{rigid}$ ligand:

The ligand $L2_{rigid}$ was synthesized by following a previously reported procedure.[58] Dimethyl acetonedicarboxylate (4.80 mL, 33.33 mmol) was dissolved in 20 mL of methanol and cooled to -10 °C. To this solution, a mixture of pyridine-2-carboxyaldehyde (6.37 mL, 66.66 mmol) and methylamine (33.33 mmol) was added dropwise. Following the complete addition, the reaction mixture was stirred at room temperature overnight. The resulting white precipitate of piperidone was collected by filtration, washed with cold ethanol, and dried under vacuum. The obtained product exhibited sufficient purity and was directly used for the synthesis of bispidines ligand L2. The yield was approximately 84%.

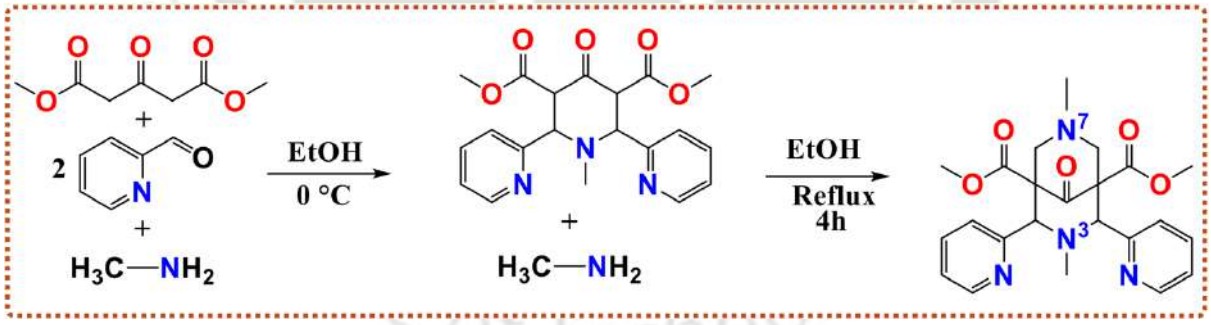

Figure 6a.3. *Synthetic rout for the preparation of L2 rigid ligand.*

A suspension of the above synthesized piperidone (12.70 g, 33.10 mmol) in 200 mL of ethanol was prepared. To this, aqueous formaldehyde (37%, 6.50 mL, 79.40 mmol) and methylamine (39.70 mmol) were added dropwise. The mixture was then refluxed for 4 hours. After the reaction, the resulting clear brown solution was concentrated to half its volume and stored at -20 ºC. White crystals formed after several days.

6a.2.2.3. Synthesis of Ni(II) complexes:

Ligand L_1^{Flex} & L_2^{Rigid} were reacted with Ni(II) perchlorate. Hydrate in acetonitrile as solvent. The reaction was continued overnight. The reaction mixtures were filtered using PTFE filters and the solution were layered with ether and kept inside the fridge at 233 K to get the desired Ni(II) complexes. Suitable crystal for $[Ni_{L1}^{Flex}(ClO_4)]$ were grown by slow vapor diffusion to the acetonitrile solution of the complexes. Whereas we didn't get the crystals for $[Ni_{L2}^{Rigid}(ClO_4)]$. So, we choose Ni(II)-$BF_4.4H_2O$ as the metal precursor and reacted with ligand L2 in acetonitrile solvent. The reaction continued overnight and then the reaction mixture was filtered and the solution was layered with ether to get the Ni(II) complex. The $[Ni_{L2}^{Rigid}]$ rigid complex was dissolved in water and to it added aqueous NH_4PF_6 solution. The solution was filtered and kept at room temperature to get the purple crystal of $[Ni_{L2}^{Rigid}(PF6)]$.

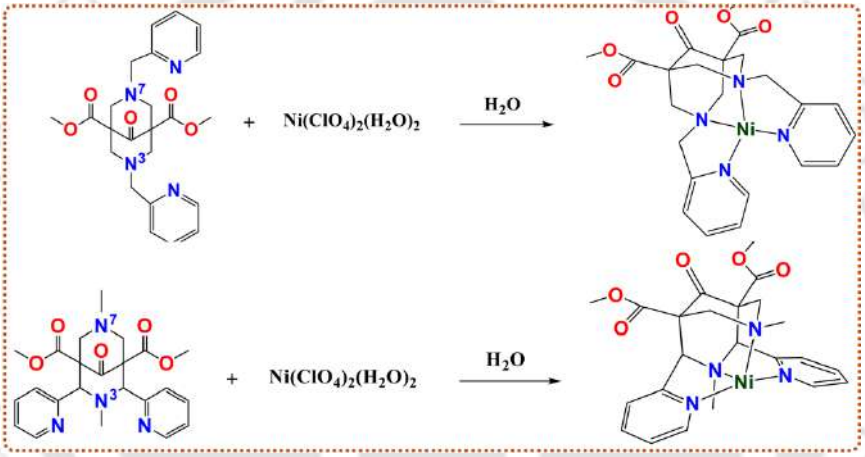

Figure 6a.4. *Schematic representation for the synthesis of* Ni_{L1}^{Flex} *and* Ni_{L2}^{Rigid} *complexes.*

6a.3. Results and discussion:

For the synthesis of the heterogeneous catalyst β-$Ni(OH)_2$ nanoflowers on Ni-foam (NF) substrate, a hydrothermal process was employed, as detailed in the experimental section. The X-ray diffraction (XRD) spectra confirmed the formation of the β-$Ni(OH)_2$ deposited over NF, displaying characteristic peaks associated with its hexagonal phase (ICSD no. 00-001-1047). Specifically, the observed peaks at (2θ) 19.2°, 33.1°, 38.7°, 59.1°, and 62.9° can be attributed to the (001), (100), (101), (110), and (111) planes of β-$Ni(OH)_2$, respectively (Figure 6a.5a). The morphological features of the heterogeneous catalyst are depicted in Figure 6a.5(b), where the Field Emission Scanning Electron Microscopy (FESEM) images reveal the nanoflower structure of the synthesized β-$Ni(OH)_2$. The flower-like structures observed are an accumulation of two-dimensional β-$Ni(OH)_2$ layers. This morphology results in an increased

surface-to-volume ratio, thereby creating a larger electrocatalytically active reaction sites.[32] Additionally, the High-Resolution Transmission Electron Microscopy (HRTEM) image in Figure 6a.5(c) identifies a lattice spacing of 0.16 nm, corresponding to the (110) lattice plane of β-$Ni(OH)_2$. This observation confirms the specific crystal structure and lattice arrangement of the β-$Ni(OH)_2$ catalyst.

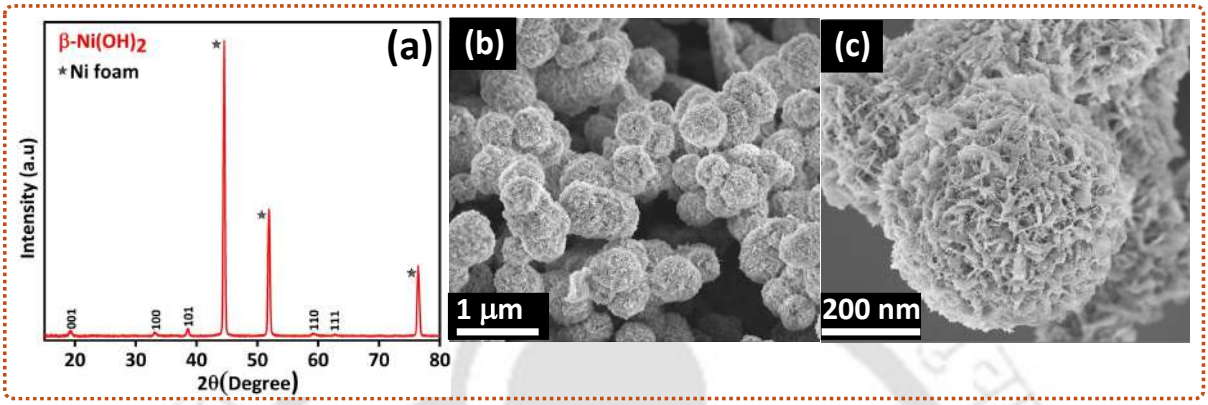

Figure 6a.5. *(a) XRD patterns of β-$Ni(OH)_2$ nanoflowers; (b,) FESEM images of β-$Ni(OH)_2$ nanoflowers; (c) HRTEM images of β-$Ni(OH)_2$ nanoflowers.*

For homogeneous catalysts, we have opted for bispidine based tetradentate ligands. Metal complexes bearing bispidine ligands are well documented to be an excellent bioinspired oxidants due to their ability to form and stabilize high valent metal center.[52] The ligands ($L1_{Flex}$ & $L2_{Rigid}$) were synthesized by employing double Mannich reactions to give white solid in good yields. The ligands were well characterized by ^{1}H and ^{13}C NMR (Figure 6a.6). Addition of $[Ni^{II}(H_2O)_6](ClO_4)_2$ to a solution of ligands L_1^{Flex} and L_2^{Rigid} in acetonitrile yielded the corresponding Nickel(II) complexes: $[Ni^{II}(L_1^{Flex})(H_2O)_2](ClO_4)_2$ (Ni_{L1}^{Flex}) and $[Ni^{II}(L_2^{Rigid})(H_2O)_2](ClO_4)_2$ (Ni_{L2}^{Rigid}) (detail explanations are given in the experimental section).

Single crystals suitable for XRD studies were grown by slow vapor diffusion to the acetonitrile solution of the metal complexes. These Nickel (II) complexes were characterized with UV-vis absorption spectroscopy (Figure 6a.7a), electrospray ionization mass spectrometry (ESI-MS) (Figure 6a.7b-c) and single crystal X-ray diffraction studies Figure 6a.1(d,e).[65] The UV-vis spectrum of both Nickel(II) complexes shows a ligand-to-metal charge-transfer band with a notable shift in the molar extinction coefficient (ε) and λ_{max} values (Figure 6a.7a). The difference in the absorption coefficient and λ_{max} values observed in the UV-vis spectra clearly illustrate the difference in the electron density arising due to change in the coordination environment. The ESI-MS spectra of both these complexes show prominent

peaks at m/z of 613.08 and 257.06, which corresponds to the $[Ni(II)^{Flex,Rigid}_{L1,L2}(ClO_4)(H_2O)]^+$ and $[Ni(II)^{Flex,Rigid}_{L1,L2}(H_2O)]^{2+}$ molecular ion fragments. The single crystal

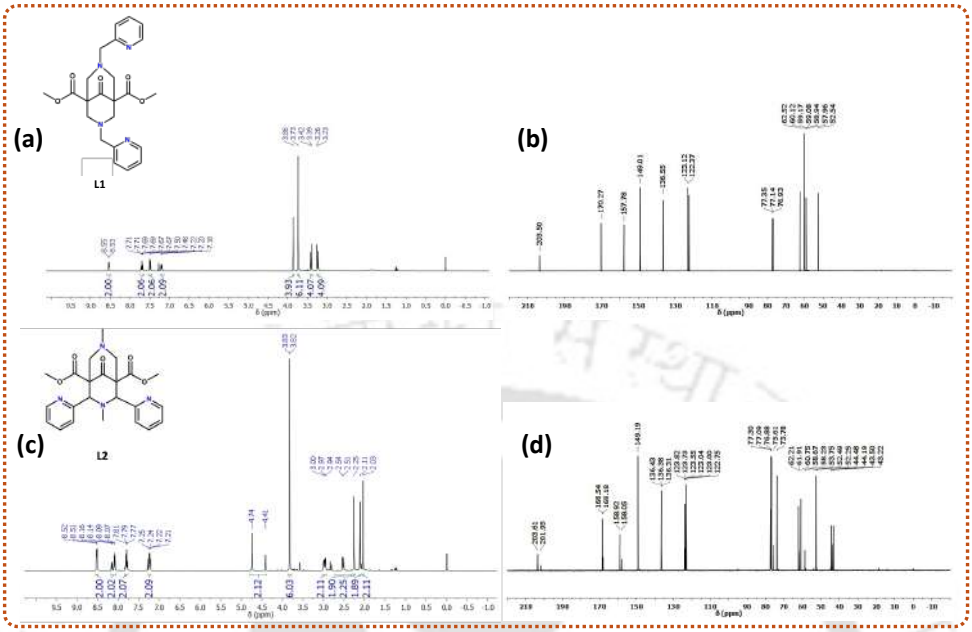

Figure 6a.6. *(a-b) ^1H NMR and ^{13}C NMR data for L_1^{Flex} ligand in $CDCl_3$ confirming the successful formation of the ligand framework and the expected proton and carbon environments.; (c-d) ^1H NMR and ^{13}C NMR data for L_2^{Rigid} ligand in $CDCl_3$ validating its molecular structure and chemical integrity prior to metal coordination.*

structure of the complex; $[Ni^{Rigid}_{L2}]$ was reported earlier with Ni in the distorted octahedral geometry with aqua coordinated to the two vacant sites. The structure shows that the two coordinatively vacant sites occupied by water are at positions trans to N7 (axial) and N3 (equatorial) histidine nitrogens. The two pyridine N atoms occupy the equatorial plane. On contrary, the single crystal structure of $[Ni^{Flex}_{L1}]$ is in distorted tetrahedral geometry with no coordination of water molecules. This clearly illustrates that the rigid backbone of Ni^{Rigid}_{L2} ligand facilitates the coordination of the water to the metal center which was not the case with a more flexible L_1^{Flex} ligand. The two-pyridine nitrogens in $[Ni^{Flex}_{L1}]$ are bound to the Ni at the equatorial position and the other two nitrogens i.e. N3 & N7 occupy the equatorial and axial position respectively. The comparison of the crystal structures of the two Ni complexes prima facie leads to the understanding that the rigid framework which supports water coordination may act as a better catalyst over the flexible framework. Based on the understanding from UV-Vis data (Figure 6a.7a) and the structural information, we then carried out electrochemical analysis of the two metal complexes. Differential pulse voltammograms

were recorded in phosphate buffer solvent. Both $[Ni_{L2}^{Rigid}]$ and $[Ni_{L1}^{Flex}]$ gave irreversible oxidation voltammograms albeit at different potentials. The differential pulse voltammogram (DPV) of $[Ni_{L2}^{Rigid}]$ showed oxidation of $Ni^{2+} \rightarrow Ni^{3+}$ at 1.41 V (vs RHE). On the other hand, the oxidation of $Ni^{2+} \rightarrow Ni^{3+}$ in $[Ni_{L1}^{Flex}]$ was at 1.58 V (vs RHE). Thus, a difference of about 170 mV was observed in the oxidation potential of the two complexes. This result indicates that there are much more distinct electron density distributions centered over the Ni in $[Ni_{L2}^{Rigid}]$ and $[Ni_{L1}^{Flex}]$.

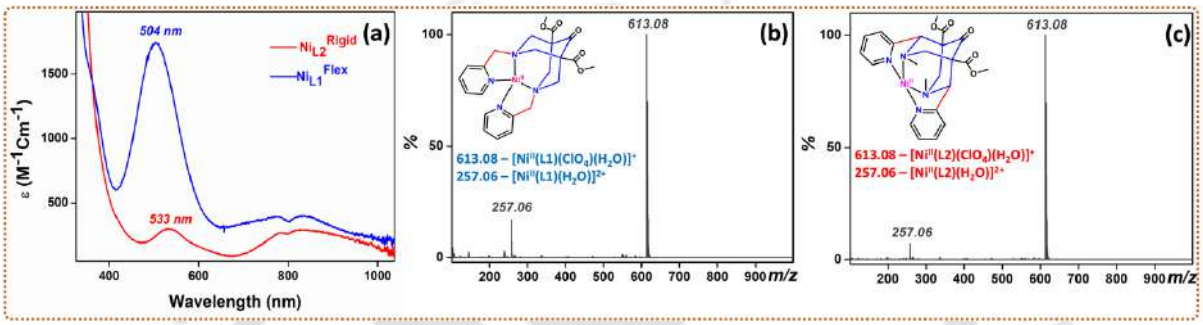

Figure 6a.7. *(a) UV-vis absorption spectra for* $[Ni(II)_{L2}^{Rigid}]$ *and* $[Ni(II)_{L1}^{Flex}]$ *complexes in acetonitrile, illustrating the ligand-to-metal charge-transfer (LMCT) bands and the notable shifts in* λ_{max} *and molar extinction coefficients (ϵ) resulting from changes in the coordination environment; (b) ESI-MS spectrum for the* $[Ni(II)_{L1}^{Flex}]$ *complex, showing a prominent molecular ion fragment peak at* $m/z = 613.08$ *corresponding to* $[Ni(II)_{L1}^{Flex}(ClO_4)(H_2O)]^+$*; (c) ESI-MS spectrum for the* $[Ni(II)_{L2}^{Rigid}]$ *complex, identifying the peak at* $m/z = 257.06$ *which corresponds to the* $[Ni(II)_{L2}^{Rigid}(H_2O)]^{2+}$ *molecular ion fragment.*

To gain further insights into the differences in redox potential values between the two complexes, we have performed density functional theory (DFT) calculations. Both the systems have a total spin of S=1 hence the ground state should be a triplet. Spin density plots were made along with the Mulliken spin density calculations. In case of the Ni_{L1}^{Flex} complex, Figure 6a.8a, the spin density is majorly localized between the two oxygen atoms (~40-50%) and the Nickel center is devoid of the electronic spin population. Whereas in Ni_{L2}^{Rigid} complexes the spin density is highly localized on the Nickel atom i.e ~80% of the total spin density, Figure 6a.8b. These results indicate that the redox potential values should be lower for the Ni_{L2}^{Rigid} than the Ni_{L1}^{Flex} one. The theoretical results are consistent with the experimentally observed redox values, providing further validation of the findings. The theoretical findings are further supported by X-ray photoelectron spectroscopy (XPS) analysis, which reveals that

the binding energy peaks for Ni in the Ni_{L2}^{Rigid} complex are shifted to lower values compared to those in Ni_{L1}^{Flex}. This shift indicates an increased electron density surrounding the Ni atom in the Ni_{L2}^{Rigid}complex relative to the Ni_{L1}^{Flex}.(Figure 6a.8c)

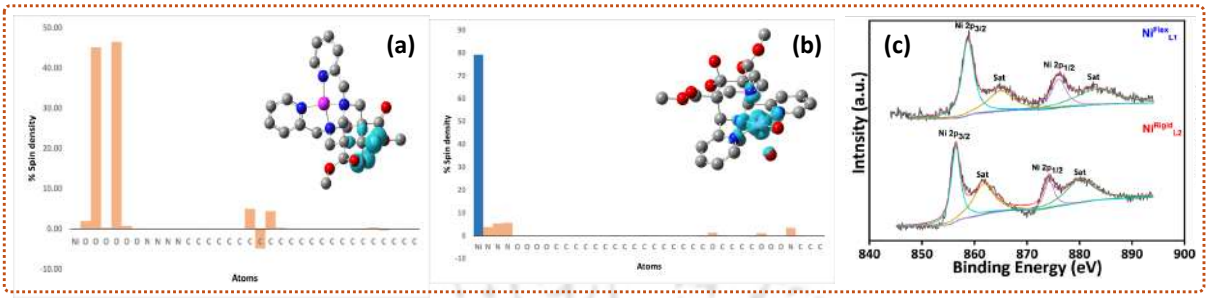

Figure 6a.8. *(a-b) Spin density distribution plots and Mulliken calculations for the* $[Ni(II)_{L1}^{Flex}]$ *and* $[Ni(II)_{L2}^{Rigid}]$ *complexes. In the* $[Ni(II)_{L1}^{Flex}]$ *complex (a), the spin density is primarily localized between the two oxygen atoms (~40-50%), with the Nickel center showing a lack of electronic spin population. Conversely, in the* $[Ni(II)_{L2}^{Rigid}]$ *complex (b), the spin density is highly concentrated on the Nickel atom, accounting for approximately 80% of the total density. (c) X-ray photoelectron spectroscopy (XPS) spectra for the* $[Ni(II)_{L1}^{Flex}]$ *and* $[Ni(II)_{L2}^{Rigid}]$ *complexes. The data reveals a shift to lower binding energy peaks for Nickel in the* $[Ni(II)_{L2}^{Rigid}]$ *complex compared to* $[Ni(II)_{L1}^{Flex}]$*, indicating an increased electron density surrounding the Nickel atom in the rigid framework.*

Table 6a.1. *Comparison of electrocatalytic water oxidation activity of β-Ni(OH)₂ heterogeneous catalyst under different electrolytic environment.*

Sl. No.	Materials	Overpotential (mV) @ 10 mA/cm²	Tafel slope (mV/dec)	Electrolytic solution	Reference
1	β-Ni(OH)₂ NPs	444	111	1M KOH (Alkaline medium)	49
2	β-Ni(OH)₂ NPs	331	47	1M KOH (Alkaline medium)	51
3	β-Ni(OH)₂ NRs	312	85	1M KOH (Alkaline medium)	50
4	β-Ni(OH)₂ NFs	___	145.9	1M KOH (Alkaline medium)	52
5.	β-Ni(OH)₂ NFs	330	97	0.1 M phosphate buffer in presence of homogeneous catalyst (Neutral medium)	This work

For the β-Ni(OH)₂ heterogeneous catalyst, the overpotential value ranges from 312 mV to 444 mV at a current density of 10 mA/cm² without any modifications, depending on the substrate and methods of preparation (See Table 6a.1).[49,50,51,52] However, this result is only achievable in the harsh basic environment. As far as we are aware, there are no reports of the

β- $Ni(OH)_2$ heterogeneous catalyst achieving such a low overpotential at a current density of 10 mA/cm^2 in neutral conditions. Similarly, while homogeneous catalysts can operate in a neutral buffer environment for water oxidation, they exhibit low current density values and high overpotential compared to its heterogeneous counterpart. We initially conducted the electrochemical measurements, using linear sweep voltammetry (LSV) at a scan rate of 5 mV/s in a 0.1 M phosphate buffer solution using a three-electrode system. A platinum electrode served as the counter electrode, Ag/AgCl electrode as the reference electrode, and the synthesized β-$Ni(OH)_2$@NF as the working electrode. All LSV curves for the homo-hetero system were measured with 1 mM of a homogenous catalyst dissolved in the phosphate buffer electrolyte. From the LSV measurements, it was observed that the Ni_{L2}^{Rigid} complex, with an octahedral geometry derived from a rigid bispidine ligand, required only 330 mV overpotential to achieve a current density of 10 mA/cm² (Figure 6a.9a) at pH 7 in a phosphate buffer electrolyte. This overpotential is 70 mV lower compared to the Ni_{L1}^{Flex} complex and 155 mV lower compared to when devoid of any homogenous catalyst in phosphate buffer. In terms of energy consumption, the Ni_{L2}^{Rigid} complex in the homo-hetero system consumes 27 kJ/mol less energy compared to the Ni_{L1}^{Flex} complex and 59.82 kJ/mol less compared to only the heterogeneous catalyst to drive 10 mA/cm^2 of current density. These results are in agreement with similar trends observed in the DPV analysis of the Ni complexes. Tafel slope analysis was performed to understand the reaction kinetics and the pathway contributing to the enhanced efficiency. As shown in Figure 6a.9b, a Tafel slope of 97 mV/dec was observed for the electrocatalytic system using the Ni_{L2}^{Rigid} complex as a homogeneous counterpart. The Ni_{L1}^{Flex} complex exhibited a Tafel slope of 108 mV/dec, indicating superior catalytic water oxidation kinetics for the Ni_{L2}^{Rigid} complex in the homo-hetero system. Electrochemical impedance spectroscopic (EIS) measurements were conducted to determine the charge transfer resistance (R_{ct}) in the presence and absence of a homogeneous catalyst at 0.9 V vs. Ag/AgCl, using β-$Ni(OH)_2$ as the working electrode. As depicted in the Nyquist plot in Figure 6a.10a, the system incorporating the Ni_{L2}^{Rigid}complex in the phosphate buffer electrolyte exhibited the smaller semicircle, corresponding to an R_{ct} value of 80 Ω. In comparison, the system with the Ni_{L1}^{Flex}complex demonstrated a R_{ct} of 145 Ω, while the experiments in the absence of homogenous catalyst in phosphate buffer solution exhibited an R_{ct} of 229 Ω.

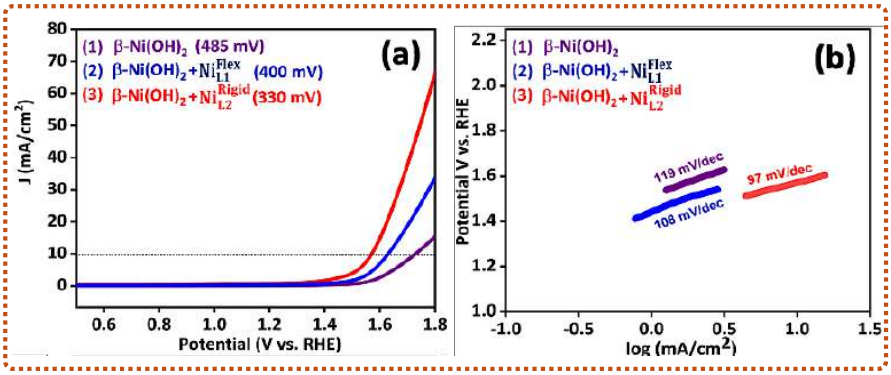

Figure 6a.9. *(a) Linear Sweep Voltammetry (LSV) curves for the homo-hetero catalytic systems, measured at a scan rate of 5 mV/s in a 0.1 M phosphate buffer (pH 7). The plot demonstrates that the* $[Ni(II)_{L2}^{Rigid}]$ *complex requires a significantly lower overpotential of 330 mV to reach a current density of 10 mA/cm², outperforming the* $[Ni(II)_{L1}^{Flex}]$ *complex by 70 mV. (b) Tafel plots derived from the LSV data to evaluate reaction kinetics. The* $[Ni(II)_{L2}^{Rigid}]$ *complex exhibits a lower Tafel slope of 97 mV/dec compared to 108 mV/dec for* $[Ni(II)_{L1}^{Flex}]$*, indicating superior catalytic kinetics and more efficient water oxidation for the rigid bispidine-based system.*

To understand the time constants associated with different relaxation processes, we have analyzed the distribution of relaxation time (DRT) constants using DRT tool in MATLAB based on the data of AC impedance spectra.[67,68] DRT represents the time required for the system to transit from one equilibrium state to another at a given frequency, with different chemical processes corresponding to distinct relaxation times at interfaces. Typically, catalysts exhibit various relaxation processes during the oxygen evolution reaction, which comes from the combination of series resistances, resistance of the active material, charge transfer resistance between the electrode and electrolyte solution, and resistance due to the diffusion dynamics. In this analysis the signature peaks at high-frequency primarily arise from the series resistance, those at the intermediate-frequencies are from the active-materials and charge-transfer reactions, and those at the low-frequency are associated with electrode polarization and diffusions. Our analytical approach involves determining the DRT of the different chemical and electrical processes occurring in the system are described in Equation 6a.3.

$$Z(\omega) = R_{pol} \int_{-\infty}^{+\infty} \frac{\tau(\log(\tau))}{1 + j\omega\tau} d(\log(\tau)) \qquad (6a.3)$$

In this context, $Z(\omega)$ represents the impedance of the processes, R_{pol} stands for the total polarization resistance, τ signifies the relaxation time, and ω denotes the frequency. To identify the relevant physical processes, we observed the total number of peaks and their shifts with respect to relaxation time, providing a precise understanding of the phenomena

occurring within the electrode and electrolyte system (Figure 6a.10b). In our observations, three distinct major peaks were identified. Peak, designated as **P1**, occurring at the lower relaxation time, corresponds to the series resistance across electrolyte and electrode interface. Peak **P2**, at an intermediate relaxation time, represents the charge transfer resistance between the electrode and the electrolyte solution. Finally, peak **P3**, observed at the larger relaxation time, corresponding to diffusion related resistance. Peak **P2**, which represents the time constant associated with the charge transfer process in a homogeneous-heterogeneous mixed system, we observe a significant shift in its position towards lower average time scales depending on the differences in the ligand architectures in the homogeneous catalyst. For β-$Ni(OH)_2$, the heterogeneous catalyst, the peak corresponding to relaxation processes appear at 8 ms. When the Ni_{L1}^{Flex} complex is added to the electrolyte containing the heterogenous counterpart, the peak shifts to lower relaxation time of 4 ms. This average relaxation time further gets lower to 2 ms in the system having Ni_{L2}^{Rigid} complex and β-$Ni(OH)_2$. This faster relaxation times indicate a facile charge transfer kinetics between the electrode and the electrolyte containing the Ni(II) complex with octahedral geometry.

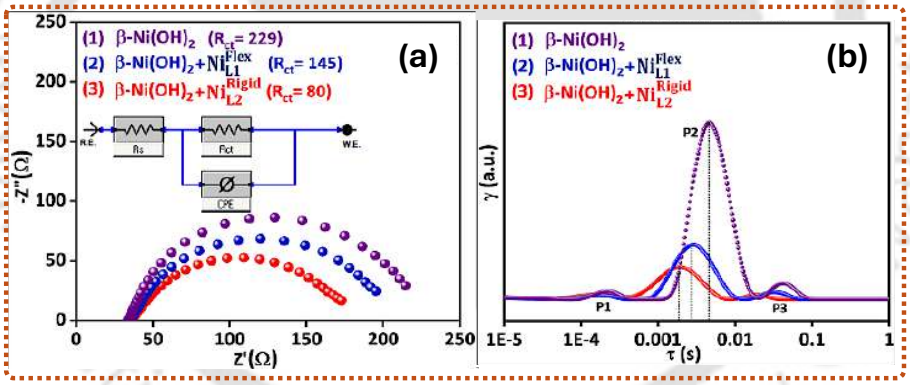

Figure 6a.10. *(a) Nyquist plots of homo-hetero system where β-$Ni(OH)_2$@NF is used as the heterogeneous electrode material and in homogeneous electrolyte we have taken phosphate buffer solution (purple), Ni_{L1}^{Flex} (blue) and Ni_{L2}^{Rigid} (red) at phosphate buffer; (b) DRT analysis performed from EIS data.*

To measure the number of cycles the catalyst can sustain the catalytic activity at the active sites per unit increase of time, the turnover frequency (TOF) was calculated from Figure 6a.11a. The results indicate that in homo-heterogenous catalytic system having Ni_{L2}^{Rigid} in the homogeneous medium shows a two-fold increase in turnover frequency compared to Ni_{L1}^{Flex} and an overall four-fold improvement compared to the heterogeneous catalyst. All detailed calculations pertaining to TOF are given in supporting information.

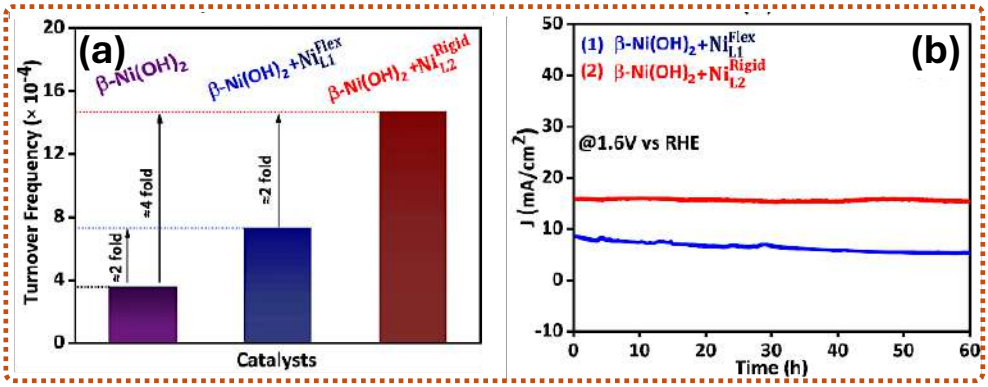

Figure 6a.11. *(a) Turnover Frequency (TOF) comparison calculated for both the standalone heterogeneous and the homo-heterogeneous mixed catalytic systems. The results indicate that the homo-heterogeneous system utilizing* Ni_{L2}^{Rigid} *shows a two-fold increase in turnover frequency compared to the* Ni_{L1}^{Flex} *system and an overall four-fold improvement over the heterogeneous catalyst alone. (b) Stability test of the homo-heterogeneous system in the presence of* Ni_{L1}^{Flex} *(blue) and* Ni_{L2}^{Rigid} *(red) complexes performed at a constant applied potential of 1.6V vs. RHE. This evaluation demonstrates the long-term durability and sustained catalytic activity of the rigid bispidine-based framework under operating conditions.*

The long-term durability test for the oxygen evolution reaction (OER) of both the $\mathrm{Ni}_{\mathrm{L2}}^{\mathrm{Rigid}}$ and $\mathrm{Ni}_{\mathrm{L1}}^{\mathrm{Flex}}$ complexes in the homo-hetero system was conducted at a constant potential of 1.6 V vs. RHE. This test produced a current density of approximately 15 mA/cm^2 for the $\mathrm{Ni}_{\mathrm{L2}}^{\mathrm{Rigid}}$ complex and approximately 8 mA/cm^2 for the $\mathrm{Ni}_{\mathrm{L1}}^{\mathrm{Flex}}$complex in the homogeneous system at the tested potential (Figure 6a.11b). The results demonstrate that the homogenous-heterogenous mixed system under investigation exhibits excellent electrochemical durability, with negligible reduction in current density even after continuous operation for 60 hours. To assess the state of the catalysts after 60 hours of durability test, we have conducted a PXRD analysis on the heterogeneous catalyst. The XRD patterns of β-$Ni(OH)_2$ showed no discernible changes, indicating structural stability. Additionally, we have evaluated the homogenous catalyst's integrity by comparing the molar absorption coefficient values before and after the durability test. The results revealed no appreciable alterations in either the molar absorption coefficient or the λ_{max} values. These findings collectively demonstrate that both the heterogeneous and homogeneous catalysts maintained their structural and chemical integrity without undergoing any degradation during the reaction.

Catalyst deactivation is a major problem during electrochemical reactions, occur through dissolution, passivation, crystal phase changes, mechanical damage, and gas bubble effects.[69] Catalyst and supporting material dissolution during electrolysis is a primary cause of deactivation, critically impairing performance and stability. Passivation is caused by an insulating layer at high potential, increasing resistance and causing deactivation. Crystal structure changes, like amorphization or segregation, reduce catalytic activity, while agglomeration and detachment due to gas bubble formation compromise stability. In our system, the combination of a β-$Ni(OH)_2$ nanoflower directly deposited on Ni foam substrate as a heterogeneous catalyst and two geometrically different Ni-complexes complexes as homogeneous catalysts effectively minimizes these deactivation mechanisms. Dissolution is typically more prominent under harsh acidic or basic conditions; however, performing electrolysis under neutral conditions in this work minimizes dissolution. Growing the β-$Ni(OH)_2$ catalyst directly on a highly conductive Ni foam substrate reduces passivation risks while ensuring high ohmic contact and mechanical stability, as it prevents detachment and leaching during bubble formation.

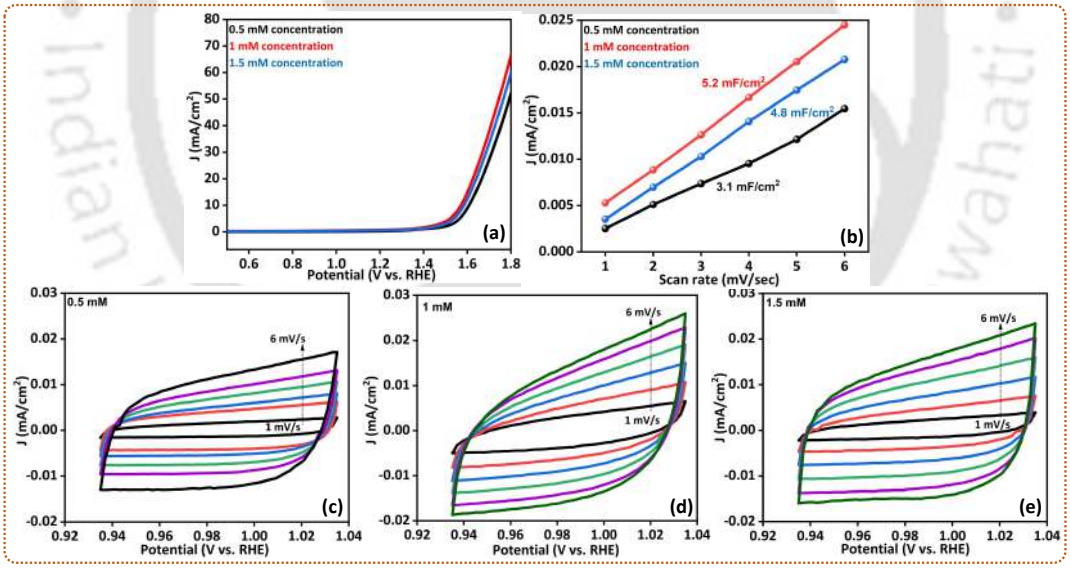

Figure 6a.12. *(a) Linear sweep voltammetry curve for homo-hetero system with* Ni_{L2}^{Rigid} *complex as the homogeneous catalyst with three different concentrations in the electrolytic solution; (b)* C_{dl} *plot of the homo-hetero system at three different concentrations of* Ni_{L2}^{Rigid} *complex derived from the cyclic voltammogram (c-e).*

To confirm that the optimal results that is achieved with a 1 mM concentration of the homogeneous catalyst in the electrolyte, we have performed linear sweep voltammetry (LSV) measurements at three different concentrations: 0.5mM, 1mM, and 1.5mM of Nickel

complexes. The best results were observed with a 1 mM solution of the homogeneous catalyst in phosphate buffer solution (Figure 6a.12a). To understand the effect of concentration on the catalytic behavior, electrochemically active surface area (ECSA) at all three concentrations were done as shown in Figure 6a.12b. Since ECSA is directly proportional to the double-layer capacitance (C_{dl}), measuring the C_{dl} provides an estimate of the electrochemically active surface sites. The C_{dl} values of the catalyst were obtained from cyclic voltammetry (CV) at different scan rates (1–6 mV/s) (Figure 6a.12(c-e)). From the calculations it is observed that the C_{dl} value is highest for the 1 mM solution, with a value of 5.2 mF/cm^2, compared to 3.1 mF/cm^2 for the 0.5 mM solution and 4.8 mF/cm^2 for the 1.5 mM solution. The decrease in C_{dl} value at concentrations above 1 mM might be due to the accumulation of the homogeneous catalyst on the surface of the β-Ni(OH)$_2$ electrode, blocking its electrocatalytically active surface sites.

Continuing the electroanalysis, we have performed faradaic yield measurements for the homo-heterogeneous system in the presence of $\mathrm{Ni}_{\mathrm{L1}}^{\mathrm{Flex}}$ and $\mathrm{Ni}_{\mathrm{L2}}^{\mathrm{Rigid}}$ complexes in the homogeneous medium, along with the quantification of gas evolution during the electrocatalytic process (Figure 6a.13(a,b)). Faradaic yields indicate that the efficiency of the electrocatalytic system for the water oxidation process ruling out the possibility of side reactions. Our system achieved an average faradaic yield of approximately 96.5% with $\mathrm{Ni}_{\mathrm{L2}}^{\mathrm{Rigid}}$ and 96.2% with $\mathrm{Ni}_{\mathrm{L1}}^{\mathrm{Flex}}$ complex, indicating that the current density observed in Figure 3(a) is exclusively attributable to oxygen evolution.

Continuing this investigation, we also performed CV measurements in the homo-hetero system using β-Ni(OH)$_2$@NF as the working electrode, with Ag/AgCl and platinum as the reference and counter electrodes, respectively, in a 1 mM solution of the metal complex in phosphate buffer solution as electrolyte (Figure 6a.14a). The CV results indicate that the overall peak current density for the Ni^{2+}→ Ni^{3+} redox couple increases in the presence of homogeneous catalyst, $\mathbf{Ni}_{\mathbf{L2}}^{\mathbf{Rigid}}$. This increase in current density observed with the $\mathbf{Ni}_{\mathbf{L2}}^{\mathbf{Rigid}}$ can be attributed to two factors. Firstly, by utilizing the $\mathrm{Ni}_{\mathrm{L2}}^{\mathrm{Rigid}}$ complex in the electrolyte effectively synchronizes the Ni^{2+}→ Ni^{3+} transition within the homogeneous and heterogeneous medium.

By comparing the cyclic voltammetry (CV) of the homogeneous-heterogeneous mixed system (Figure 4) with the differential pulse voltammetry (DPV) (Figure 6a.14b) shows that the $Ni^{2+} \rightarrow Ni^{3+}$

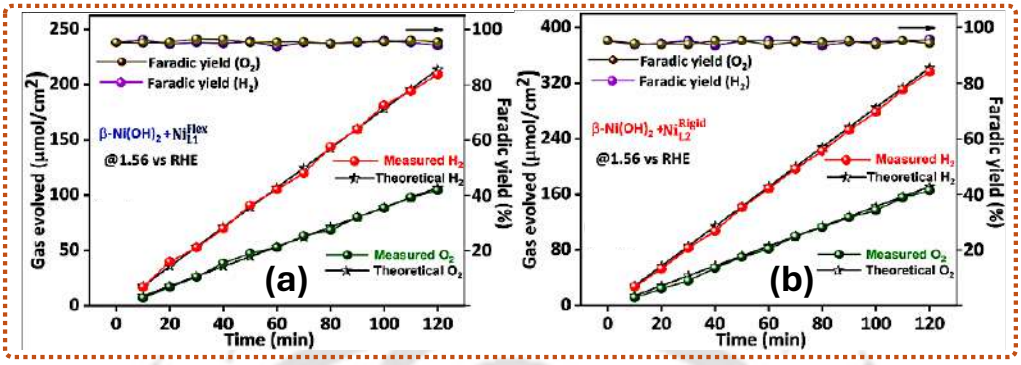

Figure 6a.13. *(g - h) Faradic yields for the homo-heterogeneous system in presence of Ni_{L1}^{Flex} (g) and Ni_{L2}^{Rigid} (h) in the homogeneous medium and the amount of gas evolved collected through online gas chromatography.*

transition for both Ni_{L2}^{Rigid} (at 1.41 V vs. RHE) and β-Ni(OH)$_2$@NF electrode (at 1.42 V vs. RHE) occurs within a very narrow potential range. This close alignment of potentials enhances the redox synchronization between the homogeneous and heterogeneous components, leading to a higher current density. In contrast, the Ni_{L1}^{Flex} complex has its redox peak at a higher potential (1.58 V vs. RHE), resulting in a less effective synchronization with the heterogeneous component. Secondly, the

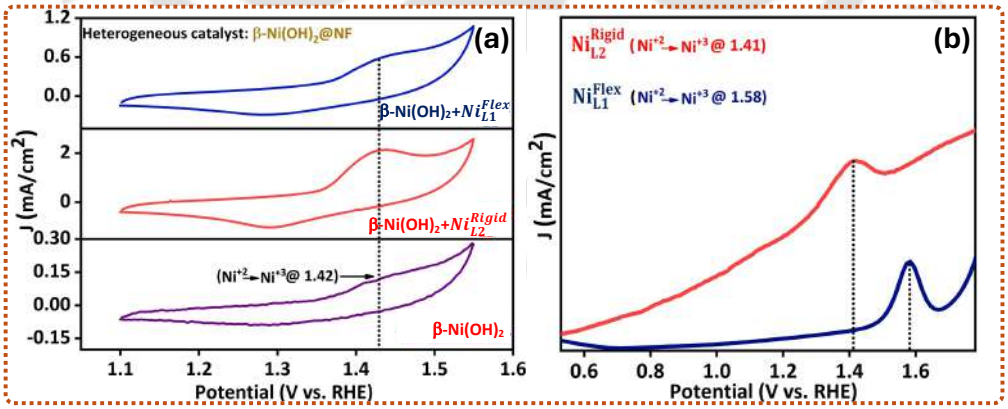

Figure 6a.14. *(a) cyclic voltammetry showing the Ni^{2+} to Ni^{3+} transition for homo hetero system; (b) Differential Pulse Voltammetry (DPV) analysis for homogeneous catalyst representing the Ni^{2+} to Ni^{3+} transition.*

higher current density for the Ni_{L2}^{Rigid} complex in the homogeneous system can be attributed to the favorable geometry of the complex derived from the rigid L2 ligand. Single crystal XRD

analysis suggests that the octahedral geometry of the Ni_{L2}^{Rigid} complex derived from rigid L2 ligand is coordinated with two cis labile sites with water molecule, which is beneficial for the O-O coupling to generate O_2 product. In contrast, the Ni_{L1}^{Flex} complex derived from flexible L1 ligand is showing distorted tetrahedral ligand environment and without any labile water molecule attached to it. These observations could also explain the lower overpotential and higher charge transfer kinetics obtained in the presence of the Ni_{L2}^{Rigid} complex.

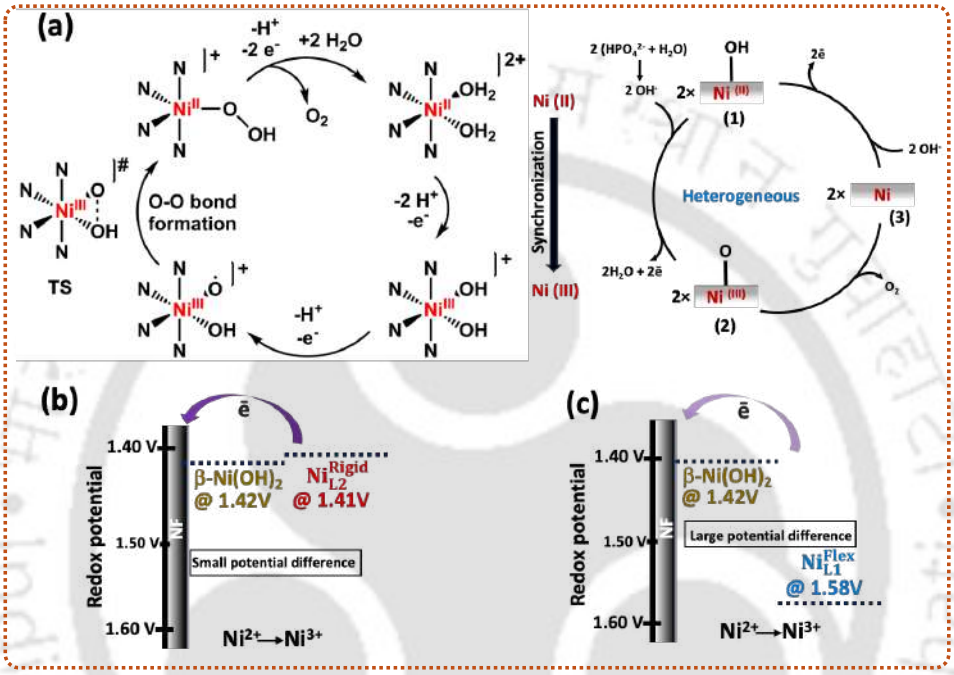

Scheme 6a.15. *a) Plausible mechanistic pathway for OER in homogeneous (left) and heterogeneous (right) system with their synchronization process; Schematic representation of potential difference required for the Ni^{2+} to Ni^{3+} transition in homo-hetero system with respect to (b) Ni_{L2}^{Rigid} and (c) Ni_{L1}^{Flex} complex.*

Based on the aforementioned experimental results and the mechanisms proposed previously for the OER catalysis in the literature for the homogeneous catalysis we have proposed the plausible mechanism in scheme 6a.15(a) (left).[70] In the initial step of the mechanism, we use the crystallographic structure of the cationic $[Ni(II)_{L2}^{Rigid}]^{2+}$ as the starting point of the catalytic cycle. The first step involves the oxidation of Ni^{2+} to Ni^{3+} through a $1\bar{e}/2H^+$ proton-coupled electron transfer (PCEP), which is synchronized with the heterogeneous catalyst. Efficient synchronization is observed for Ni_{L2}^{Rigid} due to its identical energetics of the $Ni^{2+} \rightarrow Ni^{3+}$ transition with the heterogeneous component, as demonstrated by CV and DPV. The second step involves another $1\bar{e}/2H^+$ PCEP, leading to the formation of a labile high

oxidation Ni intermediate (Ni^{4+}).[71,72] After two one-electron oxidation steps, the formal Ni^{4+} intermediate exists as a triplet species, with one electron residing on an oxygen atom ($[\dot{O} - Ni(III)_{L2}^{Rigid}]^{+}$). In the final step, O-O bond formation occurs through intramolecular oxygen coupling, where the hydroxyl group couples with the adjacent cis-related oxy radical to form a peroxide intermediate ($[HOO - Ni(II)_{L2}^{Rigid}]^{2+}$). This intermediate is further oxidized, releasing O_2 and completing the catalytic cycle. This mechanism also explains why the geometry of the Ni_{L2}^{Rigid} complex is critical for enhanced water oxidation. Both water molecules attached to it are in the cis conformation, facilitating better O-O coupling without requiring a change in conformation. Similar to the process in homogeneous catalysts, the first step in heterogeneous catalysts involves the oxidation of Ni^{2+} hydroxide to a Ni^{3+} species, as depicted in Scheme 6a.15(a) (right).[73,74] This Ni^{3+} species then releases oxygen from the electrode surface through O-O coupling and regenerates the metal hydroxide in the presence of OH^- from phosphate buffer, thereby completing the catalytic cycle.[63] Between the two homogeneous catalysts, we observed that for the Ni_{L2}^{Rigid} complex has the most feasible energetics for the $Ni^{2+} \rightarrow Ni^{3+}$ redox synchronization with the heterogeneous part as represented in scheme 5.13(b). The aforementioned mechanism effectively demonstrates how the homo-hetero system can operate synergistically under ambient electrocatalytic conditions, resulting in superior outcome.

6a.4. Conclusions:

In this work we have used β-$Ni(OH)_2$@NF as a heterogeneous catalyst and employed two distinct Ni^{2+} complexes as homogeneous catalysts in the electrolyte solution for the electrocatalytic water oxidation process. The Ni_{L2}^{Rigid} complex with an octahedral geometry, derived from a rigid bispidine ligand, demonstrated superior water oxidation performance with an overpotential of 330 mV at 10 mA/cm² and a Tafel slope of 97 mV/dec in neutral phosphate buffer solution. Electrochemical impedance spectroscopy revealed a lower charge transfer resistance (R_{ct}) of 80 Ω for the Ni_{L2}^{Rigid} complex dissolved in the electrolytic system, indicating enhanced charge transfer kinetics compared to Ni_{L1}^{Flex} (145 Ω) and the β-$Ni(OH)_2$@NF in phosphate buffer (229 Ω). Distribution of relaxation time (DRT) analysis identified three peaks, with a notable shift in the peak representing charge transfer resistance towards lower relaxation times for the Ni_{L2}^{Rigid} complex system, indicating faster charge

transfer dynamics. Electrochemically active surface area (ECSA) measurements confirmed optimal catalytic activity at a 1 mM concentration of the homogeneous catalyst, with a C_{dl} value of 5.2 mF/cm². Long-term durability tests further showcased the excellent stability of the Ni_{L2}^{Rigid} complex, maintaining a current density of 15 mA/cm² over 60 hours. Cyclic voltammetry indicated that the redox processes for the Ni^{2+} to Ni^{3+} transition occurred at lower potential ranges for the Ni_{L2}^{Rigid} complex, corroborating the observed lower overpotential. The integration of homogeneous and heterogeneous catalytic systems demonstrated enhanced electrochemical performance, with the geometrically favorable Ni_{L2}^{Rigid} complex playing a pivotal role in achieving efficient and stable water oxidation at neutral pH. This study highlights the potential of combining homogeneous and heterogeneous catalysis to overcome individual limitations and achieve superior water oxidation performance.

While the successful integration of these homogeneous and heterogeneous catalysts marks a significant milestone in neutral water electrolysis, realizing a comprehensive carbon-neutral energy cycle also necessitates the direct conversion of greenhouse gases into value-added fuels. Consequently, the electrocatalytic reduction of CO_2 into value-added liquid fuels, such as ethanol, serves as a vital and complementary pathway to water splitting. However, CO_2 reduction is an immensely complex, multi-electron process plagued by sluggish kinetics and fierce competition from the hydrogen evolution reaction. To address these barriers, the final chapter of this thesis applies the foundational knowledge established in this study - specifically the principles of redox synchronization and interfacial charge management - to the intricate realm of CO_2 electrocatalysis. By utilizing these advanced tandem catalytic strategies, the following work aims to precisely control intermediate stabilization and selectively drive carbon-carbon coupling, culminating the thesis in a highly integrated approach to advanced energy conversion.

6a.5. References:

1. L. Gao, X. Cui, C. D. Sewell, J. Li, Z. Lin, *Chem. Soc. Rev.* **2021**, *50*, 8428.
2. J. Hao, W. Luo, S. Wang, K. Zhao, J. Hou, L. Li, B. Ge, W. Yang, W. Shi, *Angew. Chem. Int. Ed.* **2021**, 60, 20042.

3. J. Wei, H. Tang, L. Sheng, R. Wang, M. Fan, J. Wan, Y. Wu, Z. Zhang, S. Zhou, J. Zeng, *Nat. Commun.* **2024**, *15*, 559.
4. L. Wang, L. Duan, R. B. Ambre, Q. Daniel, H. Chen, J. Sun, B. Das, A. Thapper, J. Uhlig, P. Dinér, L. Sun, *J. Catal.* **2016**, *335*, 72.
5. M. Kondo, H. Tatewaki, S. Masaoka, *Chem. Soc. Rev.* **2021**, *50*, 6790.
6. A. M. Geer, C. Musgrave, C. Webber, R. J. Nielsen, B. A. McKeown, C. Liu, P. P. M. Schleker, P. Jakes, X. Jia, D. A. Dickie, J. Granwehr, S. Zhang, C. W. Machan, W. A. Goddard, T. B. Gunnoe, *ACS Catal.* **2021**, *11*, 7223.
7. M. Zhang, M. Zhang, C. Hou, K. Ke, T. Lu, *Angew. Chem.* **2014**, *126*, 13258.
8. Y. Liu, Y. Han, Z. Zhang, W. Zhang, W. Lai, Y. Wang, R. Cao, *Chem. Sci.* **2019**, *10*, 2613.
9. L. Li, H. Sun, H. Hu, Z. Hu, J. Zhou, Y. C. Huang, H. Huang, S. Song, C. W. Pao, Y. C. Chang, A. C. Komarek, A. C. Lin, H. J. Lin, C. Chen, C. Te, C. L. Dong, J. Wang, J. Q. Zhang, L. Zhang, *Adv. Funct. Mater.* **2021**, *31*, 2104746.
10. J. Nai, H. Yin, T. You, L. Zheng, J. Zhang, J. Wang, P. Wang, Z. Jin, Y. Tian, Y. Liu, J. Liu, Z. Tang, L. Guo, *Adv. Energy Mater.* **2015**, *5*, 1401880.
11. Y. Wang, C. Chen, X. Xiong, S. A. Skaanvik, Y. Zhang, E. D. Bøjesen, Z. Wang, W. Liu, M. Dong, *J. Am. Chem. Soc.* **2024**, *25*, 17032.
12. X. Bo, Y. Li, X. Chen, C. Zhao, *Chem. Mater.* **2020**, *32*, 4303.
13. S. J. Koepke, K. M. Light, P. E. Vannatta, K. M. Wiley, M. T. Kieber-Emmons, *J. Am. Chem. Soc.* **2017**, *139*, 8586.
14. G. Wang, G. Zhang, X. Chen, *Small* **2024**, *20*, 2310372.
15. J. Yang, L. Wang, S. Zhan, H. Zou, H. Chen, M. S. G. Ahlquist, L. Duan, L. Sun, *Nat. Commun.* **2021**, *12*, 373.
16. J. M. Thomsen, D. L. Huang, R. H. Crabtree, G. W. Brudvig, *Dalton Trans.* **2015**, *44*, 12452.
17. J. Zhang, X. Cao, Y. F. Jiang, S. F. Hung, W. Liu, H. Bin Wang, X. C. Q. Xu, D. S. Li, T. Zhang, Y. Li, J. Li, B. Liu, *Chem. Sci.* **2022**, *13*, 12114.
18. D. Shao, Q. Wang, X. Yao, Y. Zhou, Y. Yu, X. Y. Yu, *J. Mater. Chem. A* **2022**, *10*, 21848.
19. D. Ressnig, M. Shalom, J. Patscheider, J. Moré, R. Evangelisti, F. Antonietti, M. Patzke, G. R. Patzke, *J. Mater. Chem. A* **2015**, *3*, 5072.

20. B. H. R. Suryanto, Y. Wang, R. K. Hocking, W. Adamson, C. Zhao, *Nat. Commun.* **2019**, *10*, 5599.
21. T. O. Schmidt, A. Wark, A. Haid, R. W. Kluge, R. M. Suzuki, S. Kamiya, K. Bandarenka, A. S. Maruyama, J. Skúlason, E. Skúlason, *Adv. Energy Mater.* **2023**, *13*, 2302039.
22. B. Mondal, A. Jana, J. Roy, A. C. Mata, A. S. Nair, A. Mahendranath, S. Roy, B. Pathak, P. M. Ajayan, T. Pradeep, *ACS Mater. Lett.* **2023**, *5*, 3306.
23. Q. Wang, H. Zhao, F. Li, W. She, X. Wang, L. Xu, H. Jiao, *J. Mater. Chem. A* **2019**, *7*, 7636.
24. K. Kannimuthu, K. Sangeetha, K. Sam Sankar, S. Karmakar, A. Madhu, R. Kundu, S. Kundu, *Inorg. Chem. Front.* **2021**, *8*, 234.
25. F. Yu, F. Li, B. Zhang, H. Li, B. Sun, L. Sun, *ACS Catal.* **2015**, *5*, 627.
26. J. Zhou, C. Huang, Q. Zhou, Y. Xie, Y. Yang, L. Yu, Y. Yu, *Inorg. Chem.* **2022**, *61*, 9318.
27. N. Rajaram, J. Gopi, V. Sukumaran Nair, S. SarojiniAmma, S. A. Ilangovan, *ACS Appl. Energy Mater.* **2023**, *6*, 7908.
28. M. G. Kibria, F. A. Chowdhury, S. Zhao, B. AlOtaibi, M. L. Trudeau, H. Guo, Z. Mi, *Nat. Commun.* **2015**, *6*, 6769.
29. L. Qiao, W. Zhu, R. Dong, T. Tan, P. Ding, Z. Gao, P. Wang, S. Pan, J. Pan, *J. Mater. Chem. A* **2020**, *8*, 2453.
30. P. Babar, A. Lokhande, A. Karade, V. Pawar, B. Gang, M. G. Pawar, S. Kim, J. H. Kim, *ACS Sustain. Chem. Eng.* **2019**, *7*, 10035.
31. X. Yang, Y. Liu, R. Guo, J. Xiao, *Dalton Trans.* **2022**, *51*, 11208.
32. Y. Zeng, M. Zhao, Z. Huang, Z. Zhu, W. Zheng, J. Jiang, Q. Wang, Z. Liang, H. Liang, *Adv. Energy Mater.* **2022**, *12*, 2201713.
33. Y. Ding, X. Han, Q. Yang, Y. Jin, G. Bai, J. Zhang, W. Li, B. Hu, *J. Phys. Chem. Lett.* **2024**, *15*, 5985.
34. M. A. Hoque, A. D. Chowdhury, S. Maji, J. Benet-Buchholz, M. Z. Ertem, C. Gimbert-Suriñach, G. K. Lahiri, A. Llobet, *Inorg. Chem.* **2021**, *60*, 5791.
35. N. Vereshchuk, M. Gil-Sepulcre, A. Ghaderian, J. Holub, C. Gimbert-Suriñach, A. Llobet, *Chem. Soc. Rev.* **2022**, *52*, 196.

36. L. Wang, L. Duan, B. Stewart, M. Pu, J. Liu, T. Privalov, L. Sun, *J. Am. Chem. Soc.* **2012**, *134*, 18868.

37. J. J. Concepcion, J. W. Jurss, J. L. Templeton, T. J. Meyer, *J. Am. Chem. Soc.* **2008**, *130*, 16462.

38. D. E. Polyansky, J. T. Muckerman, J. Rochford, R. Zong, R. P. Thummel, E. Fujita, *J. Am. Chem. Soc.* **2011**, *133*, 14649.

39. F. Li, Y. Jiang, B. Zhang, F. Huang, Y. Gao, L. Sun, *Angew. Chem. Int. Ed.* **2012**, *51*, 2417.

40. F. Li, Y. Jiang, B. Zhang, F. Huang, Y. Gao, L. Sun, *Angew. Chem.* **2012**, *124*, 2467.

41. M. Zhang, M. Wang, Y. Yang, T. Yao, L. Sun, *Angew. Chem. Int. Ed.* **2014**, *53*, 13803.

42. S. M. Barnett, K. I. Goldberg, J. M. Mayer, *Nat. Chem.* **2012**, *4*, 498.

43. J. Shen, M. Wang, H. He, T. Jiang, J. Hu, M. Hu, *Chem. Commun.* **2018**, *54*, 9019.

44. W. Rabten, M. D. Kärkäs, T. Åkermark, H. Chen, R. Z. Liao, F. Tinnis, J. Sun, P. E. M. Siegbahn, P. G. Andersson, B. Åkermark, *Inorg. Chem.* **2015**, *54*, 4611.

45. F. Zheng, W. Zhang, X. Zhang, Y. Zhang, W. Chen, *Adv. Funct. Mater.* **2021**, *31*, 2013318.

46. S. Jiang, T. Xiao, C. Xu, S. Wang, H. Q. Peng, W. Zhang, B. Liu, Y. F. Song, *Small* **2023**, *19*, 2208027.

47. D. Zhou, P. Li, X. Lin, A. McKinley, Y. Kuang, W. Liu, W. F. Lin, X. Sun, L. Duan, *Chem. Soc. Rev.* **2021**, *50*, 8790.

48. S. Kumaravel, K. Karthick, S. S. Sankar, A. Karmakar, R. Madhu, K. Bera, S. Kundu, *Sustainable Energy Fuels* **2021**, *5*, 6215.

49. M. Gao, W. Sheng, Z. Zhuang, Q. Fang, S. Gu, J. Jiang, Y. Yan, *J. Am. Chem. Soc.* **2014**, *136*, 7077.

50. S. Kalantarifard, S. Allahverdiev, S. I. Najafpour, M. M. Najafpour, *Int. J. Hydrogen Energy* **2020**, *45*, 33563.

51. L. A. Stern, X. Hu, *Faraday Discuss.* **2014**, *176*, 363.

52. Q. Cao, M. Luo, Y. Huang, Q. Liu, X. Kong, J. Lei, Z. Jiang, J. Wang, *Sustain. Energ. Fuels* **2020**, *4*, 1522.

53. J. Lin, P. Kang, X. Liang, B. Ma, Y. Ding, *Electrochim. Acta* **2017**, *258*, 353.

54. G. Azadi, Z. Zand, Y. Mousazade, R. Bagheri, J. Cui, Z. Song, R. Bikas, K. Wozniak, S. I. Allakhverdiev, M. A. Najafpour, *Int. J. Hydrogen Energy* **2019**, *44**, 2857.

55. K. S. Egorova, V. P. Ananikov, *Angew. Chem. Int. Ed.* **2016**, *55*, 12150.

56. P. Comba, C. Lopez De Laorden, H. Pritzkow, *Helvetica* **2005**, *88*, 647.

57. G. Mukherjee, J. K. Satpathy, U. K. Bagha, M. Q. E. Mubarak, C. V. Sastri, S. P. De Visser, *ACS Catal.* **2021**, *11*, 9761.

58. G. Mukherjee, C. V. Sastri, *Isr. J. Chem.* **2020**, *60*, 1032.

59. H. Börzel, P. Comba, K. S. Hagen, Y. D. Lampeka, A. Lienke, G. Linti, M. Merz, H. Pritzkow, L. V. Tsymbal, *Inorganica Chim. Acta* **2002**, *337*, 407.

60. M. J. Frisch, et al., *Gaussian 09, Revision D.01; Gaussian, Inc.* **2009**.

61. A. D. Becke, *J. Chem. Phys.* **1993**, *98*, 5648.

62. C. Lee, W. Yang, R. G. Parr, *Phys. Rev. B* **1988**, *37*, 785.

63. P. J. Hay, W. R. Wadt, *J. Chem. Phys.* **1985**, *82*, 299.

64. M. M. Francl, W. J. Pietro, W. J. Hehre, J. S. Binkley, M. S. Gordon, D. J. Defrees, J. A. Pople, *J. Chem. Phys.* **1982**, *77*, 3654.

65. M. Atanasov, P. Comba, S. Helmle, D. Müller, F. Neese, *Inorg. Chem.* **2012**, *51*, 12324.

66. D. F. Evans, A. Jakubovic, *Dalton Trans.* **1988**, *12*, 2927.

67. Y. Lu, C. Z. Zhao, J. Q. Huang, Q. Zhang, *Joule* **2022**, *6*, 1172.

68. C. Sheng, F. Yu, C. Li, H. Zhang, J. Huang, Y. Wu, M. Armand, Y. Chen, *J. Phys. Chem. Lett.* **2021**, *12*, 2064.

69. Y. Jia, Q. Li, S. Zhang, X. Yashin, K. Ma, Z. Hua, J. Shi, C. Gu, Y. Dou, S. Dou, *Carbon Energy* **2024**, *6*, e528.

70. J. W. Wang, X. Q. Zhang, H. H. Huang, T. Lu, *ChemCatChem* **2016**, *8*, 3287.

71. C. Liu, D. van den Bos, B. den Hartog, D. van der Meij, A. Ramakrishnan, S. Bonnet, *Angew. Chem.* **2021**, *60*, 13463.

72. H. Lee, X. Wu, L. Sun, *ChemSusChem* **2020**, *13*, 3277.

73. M. J. Craig, G. Coulter, E. Dolan, J. Soriano-López, E. Mates-Torres, W. Schmitt, M. García-Melchor, *Nat. Commun.* **2019**, *10*, 4993.

74. T. J. Meyer, M. V. Sheridan, B. D. Sherman, *Chem. Soc. Rev.* **2017**, *46*, 6148.

6b.1. Introduction:

Excessive carbon dioxide (CO_2) emissions have raised serious environmental concerns, including global warming, ocean acidification, and climate change. The catalytic hydrogenation of CO_2 into value-added chemicals, utilizing H_2 derived from water splitting via photo- or electrolysis, offers a promising route to mitigate carbon emissions.[1,2] In recent years, significant progress has been made in the selective hydrogenation of CO_2 toward specific products such as liquid fuels, light olefins, and aromatics using multifunctional catalysts comprising various metal components including **Fe**, **Ni**, **Cu**, **Zn**, **Ag**, and **Au** etc.[3] However, the inherent thermodynamic and kinetic stability of CO_2, arising from its linear structure and two strong C=O double bonds - each consisting of a σ- and a π-bond—poses substantial challenges to its activation and conversion.[4] Overcoming these barriers necessitates the development of highly efficient catalysts and innovative reaction strategies. Among the various CO_2 reduction approaches, including thermal catalysis, photocatalysis, and bioconversion; electrocatalytic CO_2 reduction (CO_2RR) has emerged as particularly attractive due to its operational simplicity, environmental compatibility, and potential integration with renewable energy sources.[5] These advantages position electrocatalysis as a promising platform for sustainable CO_2 valorization. In electrocatalytic CO_2RR, two main catalytic strategies are employed: heterogeneous[6] and homogeneous[7] catalysis (Figure 6b.1). Heterogeneous systems involve the design of solid-state electrode materials that promote efficient electron transfer at the electrode–electrolyte interface, offering structural stability and integration ease.[8] In contrast, homogeneous catalysis utilizes molecularly defined transition or non-transition metal complexes dissolved in the electrolyte, enabling precise control over the reaction environment through ligand tuning.[9] Recent efforts have focused on optimizing these molecular systems and electrolyte compositions to enhance catalytic selectivity, activity, and stability under electrochemical conditions. In the context of CO_2 electroreduction (CO_2RR), both homogeneous and heterogeneous catalytic platforms offer distinct advantages and inherent limitations. Heterogeneous catalysis is widely valued for its operational robustness, scalability, and cost-effectiveness, particularly in long-term applications. Nevertheless, it often exhibits suboptimal catalytic activity and selectivity, largely due to limited accessibility and distribution of electrocatalytically active sites.[10] In contrast, homogeneous systems provide unique opportunities for precise molecular design and in-

depth mechanistic elucidation, enabling fine-tuning of catalyst structure to achieve improved selectivity.[11]

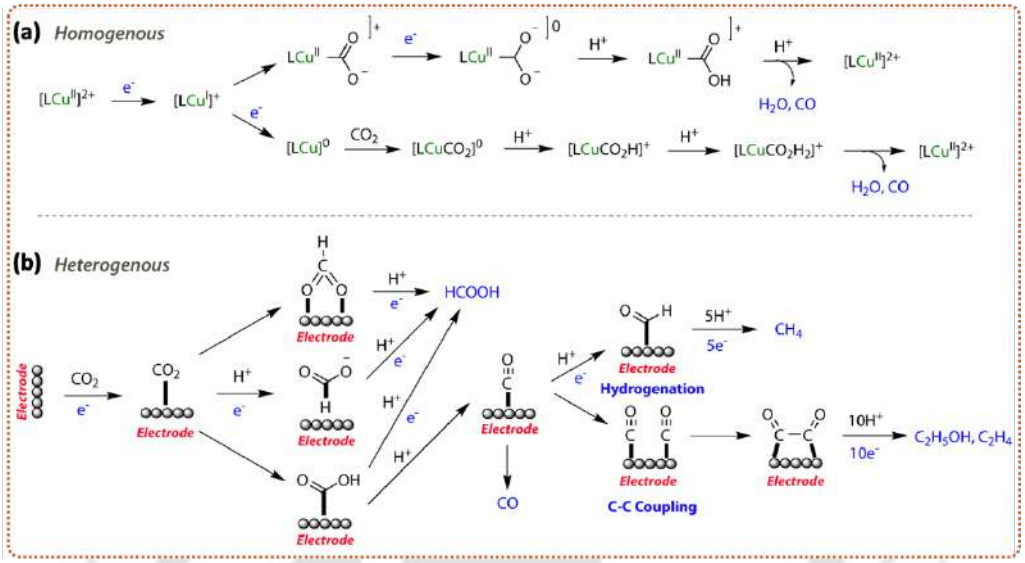

Figure 6b.1. *(a) Alternative CO_2 reduction mechanisms for the formation of CO by Cu(II) complexes via CO_2 binding route (top) and the Cu(I) reduction route (bottom).[5] (b) Proposed CO_2 reduction mechanism on Cu based hetrogeneous catalyts.[14]*

Despite these advantages, homogeneous electrocatalysis faces significant hurdles in attaining high faradaic efficiency and selectivity, especially for multicarbon (C_2^+) product formation. These limitations stem, in part, from the lack of suitable heterogeneous electrode materials that can function synergistically with molecular catalysts to facilitate efficient and selective C–C coupling.[12] To date there are numerous reports that has been present dual metallic heterogeneous electrocatalyst for CO_2RR including metal oxides,[13] sulfides, nitrides[15] and alloys[16] for generating C_1,C_2 and C_2^+ products. Ruru et al. employed a single-atom Cu-modified Tin(IV) sulfide (Cu_1/SnS_2) catalyst for electrochemical CO_2 reduction to formate, achieving enhanced selectivity with high faradaic efficiency of ~90.9% in $KHCO_3$ electrolyte.[17] The anchored Cu atom facilitated SnS reduction to Cu_1/Sn under cathodic potentials, promoting *OCHO intermediate formation lowering the activation energy for CO_2 activation, enabling superior formate production. Junjun et al. developed Ag-doped copper nitride nanocubes (Cu_3N–Ag NCs) as a cascade catalyst for CO_2-to-C_2H_4 conversion, achieving a 7.8-fold increase in faradaic efficiency and 9.0-fold enhancement in partial current density over pristine Cu_3N in $KHCO_3$ electrolyte.[18] The atomically dispersed Ag–Cu dual sites enabled CO generation on Ag followed by spillover to Cu, promoting asymmetric C–C coupling via

enhanced *CO coverage and lowered CO protonation barriers. Another report by Chen et al. used a (111)-oriented Cu_2Mg alloy intermetallic catalyst in 1 M KOH, achieving 76.2 ± 4.8% faradaic efficiency for ethanol formation at 600 mA/cm^2 of current density. [19]

Mg–Cu electronic interactions enhanced *CO coverage and stabilized oxygenated intermediates, promoting selective C_2H_5OH production. Among various catalyst systems, metal oxides have demonstrated notable efficacy in CO_2 electroreduction by providing abundant active sites and tailoring the local electronic environment to facilitate C–C coupling and enhance C_2 product selectivity. Specifically, the bimetallic oxide systems further improve catalytic performance through synergistic modulation of intermediate adsorption and reaction energetics, thereby enabling higher C_2 yields.[20] Qiang et al. developed oxygen-vacancy (Vo)-rich 2D $CuMnO_2$ nanosheets ($CuMnO_2$–Vo) via O_2 cold plasma, achieving 93.4% faradaic efficiency for ethylene at –1.0 V vs. RHE with 192 h stability in CO_2-saturated 0.5 M $KHCO_3$ electrolyte.[21] The enhanced C_2 selectivity is attributed to Vo-induced d-band upshift at Mn sites, strengthening *COOH/*CO adsorption and promoting C–C coupling. To date, there are no reports demonstrating the selective formation of C_2 products using bimetallic oxides under neutral buffer conditions. Only a few studies have explored related systems; for instance, Ju Young et al. employed sputtered Au/Ti electrodes in phosphate buffer for electrochemical CO_2/CO reduction, achieving C_2^+ gaseous hydrocarbon formation through interfacial synergy where Au facilitated CO generation and Ti provided surface-bound hydrogen, promoting CO dimerization and hydrogenation.[22] In another example, Mengwei et al. utilized Mo-FDH immobilized within a cobaltocene-based redox polymer (Cc-PAA) for CO_2-to-formate conversion in 1 M phosphate buffer with 50 mM $NaHCO_3$, achieving a Faradaic efficiency of 99 ± 5% and a current density of 62 ± 1 μA cm^{-2}, enabled by effective electron mediation and high enzyme specificity.[23]

In this work we have reported a selective electrocatalytic CO_2 reduction strategy for ethanol production under neutral pH, enabled by the synergistic interaction between homogeneous and heterogeneous catalysts. Homogeneous metal complexes are known to efficiently reduce CO_2 to CO, an energetically demanding step - under buffered aqueous conditions. This CO intermediate can then be utilized by a heterogeneous catalyst to form C_2 products. Recent work by Somnath et al. demonstrated that Cu(I) complexes bearing (phenylazo) pyridine-based redox-active ligands achieve nearly 100% Faradaic efficiency for

reversible CO_2-to-CO conversion in phosphate buffer (pH 6.5–7).[24] The high activity was attributed to a synergistic electron supply from both the Cu center and the redox-active ligand, with peripheral amine groups promoting efficient proton-coupled electron transfer and modulating catalytic bias.

In the present work to construct an effective homogeneous–heterogeneous hybrid system, we employed two geometrically distinct Cu(II) tetradentate bispidine-based complexes as homogeneous catalysts in the electrolyte. Both ligands share the molecular formula $C_{23}H_{26}N_5O_5$ but differ in topology. The flexible ligand $L1_{Flex}$ [dimethyl-3,7-bis(pyridine-2-ylmethyl)-9,9-hydroxo-3,7-diazabicyclo[3.3.1]nonane]-1,5-dicarboxylate] features pyridyl arms on the N3 and N7 positions, allowing coordination flexibility. In contrast, the rigid ligand $L2_{Rigid}$ [dimethyl-2,4-bis(2-pyridyl)-3,7-dimethyl-9,9-hydroxo-3,7-diazabicyclo [3.3.1] nonane]-1,5-dicarboxylate] anchors pyridine groups directly to the bispidine scaffold, restricting ligand dynamics. These structural differences create distinct coordination environments around the Cu center, altering electron density and yielding distinct redox signatures for both Cu^{2+}/Cu^{+} and Cu^{+}/Cu^{0} transitions.[25] For the heterogeneous catalyst, we employed a $Cu_{1.5}Mn_{1.5}O_4$ (CMO) electrode, where the Cu^{+}/Cu^{0} redox couple from CMO aligns closely with a specific Cu complex in the homogeneous medium. This redox potential overlap facilitates rapid charge transfer between the homogeneous and heterogeneous components. C_2 product formation on Cu-based surfaces proceeds via *CO dimerization to *HCCOH, with selectivity dictated by intermediate stability.[26] In $Cu_{1.5}Mn_{1.5}O_4$, Mn enhances *H adsorption and lowers water dissociation energy, boosting *HCCOH formation and ethanol selectivity.[27] To address the sluggish CO_2-to-CO step, bispidine-based Cu complexes ($[Cu^{L1}_{Flex}]$, $[Cu^{L2}_{Rigid}]$) were introduced, where $[Cu^{L2}_{Rigid}]$ undergoes Cu^{+}/Cu^{0} redox synchronization with the heterogeneous surface. This transition is crucial since Cu^{0} provides the active sites for C–C coupling, while the coexistence of Cu^{+} stabilizes oxygen-bound intermediates, collectively enabling efficient CO transfer from homogeneous catalyst to heterogeneous surface causing higher ethanol production.

Electrochemical analysis revealed a ~68% Faradaic efficiency for ethanol at –0.5 V vs RHE when Cu^{L2}_{Rigid} was used as the homogeneous catalyst. Additionally, turnover frequency (TOF) increased 1.5-fold compared to the Cu^{L1}_{Flex} system, indicating improved catalytic efficiency. Distribution of relaxation time (DRT) analysis further confirmed accelerated charge transfer

kinetics, with the lowest time constants observed for the Cu^{L2}_{Rigid}-CMO system. The synergistic mechanism for ethanol selectivity in this hybrid architecture was further elucidated through in-situ IRAS (Infrared Reflection Absorption Spectroscopy). spectroscopy and theoretical study.

6b.2. Experimental Section:

6b.2.1. Synthesis of heterogeneous catalyst ($Cu_{1.5}Mn_{1.5}O_4$):

Commercial carbon paper (0.2 × 0.5 cm^2) was initially cleaned to eliminate surface impurities. The pretreated substrate was then immersed in a homogeneous aqueous solution containing 0.5 M manganese(II) acetate, 0.2 M copper(II) acetate, and 0.5 M urea (total volume: 30 mL). This precursor solution was transferred into a 50 mL Teflon-lined stainless-steel autoclave and subjected to hydrothermal treatment at 160 °C for 20 h to promote the in situ growth of a $CuMn(OH)_x$ intermediate layer on the substrate. Upon completion, the resulting film was thoroughly rinsed with ethanol and deionized water, followed by vacuum drying at 60 °C. Final crystallization was achieved by calcination in air at 900 °C for 2 h using a ramp rate of 5 °C min^{-1}, yielding the phase-pure $Cu_{1.5}Mn_{1.5}O_4$ catalyst.

6b.2.2. Synthesis of homogeneous catalyst:

6b.2.2.1. Synthesis of flexible ligand ($L1_{Flex}$)

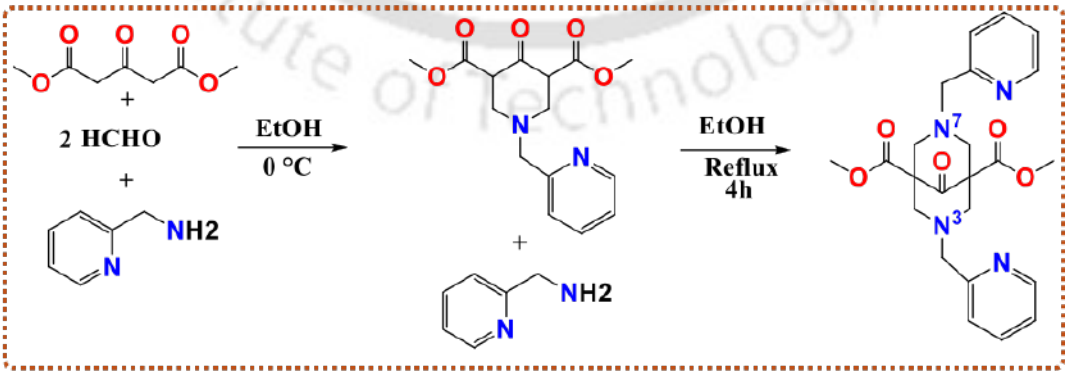

Figure 6b.2. *Synthetic rout for the preparation of $L1_{Flex}$ ligand.*

Ligand $L1_{Flex}$ was synthesized following a modified procedure based on previously reported methods. [1-3] Briefly, dimethyl acetonedicarboxylate (1.0 equiv) was dissolved in 20 mL of methanol and cooled to 273 K. A premixed solution of aqueous formaldehyde (2.0 equiv) and 2-picolylamine (1.0 equiv) was added dropwise under stirring. After complete addition, the reaction mixture was stirred overnight at 273 K. The resulting white precipitate was collected by filtration, washed with cold ethanol, and dried under vacuum. The product, obtained in >97% purity, was used directly in the subsequent step without further purification.

For the second condensation step, the above white solid (1.0 equiv) was suspended in 200 mL of ethanol. Aqueous formaldehyde (37%, 2.1 equiv) and 2-picolylamine (1.0 equiv) were added dropwise to the suspension under continuous stirring. The reaction mixture was refluxed for 4 h, yielding a brown solution upon completion. The solvent was then concentrated, and the solution was stored at 258 K. After several days, a white crystalline solid formed, which was collected and recrystallized from acetonitrile to afford the final ligand.

6b.2.2.2. Synthesis of rigid ligand ($L2_{Rigid}$):

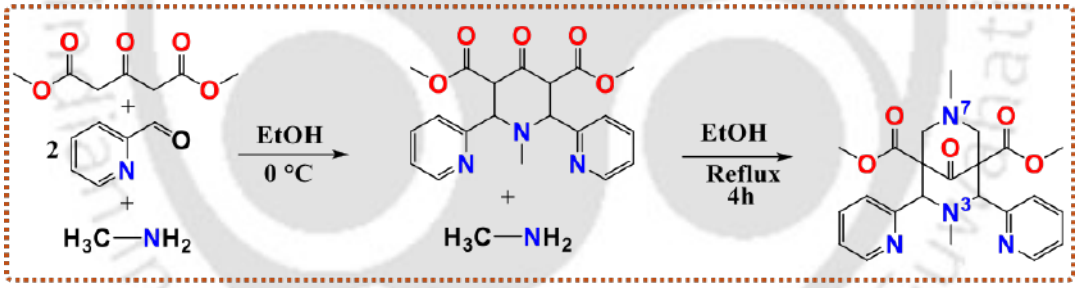

Figure 6b.3. *Synthetic rout for the preparation of $L2_{rigid}$ ligand.*

The ligand $L2_{Rigid}$ was synthesized following a modified literature procedure.[4] Dimethyl acetonedicarboxylate (4.80 mL, 33.33 mmol) was dissolved in 20 mL of methanol and cooled to −10 °C. A premixed solution of pyridine-2-carboxaldehyde (6.37 mL, 66.66 mmol) and methylamine (33.33 mmol) was added dropwise under continuous stirring. Upon complete addition, the reaction mixture was allowed to warm to ambient temperature and stirred overnight. A white precipitate of the piperidone intermediate formed, which was collected by filtration, washed thoroughly with cold ethanol, and dried under reduced pressure. The product was obtained in ~84% yield and used directly in the subsequent step without further purification.

To synthesize the bispidine ligand $L2_{Rigid}$, the isolated piperidone (12.70 g, 33.10 mmol) was suspended in 200 mL of ethanol. Aqueous formaldehyde (37%, 6.50 mL, 79.40 mmol) and methylamine (39.70 mmol) were added dropwise under stirring. The mixture was refluxed for 4 h, yielding a clear brown solution. After cooling, the reaction mixture was concentrated to half of its original volume and stored at −20 °C. After several days, white crystalline solids were obtained and collected by filtration.

6b.2.3. Synthesis of Cu Complexes (Cu^{L1}_{Flex} Cu^{L2}_{Rigid}):

Ligands $L1_{Flex}$ and $L2_{Rigid}$ were individually reacted with Cu (II)$(ACN)_2(OTf)_2$ in acetonitrile under ambient conditions. Each reaction mixture was stirred overnight and subsequently filtered through PTFE membranes. The resulting filtrates were layered with diethyl ether and stored at 233 K to facilitate crystallization. Single crystals suitable for X-ray diffraction of the complex $[Cu^{L1}_{Flex}]$ and $[Cu^{L2}_{Rigid}]$ were obtained by slow vapor diffusion into the acetonitrile solution.

6b.3. Results and Discussion:

The CMO were synthesized directly on carbon paper via a hydrothermal method, as described in section (6b.2.1). The crystalline phase and deposition of CMO were verified by X-ray diffraction (XRD), which exhibited distinct reflections corresponding to the hexagonal structure of CMO (ICSD No. 01-070-0260). The diffraction peaks located at 2θ = 18.1°, 28.6°, 30.5°, 33.0°, 35.6°, 38.8°, 43.6°, 45.3°, 48.7°, 53.8°, 55.3°, 57.7°, 61.5°, 63.4°, 66.1°, 68.0°, 72.5°, and 75.1° were indexed to the (111), (211), (220), (221), (311), (222), (400), (410), (331), (422), (430), (511), (521), (440), (433), (610), (620), and (540) crystallographic planes, respectively (Figure 6b.4a), confirming the successful growth of phase-pure CMO on the substrate. The morphological characteristics of the heterogeneous catalyst are presented in Figure 6b.4(b,c). Field-emission scanning electron microscopy (FESEM) reveals the formation of well-defined hexagonal disc-like structures of the synthesized CMO. The sheet-type morphology offers a high surface-to-volume ratio, abundant edge-active sites, and preferential facet exposure, collectively facilitating efficient charge transport and enhanced catalytic activity.[28] Notably, the hexagonal sheets are arranged without lamellar stacking, which ensures improved electrolyte accessibility and uniform contact of reactant with the

active sites, thereby contributing to superior electrocatalytic performance.[29] FETEM analysis further confirm the thin sheet-like morphology of the CMO, as shown in Figure 6b.4d. High-resolution TEM (HRTEM) imaging of the CMO surface (Figure 6b.4e) reveals a distinct lattice spacing of 0.27 nm, which corresponds to the (221) crystallographic plane of CMO. This result provides direct evidence of the well-defined crystal structure and ordered lattice arrangement of the catalyst.

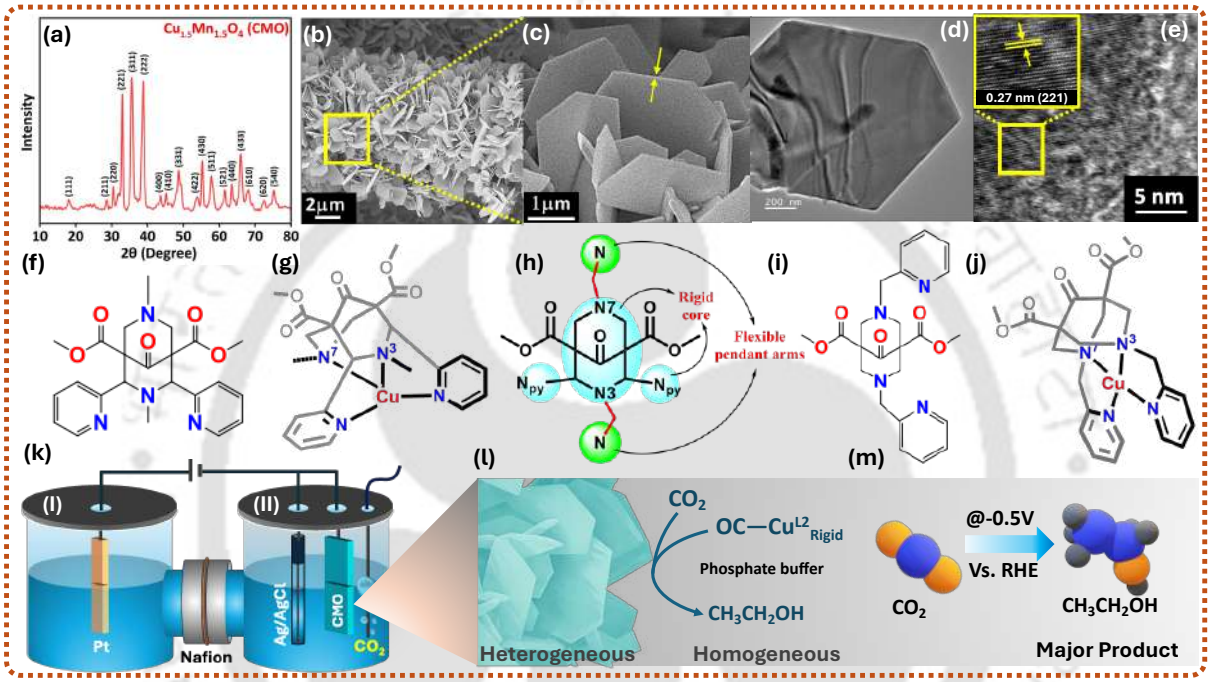

Figure 6b.4. *(a) XRD pattern of CMO, indexed to the hexagonal phase of $Cu_{1.5}Mn_{1.5}O_4$ (ICSD No. 01-070-0260); (b, c) FESEM images showing well-defined hexagonal sheet-like morphology of CMO with non-stacked arrangement; (d) FETEM image confirming thin sheet structures; (e) HRTEM image displaying a lattice spacing of 0.27 nm corresponding to the (221) plane of CMO; (f, i) molecular structures of bispidine ligands $L1_{Flex}$ and $L2_{Rigid}$, confirmed by NMR spectroscopy; (h) comparison of ligand architectures, emphasizing the structural differences in backbone rigidity and flexibility; (g, j) single-crystal structures of Cu(II) complexes, $Cu^{L1}{}_{Flex}$ and $Cu^{L2}{}_{Rigid}$, obtained from X-ray crystallography; (k) schematic of the H-cell setup used for electrochemical CO_2 reduction; (l, m) schematic representation of CO_2 reduction using heterogeneous (CMO) and homogeneous (Cu–bispidine) catalysts.*

For the homogeneous catalyst design, bispidine-based tetradentate ligands were selected owing to their established ability to stabilize low-valent metal centers, making them effective bioinspired reductants. The ligands $L1_{Flex}$ and $L2_{Rigid}$ were synthesized via double Mannich

reactions, (Section 6b.2.2) affording white crystalline solids in high yields. Their structures were confirmed by ^{1}H and ^{13}C NMR spectroscopy (Figure 6b.5 and 6b.6).

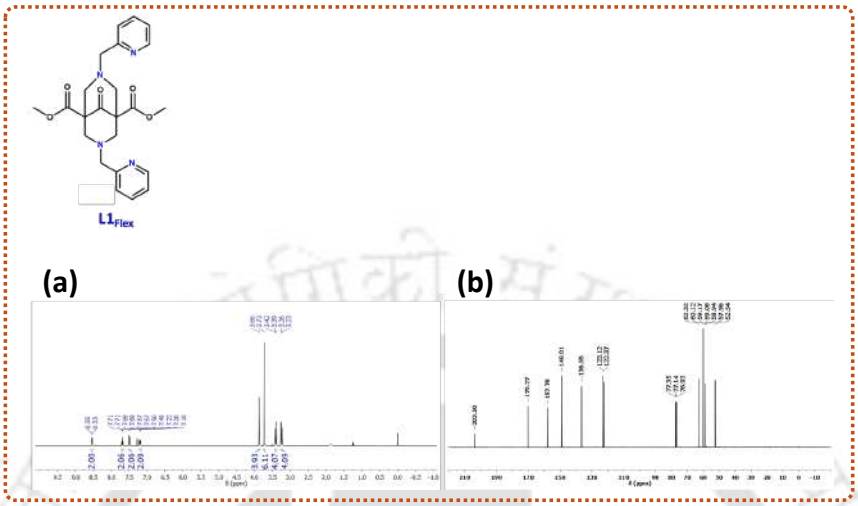

Figure 6b.5. *^{1}H (a) and ^{13}C (b) NMR spectra of the $L1_{Flex}$ ligand in $CDCl_3$ confirming the successful formation of the ligand framework and the expected proton and carbon environments.*

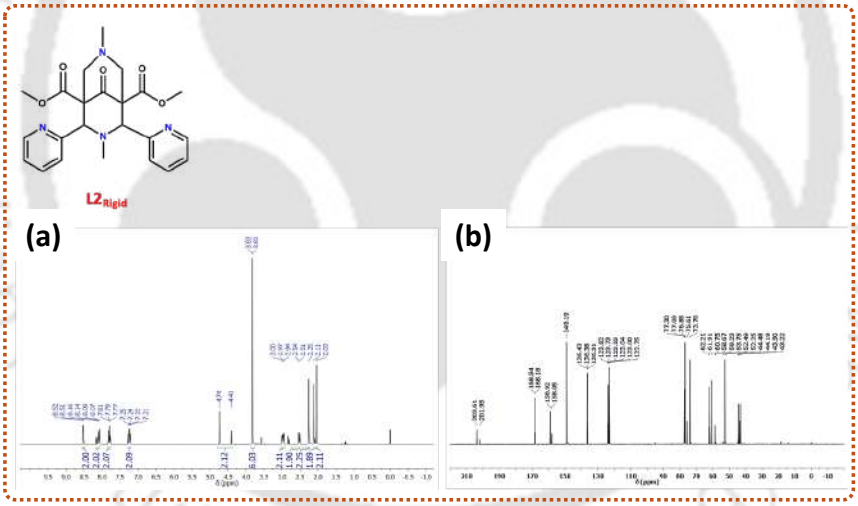

Figure 6b.6. *^{1}H (a) and ^{13}C (b) NMR spectra of the $L2_{Rigid}$ ligand ligand in $CDCl_3$ confirming the successful formation of the ligand framework and the expected proton and carbon environments.*

Subsequent coordination of $[Cu^{II}(ACN)_2(OTf)_2]$ with $L1_{Flex}$ and $L2_{Rigid}$ in acetonitrile furnished the corresponding copper(II) complexes, $[Cu^{II}(L1_{Flex})(ACN)_2](OTf)_2$ ($Cu^{L1}{}_{Flex}$) and $[Cu^{II}(L2_{Rigid})(ACN)_2](OTf)_2$ ($Cu^{L2}{}_{Rigid}$), as detailed in the section 6a.2.3. Single crystals suitable for X-ray diffraction (XRD) analysis were obtained via slow vapor diffusion of the metal complexes into acetonitrile solutions. The molecular structures of the bispidine ligands $L1_{Flex}$ and $L2_{Rigid}$, confirmed by NMR spectroscopy, are shown in Figures 6b.4f and 5b.4i, while the corresponding molecular structures of their Cu(II) complexes are displayed in Figures 6b.4g

and 6b.4j. A schematic comparison (Figure 6b.4h) highlights the difference in the ligand backbones, illustrating how the same molecular formula imparts flexible (L1) or rigid (L2) structural characteristics. The average equatorial Cu-N distances measured from the X-Ray structures were 2.008 Å and the axial Cu-N bond distance is 2.362 Å for the [Cu^{L2}_{Rigid}] complex, whereas the average bond distances for the [Cu^{L1}_{Flex}] complex is found to be 1.995 Å.

The copper(II) complexes were further characterized by UV–vis spectroscopy (Figure 6b.7a), EPR spectroscopy, single-crystal XRD and electrospray ionization mass spectrometry (Figure 6b.7(a,b); 6b.9; and 6b.8). The UV–vis spectra exhibit ligand-to-metal charge transfer bands with distinct shifts in both λ_{max} and molar extinction coefficients (ε), reflecting differences in electron density associated with the altered coordination environments. The EPR spectra for both the complexes show isotopic signals at g = 2.11 and 2.13 for [Cu^{L1}_{Flex}] and [Cu^{L2}_{Rigid}] respectively (Figure 6b.7b and c). ESI-MS spectra further confirm the molecular formulations, displaying characteristic peaks at m/z 259.56 and 618.08, corresponding to the molecular ion fragments of $[Cu^{II}L]^{2+}$ and $[Cu^{II}L(ClO_4)]^{+}$ respectively for both the Cu(II) complexes (Figure 6b.8).

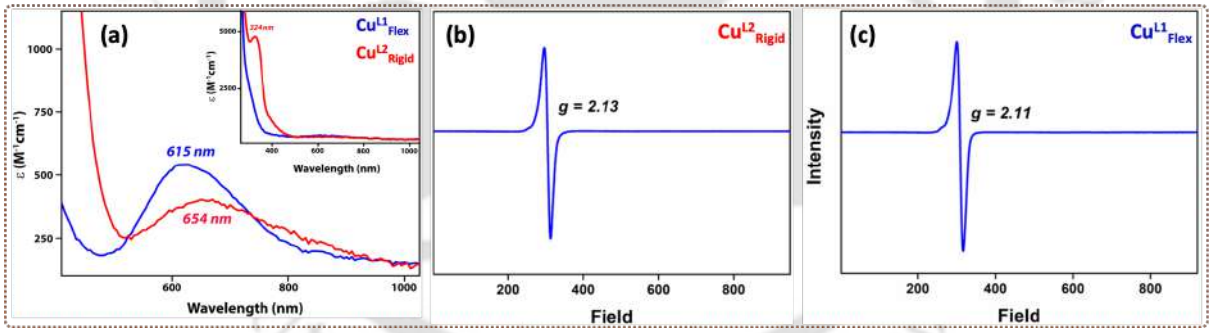

Figure 6b.7. *(a) UV–vis absorption spectra of the copper(II) complexes, displaying characteristic ligand-to-metal charge transfer (LMCT) bands with variations in λ_{max} and molar extinction coefficients arising from differences in ligand flexibility and coordination environments. (b) X-band EPR spectrum of the [Cu^{L2}_{Rigid}] complex, exhibiting a characteristic Cu(II) isotropic signal with a g-value of 2.13. (c) X-band EPR spectrum of the [Cu^{L1}_{Flex}] complex, showing a similar Cu(II) signal with a g-value of 2.11, confirming the paramagnetic Cu(II) oxidation state in both complexes.*

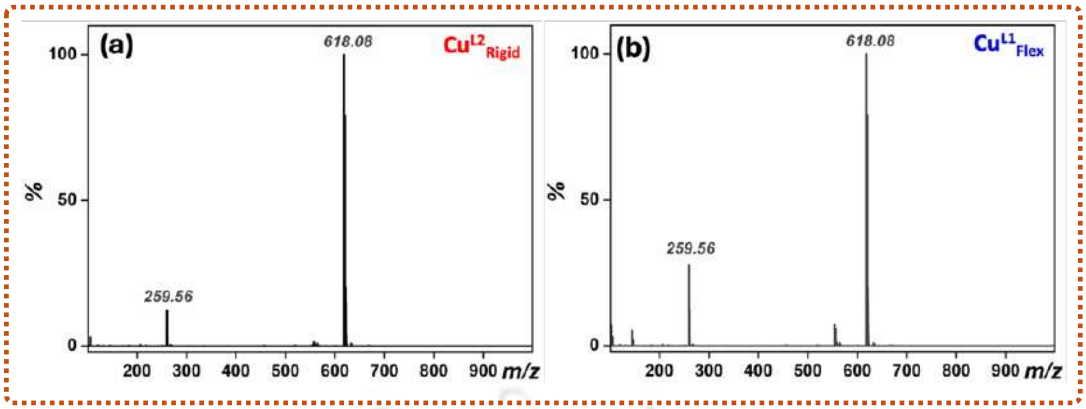

Figure 6b.8. *ESI-MS spectra of (a) [Cu^{L2}_{Rigid}] and (b) [Cu^{L1}_{Flex}] complex.*

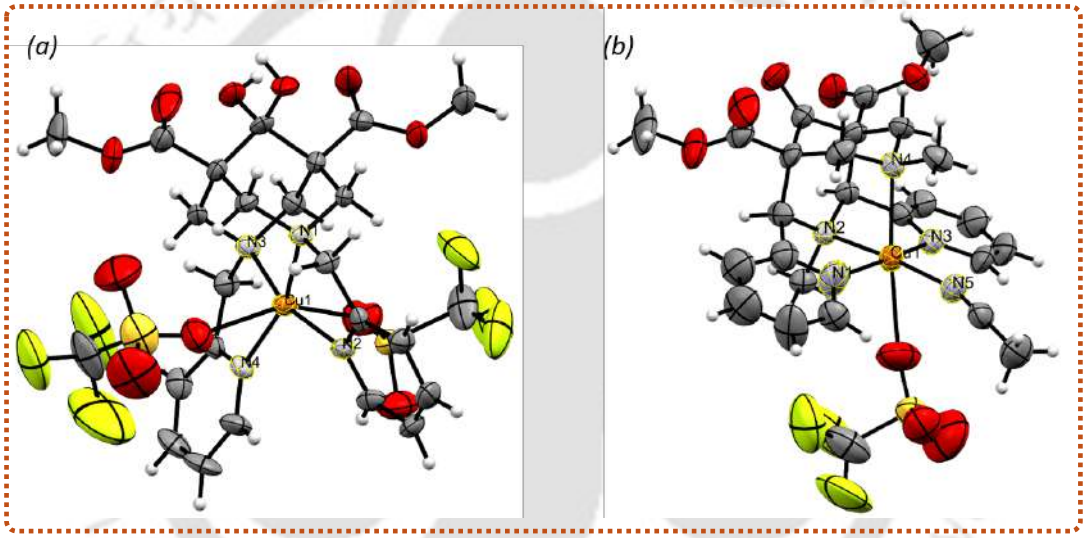

Figure 6b.9. *ORTEP images of (a) [Cu^{L1}_{Flex}] and (b) [Cu^{L2}_{Rigid}] complex (Probability=50%). Counter ions were omitted for better clarity.*

Single-crystal XRD analysis revealed that [Cu^{L2}_{Rigid}] adopts a trigonal pyramidal geometry, with triflate and acetonitrile ligands occupying coordination sites trans to the N7 (axial) and N3 (equatorial) donor atoms of the bispidine core, while the two pyridine donors define the equatorial plane. These OTf and acetonitrile ligands, weakly coordinated at *cis*-labile positions, are readily exchangeable with CO_2 under CO_2-saturated conditions, thereby enabling efficient catalytic participation. In contrast, [Cu^{L1}_{Flex}] crystallizes in a distorted square planar geometry with the two OTf ligands bind to the copper atom, *trans* to each other. The trans positioning of the two labile ligand moieties combined with a nearly symmetric ligand environment around the Cu(II) centre, significantly restricts its ability to interact with CO_2. ORTEP diagrams, along with bond lengths and bond angles for both the complexes, are

provided bellow (Figure 6b.9, Table 6b.1). Collectively, the comparative crystallographic analyses suggest that the rigid bispidine framework, by facilitating aqua coordination and creating accessible substitution sites, is intrinsically more favourable for catalytic CO_2 reduction than its flexible counterpart.

Table 6b.1. *Crystallographic bond distances and bond angles for both complexes.*

Complexes:	**$Cu(II)_{Rigid}$**			**$Cu(II)_{Flex}$**		
	Bonds	*r* in Å		Bonds	*r* in Å	
Axial bond	Cu1-N4	2.362	-	Cu1-N4	1.971	1.995*
Equatorial bonds	Cu1-N1	1.986	2.008*	Cu1-N1	2.016	
	Cu1-N2	2.045		Cu1-N2	1.974	
	Cu1-N3	1.995		Cu1-N3	2.022	
	Angles	θ in °		Angles	θ in °	
Trans-dihedral angles	N1-Cu1-N3	163.75		N1-Cu1-N4	160.80	
	N2-Cu1-N5	175.49		N2-Cu1-N3	162.29	
	N4-Cu1-O8	171.70		O8-Cu1-O11	158.65	
Cis-bond angles	N1-Cu1-N2	82.78		N1-Cu1-N2	85.37	
	N1-Cu1-N4	93.04		N1-Cu1-N3	88.34	
	N1-Cu1-N5	95.50		N2-Cu1-N4	105.21	
	N2-Cu1-N3	82.91		N3-Cu1-N4	85.74	
	N2-Cu1-N4	52.79				
	N3-Cu1-N4	92.96				
	N3-Cu1-N5	98.19				

Guided by the UV–vis data and structural insights, we have investigated the electrochemical properties of the two Cu(II) complexes in the absence of heterogeneous catalysts. Cyclic voltammetry (CV) and differential pulse voltammetry (DPV) were performed in phosphate buffer. Both [Cu^{L2}_{Rigid}] and [Cu^{L1}_{Flex}] exhibited reversible redox behaviour, though at distinct potentials. For [Cu^{L2}_{Rigid}], the Cu^{+2}/Cu^{+1} reduction was observed at 0.39 V (vs RHE), while the subsequent Cu^{+1}/Cu^{0} reduction occurred at 0.22 V (vs RHE). In contrast, [Cu^{L1}_{Flex}] displayed reduction transitions at 0.44 V and 0.34 V (vs RHE), respectively. The comparatively lower

positive potentials required for [Cu^{L2}_{Rigid}] indicate that, once the Cu center is electrochemically reduced, it can readily donate (via self-oxidation) electrons to CO_2, facilitating its activation and subsequent reduction. As the electrocatalytic process involves only reductive pathways, our analysis is focused on these reduction potentials only.

To further probe the distinct electronic environments of the metal centers, X-ray photoelectron spectroscopy (XPS) of the Cu 2p core levels was carried out (Figure 6b.10). The binding energies of Cu in [Cu^{L2}_{Rigid}] were shifted to lower values relative to those in [Cu^{L1}_{Flex}], consistent with a higher electron density around the Cu center in [Cu^{L2}_{Rigid}]. This increased electron density renders the Cu site more prone for electron donation to reduce CO_2, aligning with the electrochemical data and explaining the high Faradaic efficiency in presence of [Cu^{L2}_{Rigid}] hybrid system.

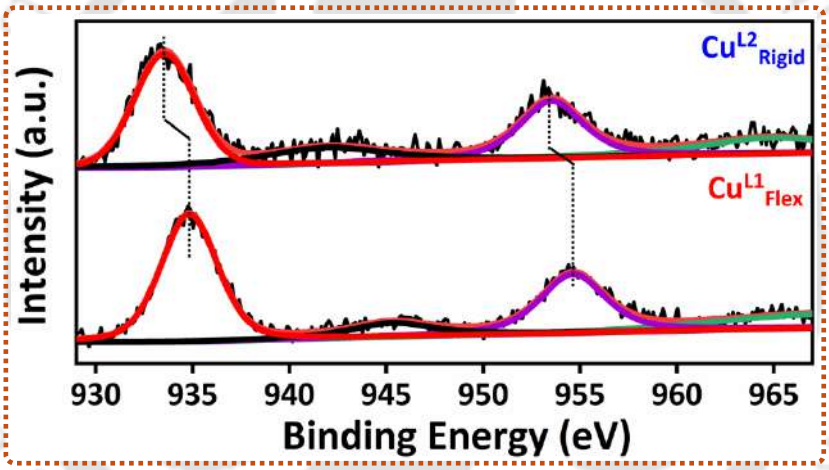

Figure 6b.10. *High-resolution X-ray photoelectron spectroscopy (XPS) Cu 2p core-level spectra of the copper(II) complexes [Cu^{L2}_{Rigid}] and [Cu^{L1}_{Flex}], illustrating a noticeable shift of the Cu 2p binding energies toward lower values for [Cu^{L2}_{Rigid}]. This shift indicates a higher electron density at the Cu centre in the rigid ligand environment, consistent with its enhanced electron-donating ability and superior CO_2 reduction performance.*

The electrochemical H-cell employed for CO_2 reduction is schematically illustrated in figure 6b.4k. In this setup, the working and reference electrodes were positioned within chamber (II) of the H-cell, which was continuously purged with CO_2, and the reduction potential was applied. The homogeneous catalyst was dissolved in the electrolyte within this cathodic compartment, where CO_2 reduction occurred. The chamber (I) housed a platinum counter electrode for the anodic half-reaction. The two compartments were separated by a Nafion proton-exchange membrane, which permits selective H^+ transport from the anode to the

cathode, thereby maintaining ionic conductivity and charge balance while preventing crossover of products or catalysts.[30] This separation also ensures that the homogeneous catalyst remained confined to the cathodic chamber, eliminating undesired anodic side reactions.

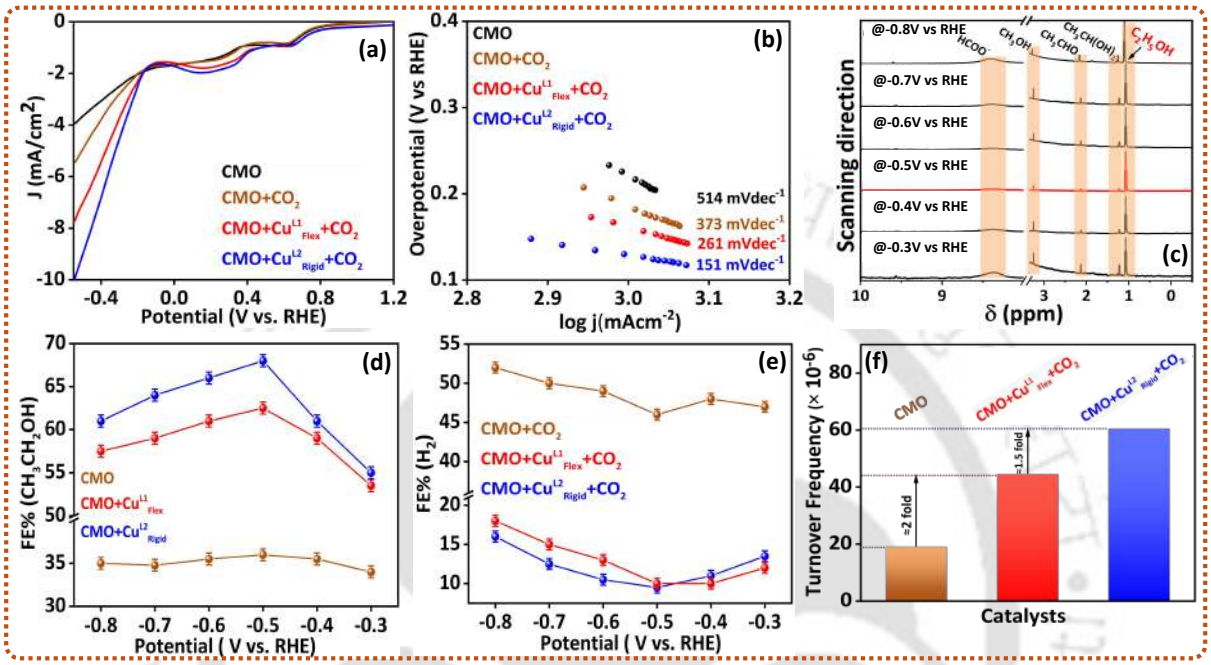

***Figure 6b.11**. (a) Linear sweep voltammetry (LSV) analysis for homogeneous-heterogeneous hybrid system as well as stand-alone heterogeneous system; (b) Tafel slope analysis showing improved charge-transfer kinetics; (c) ^1H NMR spectra of liquid products at different applied potentials for [Cu^{L2}_{Rigid}]/CMO system; (d) Faradaic efficiencies for ethanol and other products; (e) Faradaic efficiencies for H_2 (HER suppression); (f) turnover frequencies (TOF) of different catalytic system.*

To assess the electrocatalytic activity towards the CO_2 reduction, linear sweep voltammetry (LSV) was performed for both the heterogeneous system and the homogeneous–heterogeneous hybrid configuration under CO_2-saturated and N_2-saturated conditions. As shown in Figure 6b.11a, the CMO heterogeneous catalyst alone exhibited an increased current density upon CO_2 saturation, indicating the occurrence of additional reduction pathways beyond the hydrogen evolution reaction, consistent with CO_2 reduction to value-added products. Incorporation of the homogeneous catalysts led to a further enhancement in current density, with the most pronounced effect observed for the [Cu^{L2}_{Rigid}]-modified system, which achieved a current density of ~9.8 mA cm^{-2} at –0.5 V vs RHE. This

significant increase demonstrates accelerated electron-transfer kinetics and higher catalytic turnover, reflecting the superior efficiency of [Cu^{L2}_{Rigid}] in promoting CO_2 reduction. The kinetics of CO_2 reduction were further evaluated by Tafel slope analysis, which provides insights into charge-transfer efficiency. As shown in Figure 6b.11b, the lowest Tafel slope was obtained for the [Cu^{L2}_{Rigid}]-containing system, with a value of 151 mV dec^{-1}, compared to 261 mV dec^{-1} in the presence of [Cu^{L1}_{Flex}]. The smaller Tafel slope for [Cu^{L2}_{Rigid}] signifies more favorable kinetics, as it indicates that only a modest increase in applied potential is required to achieve a substantial rise in current density. This result highlights the faster electron-transfer dynamics and the less energy-demanding rate-determining step associated with [Cu^{L2}_{Rigid}].

Quantitative analysis of the CO_2 reduction products was performed by determining the Faradaic efficiency, with liquid-phase products identified and quantified using NMR spectroscopy in the presence of an internal standard. Given that the [Cu^{L2}_{Rigid}]/CMO hybrid system exhibited the highest current density and the lowest Tafel slope, NMR spectra were recorded for this configuration at applied potentials ranging from –0.3 to –0.8 V vs RHE in 0.1 V increments (Figure 6b.11c). The spectra indicate ethanol as the dominant product, with minor byproducts diminishing in intensity as the potential shifts from –0.3 to –0.5 V. Consequently, the Faradaic efficiency for ethanol increased, reaching a maximum of ~68% at –0.5 V (Figure 6b.11d). Beyond this potential, the ethanol yield declined due to the resurgence of side-product formation, as evidenced by the increasing relative intensities of their spectral features. A comparative analysis of Faradaic efficiencies (Figure 6b.11d) further demonstrates that the [Cu^{L2}_{Rigid}]/CMO system significantly outperforms both the [Cu^{L1}_{Flex}]/CMO hybrid and the CMO-only control. The corresponding NMR spectra, from which the Faradaic efficiencies of [Cu^{L1}_{Flex}]/CMO and the CMO-only control were determined based on the NMR spectra provided in figure 6b.12.

In aqueous CO_2 reduction, the primary competing side reaction is the hydrogen evolution reaction (HER), and its suppression is critical for achieving high selectivity towards the CO_2 reduction. Figure 6b.11e illustrates the Faradaic efficiency associated with HER, showing that the [Cu^{L2}_{Rigid}]/CMO system exhibits the lowest hydrogen production at –0.5 V, underscoring its superior selectivity for CO_2 reduction. To further probe the role of the homogeneous catalyst, CO_2 reduction was carried out using a glassy carbon electrode in place of CMO. Under

these conditions, no liquid products were detected; however, gas-phase analysis revealed substantial CO evolution. Gas chromatography confirmed that [Cu^{L2}_{Rigid}] generated higher CO yields than [Cu^{L1}_{Flex}], consistent with its ability to easily donate electron from the metal center after accessing catalytically active low-valent states at reduced overpotentials, thereby facilitating CO_2-to-CO conversion. These findings suggest that the homogeneous complex functions as a continuous CO generator, which subsequently feeds into the heterogeneous catalyst, where CO dimerization and downstream C–C coupling led to C_2 product formation.

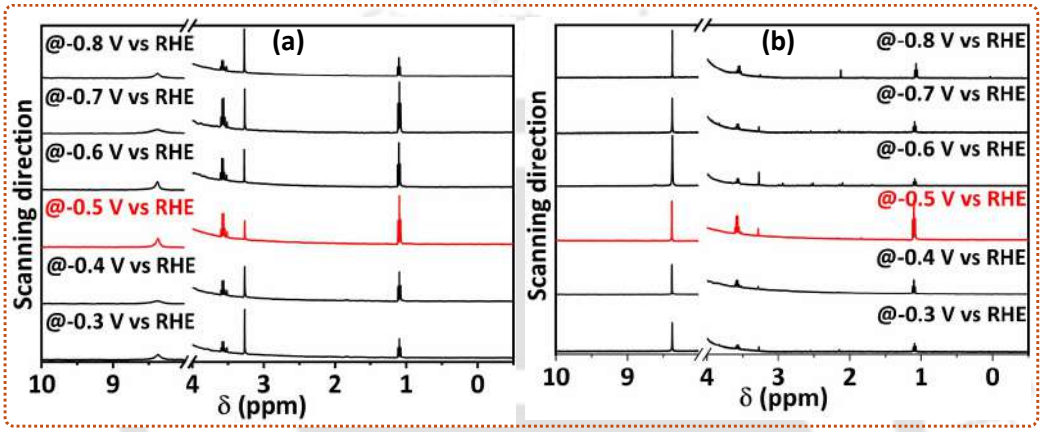

Figure 6b.12. *(a) ^{1}H NMR spectrum of the [Cu^{L1}_{Flex}]/CMO hybrid system, used to identify and quantify the reaction products for the determination of Faradaic efficiency. (b) ^{1}H NMR spectrum of the stand-alone CMO system recorded under identical electrochemical conditions, serving as a reference for comparison of product distribution and Faradaic efficiency with the hybrid catalyst systems.*

Turnover frequency (TOF) was evaluated to assess the catalytic cycles sustained per active site over time (Figure 6b.11f). The homogeneous–heterogeneous system incorporating [Cu^{L2}_{Rigid}] exhibited a 1.5-fold enhancement in TOF relative to [Cu^{L1}_{Flex}] and nearly a threefold improvement compared to the stand-alone heterogeneous catalyst. The enhanced TOF of [Cu^{L2}_{Rigid}] arises from its rigid ligand framework that promotes efficient electron transfer through synchronized Cu(I)/Cu(0) redox couple with the heterogeneous counterpart. Additionally, its coordination geometry ensures optimized substrate orientation and facile CO_2 interaction, facilitating faster catalytic cycling and intermediate transformation.

To quantify the electrochemically active surface area (ECSA), double-layer capacitance (C_{dl}) was determined from cyclic voltammograms recorded in the non-faradaic region at varying scan rates (Figure 6b.13).

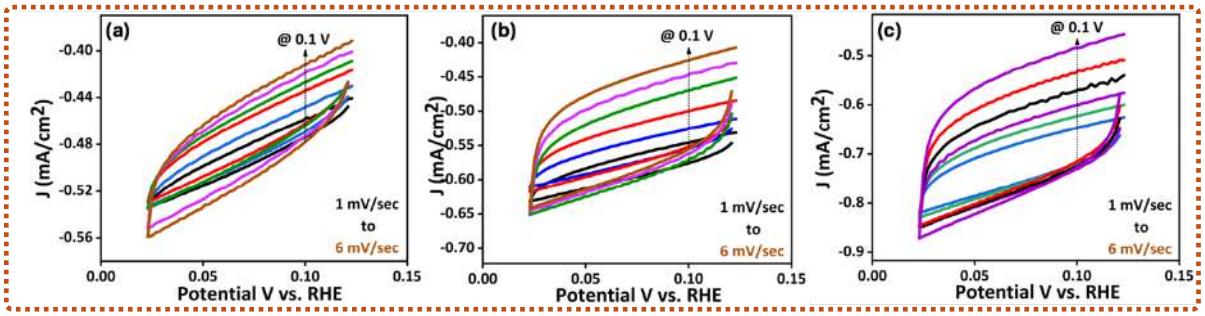

Figure 6b.13. *CVs in the non-faradaic region (0.025–0.125 V vs. RHE) at varying scan rates for C_{dl} determination.*

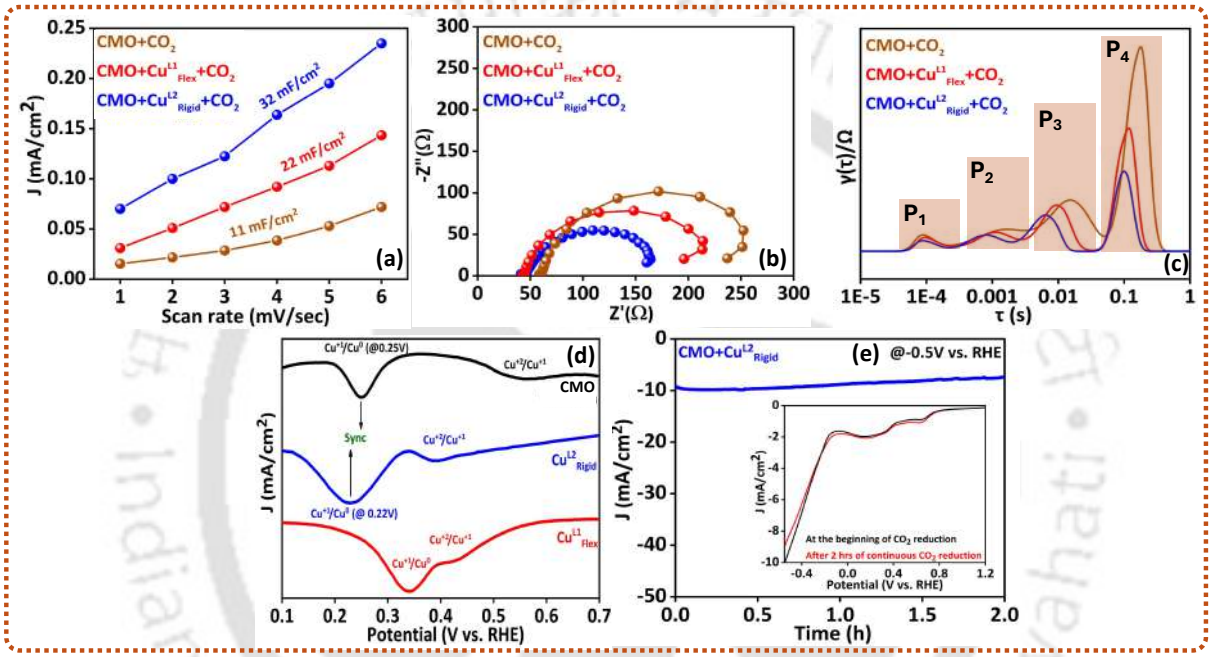

Figure 6b.14*. (a) electrochemically active surface area (ECSA) derived from double-layer capacitance; (b) Nyquist plots from electrochemical impedance spectroscopy (EIS) at –0.5 V vs RHE; (c) distribution of relaxation times (DRT) analysis highlighting interfacial processes (P1–P4); (d) differential pulse voltammetry (DPV) showing redox synchronization between homogeneous and heterogeneous catalysts; (e) chronoamperometry at –0.5 V vs RHE, demonstrating catalytic stability and sustained activity.*

As shown in Figure 6b.14a, C_{dl} increased markedly from 11 µF cm^{-2} for the stand-alone heterogeneous catalyst to 22 µF cm^{-2} in presence of [Cu^{L1}_{Flex}] , and further to 32 µF cm^{-2} upon addition of [Cu^{L2}_{Rigid}]. This enhancement arises from the uniform dispersion of polarized species at the electrode–electrolyte interface, which increases interfacial charge density and capacitance. The highest C_{dl} observed for [Cu^{L2}_{Rigid}] may be attributed to its asymmetric coordination environment, which induces more polarity between ligand and metal center facilitating stronger interfacial interactions. Furthermore, the slightly higher polarity of

[Cu^{L2}_{Rigid}] enables faster migration toward the electrode surface, allowing more efficient delivery of the –CO intermediate compared to [Cu^{L1}_{Flex}]

Enhanced electrochemical performance is closely associated with efficient charge-transfer kinetics at the electrode–electrolyte interface. To probe this, electrochemical impedance spectroscopy (EIS) was employed to evaluate the charge-transfer resistance (R_{ct}). Nyquist plots recorded at –0.5 V vs RHE (Figure 6b.14b) reveal that the R_{ct} values follow the same trend as the Tafel slopes, consistent with improved reaction kinetics. As the Tafel slope is inversely related to the charge-transfer coefficient (Tafel slope $\propto 1/\alpha$). Among the systems examined, the [Cu^{L2}_{Rigid}]/CMO hybrid exhibited the smallest semicircle, indicative of a lower R_{ct} compared to the [Cu^{L1}_{Flex}]/CMO system. The reduced R_{ct} for [Cu^{L2}_{Rigid}] highlights its superior charge-transfer capability, stemming from an energetically favorable alignment between the redox processes of the rigid Cu complex and the CMO support, thereby facilitating more synchronized and efficient electron transfer.

To further resolve the time constants and resistance values associated with interfacial relaxation processes, Distribution of Relaxation Times (DRT) analysis was performed using MATLAB on the acquired AC impedance spectra (Figure 6b.14c).[31,32] This method deconvolutes the impedance response into distinct processes, each defined by a characteristic relaxation time, enabling separation of overlapping electrochemical phenomena across different timescales. In the context of CO_2 electroreduction, timescale-resolved analysis can also provide critical insights into ionic transport, charge transfer, diffusion constraints and interfacial dynamics, along with contributions from less resolved processes. The detailed methodology is provided in the supporting information (Section 2.6.7.2), and the mathematical relationship between the impedance response and the DRT function is expressed in equation (6b.1).

$$Z(\omega) = R_{\infty} + R_{pol}\int_{-\infty}^{\infty}\frac{\Gamma(\log(\tau))}{1+i\omega\tau}d(\log(\tau)) \qquad (6b.1)$$

In this context, $Z(\omega)$ denotes the overall impedance, where R_{∞} corresponds to the series (ohmic) resistance, and R_{pol} represents the total polarization resistance associated with the electrochemical processes. Γ is the distribution function of relaxation times, τ signifies the

characteristic relaxation time, and ω denotes the angular frequency of the applied perturbation.

DRT analysis of the EIS spectra (Figure 6b.14c) reveals four distinct relaxation features (P_1–P_4), each corresponding to a specific electrochemical process contributing to the overall polarization resistance. The characteristic time constant (τ) defines each process, while the integrated peak area reflects its resistance contribution. P_4, observed in the low-frequency region, is assigned to mass transport and diffusion; P_3, appearing in the mid-frequency domain, corresponds to interfacial charge transfer; whereas P_2 and P_1, located in the high-frequency region, are associated with the intrinsic resistance of the active material and the uncompensated series resistance, respectively. Notably, the DRT profiles undergo pronounced changes upon incorporation of the homogeneous catalyst. Both P_4 and P_3 shift toward higher frequencies with reduced intensities relative to the stand-alone heterogeneous system, indicating diminished diffusion and charge-transfer resistances. The most significant reduction in P_4 and P_3 intensities is observed for the [Cu^{L2}_{Rigid}] complex in the homogeneous–heterogeneous hybrid system, highlighting accelerated ion transport and more efficient interfacial kinetics.

This improvement can be attributed to the superior redox synchronization between [Cu^{L2}_{Rigid}] and CMO reduction potential, which facilitates rapid electron exchange. The relaxation time constant (τ) corresponding to charge transfer (P_3) is ~7 ms for [Cu^{L2}_{Rigid}], nearly 3 ms shorter than that of [Cu^{L1}_{Flex}], further underscoring the enhanced charge-transfer kinetics. The effective resistance values associated with each process for all catalytic systems are summarized in Table 6b.2.

To further validate the proposed redox synchronization between the [Cu^{L2}_{Rigid}] complex in the homogeneous phase and CMO in the heterogeneous framework, particularly concerning the Cu^{+1}/Cu^0 transition, differential pulse voltammetry (DPV) was carried out on the individual catalytic components. For homogeneous complexes, measurements were performed in the absence of CMO using a three-electrode configuration consisting of Ag/AgCl as the reference, Pt as the counter, and a glassy carbon working electrode. In case of stand-alone heterogeneous system, CMO itself served as the working electrode without homogeneous additives.

***Table 6b.2**. Summary of effective resistance parameters for electrochemical processes in different hybrid catalytic systems.*

System	$P_1 + P_2$ (Ω)	P_3 (Ω)	P_4 (Ω)
CMO	0.27	6.26	**253.46**
$[Cu^{L1}{}_{Flex}]$/CMO	0.26	5.86	**168.87**
$[Cu^{L2}{}_{Rigid}]$/CMO	0.24	4.66	**145.10**

The DPV profiles display two reduction features corresponding to the Cu^{+2}/Cu^{+} and Cu^{+1}/Cu^{0} couples. Importantly, $[Cu^{L2}{}_{Rigid}]$ exhibits both reductions at less positive potentials compared to $[Cu^{L1}{}_{Flex}]$, signifying that, once $[Cu^{L2}{}_{Rigid}]$ complex electrochemically reduced to the Cu^0 state, it can more effectively deliver electrons to CO_2 by oxidising itself, promoting the CO_2 to the *CO intermediate conversion thermodynamically more favourable. A closer comparison reveals that the Cu^{+1}/Cu^0 transition of $[Cu_{L1}{}^{Flex}]$ occurs at ~0.1 V away from that of CMO, whereas $[Cu^{L2}{}_{Rigid}]$ shows only a minimal offset (~0.03 V) relative to CMO (Figure 6b.14d). This near-perfect alignment of potentials underscores superior redox synchronization between $[Cu^{L2}{}_{Rigid}]$ and CMO, enabling faster interfacial charge transfer. The resulting rapid electron transfer enhances *CO generation in $[Cu^{L2}{}_{Rigid}]$, thereby establishing a favourable pathway toward subsequent C–C coupling and selective C_2 product formation at the heterogenous surface.

Since CO_2 reduction was carried out under chronoamperometric conditions with continuous potential application, the analysis at – 0.5 V vs. RHE - where the highest selectivity was achieved - is presented in Figure 6b.14e. The chronoamperometric profile not only highlights the product selectivity at this potential but also serves as a measure of catalytic stability. Notably, the current density remains essentially unchanged over prolonged electrolysis, indicating robust and sustained performance of both catalytic systems.

The structural stability of both the heterogeneous and homogeneous catalysts was thoroughly examined after electrocatalysis (Figure 6b.15). FESEM imaging of the heterogeneous catalyst confirmed the preservation of its hexagonal sheet-like morphology, while post-electrocatalysis XRD analysis showed no evidence of metallic Cu deposition, underscoring the stability of homogeneous Cu complexes under the reaction conditions. In

addition, UV–Vis spectra of the homogeneous complexes (Cu^{L1}_{Flex} and Cu^{L2}_{Rigid}) recorded before and after electrolysis revealed unchanged absorption features, confirming the retention of their molecular frameworks.

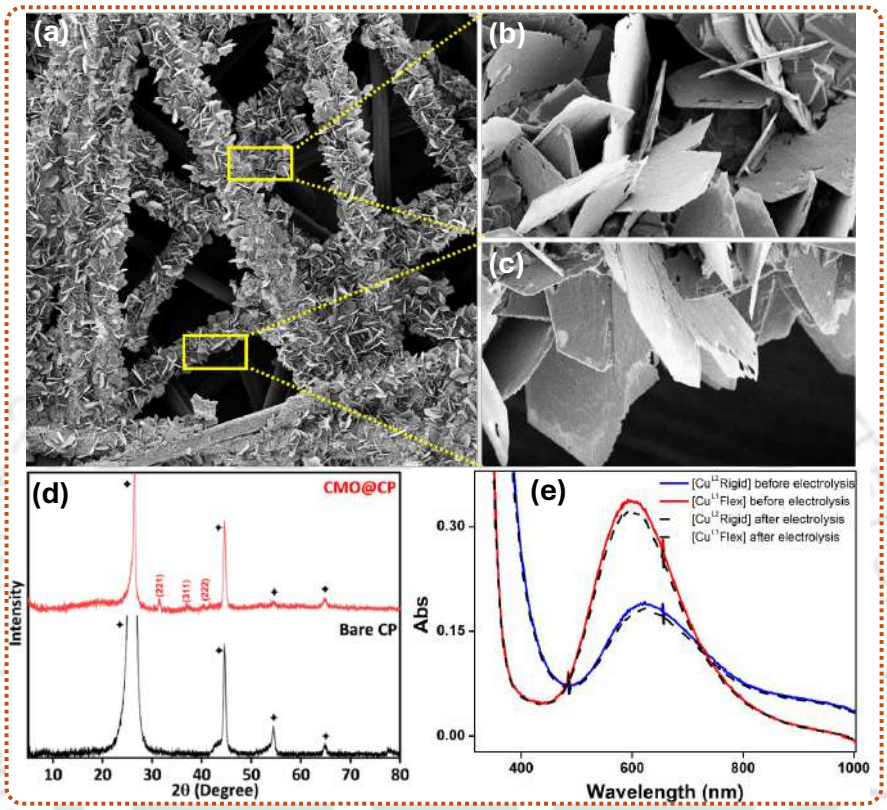

Figure 6b.15. *(a-c) FESEM image of the catalyst after electrocatalysis showing intact hexagonal sheet morphology; (d) XRD pattern of the heterogeneous catalyst recorded after electrocatalysis; (d) UV–Vis spectra of* Cu^{L1}_{Flex} *and* Cu^{L2}_{Rigid} *recorded before and after electrocatalysis.*

The reaction pathways leading to C_2H_5OH and C_2H_4 on Cu-based heterogeneous surfaces proceed through a common mechanism, initiated by the dimerization of two adsorbed *CO species, followed by sequential protonation and dehydration steps to yield the key intermediate *HCCOH.[33,34] The eventual branching toward ethanol or ethylene formation is dictated by the relative stability of intermediates derived from *HCCOH.[33-35] Ethanol selectivity is favoured on Cu containing surfaces with low coordination and an optimal oxidation state, as these sites stabilize oxygenated intermediates more effectively, facilitating the hydrogenation steps necessary for C_2H_5OH formation.[36] Previous studies have shown that Mn incorporation into Cu-based systems enhances $*H_{ad}$ coverage by stabilizing hydrogen

adsorption and lowering the water dissociation barrier relative to pure Cu.[27] This stabilization of surface hydrogen directly facilitates C–C coupling to form HCCOH, thereby accelerating pathways toward C_2 products such as ethanol. To gain further atomistic insights into this cooperative effect, we conducted first-principle calculations using CuO as the Mn-absent reference system and $Cu_{1.5}Mn_{1.5}O_4$ as the Mn-incorporated catalyst to elucidate the influence of Mn on hydrogen adsorption behavior. As shown in Figure 6b.16(b,c), the most favorable H_2-adsorption configuration exhibits a higher adsorption energy (E_{ads} = 0.099 eV) for $Cu_{1.5}Mn_{1.5}O_4$ than for CuO (0.049 eV), with corresponding adsorption distances of 2.58 Å and 2.05 Å, respectively. This indicates a stronger H_2–surface interaction in $Cu_{1.5}Mn_{1.5}O_4$, which could promote the subsequent hydrogen dissociation and reduction steps.

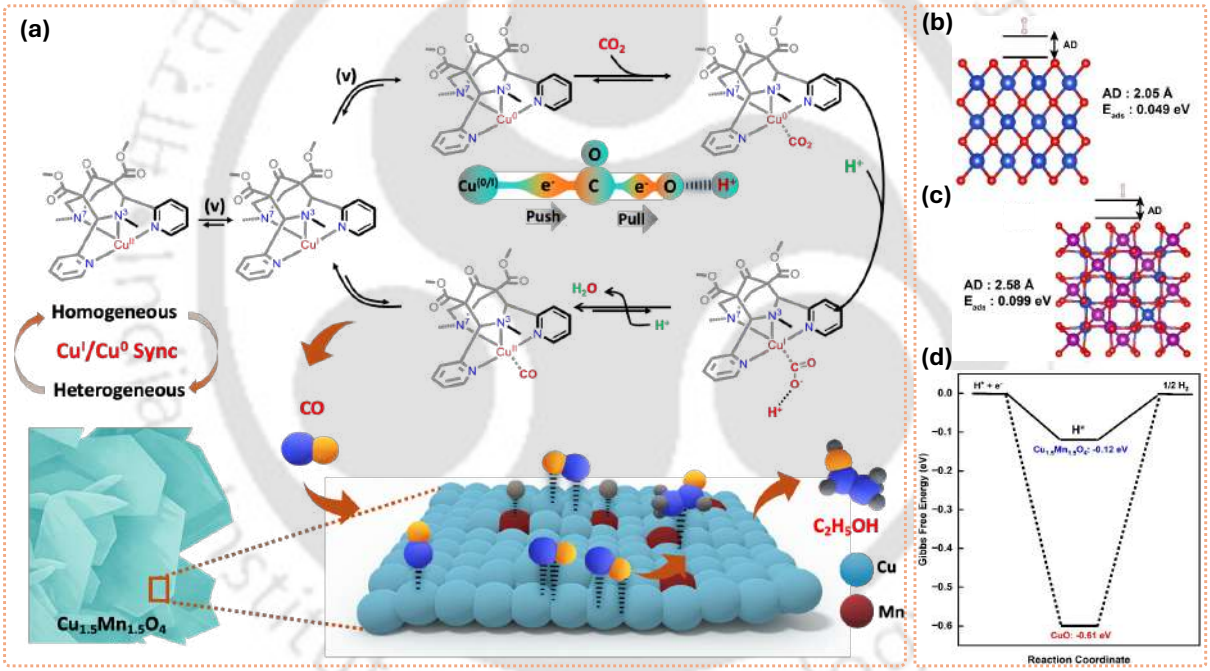

***Figure 6b.16**. (a) Schematic illustration of the cooperative mechanism in the homogeneous–heterogeneous hybrid catalyst system, highlighting the synergistic pathway for enhanced ethanol selectivity during CO_2 electroreduction; most stable hydrogen adsorption configuration of (b) CuO and (c) $Cu_{1.5}Mn_{1.5}O_4$. (d) Gibbs free energy profile for plots for HER (Oxygen, copper, manganese, and hydrogen atoms are represented by red, blue, purple, and white spheres, respectively)*

The Gibbs free energy profile of H-adsorption (Figure 6b.16d) further supports this observation, where the ΔG_{H^*ad} values are −0.12 eV for $Cu_{1.5}Mn_{1.5}O_4$ and −0.61 eV for CuO,

suggesting comparable thermodynamics but a more favorable hydrogen activation environment on the Mn-modulated surface. The inclusion of Mn thus enhances $*H_{ad}$ coverage by modulating the local electronic structure of Cu sites and facilitating more efficient proton–electron transfer. The stoichiometry of the $Cu_{1.5}Mn_{1.5}O_4$ spinel structure, containing equimolar Cu and Mn per unit cell, inherently enforces atomistic Mn–Cu pairing that maximizes dual-site synergy. This intrinsic design ensures that each Cu atom is electronically and catalytically modulated by a neighboring Mn atom, thereby amplifying cooperative effects and delivering superior C_2 selectivity.

C–C coupling via *CO dimerization is the key pathway for C_2 product formation on heterogeneous Cu-based surfaces.[37] However, the initial reduction of CO_2 to CO on such surfaces is intrinsically challenging due to less controllable active sites, causing broader adsorption energies and lower selectivity as it is one of the most energy consuming process.[38] To address this limitation, we designed a hybrid catalytic strategy that integrates homogeneous and heterogeneous systems. Homogeneous Cu(II) complexes, with their well-defined molecular coordination environments, enable precise control over *CO generation, thereby enhancing selectivity. In this study, two bispidine-derived Cu(II) complexes with distinct geometric rigidities ($[Cu^{L1}_{Flex}]$ and $[Cu^{L2}_{Rigid}]$) were employed as homogeneous co-catalysts in conjunction with a Cu–Mn oxide (CMO) heterogeneous catalyst. Importantly, $[Cu^{L2}_{Rigid}]$ exhibited superior performance due to its favourable Cu^{+1}/Cu^0 redox synchronization with the heterogeneous catalyst, which facilitated efficient interfacial electron transfer.[25,38] This cooperative effect significantly enhanced the supply of *CO intermediates from the homogeneous phase to the heterogeneous surface, where subsequent *CO dimerization and hydrogenation processes were promoted. As a result, ethanol selectivity was markedly improved, demonstrating the efficacy of this dual catalytic approach in overcoming the intrinsic limitations of heterogeneous CO_2-to-CO conversion.

The electrochemical reduction of CO_2 to CO mediated by $[Cu^{L2}_{Rigid}]$ proceeds through a two-electron “push–pull” mechanism in the presence of phosphate buffer (Figure 6b.16a). Upon electroreduction, the active $[Cu(0)^{L2}_{Rigid}]^{2-}$ species engages CO_2 to yield a $[Cu(0)(CO_2)^{L2}_{Rigid}]^{2-}$ adduct, where electron density is “pushed” from the nucleophilic Cu^0 center into the electrophilic CO_2 framework. The predominant resonance contributor is best described as $[Cu(I)(CO_2^{\bullet-})^{L2}_{Rigid}]^{2-}$, in agreement with prior DFT predictions[39,40,41]. Through hydrogen-

bonding (Brønsted) interactions, the phosphate buffer stabilizes the reaction intermediate and facilitates electron withdrawal or "pull“ from the substrate, thereby accelerating C–O bond cleavage. The resulting *CO species is then relayed to the heterogeneous surface, providing a pre-formed intermediate from the homogeneous catalyst with high selectivity.

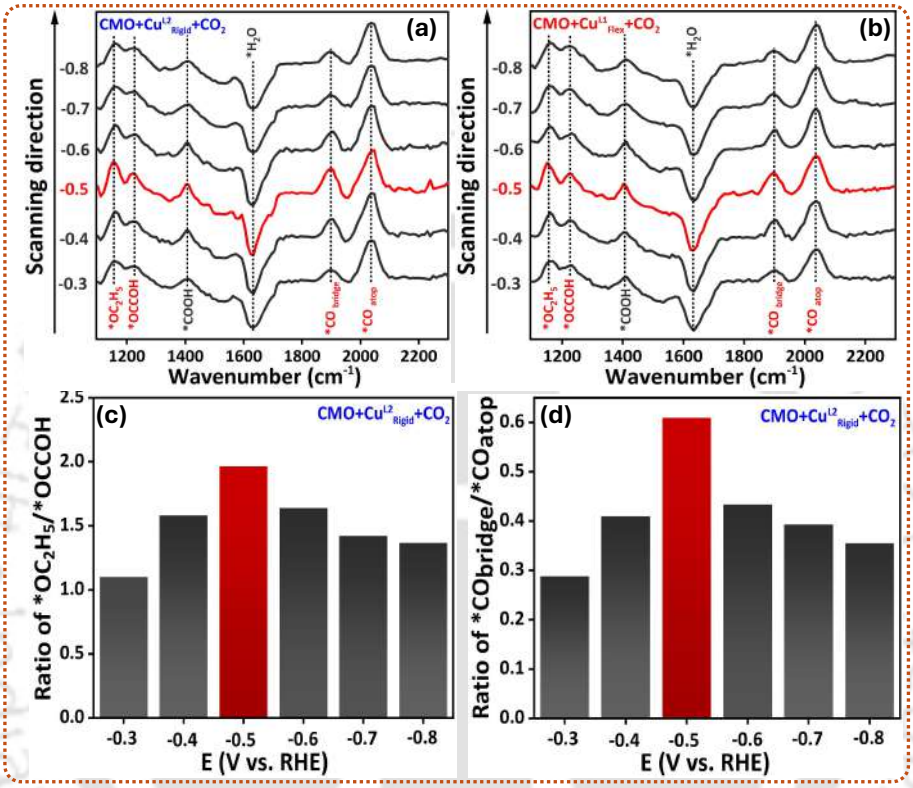

***Figure 6b.17**. (a and b) Potential-dependent operando in-situ IRAS analysis of CO adsorption and intermediate formation during CO_2 reduction on the hybrid [Cu^{L1}_{Flex}]+CMO and [Cu^{L2}_{Rigid}]+CMO systems; (c and d) quantitative *CO_{bridge}/*CO_{atop} and *OC_2H_5/*OCCOH ratios showing maximum bridge *CO and *OC_2H_5 enrichment at –0.5 V vs RHE for the [Cu^{L2}_{Rigid}]+CMO system.*

The inspection of in-situ IRAS spectra for the [Cu^{L2}_{Rigid}]–mediated hybrid system (Figure 6b.17a) reveals that upon shifting the applied potential from –0.3 V to –0.5 V vs RHE, the intensity of the *CO_{bridge} band increases relative to that of *CO_{atop}, while the latter remains largely unaffected by potential variation. Quantitative integration and statistical evaluation (Figure 6b.17d) show that the *CO_{bridge}/*CO_{atop} ratio reaches a maximum at –0.5 V vs RHE, establishing this potential as optimal for tuning the oxidation state of the CMO surface in the presence of the homogeneous co-catalyst. This condition favours a tailored *CO configuration

enriched in bridge-adsorbed species. Because $*CO_{bridge}$ and $*CO_{atop}$ differ in their back-donation and proton-accepting characteristics, their subsequent protonation energetics diverge. Prior studies indicate that $*CO_{bridge}$ protonation is energetically more favourable than that of $*CO_{atop}$ on metal oxide surfaces.[36] Consequently, the hybrid system enables C–C bond formation through an asymmetric coupling pathway between *CO and *CHO (or *COH), initiated via $*CO_{bridge}$ protonation. This asymmetric route presents a lower activation barrier compared to direct *CO dimerization, consistent with theoretical predictions, thereby rationalizing the enhanced C_2 product formation observed.

In-situ IRAS spectra revealed additional peaks at ~1410, ~1250, and ~1120 cm^{-1}, with the latter two assigned to *OCCOH and $*OC_2H_5$ intermediates.[42] Notably, the $*OC_2H_5$/*OCCOH intensity ratio reaches its maximum when $[Cu^{L2}{}_{Rigid}]$ is employed in the homogeneous medium at –0.5 V vs RHE, indicating that the key $*OC_2H_5$ intermediate associated with ethanol formation is significantly stabilized under these conditions on the CMO surface. In contrast, the spectra obtained with $[Cu^{L1}{}_{Flex}]$ (Figure 6b.17b) reveal lower $*CO_{bridge}$/$*CO_{atop}$ and $*OC_2H_5$/*OCCOH ratios, correlating with the reduced Faradaic efficiency of ethanol. The superior efficiency observed for the $[Cu^{L2}{}_{Rigid}]$ system arises from its lower Cu^{+1}/Cu^0 reduction potential and enhanced redox synchronization with the heterogeneous CMO surface. When the redox levels of homogeneous and heterogeneous components are well aligned, the energetic barrier for –CO intermediate transfer is minimized, as the matching energy levels diminish the thermodynamic driving force required for migration. This facile transfer ensures a higher surface population of –CO species, thereby promoting efficient C–C coupling pathways that favour C_2 product formation.

6b.4. Conclusions:

The present study establishes a hybrid catalytic platform where molecular bispidine–Cu complexes cooperate with a $Cu_{1.5}Mn_{1.5}O_4$ electrode to achieve selective CO_2 conversion under neutral aqueous conditions. By entangling the roles of the homogeneous and heterogeneous components, we show that molecular catalysts can efficiently mediate the energetically demanding CO_2-to-CO step, while the oxide electrode drives downstream C–C coupling. Crucially, the rigid $[Cu^{L2}{}_{Rigid}]$ complex exhibited superior performance owing to its less positive Cu^+/Cu^0 reduction potential and strong redox synchronization with the CMO surface. This dual

advantage allowed facile CO_2-to-CO conversion in solution and efficient relay of *CO intermediates to the electrode, resulting in rapid interfacial electron transfer and enhanced ethanol selectivity. Faradaic efficiency reached ~68% with a 1.5-fold higher turnover frequency compared to the flexible analogue, highlighting the importance of rigid ligand design in facilitating fast charge transfer and superior kinetics. Spectroscopic analysis confirms that this cooperation stabilizes $*CO_{bridge}$ and $*OC_2H_5$ intermediates, rationalizing the pronounced bias toward ethanol formation at optimal reduction potential. Looking forward, this molecular–oxide cooperative design provides a generalizable blueprint for tuning C_2 product formation. Future efforts directed toward ligand modification and exploration of alternative oxide supports could further refine redox alignment and intermediate stabilization, enabling access to higher value oxygenates and other multicarbon products.

6b.5. References:

1 L. Zhang, A. V. Müller, S. P. Desai, D. C. Grills, D. E. Polyansky and R. N. Sampaio, *ACS Catal*. 2024, **14**, 18477.

2 J. Meng, J. Freeze, L. Nowack, C. Li, H. Wang, H. D. Abrunna, A. P. Willard, V. S. Batista and T. Lian, *J. Am. Chem. Soc*. 2025, **147**, 25361.

3 X. She, Y. Wang, H. Xu, S. C. E. Tsang and S. Ping Lau, *Angew. Chem., Int. Ed*. 2022, **61**, e202211396.

4 X. Tian, G. Xu, S. Chen, Q. Li and J. Duan, *J. Mater. Chem. A*, 2025, **13**, 22295.

5 L. Sun, V. Reddu, A. C. Fisher and X. Wang, *Energy Environ. Sci*. 2020, **13**, 374.

6 J. J. Lv, R. Yin, L. Zhou, L. Li, R. Kikas, T. Xu, Z. Wang, H. Jin, X. Wang and S. Wang, *Angew. Chem., Int. Ed*. 2022, **61**, e202207252.

7 T. Ishizuka, A. Hosokawa, T. Kawanishi, H. Kotani, Y. Zhi and T. Kojima, *J. Am. Chem. Soc*. 2023, **145**, 23196.

8 D. Chen, B. Chu, F. Li, Y. T. Zheng, Y. Lu, B. Shao, L. Li, N. Y. Huang and Q. Xu, *J. Am. Chem. Soc*. 2025, **147**, 22705.

9 N. R. Crudo, A. Sonea, L. M. Karn, D. B. Leznoff and J. J. Warren, *ACS Catal*. 2025, **15**, 14293.

10 J. Cai and H. Zhu, *Communications Materials*, 2025, **6**, 118.

11 L. M. Gonzalez, A. L. Burnage, A. Nova and D. Balcells, *ACS Catal*. 2025, **15**, 9089.

12 S. Varhade, A. Guruji, C. Singh, G. Cicero, M. García-Melchor, J. Helsen and D. Pant, *ChemElectroChem*. 2025, **12**, e202400512.

13 T. Wissink, F. A. Rollier, V. Muravev, J. M. J. J. Heinrichs, R. C. J. van de Poll, J. Zhu, D. Anastasiadou, N. Kosinov, M. C. Figueiredo and E. J. M. Hensen, *ACS Catal*. 2024, **14**, 16589.

14 J. Kundu, B. R. Anne, J. Cho, H. Huang, D. Cho and S. Cho, *Small* 2025, **21**, e05185.

15 A. G. Yohannes, C. Lee, P. Talebi, D. H. Mok, M. Karamad, S. Back and S. Siahrostami, *ACS Catal*. 2023, **13**, 9007.

16 W. Ma, J. Morales-Vidal, J. Tian, M. T. Liu, S. Jin, W. Ren, J. Taubmann, C. Chatzichristodoulou, J. Luterbacher, H. M. Chen, N. López and X. Hu, *Nature* 2025, **641**, 1156.

17 R. Chen, J. Zhao, X. Zhang, Q. Zhao, Y. Li, Y. Cui, M. Zhong, J. Wang, X. Li, Y. Huang and B. Liu, *J. Am. Chem. Soc*. 2024, **146**, 24368.

18 J. Li, Y. Chen, B. Yao, W. Yang, X. Cui, H. Liu, S. Dai, S. Xi, Z. Sun and W. Chen, *J. Am. Chem. Soc*. 2024, **146**, 5693.

19 C. Peng, J. Ma, G. Luo, S. Yan, J. Zhang, Y. Chen, N. Chen, Z. Wang, W. Wei, T. K. Sham, Y. Zheng, M. Kuang and G. Zheng, *Angew. Chem., Int. Ed*. 2024, **136**, e202316907.

20 M. Wang, S. Liu, B. Chen, F. Tian and C. Peng, *ACS Sustain. Chem. Eng*. 2022, **10**, 5693.

21 Q. Zhang, J. Peng, S. Jiang, H. Xiong, X. Fu, S. Shang, J. Xu, G. He and P. C. Chen, *Applied Catalysis B: Environment and Energy.* 2025, **371**, 125255.

22 J. Y. Maeng, S. Y. Hwang, Y. J. Kim, C. K. Rhee and S. Sohn, *Chem. Eng. J*. 2023, **470**, 143970.

23 M. Yuan, S. Sahin, R. Cai, S. Abdellaoui, D. P. Hickey, S. D. Minteer and R. D. Milton, *Angew. Chem. Int. Ed*. 2018, **130**, 6692.

24 S. Guria, D. Dolui, C. Das, S. Ghorai, V. Vishal, D. Maiti, G. K. Lahiri and A. Dutta, *Nat. Commun*. 2023, **14**, 6859.

25 N. Kalita, J. K. Satpathy, R. Yadav, C. Sastri and M. Qureshi, *Chem. Mater*. 2025, **37**, 2026.

26 C. Zhan, F. Dattila, C. Rettenmaier, A. Herzog, M. Herran, T. Wagner, F. Scholten, A. Bergmann, N. López and B. R. Cuenya, *Nat. Energy*. 2024, **9**, 1485.

27 M. Luo, Z. Wang, Y. C. Li, J. Li, F. Li, Y. Lum, D. H. Nam, B. Chen, J. Wicks, A. Xu, T. Zhuang, W. R. Leow, X. Wang, C. T. Dinh, Y. Wang, D. Sinton and E. H. Sargent, *Nat. Commun*. 2019, **10**, 5814.

28 W. L. Armarego, D. D. Perrin, (Eds.), Purification of Laboratory Chemicals, Pergamon Press, Oxford, 1997.

29 P. Comba, C. L. de Laorden and H. Pritzkow, *Helv. Chim. Acta*. 2005, **88**, 647.

30 G. Mukherjee, J. K. Satpathy, U. K. Bagha, M. Q. E. Mubarak, C. V. Sastri and S. P. de Visser, *ACS Catal*. 2021, **11**, 9761.

31 G. Mukherjee and C. V. Sastri, *Isr. J. Chem*. 2020, **60**, 1032.

32 S. S. Nag, G. Mukherjee, P. Barman and C. V. Sastri, *Inorganica Chimica Acta*, 2019, **485**, 80.

33 K. Ament, D. R. Wagner, T. Gotsch, T. Kikuchi, J. Krohnert, A. Trunschke, T. Lunkenbein, T. Sasaki and J. Breu, *ACS Catal*. 2021, **11**, 2754.

34 C. Li, Y. Jin and Q. Shao, *Small*. 2025, **21**, 2505810.

35 X. Q. Xu, L. H. Cao, Y. Yang, F. Zhao, X. T. Bai and S. Q. Zang, *ACS Appl. Mater. Interfaces*. 2021, **13**, 56566.

36 Y. Lu, C. Zhao, J. Huang and Q. Zhang, *Joule*. 2022, **6**, 1172.

37 C. Sheng, F. Yu, C. Li, H. Zhang, J. Huang, Y. Wu, M. Armand and Y. Chen, *J. Phys. Chem. Lett*. 2021, **12**, 2064.

38 Y. Y. Birdja, E. Pérez-Gallent, M. C. Figueiredo, A. J. Göttle, F. Calle-Vallejo and M. Koper, *Nat. Energy*. 2019, **4**, 732.

39 Y. Zheng, A. Vasileff, X. Zhou, Y. Jiao, M. Jaroniec and S. Z. Qiao, *J. Am. Chem. Soc*. 2019, **141**, 7646.

40 Y. Lum, T. Cheng, W. A. Goddard and J. W. Ager, *J. Am. Chem. Soc*. 2018, **140**, 9337.

41 L. Wang, S. A. Nitopi, E. Bertheussen, M. Orazov, C. G. Morales Guio, X. Liu, D. C. Higgins, K. Chan, J. K. Norskov, C. Hahn and T. F. Jaramillo, *ACS Catal*. 2018, **8**, 7445.

42 D. Cheng, K. L. C. Nguyen, V. Sumaria, Z. Wei, Z. Zhang, W. Gee, Y. Li, C. G. Morales-Guio, M. Heyde and B. R. Cuenya, *Nat. Commun*. 2025, **16**, 4064.

43 N. Kalita, A. Sahu, S. Bhowmick and M. Qureshi, *Chem. Commun*. 2022, **58**, 13747.

44 F. Franco, C. Rettenmaier, H. S. Jeon and B. R. Cuenya, *Chem. Soc. Rev*. 2020, **49**, 6884.

45 C. Costentin, S. Drouet, G. Passard, M. Robert and J. M. Savéant*, J. Am. Chem. Soc*. 2013, **135**, 9023.

46 J. Bonin, M. Maurin and M. Robert, *Coord. Chem. Rev*. 2017, **334**, 184.

47 P. Wang, H. Yang, C. Tang, Y. Wu, Y. Zheng, T. Cheng, K. Davey, X. Huang and S. Z. Qiao, *Nat. Commun*. 2022, **13**, 3754.

CHAPTER 7

Thesis Overview and Future Perspectives

This chapter briefly summarizes the key outcomes of the present thesis. It presents an overview of water electrolysis using morphology-engineered metal oxides and hydroxides, bipolar membranes for efficient water dissociation, and electrocatalytic CO_2 reduction, with an emphasis on redox synchronisation at catalytic and interfacial sites. Additionally, the chapter discusses possible future modifications in catalyst architecture and membrane–electrode interfaces to further enhance overall electrochemical performance.

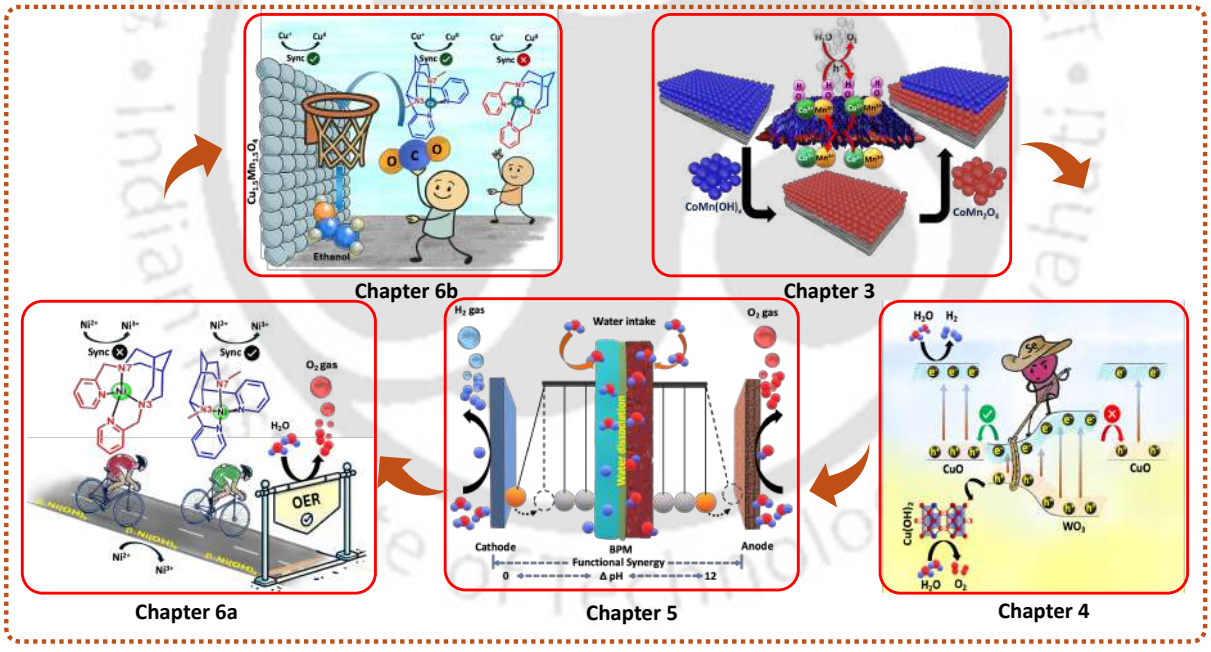

7.1. Thesis Overview:

This thesis provides a comprehensive investigation into the strategic design and development of transition metal-based electrocatalysts and membrane systems for sustainable energy conversion, focusing specifically on electrochemical water splitting and CO_2 reduction (CO_2RR). The research emphasizes modulating electronic structures and surface kinetics through elemental doping, heterojunction engineering, and the integration of novel homogeneous-heterogeneous hybrid catalytic systems. Synthesis routes predominantly involve electrochemical deposition, hydrothermal, and solvothermal methods, aimed at producing cost-effective, durable alternatives to noble-metal benchmarks. Furthermore, the work explores the development of high-performance bipolar membranes (BPM) to optimize ion transport and water dissociation for practical electrolysis. The summary and conclusions for each chapter, representing the outcomes of my Ph.D. tenure, are summarized as follows:

- **Chapter 1:** This chapter presents a comprehensive discussion on electrochemical water splitting and CO_2 reduction as promising pathways for sustainable fuel generation. It begins with an overview of the global energy landscape, emphasizing the limitations of current non-renewable energy sources and the urgent need to transition toward renewable alternatives. The section also highlights recent advancements in the design and optimization of electrode materials that govern the efficiency of electrochemical processes. Particular attention is given to the catalytic mechanisms and surface reaction kinetics of transition metal oxide and hydroxide-based electrodes, which play a pivotal role in both water splitting and CO_2 electroreduction. Furthermore, key challenges associated with the development of efficient, durable, and cost-effective electrode systems are outlined, along with strategies adopted to modulate surface activity and promote favourable adsorption–desorption behaviour of intermediate species.
- **Chapter 2:** This chapter details the synthesis strategies adopted for preparing the electrocatalysts and their corresponding support materials. It outlines the sequential procedure used for fabricating the working electrodes, primarily on carbon paper and Nickel foam substrates. In addition, a comprehensive description of the analytical and electrochemical techniques employed for catalyst characterization and performance evaluation is provided. The chapter itemizes the reagents and substrates involved in

the synthesis and provides an overview of performance metrics applied to evaluate the catalytic activity, ensuring a rigorous foundation for the subsequent experimental chapters.

- **Chapter 3.** In this chapter, we address the substantial energy input required to overcome the high potential barrier of the oxygen evolution reaction (OER). While RuO_2 and IrO_2 are benchmarks, their cost and instability in alkaline media necessitate affordable alternatives. We introduced a simple two-step electrochemical deposition strategy to synthesize a binary oxide, $CoMn_2O_4$ (CMO), which was then coated with a mixed metal hydroxide layer, $CoMn(OH)_x$, to construct a Ni/CMO/CMOH composite electrode. The rationale for this architecture stems from its ability to promote faster electron transport during OER, where Mn and Co undergo synchronized redox transitions$Mn^{3+} \leftrightarrow Mn^{4+}$ and $Co^{2+} \leftrightarrow Co^{3+}$. Because identical metal ions are present in both the oxide and hydroxide layers, charge-transfer resistance is significantly lowered. This composite achieved a remarkable overpotential of less than 300 mV at 10 mA/cm^2 in alkaline conditions, outperforming many previously reported CMO-based catalysts.
- **Chapter 4:** This chapter explores the development of earth-abundant, bifunctional electrocatalysts capable of driving overall water splitting. We introduce a photoactive cocatalyst strategy achieved by precise band-gap and band-position tuning through doping. A dendritic CuO layer was electrodeposited onto Ni foam, followed by selenium-doped WO_3(Se@WO_3), forming a CuO/Se@WO_3 p–n heterojunction. The ~6% Se substitution reduces the band gap by ~0.54 eV and introduces partial metallic character, enabling a Z-scheme charge-transfer pathway that suppresses electron–hole recombination. To further reduce resistance, a needle-like $Cu(OH)_2$ layer was electrodeposited atop the heterojunction as an efficient hole extractor. The resulting CuO/Se@WO_3/$Cu(OH)_2$ catalyst exhibited low overpotentials of 202 mV for OER and 55 mV for HER at 10 mA cm^{-2}, with favorable reaction kinetics supported by DFT calculations.
- **Chapter 5:** In this chapter, we explore a unique strategy combining homogeneous and heterogeneous catalysis to enhance charge transfer under neutral pH conditions. We synthesized β-$Ni(OH)_2$ nanoflowers on Ni foam as a heterogeneous counterpart and

utilized two geometrically distinct Ni(II) tetradentate bispidine-based complexes as homogeneous catalysts in the electrolyte. The two ligands used—flexible ($L1_{Flex}$) and rigid ($L2_{Rigid}$)—imparted different coordination environments around the Ni center. We demonstrated how these homogeneous catalysts act as redox mediators or form transient species at the phase interface, reducing activation energy and charge transfer resistance. The use of nickel throughout the system enhances redox synchronization, significantly improving catalytic activity compared to either system alone.

- **Chapter 6:** This chapter focuses on managing the transfer of reactants and ions through the development of high-performance bipolar membranes (BPM). We synthesized a BPM utilizing pyridine-functionalized polyvinyl alcohol (PVA) as the anion-exchange layer and commercial Nafion as the cation-exchange layer. To optimize water dissociation (WD) at the interface, 2D β-$Ni(OH)_2$ nanosheets were integrated as water dissociation catalysts (WDC). The large surface area of the β-$Ni(OH)_2$ nanosheets facilitates water adsorption and subsequent dissociation into H^+ and OH^-. When tested in an asymmetric electrode arrangement using hollow cuboidal CuO (anode) and Pt (cathode), the inclusion of the β-$Ni(OH)_2$ WDC reduced the transmembrane voltage for WD from 1.05 V to 0.90 V. Chronopotentiometric stability for 25 hours confirmed the durability of the membrane under rigorous electrolytic conditions.
- **Chapter 7:** The final chapter addresses the selective electrocatalytic reduction of CO_2 to value-added chemicals, specifically ethanol, under neutral pH. We reported a selective strategy enabled by the synergistic interaction between homogeneous and heterogeneous catalysts. Two geometrically distinct Cu(II) tetradentate bispidine complexes (Cu^{L1}_{Flex}) and (Cu^{L2}_{Rigid})) were utilized as homogeneous mediators to facilitate the energetically demanding CO_2-to-CO conversion. For the heterogeneous surface, a $Cu_{1.5}Mn_{1.5}O_4$ (CMO) electrode was employed. The rigid Cu^{L2}_{Rigid} complex demonstrated excellent redox synchronization with the CMO surface, promoting C–C coupling through efficient CO transfer. This hybrid architecture achieved a ~68% Faradaic efficiency for ethanol at –0.5 V vs. RHE, with a 1.5-fold increase in turnover frequency compared to the flexible system. The mechanism for ethanol selectivity was further elucidated through in-situ Infrared Reflection Absorption Spectroscopy (IRAS) and theoretical studies.

7.2. Future Perspective:

The findings presented in this thesis establish a multifaceted framework for advancing sustainable energy conversion through the strategic integration of electronic structure modulation, interfacial engineering, and hybrid catalytic architectures. By successfully demonstrating the efficacy of metal oxide/hydroxide composites, p–n heterojunctions, and homogeneous-heterogeneous cooperative systems, this work highlights the critical role of redox synchronization and charge-transfer kinetics in optimizing both the Oxygen Evolution Reaction (OER) and CO_2 Reduction Reaction (CO_2RR). The discovery that molecular catalysts, such as rigid bispidine-Cu complexes, can act as efficient redox mediators to bridge the gap between aqueous CO_2 and solid-state electrodes provides a significant blueprint for achieving high selectivity for multicarbon products like ethanol under neutral conditions. Furthermore, the development of high-performance Bipolar Membranes (BPMs) featuring functionalized polymers and integrated water dissociation catalysts (WDCs) underscores the necessity of managing ion transport and local pH environments to achieve industrial-scale durability. Moving forward, the field must transition from identifying these localized synergies to engineering integrated, scalable devices that maintain high Faradaic efficiency and structural integrity under the fluctuating power inputs characteristic of renewable energy sources.

The future perspectives of this research involve expanding these fundamental insights into complex material design and system-level integration:

- **Refinement of Redox Synchronization in Hybrid Systems**: Future efforts should focus on the precise tuning of molecular ligand environments to achieve even tighter redox potential alignment between homogeneous catalysts and heterogeneous supports. This includes investigating alternative redox-active ligands that can facilitate multi-electron transfers more efficiently causing efficient water electrolysis as well as enabling the selective synthesis of even higher-value oxygenates or long-chain hydrocarbons beyond ethanol from electrocatalytic CO_2RR.
- **Expansion of Bifunctional Heterojunctions**: Building upon the success of the Se-doped WO_3/CuO Z-scheme mechanism, future research should explore other transition metal chalcogenides and nitrides to further narrow band gaps and improve electronic conductivity. Investigating the influence of different dopant concentrations

and types on the built-in electric field at the heterojunction interface could lead to next-generation catalysts with near-zero overpotentials for both HER and OER.

- **Scaling and Long-term Durability for BPMs**: While the β-Ni(OH)$_2$-integrated BPM demonstrated stability over 25 hours, future work must evaluate these membranes under higher current densities (> 500 mA/cm^2) and over thousands of hours to meet industrial standards. Research into cross-linking strategies for functionalized PVA and other polymer backbones will be essential to enhance mechanical robustness and prevent delamination at the interfacial layer under high-pressure conditions.
- **Optimization of Asymmetric cell Configuration**: More works can be done on the integration of optimized anode and cathode materials into a single, high efficiency electrolyzer. Future perspectives include the development of asymmetric cell configurations that utilize BPMs to maintain discrete pH environments—acidic for optimal HER and alkaline for OER—thereby maximizing the performance of each half-reaction while minimizing system-wide energy losses.

LIST OF PUBLICATIONS AND CONFERENCES / WORKSHOPS ATTENDED

Scientific Contributions

- **Journal Articles Included in Thesis:**
    - **Nitul Kalita,** Alpana Sahu, Sourav Bhowmick, Mohammad Qureshi*, Synchronized redox pairs in metal oxide/hydroxide chemical analogues for an efficient oxygen evolution reaction. *Chemical Communications*, 2022, **58**, 13747-13750.
    - **Nitul Kalita,** Mohammad Qureshi*, Hollow Cuboidal Metal Oxide-Based Asymmetric Electrode Configuration for High-Performance Anion Exchange through Quaternized Pyridine-Poly(vinyl alcohol) @ Metal Hydroxide Nanosheets for Water Dissociation. *The Journal of Physical Chemistry C,* 2024, **7**, 2776-2787
    - **Nitul Kallita,** Upasana Nath, Anjana Singha, Manabendra Sarma, Mohammad Qureshi*, Electronic structure tuning to facilitate charge transfer in Z-scheme mediated CuO/Se@WO_3 aided by synchronized $Cu(OH)_2$ for efficient overall water splitting. *Journal of Materials Chemistry A*, 2025, **13**, 10723-10735
    - **Nitul Kalita,** Jagnyesh K. Satpathy, Rolly Yadav, Chivukula V. Sastri*, Mohammad Qureshi*, Integrating Homogeneous and Heterogeneous Catalytic Systems for Synergistic Water Oxidation: Role of Geometrically Distinct Bispidine Metal Complexes. *Chemistry of Materials*, 2025, **5**, 2026–2037
    - **Nitul Kalita,** Jagnyesh K. Satpathy, Ankit K. Singh, Upasana Nath, Manabendra Sarma, Chivukula V. Sastri*, Mohammad Qureshi*, Geometry-engineered copper redox interfaces drive highly selective CO_2 reduction to C_2 products. *Journal of Materials Chemistry A,* 2026, DOI: https://doi.org/ 10.1039 /D6TA02689C

- **Journal Articles off the Thesis:**
    - Ankit Sharma, **Nitul Kalita** and Mohammad Qureshi*, Push–pull electronic effects of a three-component two-heterojunction electrocatalyst for directional carrier transport in bifunctional water electrolysis. *Sustainable Energy Fuels, 2026*, **10**, 2515-2523.

- **Nitul Kalita*,** Ankit K. Singh, Mohammad Qureshi*, Self-Healing Redox Active Hydrogel-Stabilized Nickel Porphyrin Complex Infused with Metal Oxide-Hydroxide Heterojunction for Robust Bifunctional Water Electrolysis. *Applied Materials & Interfaces*, 2025, **48**, 65600-65611.
- Anjana Singha, Peeyush Pandey, Rolly Yadav, **Nitul Kalita**, Chivukula V. Sastri, Mohammad Qureshi*, Controlling Diffusion Dynamics Through Additive Electrolyte Chemistry in Flexible Free-Standing Electrode With Unified 1D-2D Morphologies, *Chemistry–An Asian Journal*. 2025, **19**, e70453.
- Moumita Chandra , Alpana Sahu , **Nitul Kalita** and Mohammad Qureshi*, Geometrically twisted intra–inter-molecular cooperative interactions for an enhanced photo-response in an ORMOSIL-based host–guest system. *Chemical Communications*. 2024, **60**, 8553-8556.
- Sourav Bhowmick, Ching Thian Moi, **Nitul Kalita**, Alpana Sahu, Shipra Suman, Mohammad Qureshi*, Spontaneous Fenton-like dye degradation in clustered-petal di-manganese copper oxide by virtue of self-cyclic redox couple. *Journal of Environmental Chemical Engineering*, 2021, **9**, 106094.
- Arabinda Baruah, Rachita Newar, Saikat Das, **Nitul Kalita**, Masood Nath, Priya Ghosh, Sampath Chinnam, Hemen Sarma* and Mahesh Narayan*, Biomedical applications of graphene-based nanomaterials: recent progress, challenges, and prospects in highly sensitive biosensors. *Discover Nano*, 2024, **19**, 103.

- **Book Chapters:**
  - *Graphene-based nanobiosensors*, 2025, Pages 95-114, ISBN: 978-0-443-23703-4, DOI: 10.1016/C2023-0-00933-5. (Publisher: Academic Press)
  - *Flow Batteries Dynamics: Analyzing Performance and Modelling,* 2026, Pages 20, ISBN: 9781003506379, DOI: https://doi.org/10.1201/9781003506379. Publisher: CRC Press)

- **Conferences/Workshops:**
  - Poster presentation at “Frontiers in Chemical Sciences-2022” organised by department of chemistry, Indian Institute of Technology-Guwahati, India.

- Poster presentation at “International Conference on Petroleum, Hydrogen, & Decarbonization-2023” organised by department of chemical engineering, Indian Institute of Technology-Guwahati, India.
- Poster presentation at “Frontiers in Chemical Sciences-2024” organised by department of chemistry, Indian Institute of Technology-Guwahati, India.
- Participated in a workshop on Hands-on-Training on Density Functional Theory of Advanced Materials-2025, organised by Centre for Advanced Computational Research, New Delhi, India.